Towards Angle and Space Resolved Photoemission: Bonding in Layered Misfit Compounds and Development of Reflective Photon Sieves

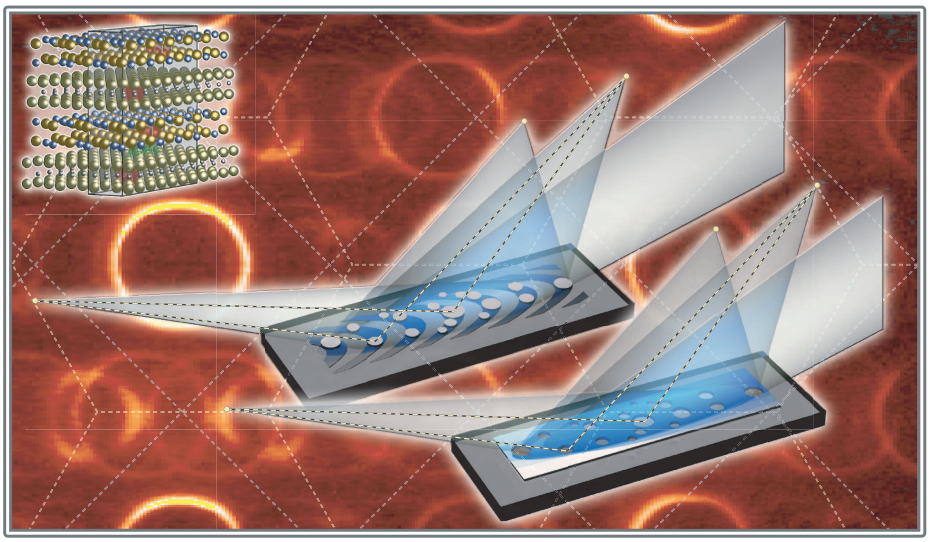

Dissertation
zur Erlangung des Doktorgrades
der Mathematisch-Naturwissenschaftlichen Fakultät
der Christian-Albrechts-Universität
zu Kiel

vorgelegt von

Matthias Kalläne

Kiel 2007

Referent: Prof. Dr. L. Kipp

Korreferent: Prof. Dr. M. Bauer

Tag der mündlichen Prüfung: 03.12.2007

Zum Druck genehmigt: Kiel, den 12.12.2007

gez. Prof. Dr. J. Grotemeyer

Dekan

Zusammenfassung

In dieser Arbeit wird die elekronische Struktur schichtartig aufgebauter, inkommensurabler Übergangsmetall–Dichalkogenid Misfitverbindungen – nämlich $(PbS)_{1.13}TaS_2$, $(PbS)_{1.14}NbS_2$, $(PbS)_{1.14}(NbS_2)_3$, $(SnS)_{1.17}NbS_2$ und $(BiS)_{1.11}NbS_2$ – untersucht. Diese Verbindungen aus hexagonal geordneten Übergangsmetall–Dichalkogeniden (ÜMDC) und kubisch geordneten Monochalcogeniden (MC) besitzen aufgrund der unterschiedlichen Symmetrie beider Teilsysteme eine komplexe Grenzschicht. Obwohl ihre Inkommensurabilität, der periodische Schichtwechsel und das Auftreten von MC Doppelschichten die Gesamtenergie der Kristalle erhöhen sollten, zeigen diese eine bemerkenswerte Stabilität. Unter Verwendung winkelauflösender Photoelektronenspektroskopie (ARPES) und Photoelektronenmikroskopie (PEM) konnte der Ursprung dieser Bindung aufgeklärt werden.

Die impulsaufgelösten photoemissionsmessungen der elektronischen Struktur zeigen Merkmale beider Teilsysteme. Insbesondere in den ÜMDC dominierten Fermiflächen sind Bänder zu erkennen, die durch Umklappprozesse an den Symmetrien beider Teilsysteme enstehen. Die Banddispersion hingegen wird offenbar nur leicht durch die verschiedenen Potentiale der Teilsysteme beeinflußt, was auf eine eher geringe Wechselwirkung zwischen den Schichten hindeutet. Während der kovalente Bindungsanteil eher von untergeordneter Bedeutung ist, da keine Banddispersion senkrecht zu den Schichten beobachtet werden kann, erscheint der ionische Beitrag signifikant: Wie experimentellen Daten zeigen, sind die ÜMDC dominierten Leitungsbänder in allen Misfitverbindungen mehr als halb gefüllt, und zwar zu etwa 0.2 bis 0.4 Elektronen pro Übergangsmetallatom. Da die Bänder der MC Schichten allerdings vollständig gefüllt sind, kann der Ladungstransfer nicht von diesen ausgehen.

Ortsauflösende Messungen von Rumpfniveauspektren der Teilsysteme von $(PbS)_{1.13}TaS_2$ konnten Ta Atome im PbS Teilsystem und Pb Atome im TaS_2 Teilsysten spektroskopisch nachweisen, welche die erhöhte Bandfüllung erklären können. Die Konzentration der substituierten Atome liegt in der Größenordnung von 5% bis 20% und führt zu einem effektiven Ladungsübertrag von etwa 0.1 Elektron pro TaS_2 Einheit, wenn ein veränderter Oxidationszustand dieser ausgetauschten Atome angenommen wird. Daher scheint ein derartiger gegenseitiger Metallatomaustausch von grundsätzlicher Bedeutung für die Stabilität von $(PbS)_{1.13}TaS_2$ und ähnlichen Misfitverbindungen zu sein, unabhängig von deren Stöchiometrie.

Die Ergebnisse der ARPES– und PEM–Messungen verdeutlichen den Bedarf an einer Kombination von Impuls– und Ortsauflösung bei der Photoelektronenspektroskopie. Zur Zeit existiert jedoch keine Apparatur zur gleichzeitigen hochauflösenden Messung beider Größen; daher wurde ein neues ortsauflösendes ARPES–Experiment entwickelt. Es basiert auf einem reflektiven Photonensieb – einer neuartigen Beugungsoptik zur Fokussierung von Synchrotronstrahlung mit verringerten Nebenmaxima und verringertem Untergrund – und wurde in dieser Arbeit erfolgreich getestet. Da das Experiment in naher Zukunft an hoch brillanten, stark kohärenten Strahlungsquellen wie dem Freie–Elektronen Laser (FEL) in Hamburg eingesetzt werden soll, wurden zur Vorbereitung ARPES Test–Experimente an diesem durchgeführt und der Einfluß der hoch intensiven FEL–Strahlung und der resultierenden hohen Photoelektronendichten auf die Photoemmissionsspektren untersucht. Es zeigte sich, dass Photoemissionsmessungen an dieser neuartigen Strahlungsquelle zwar anders und komplexer sind als solche an herkömmlichen Synchrotronstrahlungsquellen, sie dafür allerdings einen breiten Zugang zu neuartigen Erkenntnissen ermöglichen.

Abstract

In this thesis the electronic structure of the layered, incommensurate TMDC misfit compounds $(PbS)_{1.13}TaS_2$, $(PbS)_{1.14}NbS_2$, $(PbS)_{1.14}(NbS_2)_3$, $(SnS)_{1.17}NbS_2$, and $(BiS)_{1.11}NbS_2$ is investigated. Consisting of alternatingly stacked slabs of hexagonally ordered transition metal dichalcogenides (TMDCs) and cubic monochalcogenides (MCs), the layered TMDC misfit compounds are heterostructures with a complex layer–to–layer interface due to the different symmetries of the subsystems. In spite of their incommensurability, the alternation of different layers, and the occurrence of monochalcogen bilayers, all acting against a low total energy, they show a remarkable stability. Using a combination of angle–resolved photoelectron spectroscopy (ARPES) and photoelectron microscopy (PEM), the origin of the bonding between the layers is clarified in this thesis.

The ARPES investigations of the momentum resolved electronic structure show signatures of both subsystems. In particular in the TMDC dominated Fermi surface maps, umklapp shifted bands with the symmetry of both subsystems appear. However, the band dispersion seems to be only slightly affected by the different competing potentials of the layered subsystems and the interlayer interaction seems to be weak. Since band dispersion perpendicular to the layers is not ovserved, covalent bonding should only play a minor role in the bonding between the TMDC misfit layers. In contrast, the ionic contribution to the interlayer bonding seems to be significant, because the TMDC–dominated conduction bands are more than half full for all misfit compounds. The charge transfer to the TMDC subsystem could be quantified to about 0.2 to 0.4 electrons per transition metal atom. Since only completely filled MC derived bands are observable, the origin of the charge transfer cannot be attributed to the MC layers.

By performing spatially resolved measurements of core level spectra from differently terminated domains on surfaces of $(PbS)_{1.13}TaS_2$ direct spectroscopic evidence for Ta substitution into PbS layers as well as Pb substitution into TaS_2 layers could be observed, being able to explain the increased band filling. The concentrations of the substituted atoms are of the order of 5 to 20%, which leads to an effective charge transfer of about 0.1 electrons per TaS_2 unit to the TaS_2 layers if a changed oxidation state of these atoms is assumed. Therefore, such metal cross–substitution is of fundamental importance for the stability of $(PbS)_{1.13}TaS_2$ and similar misfit layer compounds and indicates that non–stoichiometry may not be a necessary condition for their stability.

The results of the ARPES and PEM measurements clearly indicate the need for a combination of momentum and spatial resolution in photoelectron spectroscopy experiments. However, there is currently no experimental station available, which allows the measurement of the momentum resolved electronic structure with simultaneous high spatial resolution. To achieve this goal, a novel spatially resolved spectroscopy experiment has been developed, using a reflective photon sieve – a novel type of diffraction optics for focusing synchrotron radiation with suppressed side lobes and reduced background. The setup has been successfully tested in this thesis. In the near future the instrument will be used at highly brilliant and coherent light sources such as the free–electron laser (FEL) in Hamburg. Therefore, we performed ARPES test experiments at the VUV–FEL and studied the influence of the highly intense FEL radiation and the resulting high photoelectron densities onto the photoemission spectra. It turned out that even if photoemission at this radiation source is different and difficult, it is in any case possible and offers to perform a variety of novel types of experiments.

Contents

1 Introduction

The investigation of the electronic structure of solids is the basis for understanding their electrical, optical, magnetic, and structural properties. On the one hand, electronic structure studies are of particular interest for basic research, because they allow to clarify a variety of physical questions and phenomena such as the nature of bonding in different crystalline compounds or the origin of phase transitions. On the other hand, a comprehensive knowledge of the electronic structure in solids is a prerequisite for technical applications such as nanoelectronics in integrated circuits or the design of new materials.

Probably the most powerful method for studying the electronic structure of solids is angle–resolved photoelectron spectroscopy (ARPES). In an ARPES experiment the electrons in a solid are excited by monochromatic photons with an energy in the ultra violet (UV) or vacuum ultra violet (VUV) range and with a certain probability emitted from the sample. By measuring the kinetic energy and momentum of the photoelectrons, detailed information on the momentum resolved, occupied electronic band structure $E(\vec{k})$, including the Fermi surface $E(\vec{k})=E_F$, as well as on electron correlation effects can be obtained. In particular, if this technique is performed with highly brilliant, tunable, narrow–band synchrotron radiation, band structures, Fermi surfaces, and correlation effects can be determined with very high precision. Moreover, by increasing the photon energy to the (soft) X–ray regime, photoelectron spectroscopy (XPS) makes it possible to gather additional information about the chemical composition of the sample and the oxidation states of its elements. Finally, since the mean free path of the excited electrons is in the range of a few atomic monolayers, photoelectron spectroscopy is an extremely surface sensitive method so that it is particularly well suited for studying the electronic structure of surfaces, interfaces, and thin films.

However, ARPES is typically a spatially integrating method with a spatial resolution of at best 50 μm. Its application for electronic structure investigations of nanostructured surfaces is therefore very limited. If the illuminated spot on the surface is larger than the structure size, the spatial origin of the photoemitted electrons cannot be distinguished. In contrast, by focusing the light spot onto the sample surface with an additional focusing device, high energy and spatial resolution can be achieved. Using such a photoelectron microscopy (PEM) experiment, it is possible to determine the local chemical composition and oxidation states in naturally inhomogeneous or intentionally structured compounds. But the local electronic band structure cannot in general be investigated. Even though photoemission electron microscopes (PEEMs) allow for the energy dependent measurement of the electron momentum or spatial distributions for the same sample successively, a simultaneous measurement of energy, momentum, and spatial origin of the photoelectrons is not possible. In fact, there is currently no experimental technique available that allows to investigate the momentum resolved electronic structure of solids with sub–micrometer spatial resolution. However, ARPES in the nanometer regime would be an important tool for studying a variety of questions regarding, for example, the properties of thin films or magnetic domains, the size dependent band structure formation in clusters, the electronic structure of nano–wires or nano–tubes, or even the miniaturization of engineered devices in technical applications, in which, e.g., finite–size effects change the electronic transport properties.

How powerful a combination of spatial and angular resolution in a photoemission experiment can be, is demonstrated in this thesis for transition metal dichalcogenide (TMDC)

misfit compounds. The physics of this class of heterostructures has for a long time been controversially discussed in the literature because the results of primarily spatially integrated measurements seem to be contradictory. Consisting of alternatingly stacked slabs of hexagonally ordered TMDCs and cubic monochalcogenides (MCs) misfit compounds have a complex layer–to-layer interface due to the different symmetries of the subsystems. This incommensurability is directly connected to a broken translational symmetry in one direction parallel to the surface and leads to a continuous change in the coordination number and the distances between the interface atoms. Nevertheless, the slabs are arranged in a very high stacking order perpendicular to the layers and the misfit crystals show a remarkable stability. In order to study the nature of the bonding between the layers, ARPES is a very promising method since particularly the measured electronic band structure and its dispersion perpendicular to the layers will help to illuminate a variety of controversially discussed topics. These current questions concern the occurrence of a possible charge transfer between the layers, the degree of electron localization, and the influence of the incommensurability on the electronic structure. In the course of this thesis it will be shown that the question of crystal stability and bonding in the layered misfit compounds can only be answered if the photoelectrons of both subsystems are analyzed separately, which again emphasizes the need for high spatial resolution in ARPES.

Towards this goal, in this thesis a novel spatially resolved spectroscopy experiment has been developed. The photon beam of the new ARPES experiment is focused by a reflective photon sieve which consists of thousands of properly placed nano–mirrors and focuses synchrotron radiation with suppressed side lobes and reduced background. Using this novel type of diffraction optics, simultaneous spatially and momentum resolved electronic structure investigations can in principle be realized. But for optimum performance the diffraction properties of reflective photon sieves have to be well characterized and optimized. Also, since an additional optical element distinctly reduces the photon flux, its use requires highly brilliant light sources such as optimized third generation synchrotron radiation facilities or free–electron lasers (FELs). This, in turn, raises questions about the potentials and limitations of photoemission at these modern light sources.

The outline of this thesis is as follows. Introducing photoelectron spectroscopy in chapter 2 and the substance class of the TMDC misfit compounds in chapter 3, ARPES measurements on a variety of misfit compounds are presented in chapter 4. They are discussed with respect to the type of bonding between the layers and the influence of the incommensurability. Followed by the presentation of spatially resolved photoemission measurements in chapter 5, the question of the origin of the stability in these compounds is discussed. Chapter 6 describes the development of the spatially resolved ARPES experiment and discusses the characterization measurements of the optical element – a reflective photon sieve – as well as first test experiments at a synchrotron beamline. Finally, in order to pave the way for future spatially resolved ARPES experiments at highly brilliant synchrotron beamlines, the results of ARPES test experiments at the VUV–FEL are presented in chapter 7.

The experiments presented in this work were performed at the Hamburger Synchrotron Strahlungslabor HASYLAB at the Deutsche Elektronensynchrotron DESY in Hamburg (Germany), the MAX–lab in Lund (Sweden), and the Advanced Light Source (ALS) in Berkeley (USA).

2 Photoelectron spectroscopy

To investigate the geometric and electronic properties of the surfaces of solids, powerful experimental techniques can be applied, such as scanning tunneling microscopy (STM), low energy electron diffraction (LEED), or angle–resolved photoelectron spectroscopy (ARPES). A main focus of this thesis is the stability of the layered TMDC misfit compounds. Since the occupied electronic band structure determines the bonding in solids, it is of particular interest in the following. In contrast to other techniques, which can only probe parts of the electronic structure like the Fermi surface (e.g., de Haas van–Alphen effect) or the local density of states (e.g., STM), ARPES allows to investigate the full momentum–resolved electronic band structure $E(\vec{k})$. Therefore, ARPES is the technique of choice in this thesis. In this chapter the relation between the measured photocurrent of an ARPES experiment and the underlying electronic band structure as well as the modern, highly precise and efficient methods for photoelectron detection will be described in more detail.

2.1 Theoretical aspects

The photoelectric effect, as theoretically explained by Albert Einstein in 1905 [1] introducing the quantum character of light (Nobel prize for this work in 1921), is the basis of angle–resolved photoelectron spectroscopy. If a photon impinges on a sample, it can totally be absorbed by an electron in an occupied electronic state. If the photon energy $h\nu$ (typically in the ultra violet (UV) or vacuum ultra violet (VUV) spectral region) is larger than the sum of the electron binding energy E_B and the work function of the sample Φ, the electron in the vicinity of the crystal surface can be liberated into the vacuum. Measuring the kinetic energy $E_{kin} = h\nu - \Phi - E_B$ and the emission angles ϑ and φ [see Figs. 2.1 and 2.2(a)], the binding energy and momentum of the electronic state before the photoemission process can be determined, i.e., the band structure $E(\vec{k})$.

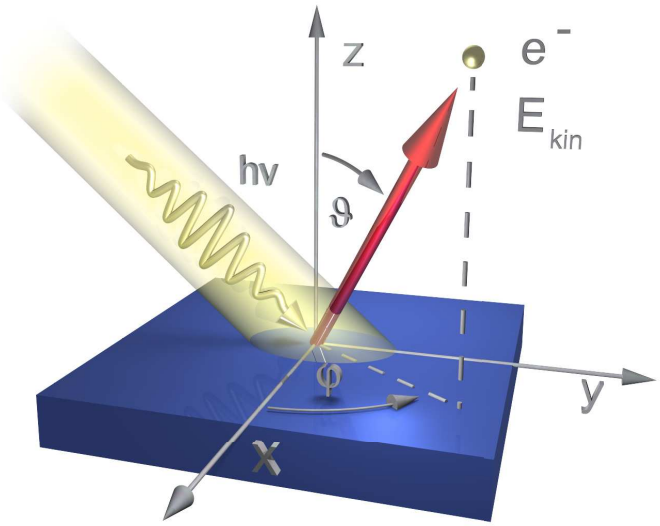

Figure 2.1: Geometry of an angle–resolved photoelectron spectroscopy experiment with incoming photon with energy $h\nu$ and outgoing photoelectron with kinetic energy E_{kin}, emitted into a direction determined by the polar angle ϑ and the azimuthal angle φ.

In order to theoretically understand the measurement results of an ARPES experiment in which the photocurrent I is detected as a function of the photon energy, the kinetic electron energy, and the emission angles, the photoemission process must, in principle, be treated as a one–step process. Following the work of Spicer [2], however, it turned out that a simple three–step model is a good approximation, subdividing the photoemission process into the three sequential steps: *(I) photoabsorption*, *(II) propagation of the excited electron to the surface*, and *(III) escape of the photoelectron into the vacuum* where it can be detected. As described in the following, the three–step model allows in particular to derive a direct connection between the measured photocurrent and the underlying electronic band structure:

(I) During the *photoabsorption* process electrons from an initial state $|i\rangle$ interact with the photon field (see Fig. 2.2), characterized by the vector potential $\vec{A}$ and the scalar potential Φ_{scalar}. The excitation probability into an unoccupied final state $|f\rangle$ can be described in first–order perturbation theory by a Golden rule–type expression:

$$I \propto \sum_{i,f} |\langle f|H_1|i\rangle|^2 \; \delta(E_f - E_i - h\nu) \; , \tag{2.1}$$

accumulating all transitions between initial and final electronic states with their appropriate energies E_i and E_f, respectively. While the energy conservation is ensured by the δ–function, the interaction is described by the first order perturbation term H_1 of the Hamiltonian H. Using the momentum operator of the interaction between electromagnetic radiation and an electron, $\vec{p_{el}} = \vec{p} - \frac{e}{c}\vec{A}(\vec{r})$ ($\vec{p} = -i\hbar\vec{\nabla}$), and a gauge of the scalar potential with $\Phi_{scalar} = 0$, the Hamiltonian has the general form:

$$H = \frac{1}{2m}(\vec{p} - \frac{e}{c}\vec{A})^2 + V = H_0 + H_1 + H_2 \; , \tag{2.2}$$

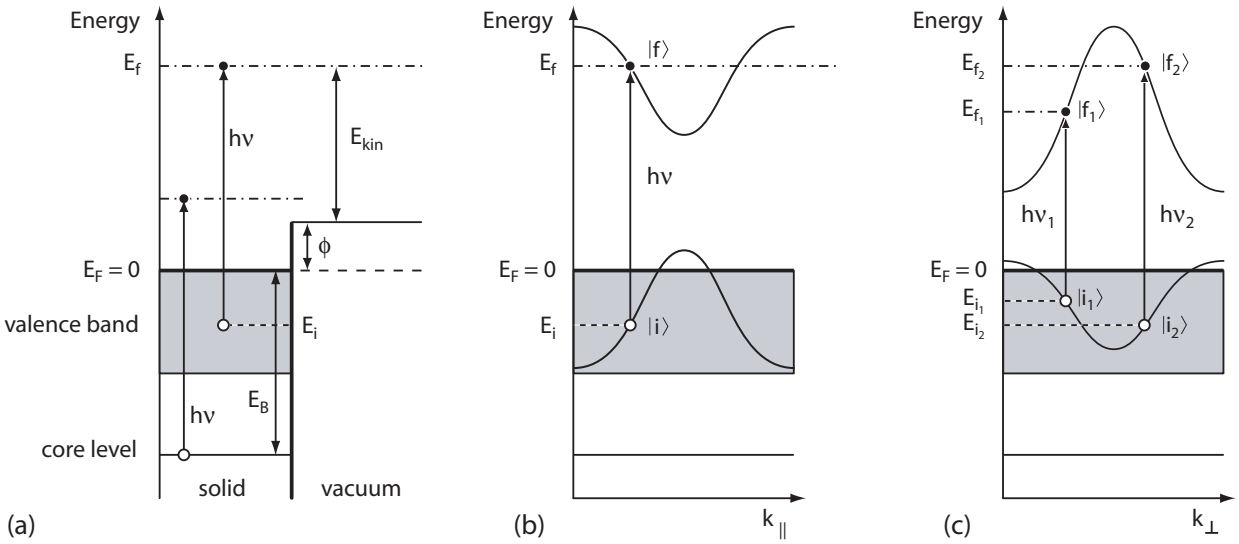

Figure 2.2: (a) In the photoemission process an electron is excited by a photon (with photon energy $h\nu$) from an initial state with the energy E_i to a final unoccupied state with the energy E_f above the Fermi level E_F. In the case of valence electrons in a crystal the band dispersion only allows specific transitions depending on the momentum (b) $\vec{k}_{||}$ parallel and (c) $\vec{k}_{\perp}$ perpendicular to the surface.

with:

$$H_0 = \frac{\vec{p}^{\,2}}{2m} + V \ , \tag{2.3}$$

$$H_1 = -\frac{e}{2mc}(\vec{A}\vec{p} + \vec{p}\vec{A}) \ , \tag{2.4}$$

$$H_2 = \frac{e^2}{2mc^2}\vec{A}\vec{A} \ , \tag{2.5}$$

where H_0 describes the unperturbated system, and H_2 the multi–photon processes that are neglected in the following ($\vec{A}\vec{A} = 0$). Using the commutation relation $\vec{A}\vec{p} + \vec{p}\vec{A} = 2\vec{A}\vec{p} - i\hbar(\vec{\nabla}\vec{A})$ and taking into account the large wavelengths of UV and VUV light in comparison to typical atomic dimensions, $\vec{A}$ can be treated as being independent of $\vec{r}$ ($\vec{\nabla}\vec{A} = 0$). This leads to the so called dipole approximation:

$$H_1 = -\frac{e}{mc}\vec{A}\cdot\vec{p} \ . \tag{2.6}$$

It can be shown [3] that, neglecting the momentum of the photon, the momentum of the electron in the initial ($\vec{k_i}$) and final ($\vec{k_f}$) state is conserved except for a reciprocal lattice vector $\vec{G}$, so that only vertical transitions in the reduced band scheme are possible (see Fig. 2.2). This can be explicitly written by introducing a matrix element M_{if} that is determined by the orbital character of the initial and final state as well as the polarization of the light:

$$|\langle f|\vec{A}\vec{p}|i\rangle|^2 = |M_{if}|^2 \ \delta(\vec{k_f} - \vec{k_i} - \vec{G}) \ . \tag{2.7}$$

If the photoabsorption process is very fast and the photoelectron immediately decouples from its binding state, the final state $|f\rangle$ can be treated as being independent of the remaining $N-1$ electron system ("sudden approximation" [4]).

(II) In the second step the excited photoelectron *propagates to the surface*. During this process it can be scattered, e.g., by other electrons or phonons, which affects the spectral peak widths, shapes, and intensities. These are particularly influenced by the lifetime of the initial–state hole and further coupling of the excited electron to the whole electronic system of the crystal. The peak positions, used to determine the band structure of the solid, are in general unaffected by the propagation process. However, the inelastic scattering produces background electrons with reduced kinetic energies. This leads to small inelastic mean free paths of electrons excited by UV and VUV radiation (sub nanometer regime [5]), so that ARPES is a highly surface sensitive method.

(III) In the third step the photoelectron *escapes into the vacuum*. This is only the case if the electron is close to the surface and the final–state energy E_f exceeds the work function of the sample Φ. The electron can be detected with the kinetic energy $E_{kin} = E_f - \Phi$ and its vacuum momentum $\vec{K}$. In order to determine the binding energy in the sample ($E_B \geq 0$), energy conservation ($E_B = h\nu - \Phi - E_{kin}$) can be used [see Fig. 2.2(a)]. Upon leaving the crystal, the electron is refracted at the crystal surface (see Fig. 2.3), similar to Snell's law in optics. The momentum component parallel to the surface is unchanged at the transition between solid and vacuum inside ($\vec{k}_{f||}$) and outside ($\vec{K}_{||}$) the crystal, only (possibly) altered by a reciprocal surface lattice vector $\vec{G}_{||}$, leading to $\vec{K}_{||} = \vec{k}_{f||} + \vec{G}_{||}$. Therefore, with the notation of Fig. 2.1 the surface parallel component of the photoelectron momentum can be calculated by:

$$\vec{k}_{f||} = \begin{pmatrix} k_{f||x} \\ k_{f||y} \end{pmatrix} = \sqrt{\frac{2m}{\hbar^2}E_{kin}} \ \sin\vartheta \begin{pmatrix} \cos\varphi \\ \sin\varphi \end{pmatrix} \ . \tag{2.8}$$

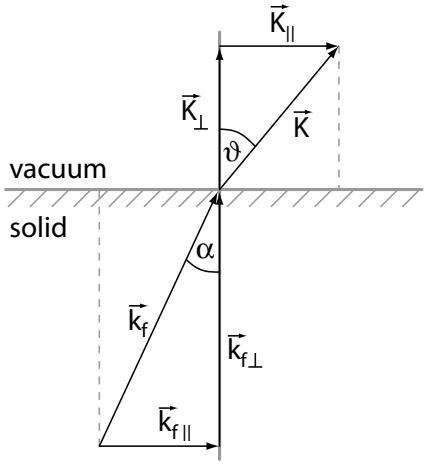

Figure 2.3: Momentum relation at the transition between solid and vacuum with conserved momentum component parallel ($\vec{k}_{f||} = \vec{K}_{||}$) and a change in the momentum component perpendicular to the surface ($\vec{k}_{f\perp} \neq \vec{K}_{\perp}$).

In contrast, the perpendicular component of the momentum is changed at the crystal surface inside ($\vec{k}_{f\perp}$) and outside ($\vec{K}_{\perp}$) the sample due to the broken symmetry in this direction. Assuming free–electron like dispersion of the final states in the sample, shifted with respect to the final states outside the sample by a phenomenological inner potential V_0 ($\frac{\hbar^2}{2m}\vec{k}_{f\perp}^2 = \frac{\hbar^2}{2m}\vec{K}_{\perp}^2 + V_0$), the absolute value of $\vec{k}_{f\perp}$ can be estimated by:

$$k_{f\perp} \approx \sqrt{\frac{2m}{\hbar^2}(E_{kin}\cos^2\vartheta + V_0)}\ . \tag{2.9}$$

As the inner potential is an empirical parameter, it has to be estimated, e.g., by fitting the experimental band dispersion in the $\vec{k}_{\perp}$–direction.

In summary, using the three–step model the measured photocurrent can be described by:

$$I \propto \sum_{\vec{k}_i,\vec{k}_f} |M_{if}|^2\ \delta(E_f - E_i - h\nu)\ \delta(\vec{k}_f - \vec{k}_i - \vec{G})\ \delta(E_{kin} - E_f + \Phi)\ \delta(\vec{K}_{||} - \vec{k}_{f||} - \vec{G}_{||})\ . \tag{2.10}$$

This formula directly describes the relation between the measured photocurrent $I(E,\vec{k})$ and the electronic band structure inside the crystal $E_i(\vec{k}_i)$, which can exactly be determined for the parallel momentum component $\vec{k}_{i,||}$, but only be estimated for the perpendicular momentum component $\vec{k}_{i,\perp}$ under reasonable assumptions for the final states as discussed above. While the peak positions are described by the δ–functions that represent energy and momentum conservation during the photoemission process, the photocurrent intensity is described by the matrix element M_{if}. However, in contrast to the assumptions of equation (2.10) for which a model of independent electrons was assumed, the experimentally observed peaks are not δ–like but broadened by lifetime effects and the instrumental resolution.

2.2 Photoemission modes

The measurement of the electronic structure of solids can be performed by different photoemission modes. Depending on the photon energy, these can be subdivided into X–ray photoelectron spectroscopy (XPS) and ultra–violet photoelectron spectroscopy (UPS) modes. Using photon energies in the extreme ultraviolet and (soft) X–ray regime ($h\nu > 100$ eV), XPS is a powerful method to analyze the non–dispersive core–level electrons by measuring the photocurrent $I = I(E_{kin})$. Since core–level binding energies are characteristic for the chemical composition of a material and sensitive to the chemical environment of the atoms (in particular their oxidation state), XPS is often used for chemical analysis [6] (electron spectroscopy for chemical analysis: ESCA). By investigating the XPS line shapes, additional information about many–body effects can be obtained such as core hole interactions with conduction band electrons [7].

On the other hand, employing UPS methods, valence electrons and the dispersion of the electronic band structure can be mapped directly. Applying photon energies in the (vacuum) ultraviolet or extreme ultraviolet regime ($h\nu \leq 100$ eV), the photocurrent $I = I(E_{kin}, h\nu, \vartheta, \varphi)$ is measured energy and angularly resolved. By the variation of a subset of the parameters $E_{kin}, h\nu, \vartheta, \varphi$, different photoemission modes can be realized. In this thesis the following modes were applied:

Energy distribution curve (EDC): The EDC mode is one of the most commonly used photoelectron spectroscopy modes. The photoelectron intensity $I(E_{kin})$ is measured in dependence of the kinetic energy at fixed values of emission angles and photon energy. Depending on the kinetic energy, $\vec{k}_\perp$ as well as $\vec{k}_{||}$ vary from datapoint to datapoint [see equations (2.8) and (2.9)], caused by the variation of both the initial and the final states. Changing the detection angles and measuring a successive series of EDCs, it is possible to map the electronic structure, e.g., along the high–symmetry directions of the crystalline sample. Taking, on the other hand, EDCs for different photon energies, more detailed information on the $\vec{k}_\perp$ dependence of the photoelectron spectra [see equation (2.9)] can be obtained.

Photoelectron angular distribution (PAD): In the PAD mode the photoelectron intensities $I(\vartheta, \varphi)$ are measured as a function of the photoelectron emission angles ϑ and φ (see Fig. 2.1). $h\nu$ and E_{kin} are kept fixed. In contrast to EDC measurements, the initial and final state energies stay constant. The resulting map represents a $\vec{k}_{||}$–cut through the $\mathrm{E}(\vec{k})$ space with high intensity values at those points in k–space where transitions between initial and final states are allowed. Taking in particular a PAD of electrons bound at the Fermi level ($E_B = E_F = 0$), the topology of the Fermi surface can be measured [8].

Employing modern multichannel photoelectron spectrometers and high intensity light sources like third generation synchrotron radiation facilities, the photoemission data acquisition times are drastically reduced in comparison to former singlechannel detection. Today, datasets can be measured that consist of PADs in a wide range of photon and kinetic energy regions (e.g., the full valence band), allowing to obtain five–dimensional datasets $\mathrm{I}(E, k_{||x}, k_{||y}, k_\perp)$. If the angle–resolved measurements are combined with XPS measurements, a nearly complete picture of the electronic structure can be obtained.

2.3 Experimental aspects

Since the experimental discovery of the photoelectric effect by Hertz in the 1880s [9], there was a great experimental effort (e.g., by K. Siegbahn, Nobel prize in 1981) in developing photoelectron spectroscopy to the most powerful experimental method for investigating the electronic structure of atoms, molecules, and solids. In particular, the experimental conditions have improved considerably, e.g., with the development of ultra high vacuum (UHV) technology, electron spectrometers, and synchrotron radiation facilities, providing highly brilliant radiation in a wide range of photon energies (microwave to hard X–ray radiation). The accuracy of ARPES measurements mainly depends on four aspects: the energy and angular resolution of the photoelectron spectrometer, the beam quality of the light source, i.e., tunability, brilliance and monochromatizity, the vacuum conditions that should be at least in the 10^{-10} mbar range in order to prevent contamination of the surface, and the sample quality. In the following subsections a brief introduction into the main principles of photoelectron detection as well as the experimental endstations at synchrotron radiation sources used in this thesis is presented.

2.3.1 Photoelectron detection

High resolution ARPES experiments can employ different types of electron analyzers such as plane or cylindrical mirror analyzers, time of flight analyzers, or hemispherical deflection analyzers. In order to detect photoemitted electrons with high energy and angular resolu-

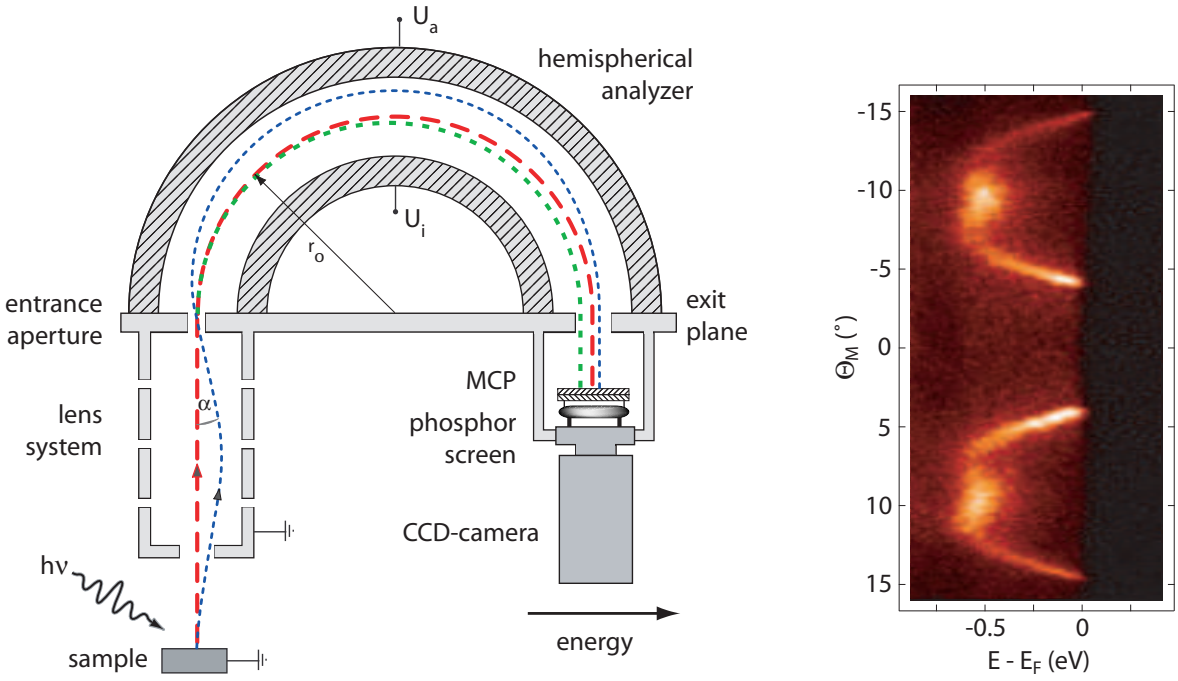

Figure 2.4: (Left) The photoelectrons are detected with a hemispherical deflection analyzer. It consists of an electron lens that images the electrons angle or spatially resolved into the entrance aperture, and a hemispherical capacitor that deflects the electrons depending on their energy onto a two dimensional CCD detector. (Right) Photoemission intensity map of $(PbS)_{1.13}TaS_2$, as it is taken by an ARPES analyzer with 2D–CCD detector in angle–resolved mode (high brightness represents high intensity).

tion, hemispherical deflection analyzers are most often used. As illustrated in Fig. 2.4(left), they consist of three parts: an electrostatic lens system, a hemispherical capacitor, and an electron detection device.

The electrostatic lens system performs three tasks: (i) *imaging* the electrons onto the entrance aperture of the hemispherical capacitor, (ii) *retarding* the incoming electrons to the so called pass energy E_{pass}, and (iii) ensuring a high electron *transmission* through the lens. The lens system can be used in different modes providing, e.g., energy and angular or energy and spatial resolution, depending on the applied lens voltages. In the energy and angularly resolved mode all incoming electrons with the same photoemission angle Θ_M (see Fig. 2.5) are imaged onto the same position in one direction of the capacitor's entrance aperture [see Fig. 2.4(right)]. Perpendicular to this angularly dispersive direction, all electrons of a limited emission angle range are focused in the center of the capacitors entrance aperture. This energy dispersive direction is normally delimited by an entrance slit (slitwidth: s_1), partly determining the instrumental energy resolution. The energy resolution ΔE of the spectrometer also depends on the kinetic energy of the electrons passing the capacitor at its central radius r_0. Therefore, the retardation of the incoming electrons to a constant pass energy E_{pass} ensures a fixed energy resolution for all electrons at r_0. The instrumental energy resolution can be calculated by:

$$\Delta E = E_{pass}\left(\frac{s_1 + s_2}{4r_0} + \alpha_{max}^2\right) , \tag{2.11}$$

where s_1 and s_2 are the entrance and exit slit widths in the energy dispersive direction of

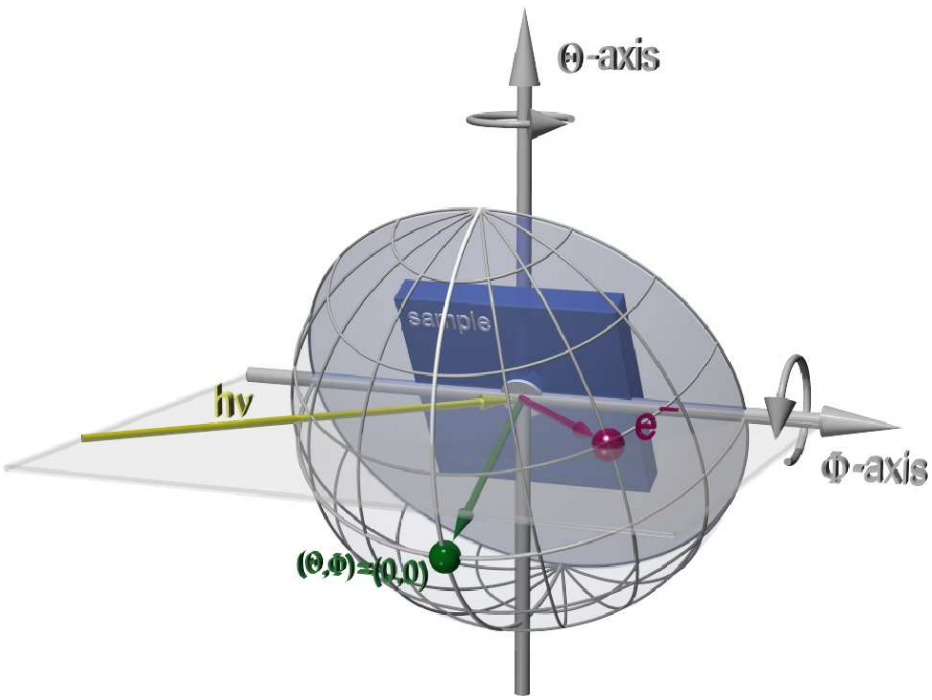

Figure 2.5: Geometry of the photoelectron detection process with movable sample, employing a 2D electron analyzer. Electrons that are emitted parallel to the analyzer entrance slit (rectangular plane) can be detected in parallel if an angle resolved lens mode is used. The illustrated electron (red dot and arrow) is emitted into the direction $\Theta_M = -45°$, and $\Phi_M = 22.5°$ with respect to the surface normal (green dot and arrow).

the capacitor and α_{max} is the maximum acceptance angle of the photoelectrons.

While the angular or spatial resolution of the spectrometer depends on the lens system, the energy resolution is determined by the capacitor. The capacitor deflects the electrons (that are imaged into the entrance slit) into different positions of the exit slit, depending on their kinetic energy. This leads to an energy dispersion in the capacitor's exit plane. In contrast, in the (perpendicular) angularly dispersive direction the electron dispersion that was generated by the lens system stays unchanged.

Finally, the electrons are detected by an electron detection device. In modern electron analyzers two–dimensional CCD detectors or delayline detectors are most often applied. Since the use of these two–dimensional detectors supersede an exit slit at the capacitor, the exit slit width s_2 in equation 2.11 depends on the pixel size of the detector (about 10 μm), which is in general smaller than the entrance slit width s_1 ($\geq$ 100 μm). Assuming a central radius of up to $r_0 = 250$ mm, energy resolutions of $E_{pass}/\Delta E$ up to 10000 can be achieved.

A photoemission intensity map, as measured by an ARPES analyzer with 2D–CCD detector in angle–resolved mode, is illustrated in Fig. 2.4(right). It can be seen that one single CCD image contains both energy and angle (momentum) information. However, an electron analyzer does not directly measure the physically interesting parameters electron energy E_i and momentum $\vec{k}_i$ in the sample but the kinetic energy of an electron outside the sample in front of the analyzer $E_{kin,a}$ and the photoelectron emission angles (machine angles) Θ_M and Φ_M.

The electron binding energy E_B can be determined as illustrated in Fig. 2.6. After section 2.1, a photoelectron excited to the final state energy E_f has a kinetic vacuum energy in front of the sample of $E_{kin,s} = E_f - \Phi_s$. Since the work function of the sample Φ_s generally differs from the work function of the analyzer Φ_a and the electrical contact between sample and analyzer ensures an equilibrium of the respective Fermi levels E_F, the kinetic energy as measured by the analyzer ($E_{kin,a}$) is shifted by the work function difference ($\Delta\Phi = \Phi_s - \Phi_a$). Therefore, the initial state energy of the electron can be determined by an electron analyzer without the knowledge of Φ_s by using the relation:

$$E_i = E_{kin,a} + \Phi_a - h\nu \ . \tag{2.12}$$

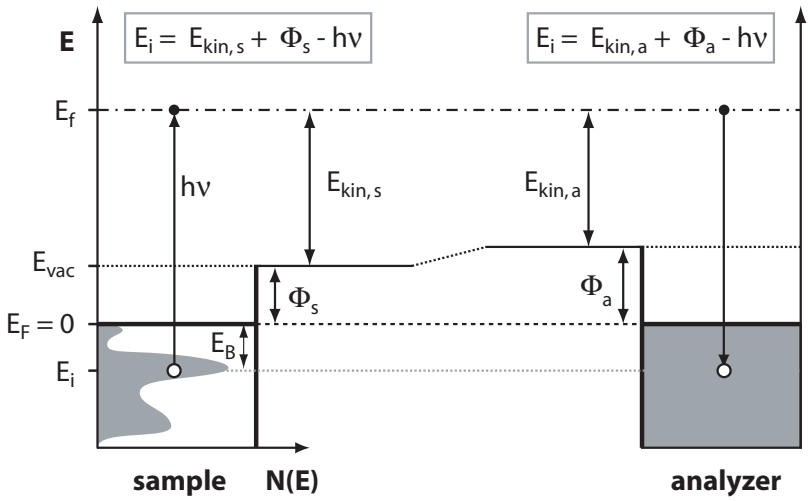

Figure 2.6: Energy scheme of a photoemission experiment with different work functions of sample and electron analyzer, Φ_s and Φ_a, respectively.

Measuring the kinetic energy of electrons emitted from the Fermi level in a metal (e.g., polycrystalline gold), the work function of the analyzer Φ_a can be determined very precisely so that E_i can easily be calculated. However, in order to calculate the momentum values $k_{||}$ and $k_\perp$, the kinetic energy of the electrons with respect to the sample $E_{kin,s}$ [see equations (2.8) and (2.9)] has to be taken into account:

$$E_{kin,s} = E_i - \Phi_s + h\nu \ = E_{kin,a} - \Delta\Phi \ , \tag{2.13}$$

with the work function difference between sample and analyzer $\Delta\Phi$. Assuming $\Phi_s > \Phi_a$ (a bias voltage at the sample can easily achieve this situation), the low energy onset in a photoemission spectrum ($E_{kin,s} = 0$) allows to measure the work function difference by $\Delta\Phi = E_{kin_{min},a}$.

The determination of the momentum in the sample $\vec{k}_i$ from the electron detection angles can be done by geometrical considerations. In order to obtain datasets for a wide solid angle a sample goniometer is normally scanned along two perpendicular polar–axes. These so called machine angles Θ_M and Φ_M (see Fig. 2.5 and [10]) – similar to longitude and latitude coordinates – are related to the polar and azimuthal angles ϑ and φ by:

$$\cos\vartheta \ = \ \cos\Theta_M \cdot \cos\Phi_M \ , \tag{2.14}$$

$$\tan\varphi \ = \ \frac{\sin\Phi_M}{\tan\Theta_M} \ . \tag{2.15}$$

Corresponding $k_{||x}$ and $k_{||y}$ values can be calculated, using the relations:

$$k_{||x} \ = \ k \cdot \sin\Phi_M \ , \tag{2.16}$$

$$k_{||y} \ = \ k \cdot \cos\Phi_M \cdot \sin\Theta_M \ , \tag{2.17}$$

$$k \ = \ \sqrt{\frac{2m}{\hbar^2} E_{kin,s}} \ . \tag{2.18}$$

Such experimental setups can achieve angle resolutions of better than $\Delta\alpha = 0.1°$.

Therefore, using a modern ARPES spectrometer a very detailed investigation of the electronic structure of solids is possible, in particular, if this technique is combined with highly brilliant, tunable light sources as described in the following section.

2.3.2 Radiation sources

Several different types of light sources are used for photoemission experiments. Providing unpolarized light, X–ray tubes with high photon energies in the range of 1–100 keV and polychromatic radiation as well as gas discharge or plasma lamps with low energy line spectra (e.g., He–discharge lamps: $h\nu_{He-I} = 21.22$ eV , and $h\nu_{He-II} = 40.8$ eV) are the most commonly used laboratory radiation sources. Because of the high photon energies X–ray tubes are only used in XPS measurements. Recent developments additionally made lasers available, providing polarized, monochromatic, and highly coherent radiation. Being limited to photon energies of several eV, lasers only allow to investigate the lowest bound valence electrons of the solid. Even though discharge lamps provide higher photon energies, similar to lasers the lack of tunability prohibits photon energy dependent ARPES scans or measurements with specific photon energy requirements like resonant photoemission.

Synchrotron radiation sources overcome these restrictions, providing a continuous spectrum (microwave to hard X–ray regime) of polarized, partly coherent, and highly brilliant

Facility	HASYLAB	ALS	MAX–lab
Undulator beamline	BW3	BL7	BL31
Source energy	4.5 GeV	1.9 GeV	0.55 GeV
Electron beam current Positron beam current Injection period	 140 mA – 90 mA 8 h	400 mA – 200 mA 8 h	250 mA – 80 mA 3 h – 6 h
Monochromator energy resolution	ΔE[meV] $\approx 2.16 \cdot 10^{-4}$ $\times$ E[eV]$^{1.5}\cdot$ s[μm]	30 meV at h$\nu = 100$ eV slit size = 40μm $E/\Delta E \leq 8000$	115 meV at h$\nu = 100$ eV slit size = 30μm
Slit size s	70 μm – 500 μm tunable	 tunable	 tunable
Beamline energy range	40 – 1800 eV	60 – 1200 eV	15 – 170 eV
Spot size (hor. $\times$ vert.)	300×100 μm^2	50×50 μm^2	1.5×1.5 μm^2
Maximum photon flux at sample	$\sim 10^{12}$ ph./s in 0.1% BW	$\sim 10^{12}$ ph./s in 0.01% BW	$\sim 10^{10}$ ph./s
Photoelectron analyzer	SPECS PHOIBOS 150	SCIENTA SES–100 and R4000	VG CLAM2
Electron detector	MCP–CCD combination	MCP–CCD combination	single channeltron
Electron detection angle	variable (sample rotation)	variable (sample rotation)	fixed angle ($47^\circ \pm 3^\circ$)
Radius of the hemispherical analyzer	150 mm	100 mm (SES 100) 200 mm (R4000)	100 mm
Best energy resolution	1 meV	3 meV (SES 100) 0.25 meV (R4000)	~ 100 meV
Best angular resolution	0.1°	0.12° (SES 100) 0.1° (R4000)	–

Table 2.1: Comparison of the synchrotron beamlines BW3 at HASYLAB (Hamburg, Germany) [11], BL7 at the ALS (Berkeley, USA) [12, 13], and BL31 at MAX–lab (Lund, Sweden) [14].

(number of photons per time, divergence, spot size and spectral bandwidth) radiation. As synchrotron radiation is produced by accelerating relativistic electrons, its generation is much more complex than for the above mentioned laboratory radiation sources. Discovered by an energy loss at the bending magnets in electron storage rings, today's third generation synchrotron facilities use periodic magnet structures called wigglers and undulators, providing photon beams with strongly increased coherence and brilliance (for more details see [12]). In order to do photoemission, the polychromatic radiation has to be filtered with a crystal or grating monochromator, providing energy resolutions of some meV, depending on the photon energy. The most important parameters of the synchrotron beamlines and experimental stations used in this thesis like photon energy, energy resolution, photon flux at the sample, or beam size are summarized in Tab. 2.1.

A further development of synchrotron radiation sources are free–electron lasers (FEL) like the recently commissioned VUV–FEL at HASYLAB (Hamburg). Using a linear electron accelerator and increased electron densities in extremely long undulators, an FEL produces tunable, short pulsed, and highly coherent radiation, exceeding the brilliance of third generation synchrotron radiations facilities by several orders of magnitude.

3 Transition metal dichalcogenide misfit compounds

Crystalline systems with broken translational symmetry due to different competing potentials are called misfit compounds. A misfit can for example be found in incommensurate charge–density–wave (CDW) systems [15,16] – compounds with a modulated electron density. Layered transition metal dichalcogenide misfit crystals are another kind of misfit compounds, composed of two subsystems with an irrational ratio of one in–plane lattice constant. They are built of alternatingly stacked slabs of hexagonally ordered transition metal dichalcogenides (TMDCs) and cubic monochalcogenides (MCs) with a lattice mismatch between 8 % and 28 % due to the different symmetries of the subsystems. But eventhough this so called incommensurability leads to a continuous change in the coordination number of the interface atoms and the distances between them, the slabs are in a very high stacking order perpendicular to the layers, and the crystals show high stability. To understand the stability it is important to give a brief overview of the geometric and electronic structure of the TMDC–misfit compounds and their subsystems.

3.1 Cubic monochalcogenides

The cubic monochalcogenides (MCs) are compounds with the general formula MX where M denotes a metal atom, i.e., Sn, Pb, Bi or rare earth metals, and X denotes the chalcogen atoms S or Se. The MC crystals which are part of the misfit compounds studied in this thesis, are PbS, SnS, and BiS.

PbS (galena) is found in nature and crystallizes in the rock salt structure [see Fig. 3.1(a)]. It shows strong ionic but also covalent bonding parts [17] and a strictly three–dimensional character. In contrast, SnS [18–20] is a layered compound with two different structure types. The so called β–phase exists above the transition temperature of $T_0 = 905$ K and forms double layers with distorted rock salt structure. The α–phase has a more complex structure identical to GeS with the double layers being less symmetric. The group IV B compounds the Pb and Sn atoms are in the formal oxidation state of 2+ and belong to the IV–VI semiconductors with a direct band gap of 0.29 eV at 4.2 K to 0.41 eV at 300 K in the case of PbS [21] and 1.12 eV at 77 K to 1.08 eV at 300 K for SnS [22], respectively. In contrast, the group V A element Bi is not found in a bismuth (II) sulphide configuration (BiS), but only as Bi_2S_3 with a formal oxidation state of 3+.

As the rock salt structure is most similar to the MC crystal structure in the misfit compounds, the properties of PbS and especially its surface will be described in more detail. The rock salt crystal structure consists of two face centered cubic (fcc) lattices that lead to a Brillouin zone with body centered cubic (bcc) symmetry. High symmetry points Γ_B, X_B, K_B and L_B are shown in Fig. 3.1(b). Its surface Brillouin zone in the (001)–direction, equivalent with the Brillouin zone of one crystal slab, is a square Brillouin zone with the high symmetry points Γ (equivalent to Γ_B), X (equivalent to L_B), and M (equivalent to X_B).

The surface geometric and electronic structure of PbS has been discussed controversially in the literature for a long time. A surface core level shift (SCLS) in PbS of +0.17 eV for the Pb and -0.37 eV for the S core levels had theoretically been predicted [17] due to a higher ionicity of the surface atoms, but was not observed experimentally for a long time. Only at lower temperatures (T = 100 K) the S $2p$ core level could clearly be identified with a SCLS of +0.3 eV [23,24]. The discrepancies of experiment and theory are explained with the

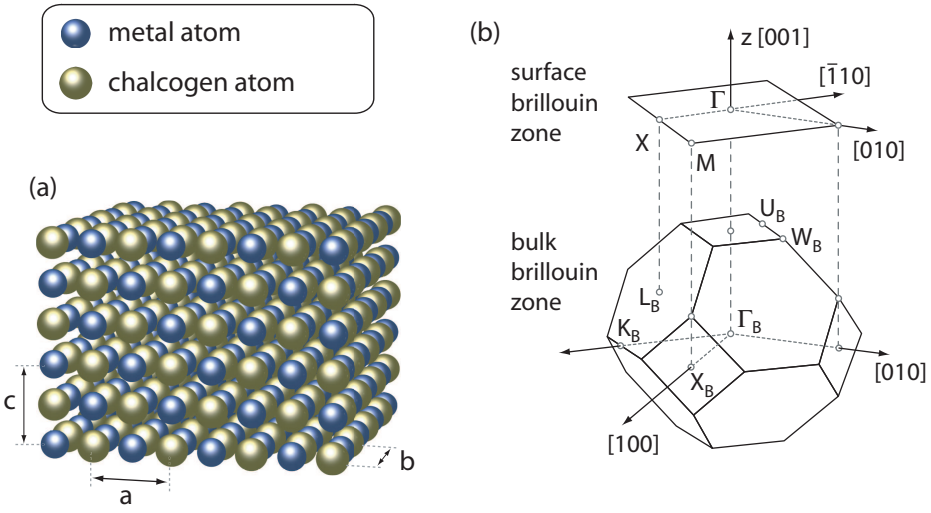

Figure 3.1: (a) Rock salt bulk crystal and (b) corresponding bulk and surface Brillouin zone in [001] direction.

strong electron–phonon coupling in PbS, making it difficult to isolate the SCLS–shifted part experimentally. Another explanation could be a relaxation of the whole surface layer [17] or only of one atom kind [25–27] so that the surface structure is changed. This leads to a reduction of the surface core level shift, but could only be observed in the isoelectric system PbTe [28] experimentally until now. A change in the surface geometry can also be motivated by the decreased Madelung constant of the NaCl (100) surface structure of about 4% in comparison to the bulk [29].

A second change in the surface structure appears, when cleaving PbS under ultra high vacuum (UHV) conditions. Typically, 0.1% of the S surface atoms are evaporated into the vacuum so that PbS becomes an n–type semiconductor at the surface after about 3 hours, independent of the bulk conducting type [30]. A Fermi level shift towards the conduction band of about +0.26 eV without changing any band structure features is observed (rigid band model). After evaporation of oxygen for at least 3 hours the band structure looks like freshly cleaved, i.e., unshifted, leading to the conclusion that the surface structure can be repaired by incorporating oxygen into the sulfur vacancies.

In addition to the sulfur evaporation, an exchange of Pb by metal atoms can also be found at PbS–metal interfaces [31]. After the evaporation of Cr, Co, Pd, Au, or In on the PbS surface, an adatom–Pb exchange has been observed. The substitution is strongest in the case of the highly reactive Cr and weakest in the case of the less reactive Au atoms. It has been determined using X-ray photoelectron spectroscopy (XPS) by the observation of additional Pb 5*d* core level states with binding energies similar to pristine Pb metal [31] and can similarly be observed in the isoelectrical system PbTe [32].

In conclusion, the above shows that the surface structure of the rock salt like compound PbS can be stabilized by relaxation, but also seems to reconstruct especially in a low pressure environment. As sulfur is mainly involved in the reconstruction process, the system tends to exchange its Pb surface atoms, if a highly reactive metal atom is offered.

3.2 Transition metal dichalcogenides

Transition metal dichalcogenides (TMDCs) are layered compounds with the general formula TX_2, where T denotes a transition metal atom of group IV B (Ti, Zr, Hf), V B (V, Nb, Ta) or VI B (Cr, Mo, W) and X denotes a chalcogen atom of group VI A (S, Se, Te). The layers are composed of transition metal atoms which are sandwiched between octahedrally (T type) or trigonal prismaticly (H type) ordered chalcogen atoms (see Fig. 3.2). The octahedral and trigonal prismatic layers can be stacked in different sequences like 1T, $2H_a$, $2H_b$, $3R$, $4H_a$, $4H_b$, $4H_c$, where the number denotes how many sandwich layers build up a unit cell [33] and the characters determine the symmetry. For example, the $2H$ structure is composed of two octahedral layers per unit cell. In the $2H_a$ polytype the layers are rotated by an angle of 180° to each other, while in the $2H_b$ polytype an additional in–plane shift perpendicular to the a direction occurs, as illustrated in Figs. 3.2(a) and 3.2(b).

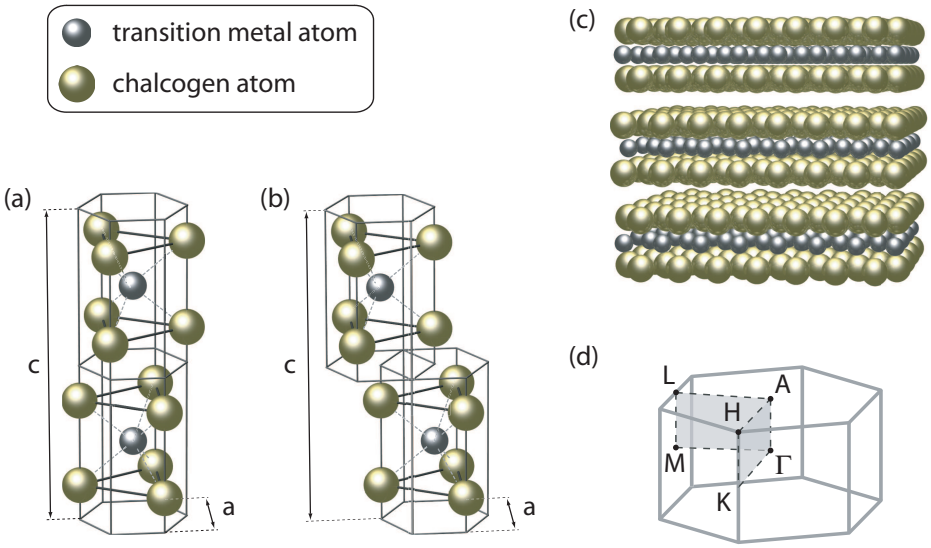

Figure 3.2: (a) Unit cell of transition metal dichalcogenides in the octahedral $2H_a$ and (b) in the $2H_b$ structure, (c) layered stacking order with van der Waals gap in between the layers, and (d) corresponding Brillouin zone.

In contrast to the strong covalent and ionic intralayer bonding, the interlayer forces have weak van der Waals character, so that most of the crystals electrical and optical properties are quasi two–dimensional. Therefore, the Brillouin zone is hexagonal and the electronic structure has a quasi two–dimensional character (see Fig. 3.2(d)).

The electronic structure of TMDCs can be described by a simple model developed by Wilson and Yoffe [33]. As illustrated in Fig. 3.3, the electronic density of states (DOS) can be divided into occupied bonding (σ) and unoccupied anti bonding ($\sigma*$) bands, derived from chalcogen s and p orbitals. In the energy gap between the σ and the $\sigma*$ states with a width of some eV, the transition metal d state derived e_g and t_{2g} bands can be found. The e_g bands originate from the d_{xz} and d_{yz} orbitals and are unoccupied. In contrast to them, the d_{z^2}, $d_{x^2-y^2}$ and d_{xy} derived t_{2g} bands are partly occupied, depending on the kind of the transition metal and the geometric structure of the unit cell.

Using a simple ionic model, the electronic properties of the TMDCs can be understood qualitatively in this model (see Fig. 3.3): If the transition metal atoms of group IV B

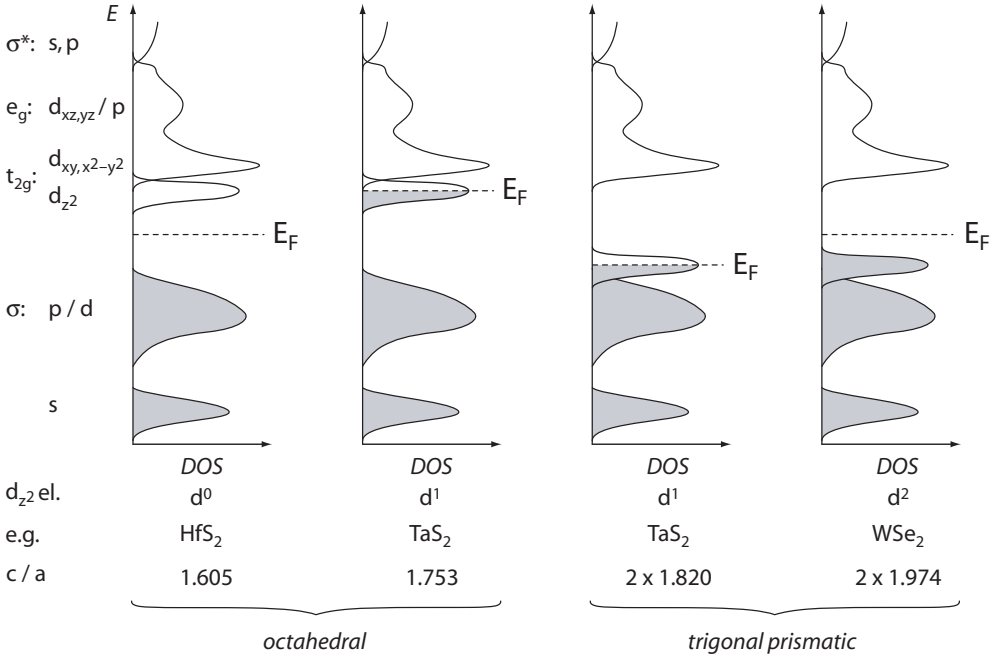

Figure 3.3: Simple electronic density of states (DOS) model of the transition metal dichalcogenides in octahedral (T type) and trigonal prismatic (H type) crystal structure with bonding and anti bonding chalcogen derived states σ and $\sigma*$ and transition metal d state derived e_g and t_{2g} states (after Ref. [33]).

transfer four electrons (s and d electrons) to the surrounding chalcogen p orbitals, a noble gas configuration is achieved with a depopulation of the d orbitals (d^0). This leads to a semiconducting behavior of these TMDCs. The same argument can be used to explain the semiconducting character of the group VI B compounds. In their case two electrons remain in the d_{z^2} orbital (d^2), which is lowered in energy due to the trigonal prismatic crystal arrangement. It is hybridized with the σ bands and totally filled. In contrast, the group V B TMDCs (d^1) have a metallic character. The only remaining d electron leads to a half filled d_{z^2} band of these T– or H–type compounds. Even if there are deviations from this model as, e.g., for the Ti compounds, where an overlap of the d_{z^2} bands with the σ states leads to a semimetallic character [34], it shows the dominating role of the d_{z^2} band regarding the electronic properties of the crystal.

A remarkable property of the TMDCs is the possibility to introduce foreign atoms into the vdW gaps of the crystals [35–38]. This so called intercalation process can take place during evaporation in the UHV on the crystal surface, electrochemically, by immersion in solution, or directly during the crystal synthesis and can be done with a variety of substances like alkali or other metals (e.g., copper or silver), organic molecules, or $3d$ transition metals. As TMDCs can only be intercalated by electron donor species and an electron transfer from the intercalant to the TMCD slabs can always be observed, charge transfer seems to be the driving force of the intercalation process [38, 39]. Following the rigid band model (RBM), the electrons are transferred from the intercalant to the TMDC valence band without changing the electronic structure of both subsystems during intercalation. This results in an increased ionicity and a stronger bonding between the layers, while the resulting band structure of the whole intercalated system is assumed to be the simple superposition of both subsystem band structures. Even though the RBM helps to understand the electronic

changes during the intercalation process qualitatively, many features of the resulting band structure – especially if the intercalation process leads to structural changes of the TMDC part – cannot be explained by it. An example is the reduced dispersion of the electronic bands in the direction perpendicular to the layers, resulting from the increased interlayer spacing after intercalation.

In the strictest definition intercalation denotes a reversible process of atom insertion into the van der Waals gap of a nearly unchanged TMDC host structure. But even if there are intercalation processes that can be reversed as in K_xVSe_2, where K can be substituted by later intercalation with Na [40], the crystal structure of the intercalated system is normally changed. This ranges from an increased interlayer spacing as mentioned before and charge transfer induced structural intralayer changes to changes in the layer stacking due to modified interlayer interactions [35, 38, 41–43]. Using a much wider definition, TMDCs are intercalated if there are foreign atoms, molecules, or even crystals in the van der Waals gap without disturbing the layered character. The last kind of substances are the so called TMDC misfit compounds.

3.3 Misfit compounds

The transition metal dichalcogenide misfit compounds are layered crystals, composed of two subsystems, i.e., the hexagonal ordered transition metal dichalcogenides (TMDCs) and the cubic rock salt like monochalcogenides (MCs). The subsystems are arranged in an alternating stacking order with double layers of the MC inserted into the van der Waals gap of the TMDC layers. Due to the similarities to intercalated TMDCs, the misfit compounds can be considered as intercalation crystals with a strongly increased vdW gap. The crystals can be described by the general formula $(MX)_{1+\delta}(TX_2)_n$ where M denotes the metal atoms Sn, Pb, Bi, or rare earth metals, X denotes the chalcogen atoms S or Se, and T denotes transition metal atoms like Ti, V, Cr, Nb, or Ta. As n – the number of TMDC slabs in between two MC layers – can vary from one to three, there are three main types of TMDC–misfit compounds, as illustrated in Fig. 3.4.

Due to the different crystal structures of the subsystems, the in–plane lattice constants do not fit in one direction. The TMDC layer with its hexagonal symmetry can be described by the primitive vector $\vec{a}$ and the vector $\vec{b}$ orthogonal to it with a length of $b = a \cdot \sqrt{3}$ for an undistorted hexagonal layer (see Fig. 3.5 and 3.6). In the MC layer the lattice vectors parallel to $\vec{a}$ and $\vec{b}$ are $\vec{a}^*$ and $\vec{b}^*$, respectively, with the length $b^* = a^*$, if the MC slab is undistorted. As in the TMDC–misfit compounds the sublattices are slightly distorted to match the lattice constants b and b^*, a is in an irrational ratio with its counterpart a^* due to the different symmetries of the sublattices. The resulting misfit of the subsystems is described by the parameter $\delta = 1 - \frac{a}{a^*/2}$. The lattice mismatch $1 + \delta$ in the TMDC misfit compounds varies between 1.08 in the case of $(BiS)_{1.08}TaS_2$ [44] and 1.28 in the case of $(Y_{0.93}S)_{1.28}CrS_2$ [45]. The basis vector perpendicular to the layers is the same in both subsystems so that the lattice constant for the whole compound is $c = c^*$. This leads to a complex symmetry of the misfit compounds with the so called commensurate a–direction and the incommensurate b–direction, and can be described by a four–dimensional superspace group [46].

The misfit crystals investigated in this thesis are sulfur compounds with the transition metal tantalum or niobium, i.e. $(PbS)_{1.13}TaS_2$, $(PbS)_{1.14}(NbS_2)_n$ with n=1, 2, 3, $(SnS)_{1.17}NbS_2$, and $(BiS)_{1.08}NbS_2$, as summarized in Tab. 3.1. The TMDC parts of these

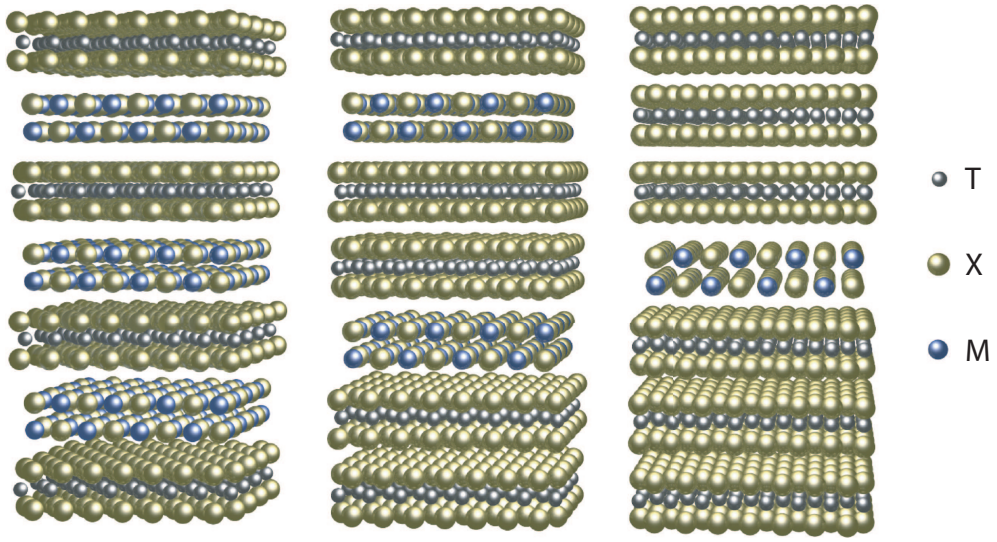

Figure 3.4: TMDC misfit compounds $(MX)_{1+\delta}(TX_2)_n$ with different numbers of transition metal dichalcogenide layers (TX_2) between two monochalcogenide (MX) double layers: (left) $n = 1$, (middle) $n = 2$, (right) n=3.

crystals show a trigonal prismatic (H type) structure, but the layer–to–layer symmetry in the c direction does not have to be of the conventional $2H_a$ or $2H_b$ type as described in section 3.2. In the case of $(PbS)_{1.13}TaS_2$, for example, the two H type TMDC layers are not rotated but only shifted by $b/2$ to each other (see Fig. 3.6 and Ref. [46]), a configuration that is not found in pure TMDCs.

While the geometric structure of the TMDC sublayers seems to be virtually undistorted, the MC subsystem shows a much stronger modulation. This can be understood if the configuration of the layers is compared to that in the pristine systems: Whereas one TMDC slab in the misfit compound with its absence of dangling bonds does not differ very much

compound		a(Å)	b(Å)	c(Å)	Γ–M(Å^{-1})	Γ–K(Å^{-1})	Γ–A(Å^{-1})	Ref.
$(PbS)_{1.13}TaS_2$	PbS	5.825	5.779	23.96				[46]
	TaS_2	3.304	5.779	23.96	1.098	1.268	0.131	
$(PbS)_{1.14}NbS_2$	PbS	5.834	5.801	11.90				[47]
	NbS_2	3.313	5.801	23.80	1.095	1.264	0.132	
$(PbS)_{1.14}(NbS_2)_2$	PbS	5.829	5.775	35.86				[48]
	$(NbS_2)_2$	3.326	5.775	35.87	1.091	1.259	0.088	
$(SnS)_{1.17}NbS_2$	SnS	5.673	5.751	11.76				[49–52]
	NbS_2	3.321	5.751	11.76	1.092	1.261	0.267	
$(BiS)_{1.11}NbS_2$	BiS	36.16	5.752	23.00				[53]
	NbS_2	3.331	5.750	23.00	1.089	1.258	0.137	

Table 3.1: Crystal data of some TMDC misfit compounds that are relevant for this thesis. The parameters of $(PbS)_{1.14}(NbS_2)_3$ are not available in the literature so that the parameters of $(PbS)_{1.14}(NbS_2)_2$ are denoted.

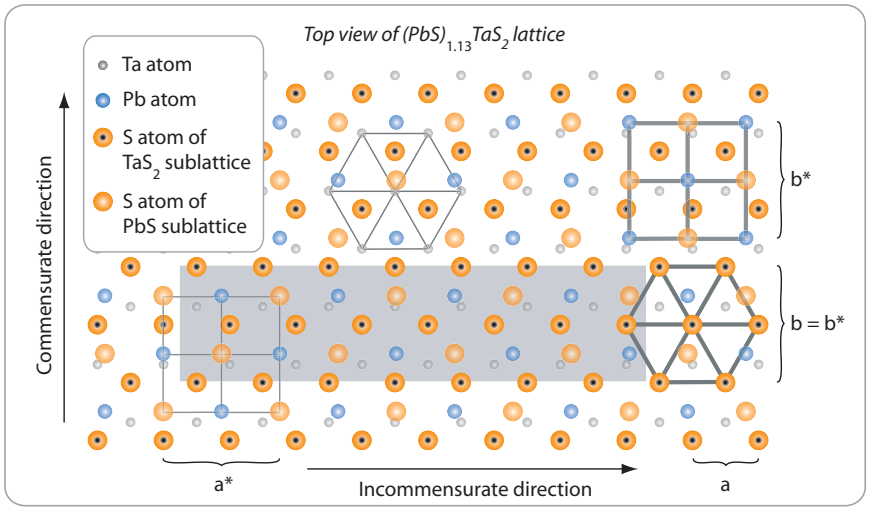

Figure 3.5: Top view of two layers of the TMDC misfit compound $(PbS)_{1.13}(TaS_2)$ with lattice constants of the hexagonal TaS_2 sandwich layers a, b and of the cubic PbS subsystem a^*, b^*. A quasi unit cell with nearly commensurate character is shown as a gray filled box.

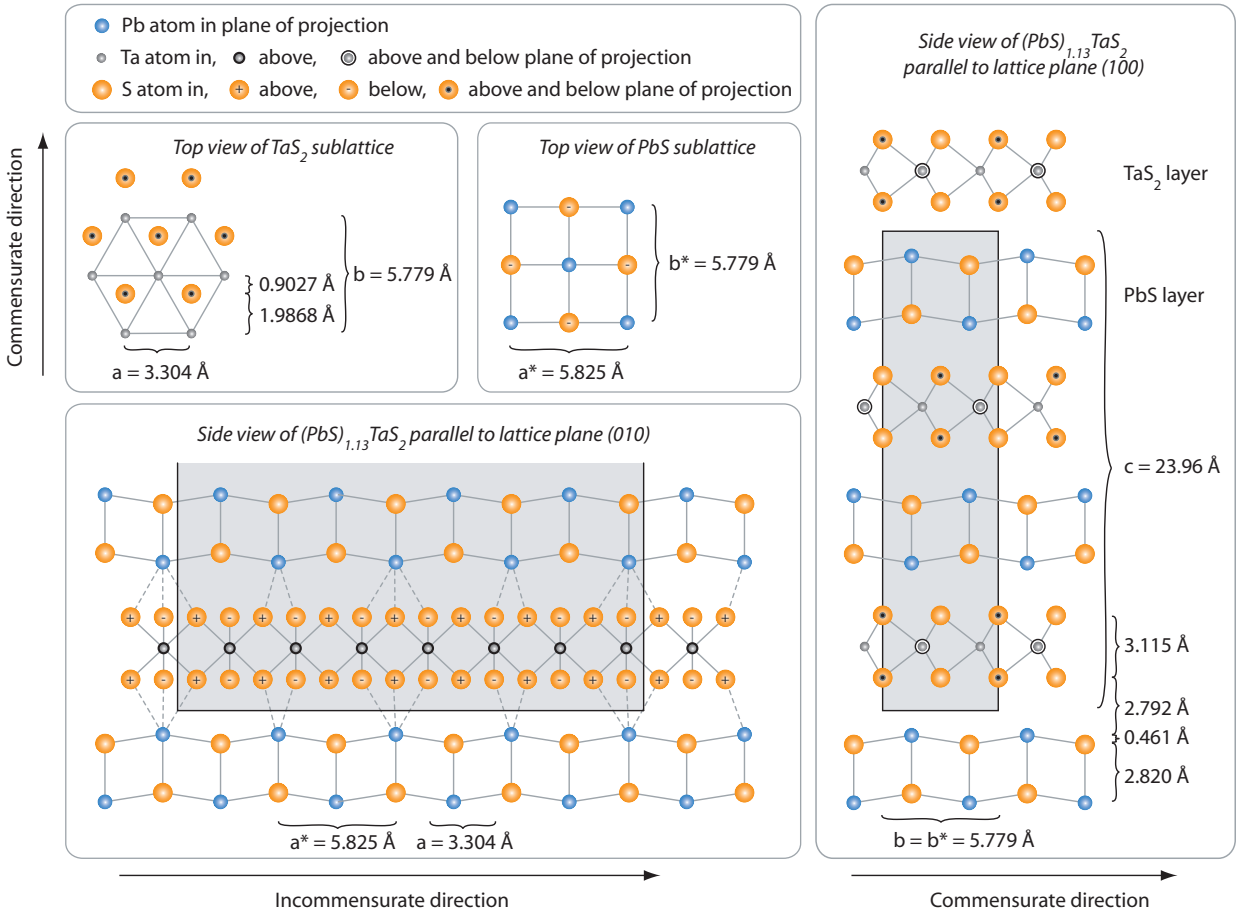

Figure 3.6: Crystal structure of the TMDC misfit compound $(PbS)_{1.13}(TaS_2)$ with lattice constants of the hexagonal TaS_2 sandwich layers a, b and of the cubic PbS subsystem a^*, b^* in the commensurate and incommensurate direction. Direct neighbor atoms in the incommensurate direction at the interface between the slabs are indicated by dashed lines. A quasi unit cell with nearly commensurate character is shown as a gray filled box.

from its counterpart in the pure crystal, for the MC slabs the situation is totally different. In contrast to its configuration in the bulk, an MC double layer consists of two monolayer slabs. Therefore, it can be considered as being composed of only surface atoms with no bulk anymore. But as the surface atoms of the rock salt like MCs have dangling bonds and tend to reconstruct (see section 3.1), the MC layer is expected to look differently from a pure compound. This leads to a simple crystal model of the TMDC misfit compounds, where the TMDC host lattice distorts the MC guest lattice in–plane to fit in the commensurate direction, while the c–spacing between the TMDC slabs is determined by the MC compound. For example, this behavior can roughly be observed in the case of $(PbS)_{1.13}TaS_2$ [46]. In comparison to $2H$–TaS_2 [54] the c–spacing of the TaS_2 layers is nearly doubled due to the insertion of the PbS double layer. However, no significant changes of the hexagonal symmetry or the in–plane lattice constants are observed. Only a slight shift in the Ta layer positions with respect to the S layer positions can be found (see Fig. 3.5). The PbS part, on the other hand, is strongly distorted. The in–plane lattice constants are reduced from $a^*_{pure} = b^*_{pure} = 5.936$ Å to $a^* = 5.825$ Å and $b^* = 5.779$ Å to fit in the commensurate direction with the virtually undistorted TMDC sublattice. As a consequence of this, the Pb atoms move 0.2 Å outside and the S atoms 0.2 Å inside the double layer to increase the Pb–S next neighbor distances (see Fig. 3.6). Consequently, there is a strongly distorted PbS double layer embedded into the van der Waals gap of nearly undistorted TaS_2. The nearest neighbor distance of Pb atoms is equal to the distance between the Pb atoms of the PbS layer and the S atoms of the adjacent TaS_2 layer (see Fig. 3.5). This interlayer distance of about 2.8 Å is comparable to the width of a $2H$–TaS_2 vdW gap (2.9 Å) but due to the incommensurability, the Pb–S distance of individual atoms varies continuously.

Following this simple approach the symmetry of the misfit compounds can be treated as a superposition of both subsystems with partly adjusted sublattices but a large separation

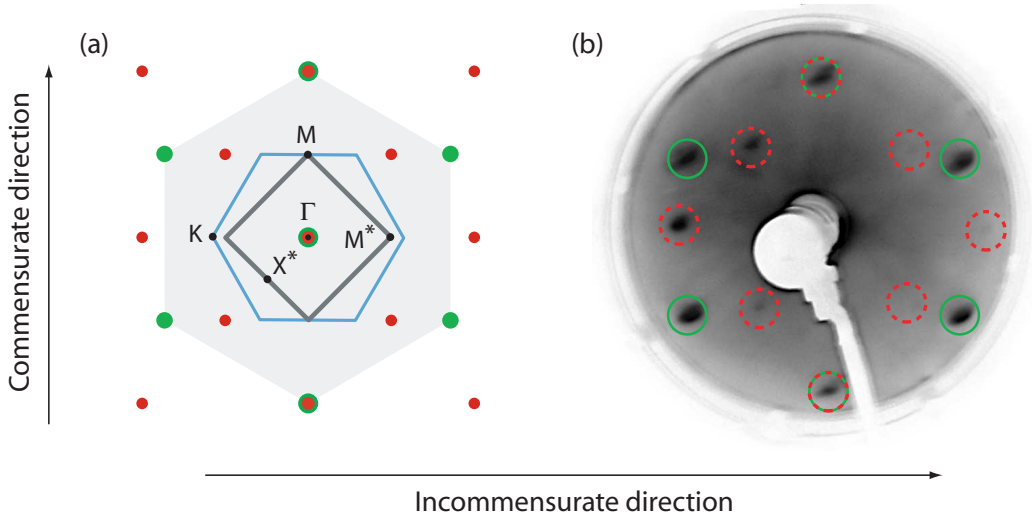

Figure 3.7: (a) Reciprocal lattice of a TMDC–misfit compound consisting of the reciprocal TMDC sublattice (large, green dots) with Brillouin zone (fine, blue line) and the reciprocal MC sublattice (small, red dots) with Brillouin zone (thick, gray line). (b) LEED image of the misfit compound $(PbS)_{1.14}(NbS_2)_2$ in which diffraction reflexes originating fron the NbS_2 subsystem (green rings) as well as from the PbS subsysten (red, dashed rings) can be seen.

between the layers. This should conserve the two–dimensional character of the layered system as in intercalated TMDC crystals. Therefore, the reciprocal lattice and its Brillouin zone can be approximated in a two–dimensional way. As shown in Fig. 3.7, the Brillouin zone of the MC subsystem is equal to the square surface Brillouin zone of pristine rock salt systems with its high symmetry points Γ, X^*, and M^*, while the hexagonal Brillouin zone of the TMDC subsystem with its high symmetry points Γ, K, and M is equal to the one in pristine TMDCs. In the commensurate direction the Brillouin zone boundaries match at M and M^*, but show a mismatch in the incommensurate direction at K and M^*.

There is currently no adequate model for the electronic band structure in TMDC misfit compounds. A first approach is the rigid band model. As discussed in section 3.2, it tries to explain the band structure of the whole system as a superposition of the pristine subsystems without any change in the band dispersion. Similar to the intercalation of TMDCs, where a charge transfer from the intercalant to the TMCD slabs is predicted to be the driving force of this process [38, 39], charge transfer is also confirmed in the misfit compounds. Since it was observed in rare earth metal misfit compounds [55–57], charge transfer is still being controversially discussed in the Pb, Sn, and Bi compounds [58–64]. As illustrated in Fig. 3.8(a), for group V B TMDC–misfit compounds an electron transfer from the totally filled MC valence band to the half filled TMDC d_{z^2} band would lead to an energetical shift of the band structure to higher binding energies in the case of the TMCD subsystem and vice versa in the MC part. In addition, analogous to the increase of the c–spacing during the intercalation process in pristine TMDCs a smaller bandwidth and the opening of a gap between the p and d bands is expected. The observation of this so called p/d gap in the misfit compounds [see Fig. 3.8(b)] contradicts the rigid band model where the semiconducting MC part has to contribute to the density of states near the Fermi energy (E_F). A more realistic model should include different types of interlayer interactions and the absence of translational crystal symmetry in the incommensurate direction of misfit compounds.

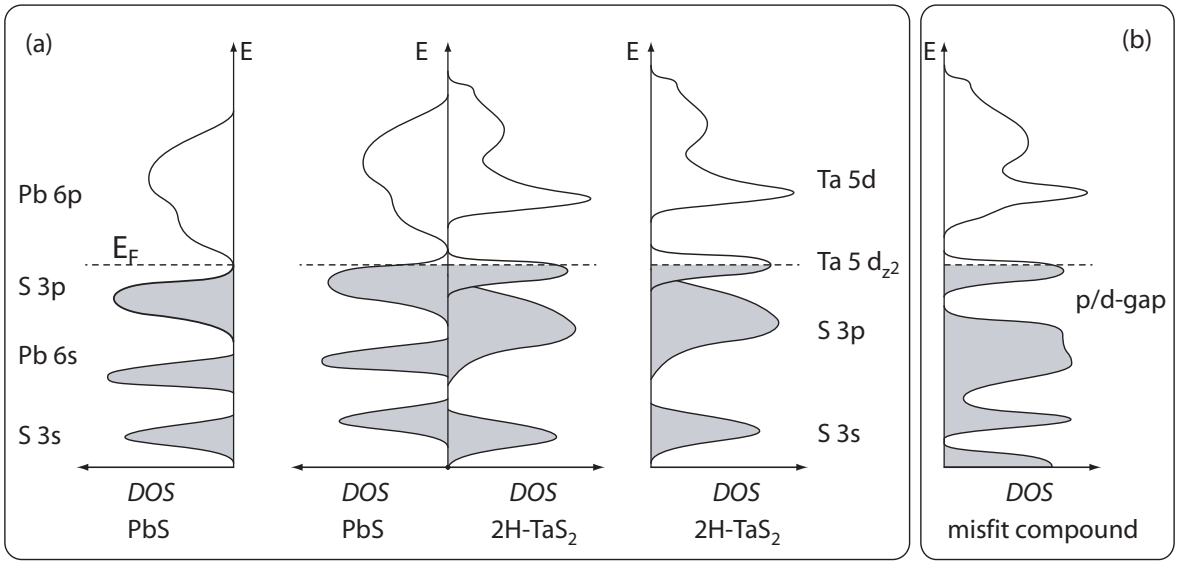

Figure 3.8: Electronic band structure of group V B TMDC misfit compounds in the case of charge transfer (a) in the rigid band model (left) and (right) for the pristine subsystems and (center) for the misfit compound (after [65–67]) and (b) with p/d–gap.

3.4 Crystal preparation and characterization

The TMDC–misfit crystals are prepared in Kiel by chemical vapor transport (CVT). In this technique a quartz glass ampule is filled by a stoichiometric amount of the pristine elements together with a transport agent like iodine. Being evacuated the ampule is transversely inclined and heated up at one end. The iodine carries the metal atoms in the direction of a temperature gradient from the hot zone at $T \approx 940°C$ to the colder zone at $T \approx 780°C$ leading to the crystallization of the metal and transition metal atoms with the evaporated chalcogen atoms within a time of about 25 days. The reaction can be described by the chemical formula:

$$TI_4 + (3+\delta)X + (1+\delta)MI_2 \rightleftharpoons (MX)_{1+\delta}TX_2 + (3+\delta)I_2, \tag{3.1}$$

with the metal atoms M = Sn, Pb, Bi, the transition metal atoms T = Ti, Nb or Ta, the iodine molecules I_2 and the misfit parameter δ as described in section 3.3. In the case of the chalcogen atoms X = S or Se the stoichiometric amount as well as a small excess supply can be offered to improve the crystal quality and prevent self intercalation of the transition metal atoms into the van der Waals gaps. The composition and the stacking order of the TMDC–misfit crystals that were prepared in Kiel were characterized in the previous work by Brandt et al. [64, 68, 69] using different methods like transmission electron microscopy (TEM), X–ray diffraction (XRD), scanning tunneling microscopy (STM), energy dispersive X–ray analysis (EDX), or X–ray photoelectron spectroscopy (XPS).

The crystals which are investigated in this thesis (see section 3.1) were additionally characterized by Laue analysis, microscopic photographs, low electron energy diffraction (LEED), XPS, and angle resolved photoelectron spectroscopy (ARPES). As illustrated exemplarily for the crystal $(PbS)_{1.13}TaS_2$ in Fig. 3.9(a), the Laue pattern shows spots only in special directions, which are marked by lines in Fig. 3.9(b). The dashed blue and the

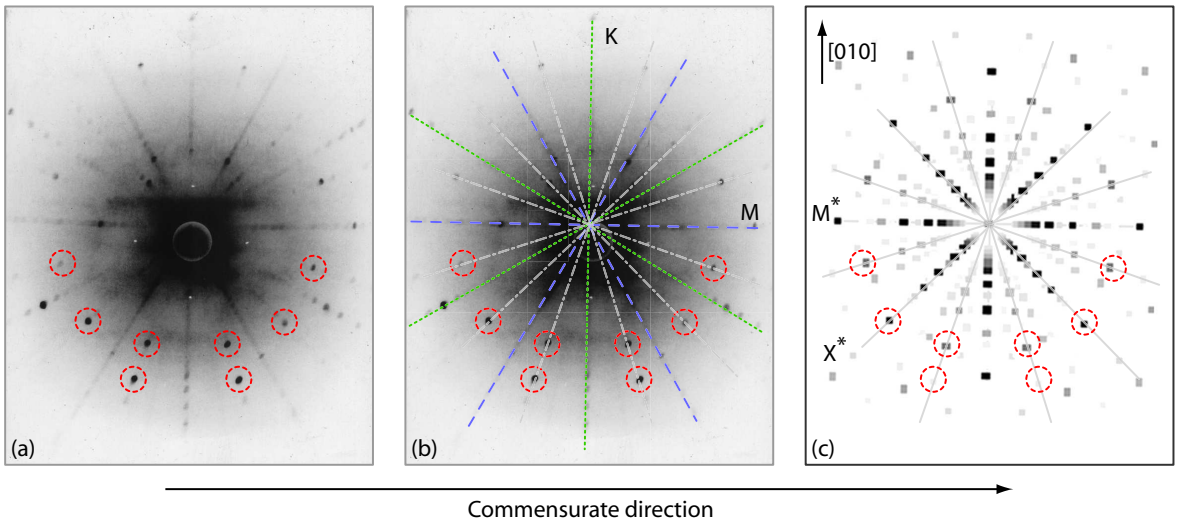

Figure 3.9: Back reflection Laue pattern (U = 25 kV, d = 3 cm) (a,b) measured for $(PbS)_{1.13}TaS_2$ with dashed blue lines indicating the Γ–M direction and dotted green lines indicating the Γ–K direction, and (c) simulated for PbS in the (001) plane with the software "Lauept" [70]. Some spots in directions originating from the PbS subsystem (dashed–dotted gray lines) are marked by dashed red circles. In the grayscale images black indicates high intensity.

dotted green lines indicate Laue reflections which are known from pure TMDC crystals. They appear at angles of multiples of 30° and indicate the high symmetry directions Γ–M and Γ–K. In combination with a Laue simulation done with the software "Lauept" [70] for a PbS crystal [see Fig. 3.9(c)], the additional reflection that is located on the gray dashed–dotted lines and marked with circles can be clearly identified as belonging to the fcc subsystem. As the PbS reflection is symmetric with respect to the high symmetry directions Γ–M^* but shows a different symmetry compared to the TMDC counterparts, the Laue method allows a preorientation of the TMCD misfit compounds for further measurements, except for a determination between the commensurate and the incommensurate direction. In addition to the crystal orientation, in being a bulk sensitive method the Laue analysis shows a high degree of orientational order among the layers in the whole crystal.

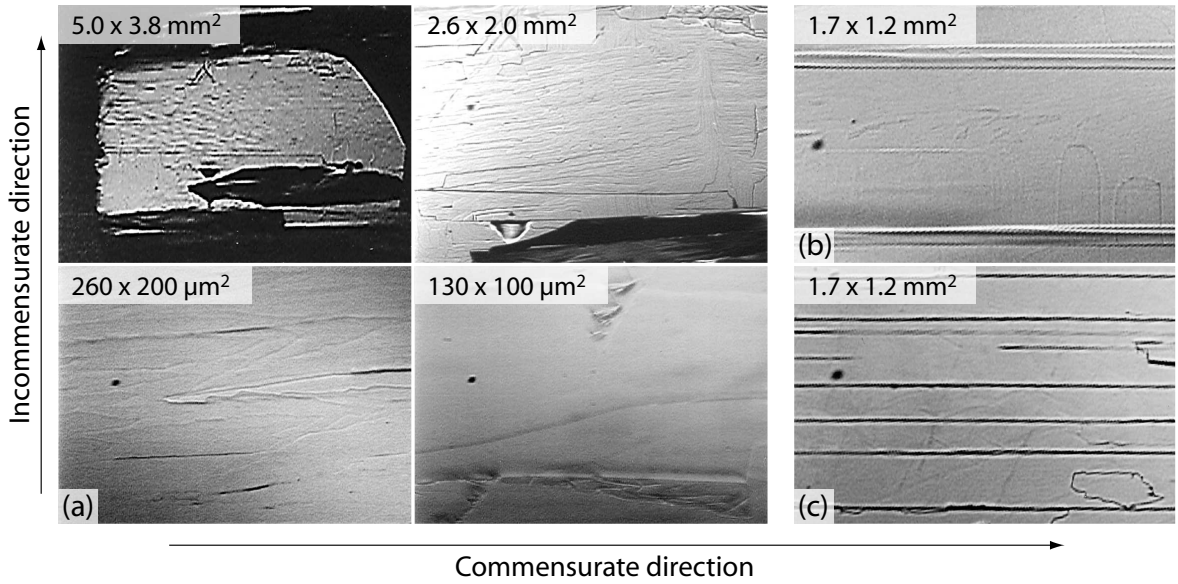

Figure 3.10: (a) Microscopic photograph of the crystal surface of $(PbS)_{1.13}TaS_2$, (b) with cracks and folds perpendicular to the incommensurate direction of $(BiS)_{1.11}NbS_2$, and (c) $(PbS)_{1.14}NbS_2$.

After cleaving the crystals parallel to the layers the surface shows some hundred micrometer wide, smooth areas, as can be seen in the photographs of Fig. 3.10. Next to these areas, regions with long cracks or folds perpendicular to the incommensurate direction can be observed, originating from the misfit between the two subsystem lattices. Since the stripe orientation does not change after repeated crystal cleavage, the layer orientation seems to remain unchanged in the hole crystal, confirming the observations from the Laue analysis.

The orientation of the crystal derived by Laue analysis and microscopic photographs was confirmed by LEED measurements. They clearly show the reciprocal lattice and therefore the commensurate and incommensurate direction, as illustrated in Fig. 3.7(b).

To get information about the chemical composition of the misfit compounds, XPS measurements were performed. Figure 3.11 shows relevant features of the XPS spectra with binding energies up to about 170 eV. Significant element–specific misfit peaks are visible and clearly resolved, indicating the high quality and purity of the misfit compounds. In all spectra the sulfur $2p$ core levels at a binding energy of $E_B(S\ 2p_{3/2}) \approx 161$ eV and a spin–orbit splitting of about 1.1 eV can be observed. Due to the different chemical environment

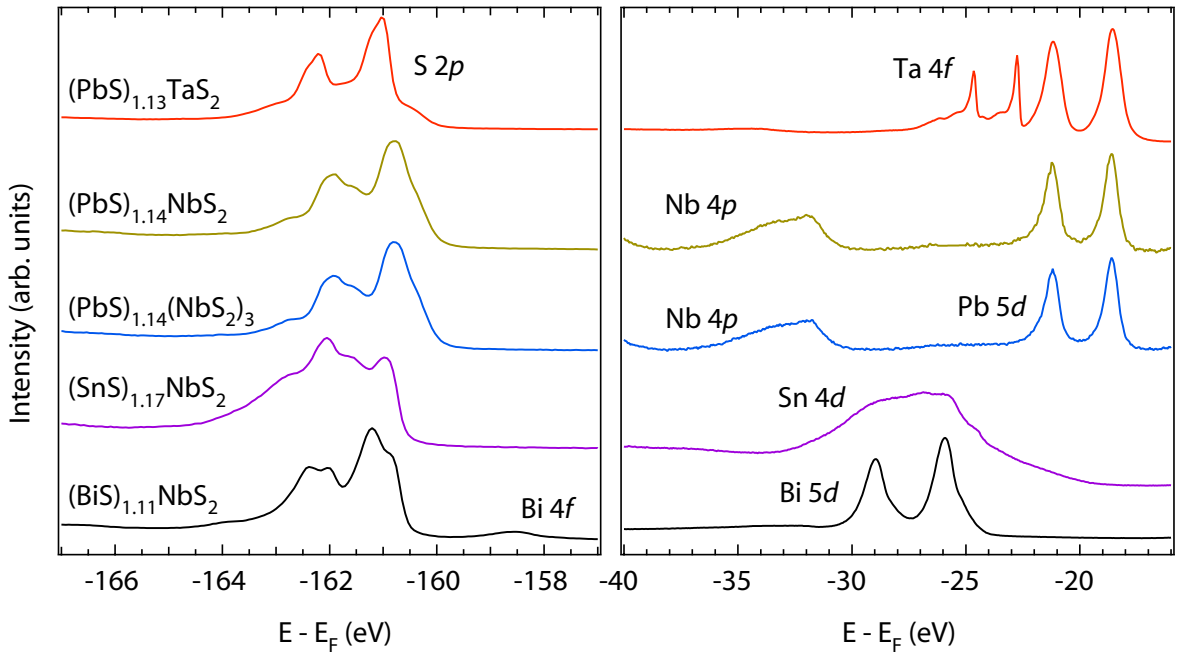

Figure 3.11: Photoelectron spectra of different TMDC–misfit compounds. Strongest core levels are labeled.

of the sulfur atoms in the different compounds, the sulfur peak positions are shifted with respect to each other by some hundred meV. In each compound more than one binding state of a specific sulfur electron is observed, as the sulfur atoms have various neighbors in dependence of their atomic position. For example, the sulfur atoms in an MX layer are surrounded by five metal atoms and one sulfur atom of the adjacent TX_2 layer, while the sulfur atoms in a TX_2 layer are surrounded by six sulfur and three transition metal atoms of the TX_2 layer and one or more metal or sulfur atoms of the adjacent MX layer, depending on the atomic position in the misfit structure (see Figs. 3.5 and 3.6). This leads to at least two significant bonding states of the sulfur atoms and an additional misfit derived broadening of the peak width. At lower binding energies the metal and transition metal atom derived core levels can be observed. These atoms are only found in one of the subsystems at predefined positions in the compounds (however, the number of next layer neighbors varies due to the misfit of the compound), leading to a fixed chemical environment. As the transition metal atoms are in the center of the TX_2 layers and do not have direct contact to the next layer, a change in the binding energies could not be observed in contrast to the core levels of the MX metal atoms with their next neighbors located in the TX_2 layer.

A more detailed analysis of the electronic structure will be presented in the following chapters.

4 Electronic structure of TMDC misfit compounds

Layered crystals composed of two subsystems with incommensurate periods show an aperiodic change in next neighbor distances perpendicular to the layers, attenuating the interlayer bonding. In order to investigate this bonding, we have employed angle–resolved photoelectron spectroscopy on different TMDC misfit compounds. By studying the electronic structure at the Fermi surface, we could clearly observe a charge transfer to the TMDC layers, indicating a ionic contribution to the interlayer bonding, similar to intercalated TMDC compounds. As we did not observe band dispersion perpendicular to the layers, the contribution of covalent bonding seems to be negligible. Additionally, the electronic structure at the Fermi surface, being dominated by the TMDC *d*–states, shows signatures of both subsystems, indicating electronic interlayer coupling.

4.1 Introduction

The electronic structure of systems with broken translational symmetry, resulting from different competing potentials with an irrational ratio of their periodicities, is a widely discussed topic. As misfit systems, for instance, do not fit into the conventional band–structure concept they are often studied to get a deeper insight into the building concepts of crystals and the mechanism of band formation in a solid [71–73]. The layered TMDC misfit compounds are model substances for studying the influence of a misfit on the electronic structure. They are composed in an alternating stacking order of hexagonally ordered TMDCs and cubic rock salt such as monochalcogenides. Fitting only along one crystallographic direction parallel to the surface (commensurate direction), the lattice constants are in an irrational ratio in the perpendicular (incommensurate) direction due to the different crystal structures of the two layered subsystems (see chapter 3). Since there is no finite unit cell in the incommensurate direction, theoretical considerations like band structure calculations and the comparison to experimental electronic structure investigations are difficult. Up to now, there is no general model that describes the electronic structure in TMDC misfit compounds adequately [63, 64, 68, 74–76].

The astonishing high stability of the TMDC misfit compounds has not been understood until now. The subsystems are arranged in a very high stacking order with the occurrence of monochalcogen bilayers while pristine monochalcogen compounds have a three–dimensional rock salt structure. In addition, the different symmetry of the subsystems result in a lattice mismatch in the incommensurate direction, so that the total energy should be increased in comparison to the pristine compounds. There are several open questions that are in particular related to the electronic structure in these compounds. For example, it has not been determined if the electronic band structure of the TMDC misfit compounds can be described by a simple superposition of the electronic band structure of the pristine subsystems (rigid band model) or if mixed states have to be taken into account. Furthermore, it is ambiguous if the incommensurability does have any effect on the electronic structure and the dominant interlayer bonding mechanism is controversially discussed [58, 61–64, 77, 78].

For example, TMCD misfit compounds can be described in a similar way as intercalated TMDC compounds with inserted monochalcogen double layers into the vdW gaps of the pristine TMDC crystals except for single metal atoms (see chapter 3). However, significant features of the electronic band structure in the misfit compounds cannot be explained if the rigid band model that describes the clearly observed electron transfer in intercalation

systems from the intercalant to the TMDC valence band rather well is applied to them. There is the experimentally observed p/d–gap – a separation of the TMDC dominated conduction band (mainly d–states) from the valence bands (mainly p–states) – that is not explained by the rigid band model, particularly not if a charge transfer from the MC subsystem to the TMDC layers takes place, changing the semiconducting character of the MC layers to metallic. While charge transfer was observed in rare earth metal misfit compounds [55–57], indicating strong ionic bonding between the layers, it is still being controversially discussed for Pb, Sn, and Bi compounds. Dominating band hybridization and covalent bonding on the other hand – also being in contrast to the p/d–gap – were predicted as a result of theoretical considerations [63], optical reflectivity [55], and X–ray photoelectron spectroscopy [61, 62] measurements, in contrast to the results of further XPS [58, 59] and Hall effect measurements [46, 50, 79–81].

In order to determine the electronic structure of TMDC misfit compounds in the commensurate and incommensurate direction and to investigate the nature of the bonding between the layers, we performed ARPES measurements on the crystals $(PbS)_{1.13}TaS_2$, $(PbS)_{1.14}(NbS_2)_x$ (x = 1, 3), $(SnS)_{1.17}NbS_2$, and $(BiS)_{1.11}NbS_2$.

4.2 Experimental setup

The ARPES measurements were performed at the synchrotron beamline 7 (BL7) of the Advanced Light Source (ALS) in Berkeley (USA). As illustrated in Fig. 4.1, BL7 uses undulator radiation (undulator period length: 5 cm), monochromatized by a spherical–grating monochromator (SX–700 design) with three interchangeable gratings. Providing an energy range from 50 eV to 1200 eV (1^{st}, 3^{rd}, and 5^{th} harmonic) the beamline can achieve a spectral resolution of up to $E/\Delta E = 8000$ by varying the monochromator entrance and exit slit widths. The photon flux on the sample is about 10^{13} photons/s for low energies ($h\nu < 150$ eV), 10^{12} photons/s for medium energies (150 eV $< h\nu <$ 500 eV), and 10^{11} photons/s for high energies ($h\nu > 500$ eV). By the use of vertical and horizontal focusing mirrors a microfocus beam with a diameter of about 50 μm on the sample can be achieved.

During our beamtime at BL7 there were two different electron analyzers at the ARPES endstations available: a Scienta SES–100 and a Scienta R4000. Both analyzers were equipped with a multi–channelplate/2D–CCD–detector unit for parallel detection of photoelectrons (see section 2.3). The simultaneously energy– and angle–resolved photoelectron

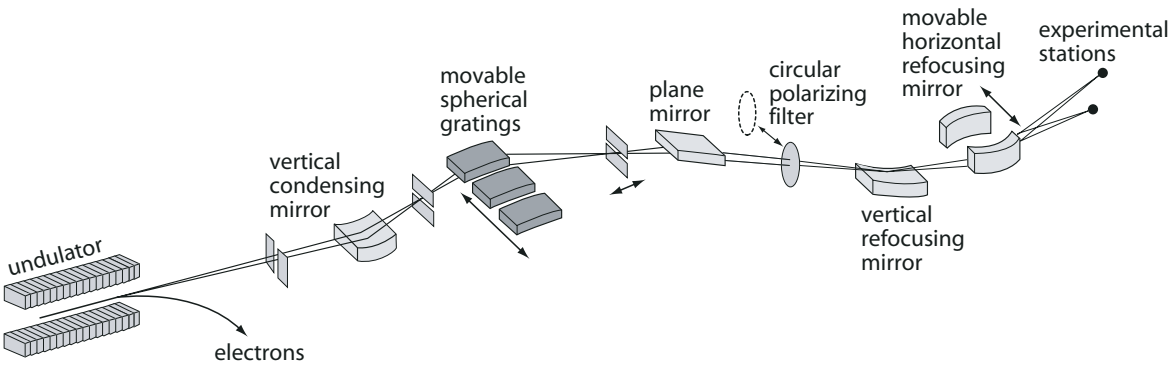

Figure 4.1: Layout of beamline 7 at the ALS, with undulator, SX–700 type monochromator, and refocusing mirror system (from Ref. [82]).

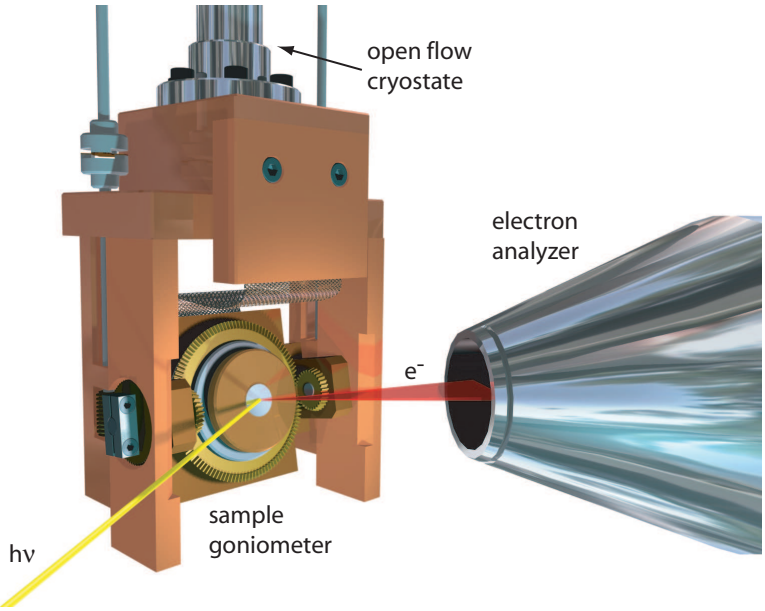

Figure 4.2: Sample goniometer at the experimental station of BL7 at the ALS (Berkeley) (from Ref. [83]).

spectra were measured with a total energy resolution of better than 100 meV ($h\nu$ = 100, 150, 180 eV), and an angular resolution of about ±0.15° (for more details see Tab. 2.1).

In order to measure the angle–resolved photoemission spectra over a large angle range, the experimental station is equipped with a fully automated stepper motor driven sample goniometer (see Fig. 4.2). This allows stitching single photoemission maps after the measurement process very precisely. By transforming the datasets into k–space (see section 2.3.1), four–dimensional datasets I($E, k_{||x}, k_{||y}$) for the different samples can be obtained. By varying the photon energy on the other hand, also the $k_\perp$ dependence of the electronic structure can be measured. However, the limited beamtime does not allow acquiring five–dimensional datasets of a whole Brillouin zone for a full $k_\perp$–period with high resolution. Therefore, during our beamtime the $k_\perp$ dependence of the electronic structure was measured for a high symmetry direction of the Brillouin zone.

The TMDC misfit crystals were attached to the sample holder by silver-filled epoxy resin and transferred into the UHV system. Cleaving the crystals in the UHV (10^{-10} mbar range), a clean (0001) surface was obtained. The measurements were performed with the sample at low temperatures of $T \approx 70$ K.

4.3 Charge transfer in TMDC misfit compounds

The nature of the interlayer bonding in the TMDC misfit compounds with Pb, Sn, and Bi in the monochalcogen sublayers is controversially discussed [55,58,59,61–63]. As in particular the electronic states with low binding energy are involved in layer–to–layer interactions, we performed ARPES measurements and mapped the electronic structure in the vicinity of the Fermi surface of the crystals $(PbS)_{1.13}TaS_2$, $(PbS)_{1.14}(NbS_2)_x$ (x = 1, 3), $(SnS)_{1.17}NbS_2$, and $(BiS)_{1.11}NbS_2$. The results of the compound $(PbS)_{1.13}TaS_2$ will exemplarily be described in more detail.

Figure 4.3 shows the results of band structure calculations for pristine 2H–TaS_2 (from

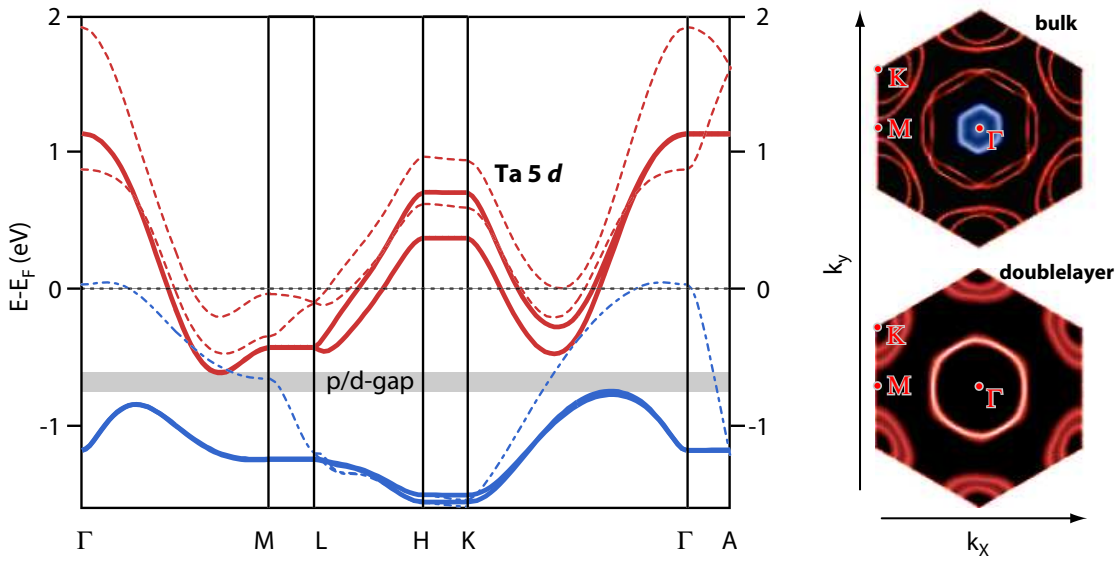

Figure 4.3: Band structure calculations of pristine 2H–TaS_2 (left) for a bulk crystal (dashed lines), and a single $2H$–doublelayer (solid lines). In the calculated slices through the Fermi surface (right) around the Γ point ($k_\perp = 0$) red indicates the mainly Ta $5d_{z^2}$, and blue indicates the S $3p$/Ta $5d$ (p/d) derived bands (from ref. [84]).

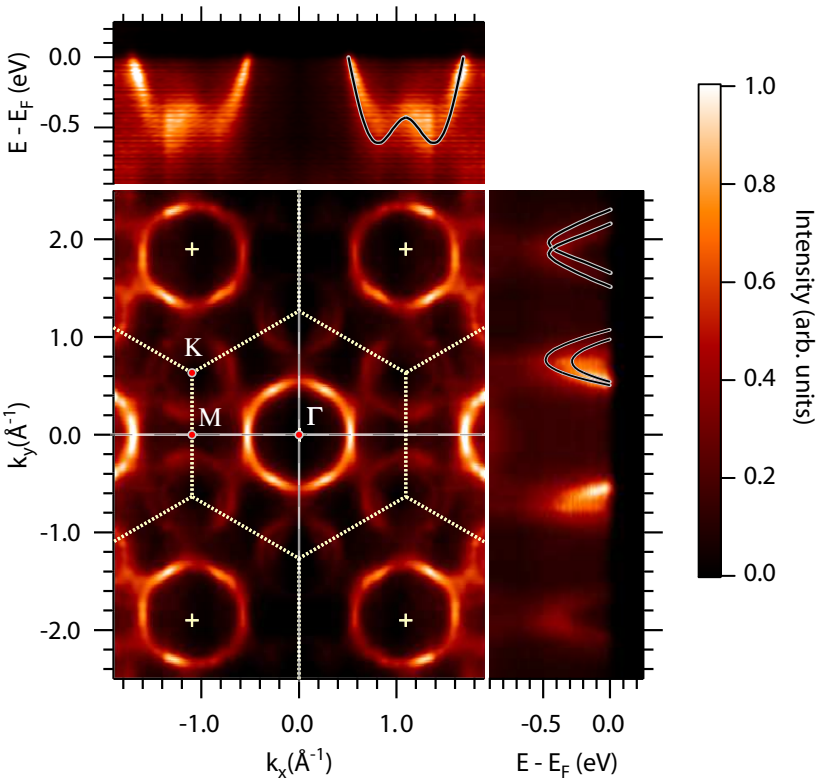

Figure 4.4: Constant energy map for electrons emitted from the Fermi level (center), and slices through the Brillouin zone along the high–symmetry directions Γ(A)–M(L) (top) and Γ(A)–K(H) (right) of $(PbS)_{1.13}TaS_2$ ($h\nu = 100$ eV, T = 65 K, E = E_F, E_{step} = 25 meV, ΔE = 80 meV, symmetrized, higher brightness represents more intensity). The black, white bordered lines are the results of the band structure calculations for $2H$–TaS_2 doublelayers from Fig. 4.3.

Ref. [84]). The calculations were performed employing the local density approximation with the fully relativistic ELAPW $\mathbf{k}\cdot\mathbf{p}$ method [85] for bulk $2H$–TaS_2 [dashed and dashed–dotted lines in Fig. 4.3(left)] as well as for one doublelayer of $2H$–TaS_2 [solid lines in Fig. 4.3(left)]. According to the model of Wilson and Yoffe [33] (see also Fig. 3.3), the electronic states at the Fermi surface are characterized by Ta $5d$ bands. The mainly Ta d_{z^2}, $d_{xy}/d_{x^2-y^2}$ derived [86] conduction bands (red lines) are non–degenerate, leading to double walled pockets around the K–points [see Fig. 4.3(right)]. In contrast to the bulk band structure with a double walled pocket around the Γ–point, the $2H$–doublelayer d–bands are degenerate there. Additionally, only the bulk crystals show a Fermi surface crossing of mainly S $3p$ derived bands (dashed–dotted, blue lines) and a small pocket around the Γ–point. For the single doublelayer these S $3p$ bands (solid, blue lines) are clearly separated from the d–bands (solid, red lines) by a gap (p/d–gap). Therefore, 50% of the Ta $5d$ conduction band states are occupied in the $2H$–doublelayer, so that the (averaged) pocket area amounts to 50% of the Brillouin zone.

In Fig. 4.4 a measured PAD at $E - E_F = 0$ (Fermi surface map: FS map), as well as I(E, k_x, $k_y = 0$)– and I(E, $k_x = 0$, k_y)–maps of the TMDC misfit crystal $(PbS)_{1.13}TaS_2$ are shown. In comparison to Fig. 4.3 in particular the band structure calculation results of the single TaS_2 doublelayer seem to be very similar to the measurements. The pockets are centered at the K(H)– and Γ(A)–points with double and single walls, respectively. As we did not observe any valence band states in the energy range of Fig. 4.4 ($E - E_F \leq -0.9$ eV), a large p/d–gap of at least 0.4 eV can be concluded. This lower limit was observed for all TMDC misfit compounds investigated in this thesis. Even though the misfit crystal consists of cubic and hexagonal ordered layers, only the hexagonal symmetry is visible at the Fermi energy. In terms of the rigid band model this could be explained by the semiconducting character of the cubic subsystem which does not contribute to the density of states (DOS) at the Fermi level. However, as the band gap of pristine PbS is smaller than 0.41 eV (0.41 eV at $T = 300$ K and smaller at lower temperatures) a simple superposition of the electronic structures of both subsystems should lead to PbS derived electronic states in the measured energy range of Fig. 4.4 (see also [65–67] and Fig. 3.8). As no bands except for the Ta $5d$ derived valence bands can be observed, the electronic structure of the PbS subsystem seems to be changed in the misfit compound in comparison to pristine crystals.

In contrast to the rigid band model, a hybridization of the electronic states of adjacent layers could explain a change in the electronic band structure and in particular a lowering of the PbS valence band energies. However, a hybridization with the Ta $5d$ derived states seems to be very unlikely due the the good agreement between the measured dispersion and the band structure calculations of the pristine TaS_2 doublelayer. In order to estimate the influence of band hybridization we performed photon energy dependent ARPES measurements, tracing the band dispersion perpendicular to the layers. Figure 4.5 shows the measurement results, applying photon energies of $h\nu = 100$ eV .. 200 eV. Assuming an inner potential of $V_0 = 16$ eV, the datasets were transformed into k–space using equation (2.9). Figure 4.5(top, left) shows an EDC sequence, depending on the momentum k_x, illustrated as grayscale image in the bottom and EDC waterfall plot above. Similar to Fig. 4.4(top) the dispersion in the Γ(A)–M(L) direction is traced ($k_z = 6.9$ Å^{-1}). Besides the Ta $5d$ derived conduction bands, at higher binding energies ($E - E_F \leq 1.5$ eV) mainly S $3p$, as well as PbS derived valence bands can be observed. Measuring the dispersion in the Γ–A [Fig. 4.4(a)] and the M–L direction [Fig. 4.4(b)], large changes in the intensity of the EDC maps can be observed. While for the M–L direction no indication of band dispersion is

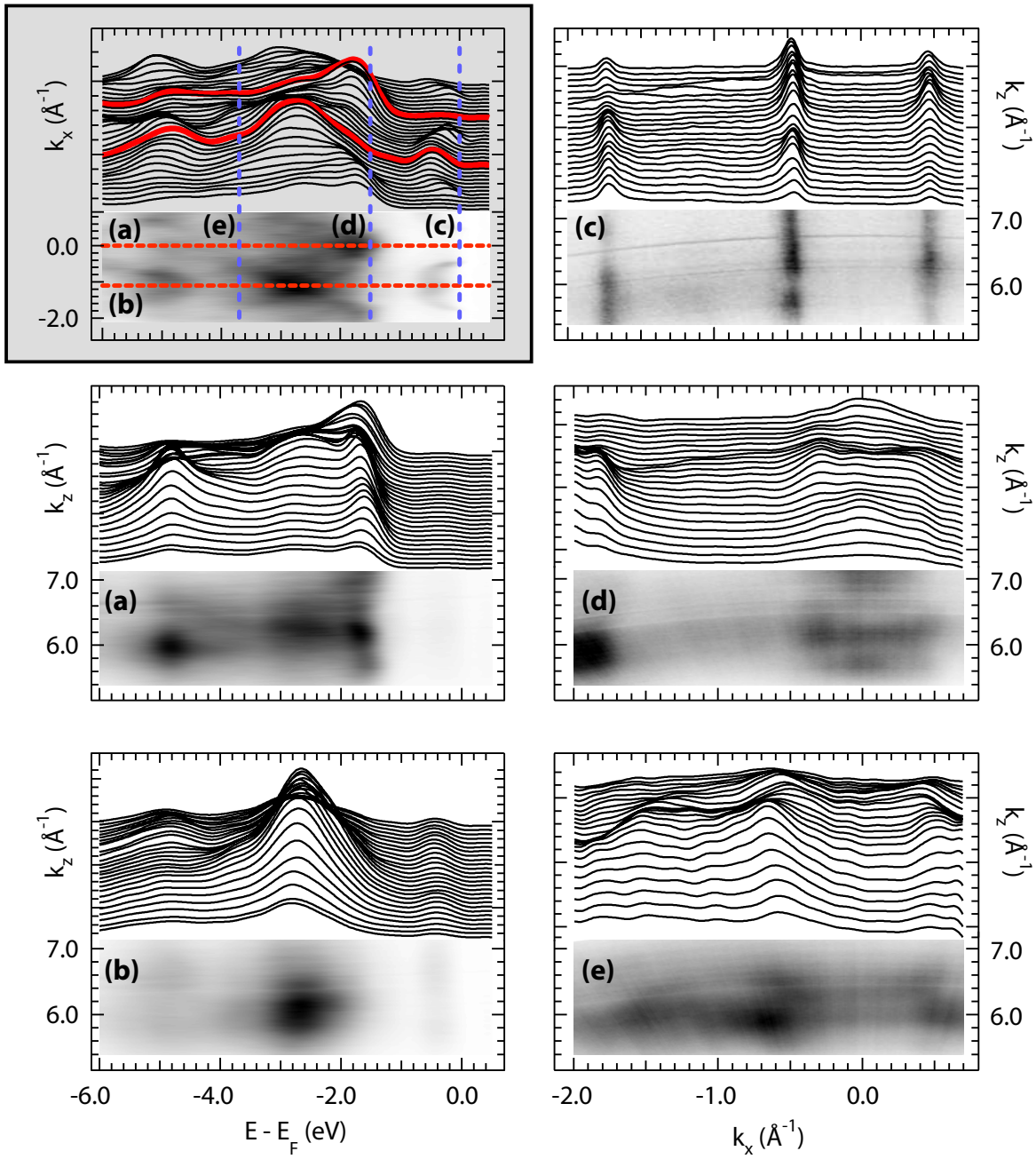

Figure 4.5: Dispersion perpendicular to the layers of $(PbS)_{1.13}TaS_2$, transformed into k–space ($h\nu$ = 100 .. 200 eV, V_0 = 16 eV, Φ = 4.5 eV)with (top, left) E(k_x)–map at k_z = 6.9 Å^{-1}, (a) Γ–A–map, (b) M–L–map, and k_x–k_z maps at (c) E - E_F = 0 eV, (d) E - E_F = -1.5 eV, (e) E - E_F = -3.7 eV.

visible, a band dispersion in the Γ–A direction is possibly hidden by a strong intensity oscillation with a periodicity of $\Delta k_z \approx 1$ Å^{-1}. Therefore, in Figs. 4.4(c), (d), and (e) the k_x–k_z dependence at specific binding energies is traced. For the Ta 5d states we observed no dispersion perpendicular to the layers [$E - E_F \approx 0$ eV in Fig. 4.4(c)], while for higher binding energies [Figs. 4.4(d) and 4.4(e)] the maps seem to be ambiguous. In particular for $E - E_F \approx -1.5$ eV in Fig. 4.4(d) there seems to be a dispersing band at $k_x \approx 0$ Å^{-1}. However, looking at the waterfall plot, the modulation in peak position could also be explained by two, non dispersing bands at $k_x = 0$ Å^{-1} and $k_x \approx 0.3$ Å^{-1} and strong matrix element effects, changing the peak intensities in dependence of the photon energy. As in addition a possible k_z–periodicity should be characterized by $\Delta k_z \approx 0.13$ Å^{-1} (see Tab. 3.1) in contrast to the observed periodicity of about 1 Å^{-1}, we conclude that band dispersion perpendicular to the layers is very weak. Since the electronic structure of $(PbS)_{1.13}TaS_2$ at the Fermi surface is very similar to the electronic structure of decoupled TaS_2 doublelayers and $k_\perp$–dispersion seems to be negligible, there should be only minor delocalization of the electrons perpendicular to the layers. Therefore, covalent bonding between the layers should only play a minor role in the bonding between the TMDC misfit layers.

In order to investigate the contribution of ionic bonding between the layers, we determined the band filling of the Ta d–bands at the Fermi energy by PAD–measurements of the conduction band. As in the TMDC misfit compounds the conduction bands are clearly separated from the valence bands (p/d–gap), in average the d–bands should be half filled, if no electrons are transferred in stoichiometric compounds. The measured four–dimensional datasets I(E, k_x, k_y) were fit to a theoretical bandstructure model, developed for pristine 2H–TMDC crystals by N. V. Smith et al. [87]. Employing a d–orbital based tight–binding approach and neglecting layer–to–layer interactions, Smith et al. [87] derived a parametrized function, describing the band energy E by:

$$\begin{aligned} E = d_{z^2} &+ d_1[2\cos(\xi)\cos(\eta) + \cos(2\xi)] + d_2[2\cos(3\xi)\cos(\eta) + \cos(2\eta)] \\ &+ d_3[2\cos(2\xi)\cos(2\eta) + \cos(4\xi)] \ . \end{aligned} \tag{4.1}$$

The parameters d_1, d_2 and d_3 are connected to the hopping integrals $dd\sigma_n$, $dd\delta_n$ by $d_n = 0.5(dd\sigma_n + 3dd\delta_n)$ (n = 1, 2, 3 runs over the first–, second–, and third–nearest neighbor atoms), but are rather to be treated as fit parameters. The angles ξ and η represent the momentum dependence with $\xi = k_x a/2$ and $\eta = \sqrt{3} \cdot k_y a/2$, where a is the lattice constant of the crystal. For the two–dimensional band structure fit different high intensity points in the experimental datasets (respectively band positions) were chosen. For the TMDC misfit crystal $(PbS)_{1.13}TaS_2$ (see Fig. 4.4) the band structure fit was applied for both d–bands separately. The fit results are shown in Fig. 4.6(left) (parameters see Tab. 4.1).

A suitable method for quantifying the band filling of the transition metal d–band is the determination of the hole/electron pocket area in a FS map with respect to the Brillouin zone size. Hole pockets are defined by the k_x, k_y values of all unoccupied electronic states, while electron pockets are complementary to these. Therefore, the ratio of the total electron (hole) pocket area A_{el} (A_{hole}) and the Brillouin zone area A_{BZ} is a measure for the band filling. As all electronic states owe the same volume in k–space and are occupied with up to two electrons each, the band filling B of one electronic band can be calculated by:

$$B = 2 \cdot \left(\frac{A_{el}}{A_{BZ}} \right) = 2 \cdot \left(1 - \frac{A_{hole}}{A_{BZ}} \right) \ . \tag{4.2}$$

In order to determine the character of the pockets (hole or electron like), all PADs are

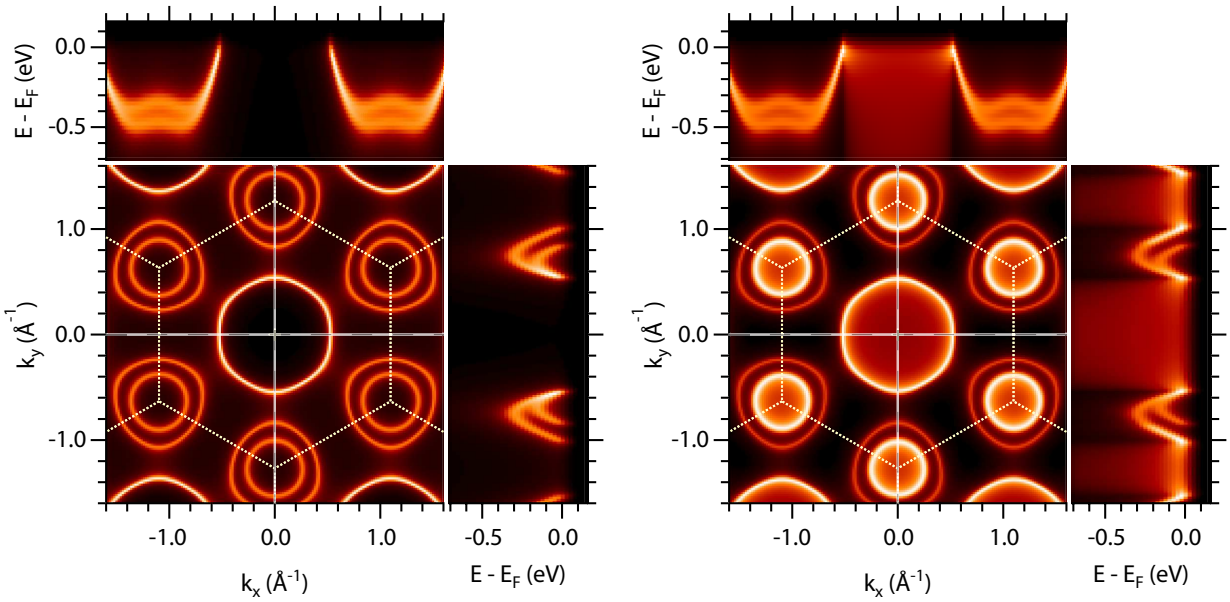

Figure 4.6: Band structure fit of the Ta 5 d_z bands of $(PbS)_{1.13}TaS_2$ using a tight binding model for 2H TMDC crystals [87] (parameters see text). The bands are broadened by a natural line width (Lorentz profile) of $\Delta E_L = 70$ meV, convolved with a Gaussian of $\Delta E_G = 70$ meV and finally multiplied with a Fermi function ($T = 65$ K). In addition to the Fermi map (left), the same dataset, normalized by the energy sum of the calculated Ta 5 d is shown (right).

divided by the sum of all energy channels of the four–dimensional dataset:

$$I_{E_{norm}}(E_0, k_x, k_y) = \frac{I(E_0, k_x, k_y)}{\sum_E I(E, k_x, k_y)} \ . \tag{4.3}$$

This normalization leads to increased intensity at all binding energies for all k_x, k_y values

Compound	d_{z^2} in eV	d_1 in eV	d_2 in eV	d_3 in eV	CT_{PES}	CT_{HE}
$(PbS)_{1.13}TaS_2$	0.0776	0.131	0.279	-0.00243	-0.04	-0.52
	-0.0630	0.247	0.239	0.0267	-0.20	
$(SnS)_{1.17}NbS_2$	0.0124	0.150	0.291	0.0228	-0.21	-0.13, +0.74
$(PbS)_{1.14}NbS_2$	-0.0507	0.190	0.257	0.0350	-0.34	-0.67, -0.80
$(PbS)_{1.14}(NbS_2)_3$	-0.0629	0.136	0.219	0.0288	-0.36	-0.69, -0.76*
$(BiS)_{1.11}NbS_2$	-0.0757	0.136	0.221	0.0284	-0.38	-0.52

Table 4.1: Fit parameters of the tight binding model by Smith et al. [87] and resulting charge transfer (CT_{PES}) to the TMDC subsystem per transition metal atom of various TMDC misfit compounds. For comparison the charge transfer values (T = 4 K) determined from Hall effect measurements (CT_{HE}) [46, 50, 79–81] are summarized in the last column, performed on crystalline samples (first value) and compacted powder pellets (second value). (*Note: As no values for $(PbS)_{1.14}(NbS_2)_3$ are available, the charge transfer measured for $(PbS)_{1.14}(NbS_2)_2$ is denoted here.)

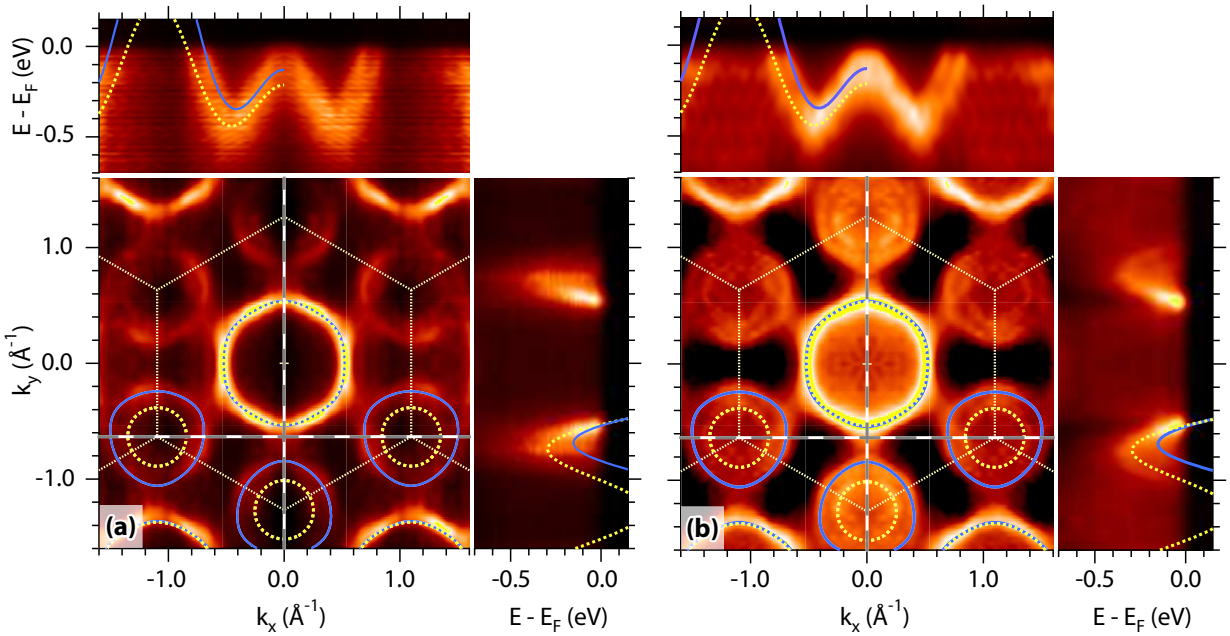

Figure 4.7: Unnormalized (a) and normalized (b) symmetrized constant energy maps of $(PbS)_{1.13}TaS_2$ (bottom, left) and slices through the dataset along the straight, dashed lines (hν = 100 eV, higher brightness represents more intensity). For fit parameters of the band structure fit (straight lines) see table 4.1.

within the hole pockets, while the intensity in the electron pockets is reduced. Applying this method, the ring structures, centered around the Γ– and K–points in the FS map of $(PbS)_{1.13}TaS_2$ [Fig. 4.6(left)], can easily be identified as hole pockets [see Fig. 4.6(right)]. A second (more experimental) advantage of these normalized PADs is that intensity fluctuations, e.g., caused by matrix element effects or detector inhomogeneities, are removed. Thus, weak structures in the spectra appear more pronounced. Comparing the unnormalized dataset of Fig. 4.7(a) (see also Fig. 4.4) with the normalized dataset in Fig. 4.7(b), in particular the shape of the K–pockets and the splitting of the Ta 5d conduction bands along the Γ–K direction is more pronounced in the normalized dataset. Therefore, band structure fitting (straight and dotted lines) was done by using the normalized datasets.

In Fig. 4.8 the band structure fit results for the TMDC misfit crystals $(SnS)_{1.17}NbS_2$ [Fig. 4.8(a)], $(PbS)_{1.14}NbS_2$ [Fig. 4.8(b)], $(PbS)_{1.14}(NbS_2)_3$ [Fig. 4.8(c)], and $(BiS)_{1.11}NbS_2$ [Fig. 4.8(d)] are illustrated. The band dispersion fits rather well to the experimental datasets, even though the intensity distribution in the measured PADs is sometimes blurry and does not show the pocket shape as pronounced as in Fig. 4.7 for $(PbS)_{1.14}TaS_2$. Fitting the band dispersion $E(k)$ and using the Fermi surface crossing of the fit results, the determined hole pocket size seems to be much more reliable than a simple "pixel counting" in the FS map. It should be mentioned that the quality of the band structure fit and the derived hole pocket size strongly depends on the dataset quality. For example, even though a (quasi) unit cell of the investigated TMDC misfit compounds spans more than one TMDC/MC doublelayer (except for $(SnS)_{1.17}NbS_2$), a splitting of the d bands could only be observed in the $(PbS)_{1.13}TaS_2$ datasets. In our NbS_2 misfit compounds only one electronic band could be observed at the Fermi surface. In contrast, band structure calculations and high resolution measurements, e.g., for pristine 2H–$NbSe_2$ crystals (isoelectrical to NbS_2)

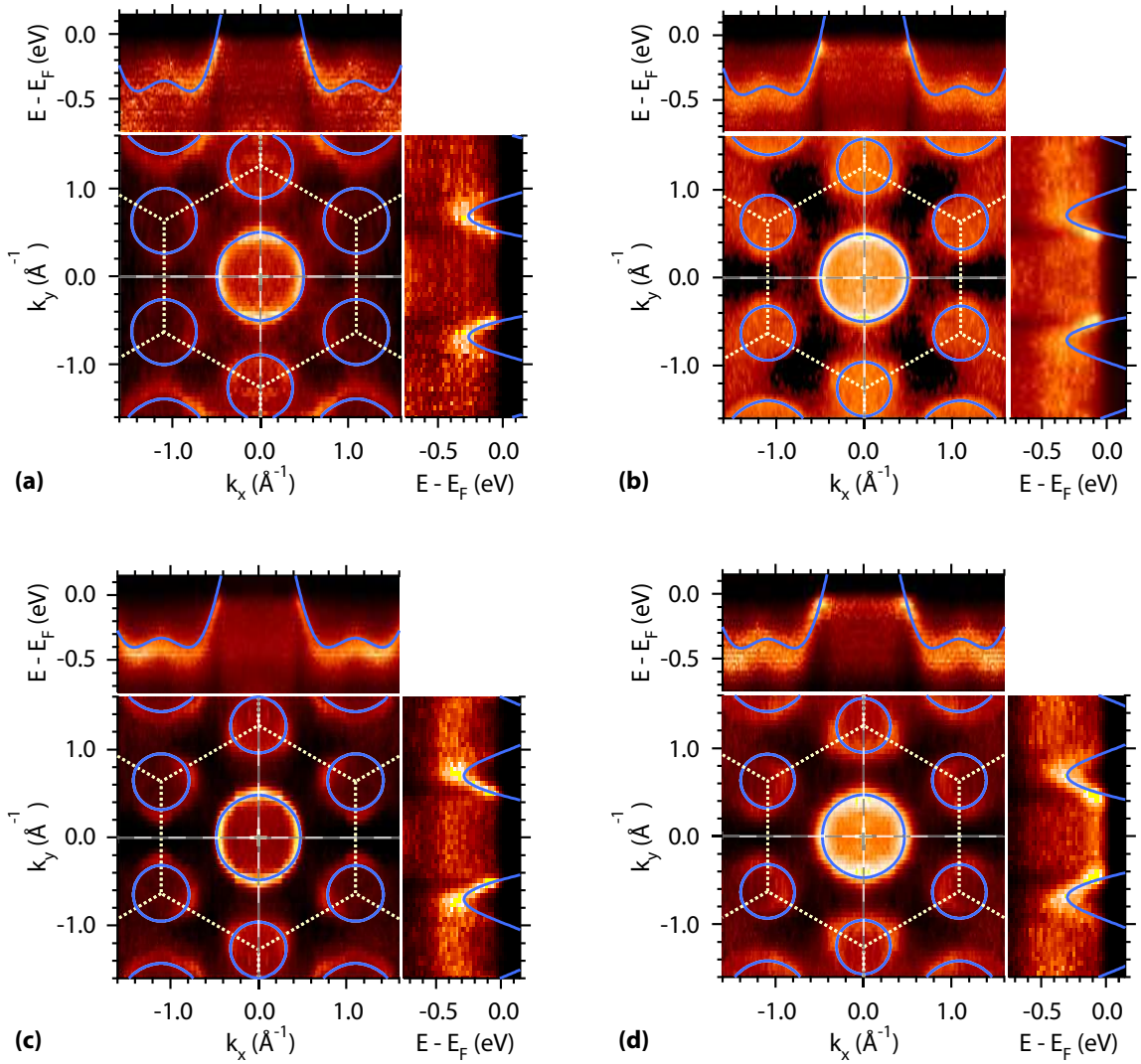

Figure 4.8: Normalized and symmetrized constant energy maps (higher brightness represents more intensity) of (a) $(SnS)_{1.17}NbS_2$ ($h\nu = 150$ eV), (b) $(PbS)_{1.14}NbS_2$ ($h\nu = 180$ eV), (c) $(PbS)_{1.14}(NbS_2)_3$ ($h\nu = 180$ eV) and (d) $(BiS)_{1.11}NbS_2$ ($h\nu = 180$ eV). For fit parameters of the band structure fit (straight lines) see Tab. 4.1.

show band splitting and double walled K–pockets [88], similar to $2H$–TaS_2. Therefore, either the TMDC interlayer interaction in the $2H$–TaS_2 misfit compounds is stronger than in the NbS_2 compounds so that the TMDC layer interaction can be neglected due to separation by a monochalcogen layer or the splitting in the Nb compounds exists but is much weaker than in the Ta compounds and cannot be resolved in our measurements. However, since the shape of the K–pockets in the $(PbS)_{1.13}TaS_2$ datasets seems to be dominated by the outer pocket–walls (see Fig. 4.7), the derived numbers for the charge transfer in $(PbS)_{1.14}NbS_2$, $(PbS)_{1.14}(NbS_2)_3$, and $(BiS)_{1.11}NbS_2$ seem to be a lower limit for the real charge transfer in these compounds.

The determined band filling for the different TMDC misfit crystals investigated in this thesis are summarized in Tab. 4.1. A band filling with more than one electron per transition metal atom can clearly be observed in all compounds, indicating a charge transfer to the TMDC subsystem in comparison to pristine TMDC compounds. Our results that are

restricted to the crystal surface (as ARPES is a surface sensitive method) are confirmed by (bulk sensitive) Hall effect measurements on crystalline and compacted powder samples [46, 50, 79–81]. In these measurements only positive Hall coefficients (in the range of $R_H \approx +10^{-9}$ m^3C^{-1} at T = 4 K and T = 300 K) were observed for all compounds, so that conduction by holes can be concluded. Calculating the number of conduction band electrons with the assumption of pure hole conduction ($R_H = 1/(pe)$, p:hole density), they derived numbers for the band filling larger than one electron per transition metal atom. Therefore, the band filling values derived by the Hall effect measurements [46, 50, 79–81] (CT_{HE} in Tab. 4.1) clearly indicate a charge transfer to the TMDC subsystem in comparison to pristine TMDC compounds.

However, the Hall effect measurements allow only the indirect determination of the band filling. The derived charge density values in general show a high uncertainty if the conduction band is nearly half filled so that the type of charge carriers cannot clearly be determined (pure electron or hole conduction leads to the better results). In addition, they crucially depend on the experimental parameters such as sample thickness, the distances between the electrical contacts, and the measurement method (e.g. two– or four–contact method). If additionally the Seebeck coefficient has an opposite sign in comparison to the Hall coefficient, such as found for all investigated misfit compounds [81, 89] (an opposite sign is also found for Ag intercalated 2*H*–TaS_2 and 2*H*–NbS_2 compounds [90] where charge transfer is established), the Hall effect measurements have a more qualitative meaning [81, 89]. Therefore, in spite of the Hall effect measurement results the existence of a charge transfer is still controversially discussed for the Pb, Sn, and Bi misfit compounds [55, 58, 59, 61–63]. In contrast to the Hall effect measurements, ARPES allows the direct determination of band filling in measuring the electronic band structure at the Fermi surface, leading to an accuracy independent of the band filling of about 10% in our measurements. This allows to compare the band filling in the different compounds.

As summarized in Tab. 4.1 an increased band filling from the Sn–compound to the Pb– and Bi–compounds can be observed. Using a simple rigid band model of charge transfer from the MC layers to the TMDC subsystem, such as mainly used in the discussions about the existence of a charge transfer, our results can hardly be understood. For example, using this model the charge transfer in $(PbS)_{1.14}(NbS_2)_3$ should be drastically reduced (e.g., by a factor 2 to 3) in comparison to the $(PbS)_{1.14}NbS_2$ compound, as the number of adjacent MC layers per TMDC layer is reduced in the $(PbS)_{1.14}(NbS_2)_3$ system. However, the observed charge transfer seems to be comparable in both compounds. Similar to this the larger band filling in the $(PbS)_{1.14}NbS_2$ compounds in comparison to the $(SnS)_{1.17}NbS_2$ compound does not agree with the stoichiometry considerations in these compounds. As the chemical composition of both compounds is identical except for an exchange of the metal atoms Pb and Sn, and there are formally only 1.14 PbS unit cells in $(PbS)_{1.14}NbS_2$ in comparison to 1.17 SnS unit cells in $(SnS)_{1.17}NbS_2$ per NbS_2 unit cell, a larger charge transfer in the SnS compound should be expected, in contrast to the observations. The contrary case is found for the $(BiS)_{1.11}NbS_2$–compounds which show the largest charge transfer of the Nb compounds, even though there are formally the fewest MC atoms per NbS_2 unit cell. Therefore, in particular the type of metal atoms in the MC layer seems to be responsible for the conduction band filling of the TMDC subsystems, independent of the stoichiometry in the misfit compounds. For example, the higher number of loosely bound outer shell electrons in the group V A–element Bi might be responsible for the high charge transfer in the Bi–compounds, while the charge transfer differences in the Pb and

Sn compounds seems to be more complicated. However, we also observed a rather large charge transfer difference between $(PbS)_{1.14}NbS_2$ and $(PbS)_{1.13}TaS_2$ that have comparable amounts of identically composed monochalcogen sublayers. Therefore, in addition to the type of the MC metal atom the transition metal atom type also plays a significant role for the charge transfer amount. The difference between the Nb and the Ta compound may be associated with the higher electron affinity of Nb–atoms in comparison to Ta–atoms so that an electron donation to the NbS_2 layers might be favored in comparison to TaS_2 layers, leading to a higher band filling in the Nb compounds.

Since in contrast to the band filling of the TMDC dominated conduction band, we did not observe any partly filled monochalcogen derived conduction bands, this type of charge transfer might be induced by single, localized metal atoms rather than by whole monochalcogen sublayers. Large charge transfer to the TMDC sublayer in comparison to the pristine TMDC compounds cannot be neglected for the Pb, Sn, and Bi compounds, so that an ionic contribution to the interlayer bonding seems to be important for the binding mechanism in these compounds. Since the origin of the charge transfer cannot be easily understood, a more complex binding mechanism has to be considered, e.g., a cross-substitution of metal atoms as described in chapter 5.

4.4 Influence of the incommensurability on the electronic stucture

In the previous section it was shown that the electronic structure at the Fermi level of TMDC misfit compounds is dominated by the hexagonally ordered TMDC subsystem. In contrast to this, PAD maps taken at higher binding energies show the symmetry of both subsystems, depending on the binding energies. For example, PAD measurements

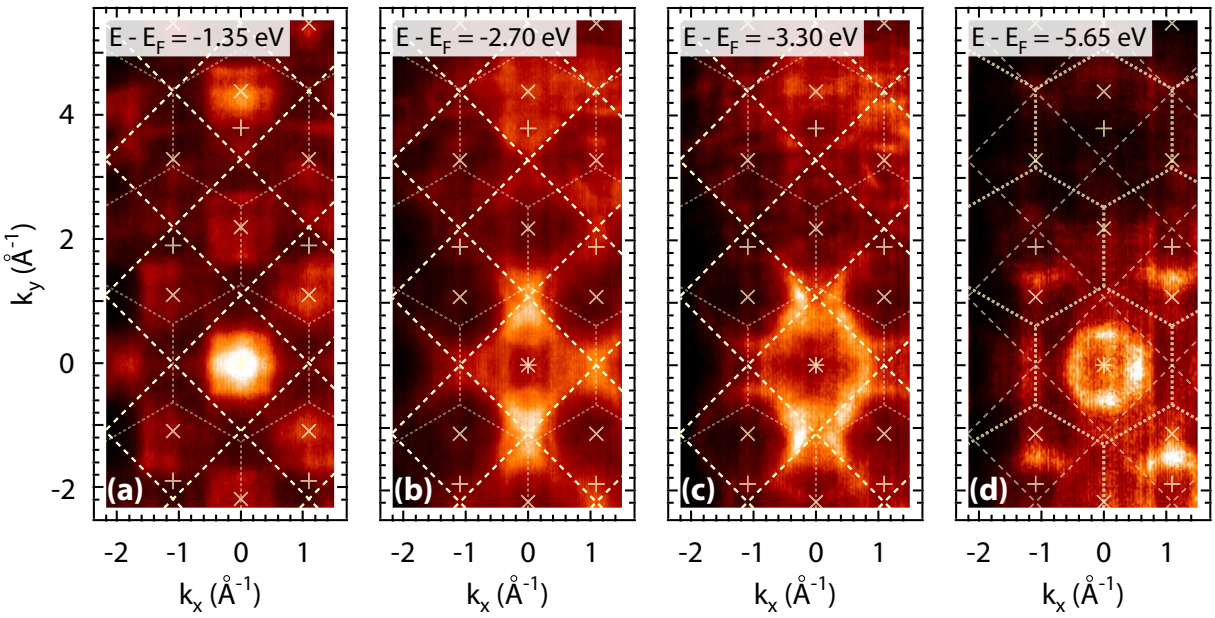

Figure 4.9: Constant energy maps of $(PbS)_{1.14}NbS_2$ at different electron binding energies showing (a)–(c) square and (d) hexagonal symmetry, depending on the electron binding energy ($h\nu = 180$ eV).

of $(PbS)_{1.14}NbS_2$ at $E - E_F = -1.35$ eV, -2.70 eV, and -3.30 eV [see Figs. 4.9(a)–(c)] clearly show cubic symmetry, while at $E - E_F = -5.65$ eV hexagonal symmetry can be observed [see Fig. 4.9(d)]. The PAD at $E - E_F = -1.35$ eV is characterized by square structures, centered on the Γ–points of the monochalcogen Brillouin zones (dashed lines). Cubic symmetry is visible in nearly all higher Brillouin zones of Fig. 4.9(a), indicating that the electronic structure is dominated by the monochalcogen sublayer. For higher binding energies [Figs. 4.9(b), (c)] the photoelectron spectral weight in the higher Brillouin zones vanishes, indicating strong matrix element effects. However, since in particular the intensity in the higher Brillouin zones vanishes for electronic states, that cannot clearly be attributed to one of the subsystems, the intensity reduction possibly indicates a superposition or mixing of electronic states of both subsystems, weakened at larger distances from the first Brillouin zone due to the higher misfit between the TMDC and monochalcogen subsystems (see Fig. 4.9).

As already mentioned in section 4.3, the electronic structure at the Fermi surface is dominated by the transition metal *d*–bands. However, in particular in the higher Brillouin zones of the Pb containing misfit compounds $(PbS)_{1.13}TaS_2$, $(PbS)_{1.14}NbS_2$, and $(PbS)_{1.14}(NbS_2)_3$ we observed additional ring structures with the same dispersion as observed for the transition metal dominated *d*–bands. In the Bi and Sn compounds only slight indications by a blurring of photoelectron intensity can be observed. As illustrated in Fig. 4.10 for $(PbS)_{1.14}NbS_2$, the additional ring structures are centered on all Γ–points of the MC Brillouin zones as well as shifted from these positions parallel to the incommensurate direction (gray rings). The ring positions can be reconstructed by backfolding the original hexagonal symmetric hole pocket positions by the reciprocal lattice vectors of both subsystems. For example the ring structure emphasized by a dotted, white line in Fig. 4.10(a) can be reconstructed by translating the hole pocket, centered at the Γ–point, by reciprocal lattice vectors (b) of the PbS subsystem to the center of the adjacent PbS Brillouin zone along the incommensurate k_y–direction and a subsequent translation by the reciprocal lattice vectors (c) of the hexagonal NbS_2 subsystem. In addition to folding out of the band structure with the symmetries of both subsystems, the photoemission spectral weight seems to decrease with the number of umklapp processes involved, similar to the case in CDW systems [71,72].

In order to examine additional interactions between the electronic structure of both subsystems that exceed the backfolding effects, we investigated the dispersion of the electronic bands in more detail. In systems with strong interacting potentials a modulation of the band dispersion at the Brillouin zone boundaries with the periodicity of both potentials is expected, as it can be found for example in CDW systems [71]. For the TMDC misfit compounds a strong electronic layer–to–layer interaction could possibly result in backbending of the transition metal derived conduction bands at the Brillouin zone boundaries of the MC subsystem as well as in a modulation of the mainly monochalcogen and TMDC sulfur derived valence bands. Figures 4.11(a) and 4.11(b) show the electronic structure of $(PbS)_{1.14}NbS_2$ by two E–k_y–maps parallel to the incommensurate direction. At binding energies below the p/d–gap, similar to Fig. 4.9 symmetries of both subsystems (indicated by guides to the eye) can be observed. Even though in specific areas bands with the symmetry of the PbS (blue, dashed lines) and NbS_2 subsystem can be clearly separated, in the vicinity of the Γ*–point the symmetry of the PbS derived bands seems to be distorted (elliptical region in Fig. 4.11). This might be an effect of the misfit in the incommensurate direction. A modulation of the conduction band dispersion by the periodicity of the cubic subsystem is hardly observable, as the superposition of various valence bands smears

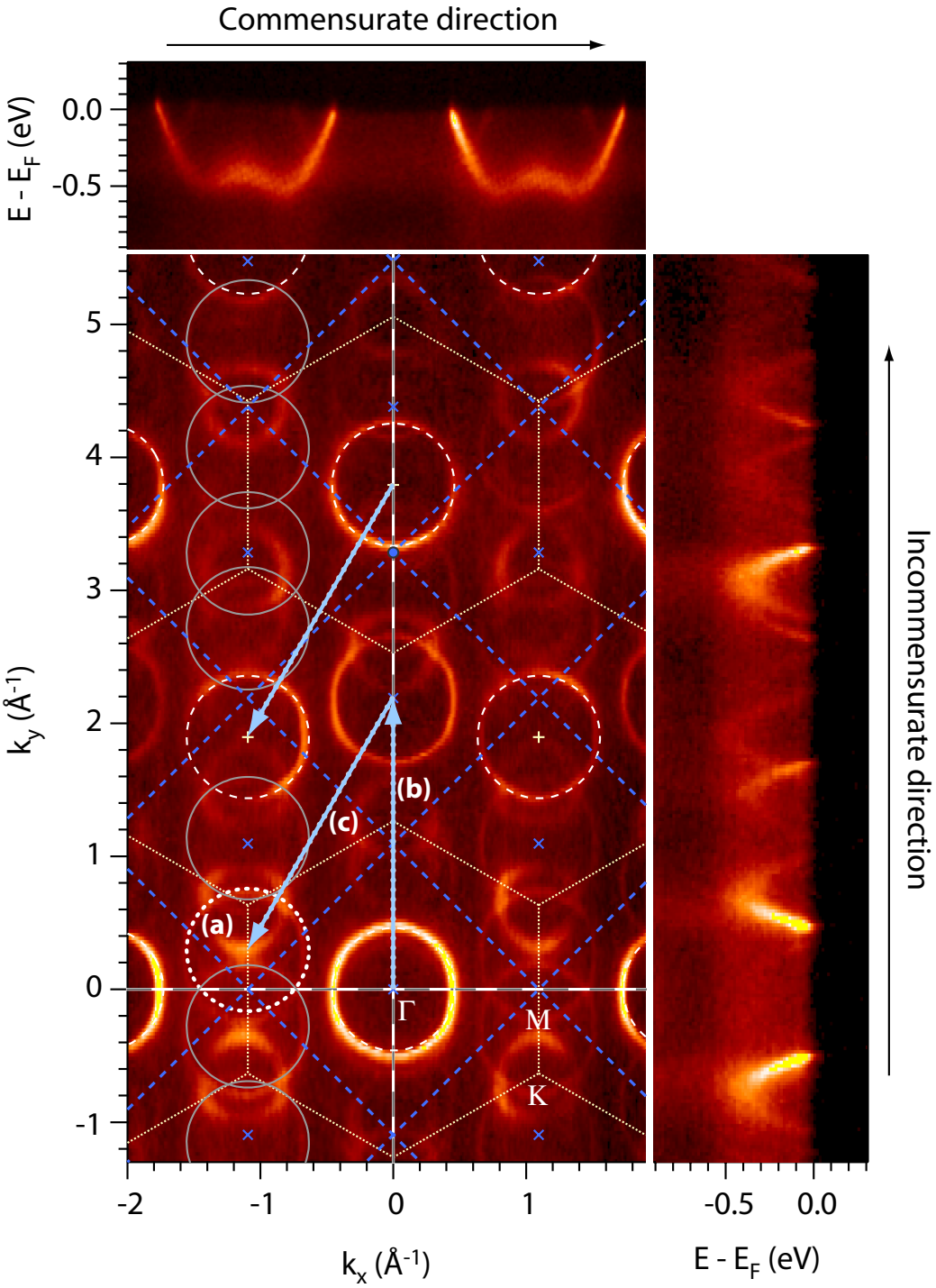

Figure 4.10: Constant energy maps of $(PbS)_{1.14}NbS_2$ at $E = E_F$ with hexagonal (dotted yellow lines) and cubic (dashed blue lines) Brillouin zones ($h\nu = 180$ eV).

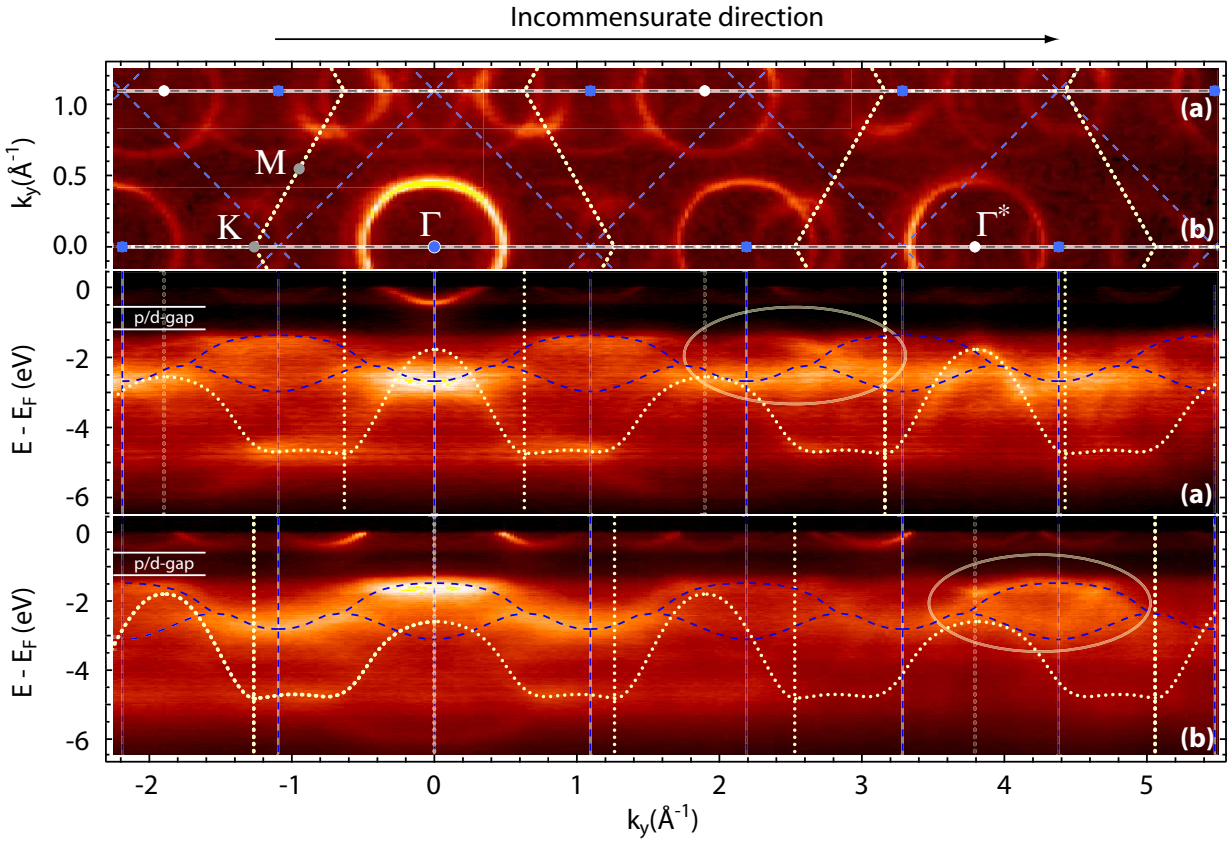

Figure 4.11: Constant energy map of $(PbS)_{1.14}NbS_2$ at $E = E_F$ (top) and slices through the dataset in the incommensurate direction along the lines (a) and (b) with Brillouin zone boundaries and guides to the eye for electronic bands with hexagonal (yellow, dotted lines) and cubic (blue, dashed lines) symmetry ($h\nu = 180$ eV).

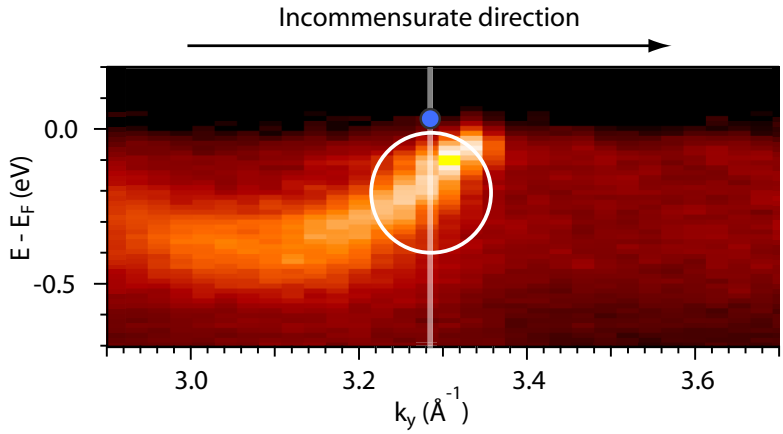

Figure 4.12: Photoemission map ($h\nu = 180$ eV) of $(PbS)_{1.14}NbS_2$ along the incommensurate k_y direction in the vicinity of the Brillouin zone boundary of the PbS subsystem (blue dot and white line). For more details see text.

out the photoemission maps in Fig. 4.11. Since the photoelectrons with energies above the p/d–gap mainly originate from Nb 4*d* states, a modulation in band dispersion of the TMDC subsysten with the symmetry of the PbS subsystem should be more pronounced here. However, observing the conduction band dispersion in more detail, we did not find any hint for a modulation of the Nb 4*d* bands except for backfolding. This can be seen for example in Fig. 4.12 where the occupied bands are crossed by the Brillouin zone boundary of the PbS subsystem while the band dispersion is not affected by the potential of the cubic subsystem. The reason for these unmodulated transition metal derived conduction bands may be a strong screening of the transition metal electrons by the surrounding TMDC sulfur atoms. As the layer–to–layer interaction in TMDC misfit compounds seems to be restricted to the monochalcogen–sulfur interface, only weakly affecting the electronic structure of the subsystems, the interlayer interaction seems to be weak.

4.5 Conclusions

In conclusion, the electronic structure of the TMDC misfit compounds containing Pb, Sn, or Bi shows signatures of both subsystems. In particular at the TMDC dominated Fermi surface umklapp shifted bands with the symmetry of both subsystems appear, while the band dispersion seems to be only slightly affected by the different competing potentials of the layered subsystems. Observing no indication for electronic dispersion perpendicular to the layers, covalent bonding should only play a minor role in the bonding between the TMDC misfit layers. In contrast, the ionic contribution to the interlayer bonding cannot be neglected, as in comparison to pristine TMDCs for all misfit compounds we clearly observed a more than half filled conduction band, indicating charge transfer to the TMDC subsystem. Since all occupied monochalcogen derived bands seem to be completely filled and the type of metal atoms in the MC layers seems to determine the charge transfer, the charge transfer might be induced by localized metal atoms more than by whole monochalcogen sublayers.

5 On the stability of TMDC misfit compounds

Photoemission micro–spectroscopy on the layered misfit compound $(PbS)_{1.13}TaS_2$ provides direct evidence for Ta substitution into PbS layers as well as for Pb substitution into TaS_2 layers. This metal cross–substitution alters the charge balance between alternating layers and can explain the remarkable stability of $(PbS)_{1.13}TaS_2$ and, possibly, of analogous misfit compounds. It is suggested that even formally stoichiometric misfit compounds can be stabilized by this mechanism.

5.1 Introduction

Bonding in layered materials is a challenging problem because it includes various types of interactions ranging from strong local covalent bonds over electrostatic interactions to rather weak nonlocal van der Waals (vdW) forces [91]. Prototype layer compounds are provided by the family of transition-metal dichalcogenides (TMDCs) whose crystal structures consist of hexagonal chalcogen—transition metal—chalcogen sandwiches. While strong covalent and ionic bonding prevail within the sandwiches, inter-sandwich bonding is dominated by weak vdW forces. Consequently, the electronic properties of TMDCs are highly anisotropic which favors, e.g., the occurrence of a plethora of charge-density-wave phases and correlation effects [92]. Moreover, due to the weak vdW interlayer interactions and the relatively large layer–to–layer distances, TMDCs allow for the insertion of foreign atoms or molecules into the vdW gaps. This intercalation is generally accompanied by a charge transfer from the intercalant to the host layers which leads to electrostatic contributions to the interlayer interactions [38].

If instead of single atoms or molecules crystalline bilayers of cubic monochalcogenides (MCs) are inserted into the TMDC vdW gaps (see Fig. 5.1), interlayer bonding and stability considerations become more complex in the resulting TMDC–misfit crystals. Due to the different crystal structures of the subsystems, the lattice constants match only along one crystallographic axis parallel to the surface. Perpendicular to this commensurate direction the lattice constants are in an irrational ratio described by the misfit parameter δ ($0.08 < \delta < 0.25$). Since the alternation of different layers, the lattice mismatch, and the occurrence of MC bilayers (whereas pristine MC compounds have a three–dimensional rock salt structure) all act against a low total energy, the high stability of the misfit compounds comes as a surprise. Yet, despite extensive efforts [58,61–64,77,78], the dominant interlayer bonding mechanism has remained elusive.

Possible bonding mechanisms are illustrated in Fig. 5.1. While vdW forces between the TMDC and MC layers are certainly present [Fig. 5.1(a)], they can probably not account for the high stability of the misfit compounds. Since it is natural to compare with other TMDC intercalation compounds, one might expect the misfit layer compounds to be stabilized by electron transfer from the MC layers to the TMDC layers [Fig. 5.1(b)]. However, there has been much controversy over whether this kind of charge transfer really occurs in these compounds [58,61–64,77,78]. Electron removal from the MX layer would imply an oxidation state of M higher than +2, which is normally not found in sulphides with the rock salt structure [77]. Furthermore, the pristine MX compounds are semiconductors, and the presence of a band gap between occupied and empty bands does not favor electron donation. From the absence of charge transfer in X–ray photoelectron spectroscopy [61] and from the results of band structure calculations [63] it was thus concluded that the interlayer

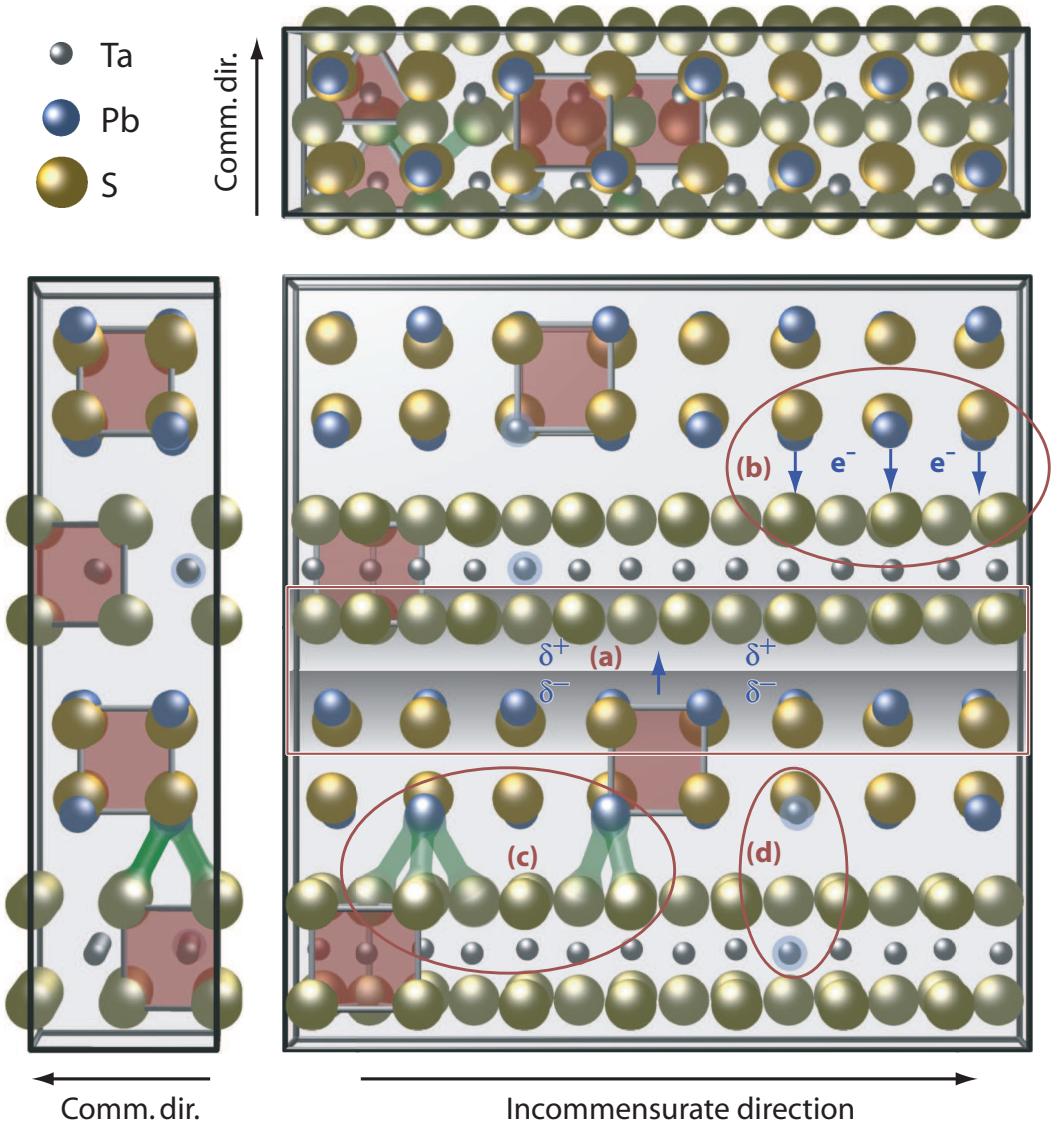

Figure 5.1: Crystal structure of the misfit layer compound $(PbS)_{1.13}TaS_2$. The large yellow spheres represent sulfur atoms of both subsystems, the smaller blue spheres correspond to the lead atoms of the PbS subsystem, and the small gray spheres represent the Ta–atoms of the TaS_2 subsystem (left: side view, right: front view, top: top view). A quasi–commensurate unit cell is shown $[(PbS)_8(TaS_2)_7]$. Commensurate and incommensurate directions are indicated. Possible interlayer bonding mechanisms (a)–(d) are described in the text.

interactions are of covalent character [Fig. 5.1(c)]. Finally, in a study of several misfit layer compounds by means of electron probe microanalysis, Moëlo *et al.* [77] found a systematic depletion of M atoms and a corresponding excess of T atoms, suggesting that T atoms were substituted into the MX layers [Fig. 5.1(d)]. They pointed out that such a substitution may provide the changes in the charge balance needed to stabilize the misfit layer structure, and suggested that the deviation from the ideal, stoichiometric structure is a necessary condition for the stability of these compounds.

In this chapter the nature of the interlayer bonding in misfit layer compounds is studied by photoelectron micro–spectroscopy measurements on the compound $(PbS)_{1.13}TaS_2$. Our results strongly support the idea that Ta atoms are substituted into the PbS layers, in accordance with the suggestions of Moëlo *et al.* [77], but we also find strong evidence for Pb substitution into the TaS_2 layers. This novel metal cross-substitution mechanism alters the charge balance between the two types of layers in a way that strongly enhances the interlayer bonding. We argue that metal cross-substitution is of fundamental importance for the stability of $(PbS)_{1.13}TaS_2$ as well as analogous misfit layer compounds and we suggest that even formally stoichiometric compounds may be stabilized by this mechanism.

5.2 Experimental details

In general, there are two different methods to do spatially resolved photoemission spectroscopy in the soft X–ray regime: spectro–microscopy and micro–spectroscopy. In spectro–microscopy experiments the sample is illuminated with a large light spot so that the photoelectrons are emitted from a large area on the sample surface. An electron optical system analyzes the emitted photoelectrons in parallel with a spatial resolution of down to about 2 nm so that the surface topology can be imaged with very high data acquisition rates [93–96]. High angular resolution of down to $\Delta\theta \approx 0.5°$ is also achievable but only in combination with a spatial resolution in the micrometer regime. Todays best energy resolution of these so called photoemission electron microscopes (PEEM) is limited to about $\Delta E \approx 100$ meV. As in general very high voltages of up to $U \approx 20$ keV between sample and microscope are applied, in particular metallic samples with very flat surfaces are

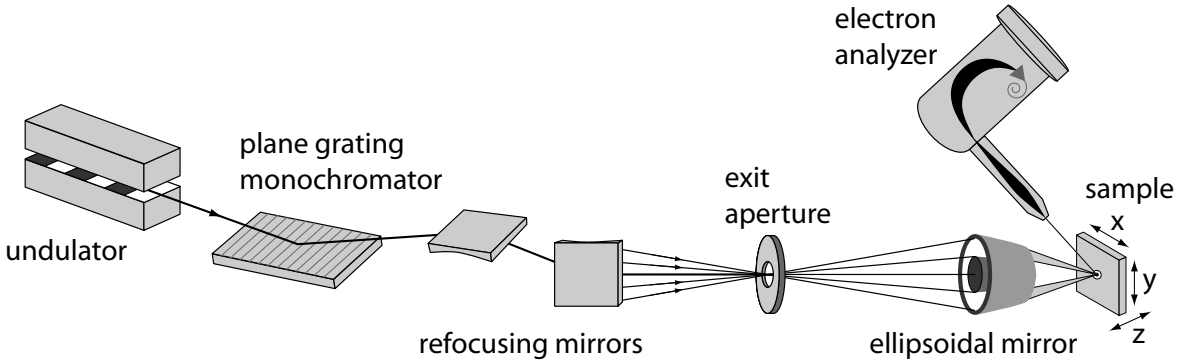

Figure 5.2: Schematic of the photoelectron microscope beamline at MAX–lab with undulator, plane grating monochromator, focusing mirrors in Kirkpatrick–Baez configuration, pinhole aperture, elliptical mirror, and movable sample. The photoelectrons are detected with a hemispherical electron analyzer VG–X900 at a fixed emission angle of 47.5° (after [14]).

investigated due to the high sensitivity to charging and spark discharges.

In micro–spectroscopy experiments on the other hand, the sample is illuminated by a highly focused light spot. Its size mainly determines the spatial resolution of the experiment as no electron imaging system is installed. Therefore, the photon densities on the sample can be much higher than in spectro–microscopy experiments, so that radiation damage of sensitive samples may become a problem. Since there is no electric or magnetic field between sample and electron analyzer, very high energy resolutions of less then $\Delta E \approx 1$ meV and angle resolutions of about $\Delta\theta \approx 0.1°$ can be achieved with modern hemispherical photoelectron analyzers.

The photoelectron microscope (PEM) at the synchrotron beamline 31 at MAX–lab (Lund, Sweden) [14] is a micro–spectroscopy experiment. As illustrated in Fig. 5.2, the undulator radiation in the range of $h\nu = 15..150$ eV is monochromatized by a plane grating monochromator with two interchangeable plane gratings of 500 lines/mm or 1000 lines/mm. Employing a Kirkpatrick–Baez mirror configuration [see also Fig. 5.3(a)], the monochromatic radiation is refocused in horizontal and vertical direction into an intermediate focus at the exit pinhole aperture. The light that is transmitted through the pinhole is focused by a ring–shaped ellipsoidal mirror [see also Fig. 5.3(b)] into the focal plane down to a spot size of about 1.5 μm in diameter. The sample is mounted on a bellow that can be moved in three dimensions from outside the vacuum. The system is controlled by Heidenhain positioning sensors. Achievable step sizes are about 1 μm. Because the hemispherical electron analyzer VG–X900 with single–channeltron detector is installed at a fixed angle of 47.5° with respect to the sample surface, photoelectrons are only measured if emitted in this direction. Therefore, spatially resolved ARPES measurements are not very meaningful at beamline 31. But since core level states are non–dispersive in k–space, spatially resolved core level spectroscopy measurements are feasible at this experiment and were done on the

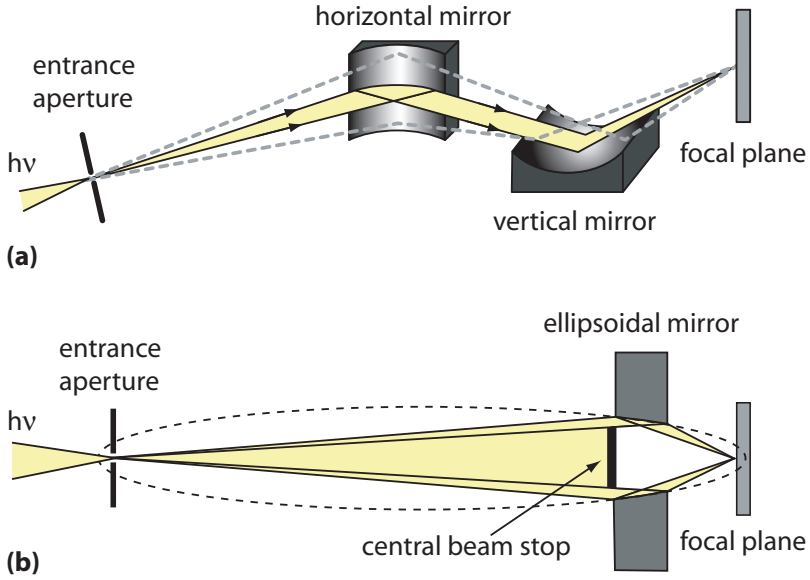

Figure 5.3: Illustration of the focusing devices used at beamline 31 at MAX–lab: (a) focusing mirrors in Kirkpatrick–Baez configuration, in which the monochromatic radiation is refocused in horizontal and vertical direction into the focal plane, and (b) ellipsoidal mirror (dashed line: ellipsoidal shape) with central stop to block directly transmitted, unreflected light (graphics after [14]).

TMDC misfit crystal $(PbS)_{1.13}TaS_2$.

The $(PbS)_{1.13}TaS_2$ crystals were attached to the sample holder by silver-filled epoxy resin and transferred into the UHV system, where a clean (0001) surface was obtained by cleavage. Further surface sensitive investigations were performed by depositing Na and Cs in situ from carefully outgassed SAES getter sources. The base pressure was in the low 10^{-10} mbar range in both the preparation and the microscope chamber. During deposition of Na and Cs the pressure in the preparation chamber increased to approximately $2 \cdot 10^{-9}$ mbar and $5 \cdot 10^{-10}$ mbar, respectively. All depositions and measurements were performed with the sample at room temperature. The total energy resolution is about 335 meV. Since Na and Cs depositions lead to similar results, only the Cs datasets are presented here.

5.3 Characterization of the TMCD misfit compound surface

As already mentioned in section 3.4, typical surfaces of TMDC misfit crystals show stress induced stripes perpendicular to the incommensurate direction that can be some hundred micrometers wide, as observable in microscopic photographs (see Fig. 3.10). A similar pattern can be seen in a typical PEM surface area map of $(PbS)_{1.13}TaS_2$ (Fig. 5.4), as

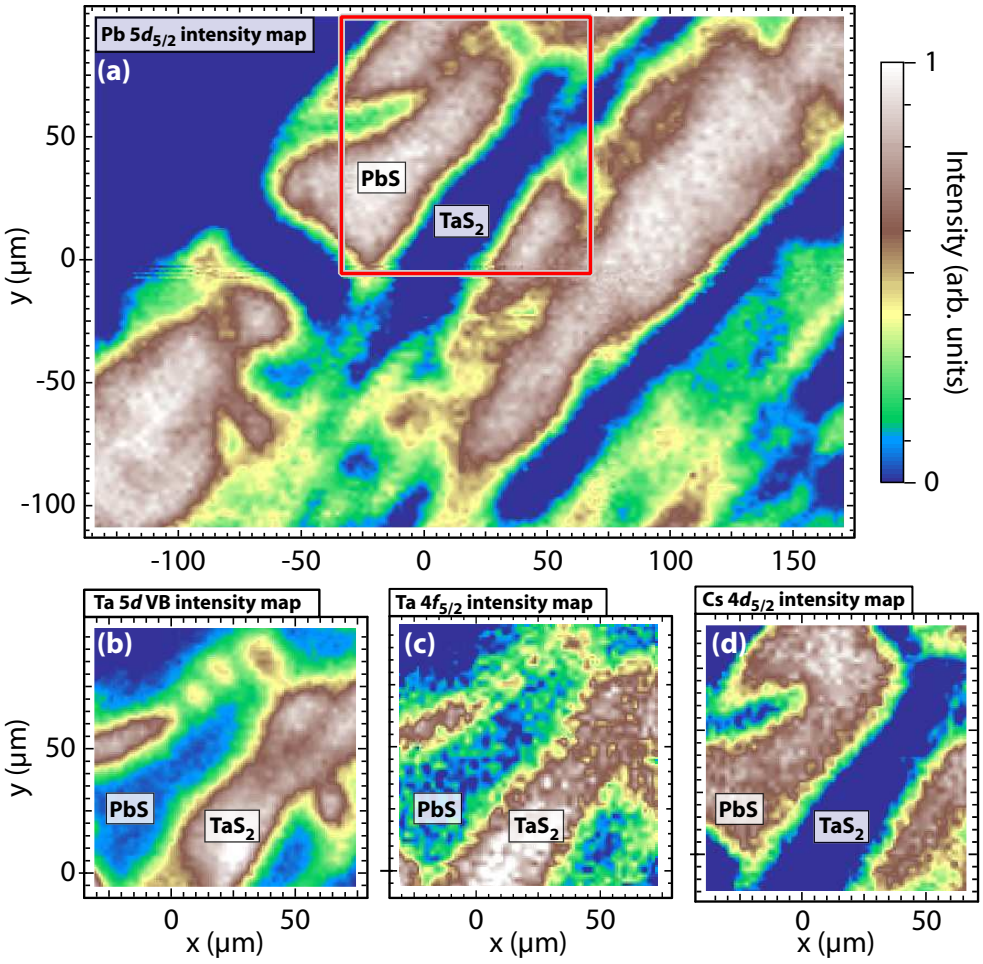

Figure 5.4: Surface area of $(PbS)_{1.13}TaS_2$, as imaged by photoemission microscopy from (a) the Pb $5d_{5/2}$ core level, (b) the Ta $5d$ valence band ($E - E_F \approx 0.5$ eV), (c) the Ta $4f_{5/2}$ core level, and (d) the Cs $4d_{5/2}$ core level (after 3 min. of Cs deposition).

imaged by photoemission from the Pb 5*d* core level as well as from Ta 5*d* valence and Ta 4*f* core states. The Pb and Ta images are clearly complementary, demonstrating that cleavage produces domains terminated either by PbS or TaS_2 layers. After Cs evaporation, significantly higher Cs 4*d* core level intensities are found on the PbS terminated regions [Fig. 5.4(d)], indicating that Cs adsorption occurs predominantly on the PbS domains.

5.4 Cross substitution of metal atoms

In order to study the binding mechanism between the layers, XPS at different surface locations was done. Figure 5.5 shows combined Ta 4*f* and Pb 5*d* core level spectra taken from PbS and TaS_2 domains, respectively. Consistent with inelastic mean free path considerations, the intensities of the Ta 4*f* emissions are reduced in the PbS domains [Fig. 5.5(a)] and the Pb 5*d* intensities are strongly suppressed in the domains terminated by a TaS_2 layer [Fig. 5.5(d)]. Comparing the Ta 4*f* core level spectra from the two domains first, an additional peak is found in the spectrum from the PbS domain, with higher binding energy as compared to the main Ta 4*f* peaks. Upon Cs deposition, this extra peak shifts towards higher binding energies and it becomes clear that it is the high-energy part of a peak doublet [Figs. 5.5(b) and 5.5(c)]. Since the separation between the two additional peaks amounts exactly to the Ta 4*f* spin-orbit splitting and since the extra peaks are only present in the spectra from the PbS domain, we attribute them to Ta atoms located in the PbS layer. The energy shift of about 2.15 eV towards higher binding energies for the substituted Ta

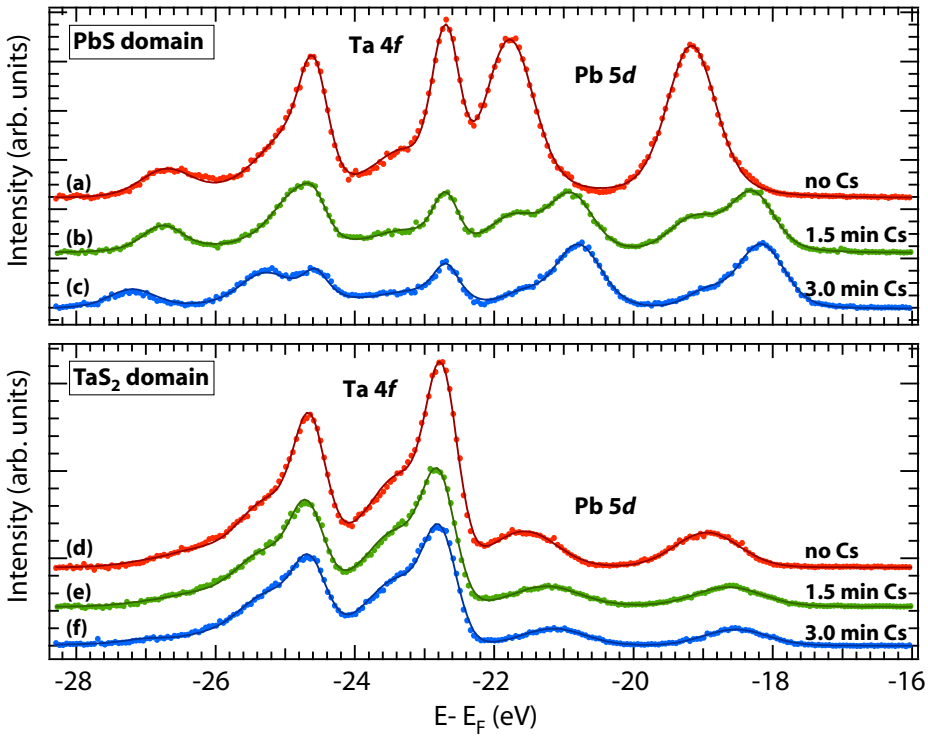

Figure 5.5: Pb 5*d* and Ta 4*f* core level spectra of $(PbS)_{1.13}TaS_2$, measured at BL31/MAX–lab from PbS (top) and TaS_2 (bottom) domains: (a),(d) clean surface, (b),(e) after 1.5 min. of Cs deposition, and (c),(f) after 3.0 min. of Cs deposition ($h\nu = 116.5$ eV). Experimental data (dots) and fit results (solid lines) are plotted. A Shirley background has been subtracted.

is then probably due to less efficient final–state screening in the semiconducting PbS layer. By contrast, the Cs induced Pb 5*d* splitting in the PbS surface domain [Figs. 5.5(b) and 5.5(c)] is probably caused by two inequivalent Pb sites: the one adjacent to the vacuum, where Cs adsorption takes place, and the one adjacent to the TaS_2 layer below.

Comparing now the Pb 5*d* core level spectra from the two domains [Figs. 5.5(a) and 5.5(d)], the Pb 5*d* peaks measured from the TaS_2 terminated region are broader and slightly shifted towards lower binding energies. Figure 5.6(g) shows a spectrum from the same TaS_2 domain but taken with a different photon energy in order to increase the Pb 5*d* photoionization cross section. It appears that the Pb $5d_{3/2}$ and Pb $5d_{5/2}$ lines each have two components. This is further corroborated by measurements with higher energy resolution on a different sample whose cleavage produced two very large domains. Upon crossing the boundary from the TaS_2 to the PbS domain, the spatially integrated photoemission spectra clearly reveal the emergence of a Pb 5*d* double peak structure [Figs. 5.6(b)–5.6(f)]: one component with the same binding energy as the corresponding peak obtained from the PbS domain [Fig. 5.6(a)], and the other component with somewhat lower binding energy. In analogy with the extra Ta 4*f* peaks in the PbS domain, we attribute the additional Pb 5*d* components seen in the TaS_2 domain to Pb atoms substituted into the TaS_2 layers, because

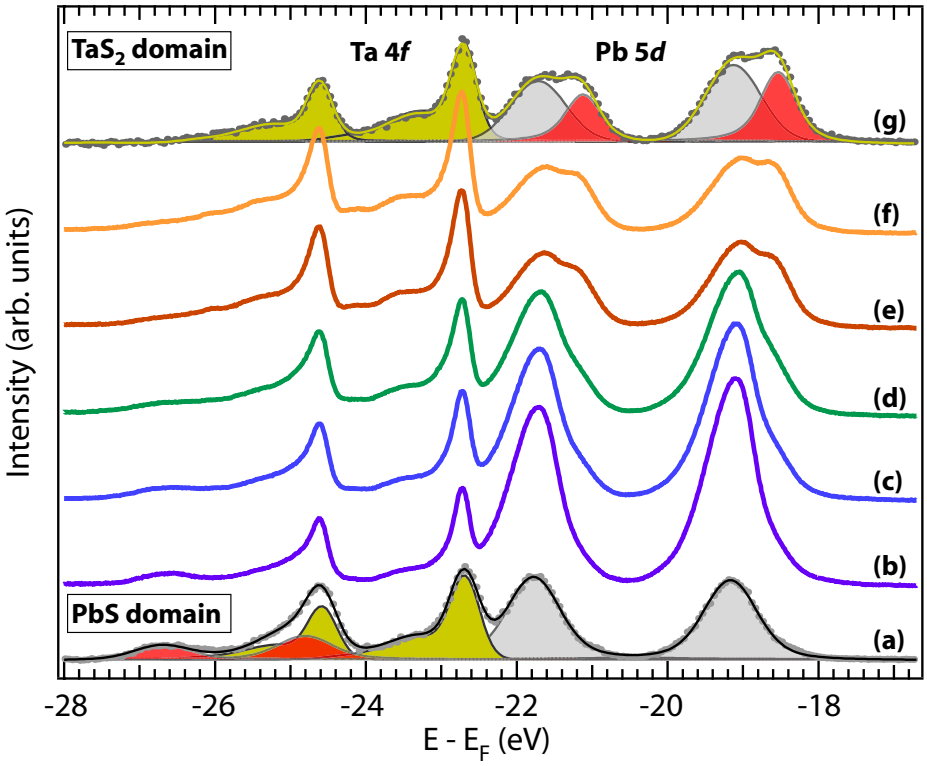

Figure 5.6: Pb 5*d* and Ta 4*f* core level spectra of $(PbS)_{1.13}TaS_2$, taken at BL31/MAX–lab with high spatial and moderate energy resolution from (a) a PbS domain ($h\nu = 116.5$ eV) and (g) a TaS_2 domain ($h\nu = 73.2$ eV). The decomposition of the spectra into different components is indicated. Components originating from cross-substituted atoms are highlighted in red. A Shirley background has been subtracted. (b)–(f) Corresponding spectra taken at BW3/HASYLAB with higher energy resolution ($\Delta E \approx 80$ meV) and moderate spatial resolution (about 100×300 μm^2) from the transition region between PbS and TaS_2 domains of a different sample ($h\nu = 116.5$ eV).

the two extra peaks are separated by a value matching the Pb $5d$ spin-orbit splitting and because they only show up in the spectra from the TaS_2 domain. Here the shift of about 0.55 eV towards lower binding energy is probably due to the more efficient final–state screening in the metallic TaS_2 layer.

Hence, from our experimental results, we may conclude that substitution of Pb atoms into TaS_2 layers as well as substitution of Ta atoms into PbS layers occurs in $(PbS)_{1.13}TaS_2$. This Pb–Ta cross-substitution can be described by the modified chemical formula $(Pb_{1-x}Ta_xS)_{1.13}(Ta_{1-y}Pb_yS_2)$. In order to determine the concentrations x and y, we have further analyzed the Pb $5d$ and Ta $4f$ spectra from the two domains by line shape fitting. To model the spectra, we have used Voigt profiles for the various emissions, except for the Ta $4f$ peaks of the TaS_2 layers. These emissions have a characteristic asymmetric line shape, which is caused by valence electron screening [7]. For them, we have used a joint density of states based model that was developed to fit the asymmetric Ta $4f$ lines in $2H$–TaS_2 and intercalated compounds [7, 97]. In our model we have calculated the joint density of states from a tight binding fit to angle-resolved photoemission spectroscopy (ARPES) data of the Ta $5d$–derived valence band [98]. Convolution of the resulting line shape with a Voigt profile then reproduces the measured spin-orbit split Ta $4f$ spectra very well [see Figs. 5.6(a) and 5.6(g)]. By contrast, the Ta $4f$ emissions originating from the semiconducting PbS domains do not show the asymmetric line shape. They are broader, which may be due to the presence of two inequivalent metal sites in the topmost PbS layer, and are well enough reproduced by Voigt profiles.

As illustrated in Figs. 5.5 and 5.6 the overall fitted line shapes are in excellent agreement with the observed complete spectra. Figures 5.6(a) and 5.6(g) show the resulting decomposition of the Ta $4f$ emissions from the PbS domain and of the Pb $5d$ emissions from the TaS_2 domain. Each emission has components originating from the buried layer and one component originating from the substituted atoms (at lower binding energy for substituted Pb and at higher binding energy for substituted Ta). Taking the ratio of the relevant peak areas and considering the different photoionization cross sections [99], we obtain concentrations of $x = 0.18 \pm 0.05$ for Ta substituted into the PbS layer and $y = 0.08 \pm 0.05$ for Pb substituted into the TaS_2 layer.

This asymmetric Pb–Ta cross-substitution will alter the charge balance of the system. In a simple ionic picture, a partial substitution of Ta^{3+} ions for x Pb^{2+} ions in the PbS layer can be assumed, which implies a PbS layer that remains semiconducting and a transfer of $1.13x$ electrons to the adjacent TaS_2 layer. If, on the other hand, y Ta^{4+} ions are substituted by Pb^{4+} ions in the TaS_2 layer, the Ta $5d$ valence band will contain $1-y$ electrons per unit cell without charge transfer and $1-y+1.13x$ electrons per unit cell with the charge transfer from the PbS layer. Although Pb is normally not found in an oxidation state higher than +2 in sulfides with the rock salt structure, there exists a polymorph of PbS_2 isostructural with the CdI_2–type SnS_2 structure with six nearest neighbor S atoms and an oxidation state of +4 [100]. Using the above values for x and y, we obtain an increased Ta $5d$ band filling of 0.12 ± 0.1 electrons per $Ta_{1-y}Pb_yS_2$ unit cell, which is in fairly good agreement with Hall effect [46] and ARPES [98] measurements.

So why are $(PbS)_{1.13}TaS_2$ and analogous misfit layer compounds stable? In accordance with Moëlo *et al.* [77], we argue that Ta atoms substituted into the PbS layers induce an electron transfer to the TaS_2 layers so that the alternating PbS and TaS_2 layers become charged and bound together by electrostatic forces. In contrast to Moëlo *et al.* [77], who pointed out that non–stoichiometry is a necessary condition for the stability, we emphasize

that the cross–substitution mechanism may work even for formally stoichiometric misfit layer compounds. The balance between the two types of substitutions may vary, depending on the crystal growth conditions, but in all cases stabilizing metal substitutions will occur.

5.5 Conclusions

In conclusion, by measurements of core level spectra from differently terminated domains on cleaved surfaces of the layered misfit compound $(PbS)_{1.13}TaS_2$ we have found direct spectroscopic evidence for Ta substitution into PbS layers as well as Pb substitution into TaS_2 layers. The concentrations of the substituted atoms are of the order of 5–20%, which leads to an effective charge transfer of about 0.1 electrons per TaS_2 unit from the PbS to the TaS_2 layers. We suggest that such metal cross–substitution is of fundamental importance for the stability of $(PbS)_{1.13}TaS_2$ and similar misfit layer compounds and that non–stoichiometry may not be a necessary condition for their stability.

6 Towards spatially resolved ARPES

The progress in micro– and nano–structuring of surfaces leads to a general interest in the electronic structure on the nano-scale, particularly with regard to the miniaturization of integrated circuits or self-organized structures such as nanowire networks. In order to process spatially and angle resolved photoemission (see Fig. 6.1), a new nano–spectroscopy experiment was designed, employing a SPECS PHOIBOS 150 electron analyzer with a two-dimensional CCD detector and a reflective photon sieve. This is a new type of diffraction optics for focusing synchrotron radiation with suppressed side lobes and reduced background in comparison to Fresnel zone plates. The optical device was aligned using ten piezodriven actuators to guarantee all necessary degrees of freedom during optics alignment and sample scanning. First measurements were performed with the new experimental station on the misfit crystal $(PbS)_{1.13}TaS_2$ at beamline BW3 at HASYLAB. Since the new setup is designed for ultra–brilliant synchrotron radiation sources, the relatively low brilliance of a conventional synchrotron beamline for such experiments leads to very long data acquisition times. With respect to better statistics and shorter data acquisition times the final setup is planned to be used at high brilliance light sources like the VUV–FEL or PETRA III at HASYLAB.

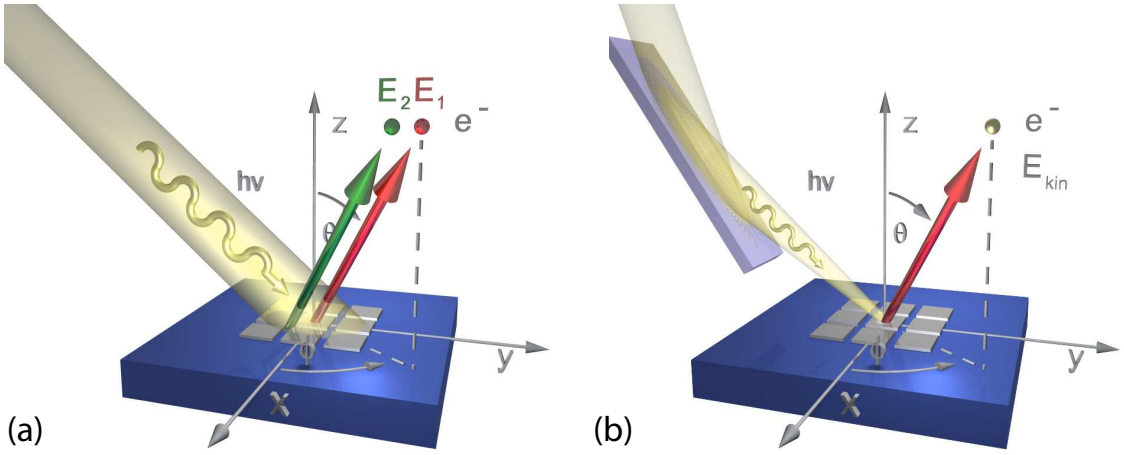

Figure 6.1: (a) On samples with micro– or nano–structured surfaces the incoming photon beam excites photo electrons from different terminated surface regions. Therefore, only a superposed photoelectron signal can be measured. (b) Focusing the photon beam onto single structures, the spatially resolved spectral information can be obtained.

6.1 Normal incidence diffraction optics for focusing synchrotron radiation

In order to focus electromagnetic radiation , different methods are employed. While refractive lenses made out of glass can be used in the visible spectral region, refraction is very low or absent for VUV and X–ray radiation and the light absorption significantly increases in most materials. Therefore, refractive lenses are not efficient for many applications. Only if arranged in linear arrays, refractive lenses can be used again for focusing hard X–rays ($h\nu = 5 - 40$ keV), as applied in Compound Refractive [101] or Multi–Prism [102] lens systems. However, for ARPES experiments VUV and soft X–ray radiation is adequate

(see chapter 2). The commonly used optical devices in this spectral region are on the one hand single or multi layer mirrors, as employed, for example, in Kirkpatrick–Baez mirror optics [103], in Schwarzschild objectives [104, 105] or elliptical mirror systems [14]. On the other hand there are diffraction optics such as Fresnel zone plates [106, 107] and photon sieves [108]. The optical device that is integrated into the new spatially resolving photoemission experiment is a reflective photon sieve. Consisting of thousands of properly placed nano–mirrors it allows the individual shaping of the focal intensity profile and a separation of the different diffraction orders in order to increase the image contrast. The fundamental working principles and properties of reflective photon sieves are similar to that of normal incidence Fresnel zone plates and Photon sieves. Therefore, the characteristic properties of the normal incidence optics will be presented in the next sections before the optics in reflection geometry are discussed.

6.1.1 Fresnel zone plates

The optical device with the highest lateral resolution so far of less than 15 nm [109] is a Fresnel zone plate (FZP). As illustrated in Fig. 6.2, a FZP consists of an alternating cycle of transmissive (white) and opaque (gray) concentric ring shaped apertures, called Fresnel zones (FZ). The transmissive FZs are centered on the radii r_n which are defined by the wave paths $p_n + q_n$. These lead from a point P in the object plane to a point Q in the image plane and only differ by an integer multiple n of the radiation wavelength λ. Taking the higher diffraction orders m into account, a general formula describing constructive interference is:

$$p_n + q_n = p + q + n \cdot m \cdot \lambda \ , \tag{6.1}$$

with the object distance p and the image distance q. As the optical retardation $m \cdot n \cdot \lambda$ of higher order diffraction increases with m (including the virtual diffraction orders at

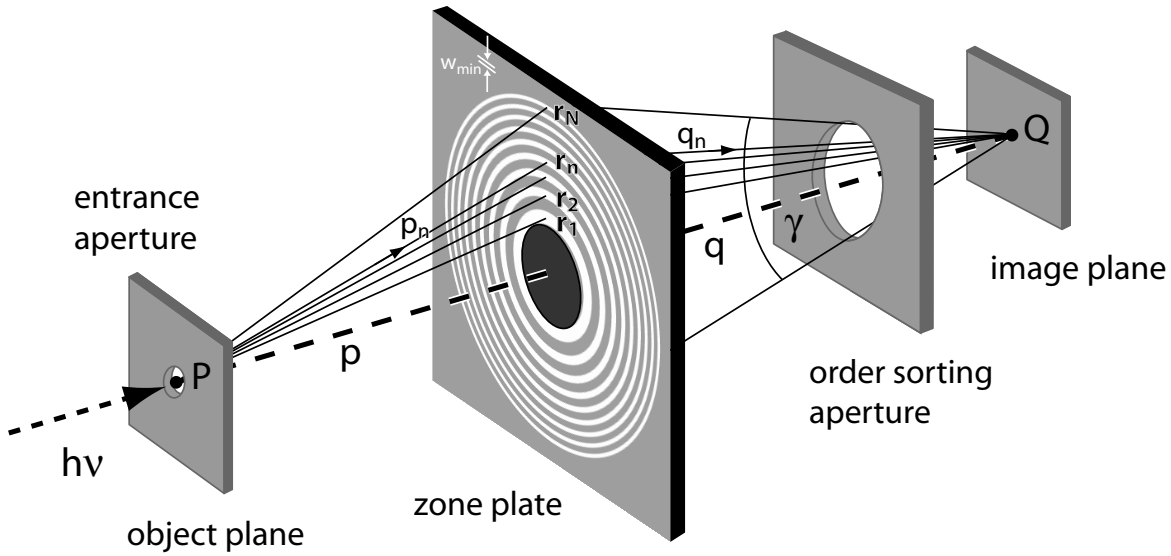

Figure 6.2: Illustration of the point–to–point imaging process with a Fresnel zone plate. The incoming light from P is diffracted at the alternating cycle of transmissive (white) and opaque (gray) Fresnel zones centered on radius r_n. It is then focused onto Q in the image plane with the aperture angle of the lens γ. The undiffracted and the higher order light can be blocked by an order sorting aperture and a central stop (black circular disc).

m = -1, -2, ...), its image distance decreases to q/m. In order to block this parasitic diverging light from blurring the image plane an order sorting aperture (OSA) has to be inserted. Additionally, the undiffracted so called zero order light is blocked by an opaque circular disc (central stop) situated in the center of the FZP (see Fig. 6.2). According to [12, 110, 111], a construction rule of the FZ positions r_n can be calculated using:

$$r_n = \sqrt{2p\ \lambda\ u_r + \lambda^2\ u_r^2} \quad \text{with} \tag{6.2}$$

$$u_r = \frac{1}{2}\ \frac{2qn + \lambda n^2}{p + q + \lambda n}\ . \tag{6.3}$$

As all waves with an optical retardation of $\pm\frac{\lambda}{4}$ – which is equivalent to a phase deviation of $-\pi/2 < \Delta\Phi < +\pi/2$ – interfere constructively in the image plane, the borders of the FZ can be determined to:

$$t_n = r_{n+\frac{1}{4}}\ , \tag{6.4}$$

$$s_n = r_{n-\frac{1}{4}}\ . \tag{6.5}$$

In combination with equation (6.2) it can be shown that the zone width $w_n = t_n - s_n$ decreases towards the FZP border and particularly that the width of the outer zone $w_{min} = t_N - s_N$ decreases with the total number of zones N.

The spatial resolution of a FZP can be determined by analyzing its diffraction pattern [112, 113]. Assuming Fraunhofer approximation and a point light source the wave amplitude in the image plane $\Psi(|\vec{r_Q}|)$ can be calculated by the Fourier transform (FT) of the diffraction optics aperture function $A(|\vec{r}|)$. The aperture function of a FZP describes the light transmission through the optics where $|\vec{r}|$ is the distance from the center of the optics (radial–symmetric geometry). In contrast to an ideal, infinitely expanded FZP ($n \to \infty$, $w_{min} \to 0$) with the concentric–ring–shaped aperture function $A_\infty(|\vec{r}|)$ and a Dirac delta function as FT [see Fig. 6.3(a)], the size of a real FZP is finite due to size limitations in the production process. Its aperture function $A_{ZP}(|\vec{r}|)$ is equal to the product of $A_\infty(|\vec{r}|)$ multiplied with a radial–symmetric Θ–function $A_{rect}(|\vec{r}|)$, also called rectangular window function [see Fig. 6.3(b)]. Its diffraction pattern can be calculated using the convolution theorem:

$$FT(A_{rect}(|\vec{r}|) \cdot A_\infty(|\vec{r}|)) = \frac{1}{\sqrt{2\pi}} FT(A_{rect}(|\vec{r}|)) * FT(A_\infty(|\vec{r}|))\ . \tag{6.6}$$

Therefore, the FT of the product aperture $A_{rect}(|\vec{r}|) \cdot A_\infty(|\vec{r}|)$ can also be calculated by convolving the FTs of each factor. As $FT(A_{rect}(|\vec{r}|))$ is invariant to a convolution with the Dirac delta function, the diffraction pattern of a real FZP can be approximated by the FT of the rectangular window function:

$$\Psi(\vec{r_Q}) \approx \frac{1}{\sqrt{2\pi}} \cdot FT(A_{rect}(|\vec{r}|))\ . \tag{6.7}$$

Its intensity distribution in the image plane, i.e., the squared absolute value of the wave amplitude, can be described by the so called Airy–pattern:

$$I(r_Q) \propto N^2 \left| \frac{2J_1\left(\frac{2\pi r_N}{\lambda q}\ r_Q\right)}{\frac{2\pi r_N}{\lambda q}\ r_Q} \right|^2\ . \tag{6.8}$$

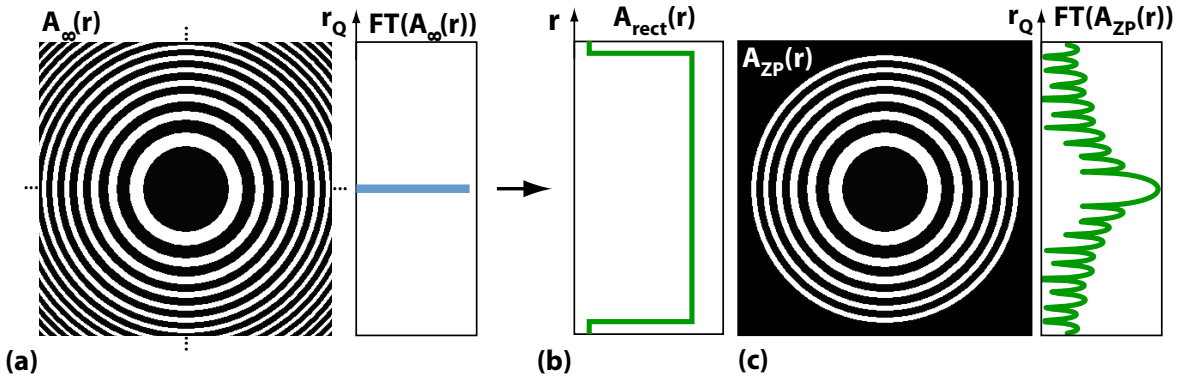

Figure 6.3: Illustration of (a) an ideal, infinitely expanded Fresnel zone plate with the aperture function $A_\infty(r)$. Its diffraction pattern $FT(A_\infty(r))$ in the image plane (r_Q, radial–symmetric geometry) is in logarithmic scale. A multiplication of $A_\infty(r)$ with (b) a circular shaped rectangle aperture function $A_{rect}(r)$ leads to (c) a real, finite FZP $A_{ZP}(r)$. Its diffraction pattern $FT(A_{ZP}(r))$ is also radial–symmetric in the image plane (logarithmic scale).

The intensity in the image plane solely depends on the radiation wavelength λ, the distance to the principal axis r_Q, the total number of FZs N and the ratio of zone plate radius r_N to image distance q. This ratio determines the resolution of an optical system. It is called numerical aperture $NA = n_{refract} \cdot \sin(\frac{\gamma}{2}) \approx \frac{r_N}{q}$, where γ is the aperture angle of the lens and $n_{refract}$ is the refraction index of the lens ($n_{refract} \approx 1$ in the VUV and soft X–ray region). J_1 is the Bessel function of first order and first kind and is responsible for the periodic shape of the diffraction pattern [see Fig. 6.3(c)].

Employing equation (6.8), the lateral resolution $\Delta X'$ of a FZP can be specified by using the Rayleigh criterion. It defines the resolution of an optical device as the smallest resolvable distance $\Delta X'_{rayleigh}$ between the image of two point sources that is reached if the maximum of one intensity profile equals the minimum of the other. In consideration of the minimum positions in the Airy pattern, the Rayleigh resolution of a FZP can be quantified in terms of the numerical aperture and the radiation wavelength, or similarly in terms of the smallest zone width:

$$\Delta X'_{rayleigh} \approx \frac{0.610\ \lambda}{NA} \approx \frac{1.22}{m}\ w_{min}\ . \tag{6.9}$$

A similar resolution criterion that sometimes fits more to the experimental needs is the full width at half maximum (FWHM) of the intensity profile. While a minimum in an intensity profile is often hard to identify due to increased noise at low intensity data points, the peak width $\Delta X'_{FWHM}$ can be determined more precisely:

$$\Delta X'_{FWHM} \approx \frac{0.510\ \lambda}{NA} \approx \frac{1.02}{m}\ w_{min}\ . \tag{6.10}$$

The proportionality of the lateral resolution and the smallest structure size w_{min} illustrate the need for highly accurate fabrication methods in order to achieve a resolution in the nanometer regime. The highest resolution zone plates with zone widths as small as 15 nm are produced using electron beam lithography with electron beam sizes below 10 nm [109], while the FZs have to be positioned within an accuracy of about $1/3 \cdot w_{min}$ [114]. Since

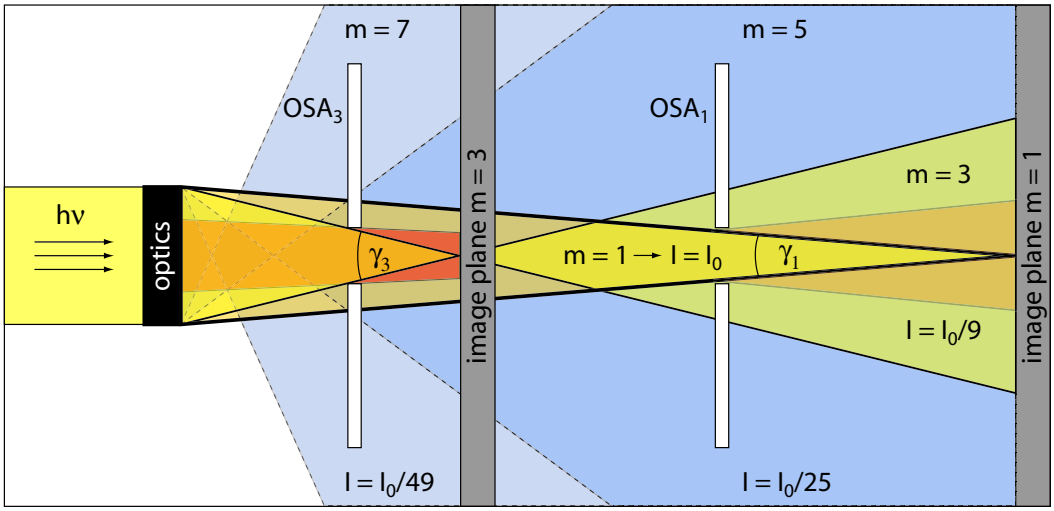

Figure 6.4: The use of higher diffraction orders as shown for third order light ($m = 3$) is directly connected with a reduced focal length, leading to a larger aperture angle $\gamma_3 > \gamma_1$ and an increased numerical aperture. In combination with the reduced focal intensity of the higher order light, increased parasitic intensities especially due to the high intense lower order light (red cone of first order light) reduce the signal–to–background ratio in the focal plane of the third order.

such small structure sizes cannot be produced free–standing, they are etched into thin films (film thickness in the 100 nm regime) on highly light transmissive substrates. Therefore, volume diffraction and refraction in the transmissive parts limit the resolution to about 10 nm, even if smaller structure sizes can be achieved [115, 116] (except for 1:1 imaging or tilted zone geometry [117]).

To realize higher lateral resolution without decreasing the structure size, higher diffraction orders can be employed [see equation (6.10)]. As illustrated in Fig. 6.4 the increase in spatial resolution can be explained by its larger aperture angles γ_m, because the focal length decreases as a function of $1/m$. But even though the resolution increases, the diffraction efficiencies η_m, i.e., the ratio of incident light intensity to the diffracted intensity in a specific diffraction order m, decrease very fast with higher diffraction orders. According to [12] η_m is given by:

$$\eta_m = \begin{cases} 1/4 & \text{m} = 0 \\ 1/(m\pi)^2 & \text{m odd} \\ 0 & \text{m even} \end{cases}, \tag{6.11}$$

so that 25% of the incident light intensity is transmitted undiffractedly into the so called zero order. About 10% is transmitted into the first diffraction order, while half of the incident light intensity is absorbed by the opaque FZs (see Fig. 6.2). Only less than 1% remains for the higher diffraction orders, decreasing in intensity with $1/m^2$. If the aperture function of a FZP can be approximated by using only the odd terms of a Fourier series expansion, there are higher diffraction orders with even index number $m = 2, 4, ...$ [12].

In addition to the low intensity of the higher diffraction orders its image contrast is reduced because of their reduced distance. As, for example, illustrated for the third diffraction order in Fig. 6.4, the relatively low intense third diffraction order is particularly blurred by lower order light ($m < 3$). This high intense light (red cone in Fig. 6.4) is difficult to

block by an OSA due to its convergent character, and reduces the signal–to–background ratio of the relatively low intense higher diffraction order in the image plane.

In addition to the above described amplitude–modulated FZP with totally absorbing and transmissive FZ and a theoretical maximum of diffraction efficiency of $\eta_{max} = 50$ % (conventional design: $\eta_{max} \approx 10$ %), there are also phase–modulated FZPs [118, 119]. In order to increase the diffraction efficiency (conventional design: $\eta_{max} \approx 40$ %), they do not have absorbing but only transmissive zones that change the phase of the passing light by $\Delta\Phi_{abs} = \pi$. In combination with changing the width ratio of adjacent absorbing and transmissive zones and a slanted zone alignment, efficiencies of up to 50% for the higher diffraction orders are theroetically predicted [120]. But even though the diffraction efficiencies are theoretically only limited by absorption in the phase shifting rings, phase–modulated FZPs are less often used than amplitude–modulated FZPs, because the large zone thickness (several micrometers for all materials [121]) is difficult to produce in combination with zone widths in the nanometer regime. A concept that might overcome these restrictions is based on so called Bragg–Fresnel optics [122–125]. It is especially applied for the hard X-ray regime and tries to increase the resolution and the diffraction efficiencies by using reflecting instead of transmissive geometry. A Bragg-Fresnel zone plate consists of a multilayer mirror that bends the radiation in the horizontal direction, while a thin phase shifting film on top is structured like a distorted elliptical Fresnel zone plate and focuses the radiation into the vertical direction [121]. While the reflecting geometry enhances the mirror reflectivity, the optical path length in the diffracting film increases as well. This leads to much smaller ratios between zone heights and zone widths so that smaller zone widths are possible to produce [126].

The longitudinal resolution of a FZP is determined by its depth of focus (DOF). It is defined by the on–axis distance in q direction, where the intensity decreases by 20 % in relation to the highest intensity spot in the image plane at q. It determines the minimum accuracy requirements of an experimental setup in the q–direction and can be calculated by:

$$DOF = \pm\frac{1}{2}\frac{\lambda}{(NA)^2} \approx \pm\frac{2w_{min}^2}{\lambda} \quad . \tag{6.12}$$

Another important experimental parameter is the spectral band width $\Delta\lambda$ of the light source, or in the case of synchrotron radiation of the monochromator. It is defined by the variation in wave length that shifts the focal spot as far as the depth of focus and should not be exceeded to avoid a blurring in the image plane. In order to obtain the expected spatial resolution, a light source that illuminates a FZP with the total number of zones N should satisfy the relation:

$$\frac{\Delta\lambda}{\lambda} \leq \frac{1}{2N} \, , \tag{6.13}$$

provided that the smallest zone width is much smaller than the radius of the optics. This is generally fulfilled for large N.

In order to achieve a small light spot in the image plane that can be used for the illumination of a small homogeneous sample region in a spatially resolving ARPES experiment, a small, uniform object like a pinhole aperture (see Fig. 6.2) can be demagnified by the FZP. In consideration of a modest numerical aperture, the magnification V of the object can be calculated similarly to the magnification in geometrical optics by:

$$V \approx \frac{q}{p} \, . \tag{6.14}$$

The total spot size of the optical system in the image plane that limits the (maximum) spatial resolution is determined by two parts: (i) the resolution of the diffraction optics, i.e., the so called Point Spread Function (PSF) quantified by the Airy pattern for a FZP [see equation (6.8)] and (ii) the demagnified object size, i.e., the image of the objects aperture function (light source). Assuming a small object size in comparison to p, the final two–dimensional spot profile in the image plane can be calculated by convolving the PSF and the demagnified aperture function of the object [127]. In the case of incoherent illumination, waves that are emitted from different locations in the object plane do not interfere constructively or destructively in the image plane. Therefore, the spot profile in the image plane is calculated by a convolution of the absolute values of the PSF – describing the intensity distribution of a point source in the image plane – and the absolute values of the demagnified image of the object aperture (light source). In contrast, in the case of coherent illumination, constructive and destructive interference of all waves has to be taken into account for the spot profile in the image plane. Therefore, the complex PSF which is also called Amplitude Point Spread Function (APSF) – describing the wave amplitude and phase in the image plane – has to be convolved with the demagnified complex aperture function of the object. Using the convolution theorem [see equation (6.6)], the final spot profile can be calculated in an efficient way in order to determine the minimum spot width and therefore the spatial resolution of the optical system.

6.1.2 Photon Sieves

Similar to Fresnel zone plates photon sieves (PS) are diffraction optics that are constructed using equation (6.1). As illustrated in Fig. 6.5 they do not consist of concentric aligned ring apertures (gray rings) but of appropriately distributed pinhole apertures (white circles) centered on the Fresnel zones at r_n [see equation (6.2)]. While the structure of a FZP is

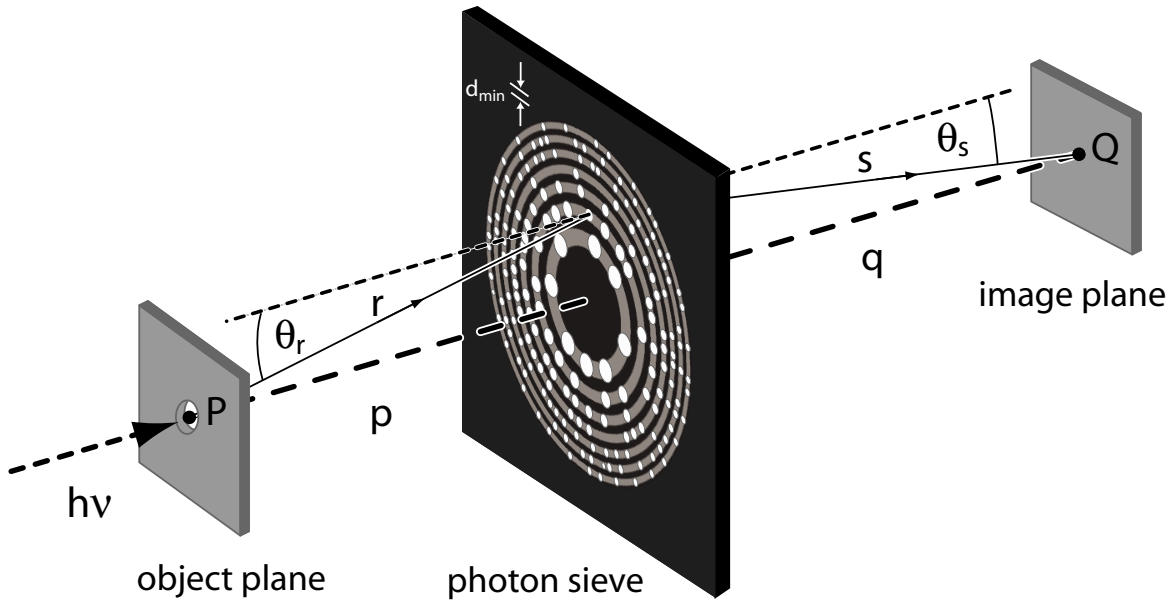

Figure 6.5: Illustration of the point to point imaging process with a photon sieve (white holes). In the figure the minimum pinhole diameter d_{min} is slightly larger than the minimum zone width w_{min} of the underlaying zone plate (gray rings).

totally determined by the object distance p, the image distance q, the radiation wavelength λ and the total number of zones N, a PS additionally allows adjusting the size and the density distribution of the pinholes [108]. Even though the diffraction efficiency of a PS is only about 10% (transmission about $15-20\%$) of a comparable FZP, photon sieves allow to overcome the limitations of zone plates regarding its spatial resolution and contrast.

The spatial resolution of a FZP is determined by the size of the outermost zone diameter w_{min}. Therefore, it is normally limited by the smallest producible structure size, which is about 10 nm at modern electron beam lithographs [109]. This limitation is hardly to overcome with FZPs, since adjacent transmissive and opaque FZs have nearly the same width. Therefore, an increase in the zone width of one kind automatically leads to a decrease in the minimum structure size of the other kind. In contrast, photon sieves consist of loosely distributed pinholes. Their diameter can be increased without decreasing the structure size of adjacent structures, so that the minimum structure size of the total optics equals the minimum pinhole diameter d_{min}. Therefore, larger numerical apertures can be achieved and the resolution of a PS follows the equation:

$$\Delta X'_{FWHM} \approx \frac{0.510\ \lambda}{NA} \approx \frac{1.02}{m}\ w_{min}^{eff} = \frac{1.02}{m}\ d_{min} \cdot \left(\frac{d_{min}}{w_{min}^{eff}}\right)^{-1}, \tag{6.15}$$

with the zone width of an underlaying FZP w_{min}^{eff} which has the same radius as the photon sieve. As illustrated in Fig. 6.6, a ratio of pinhole diameter d to underlaying zone diameter

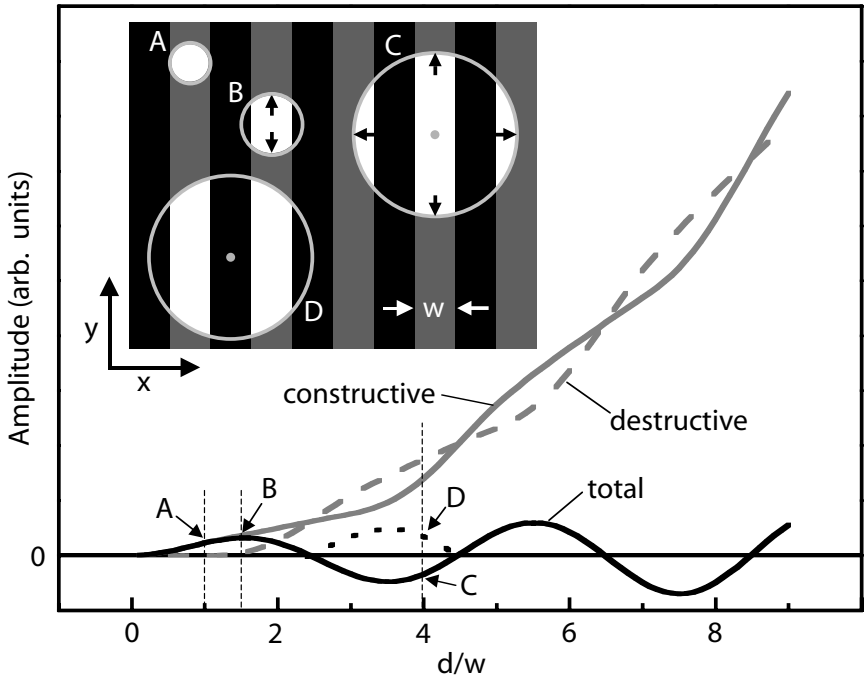

Figure 6.6: Illustration of a photon sieve pinhole with various diameters centered on different zones of an underlaying FZP. The contributions from the different (white and black) wave paths in a pinhole with a phase shift of $\Delta\Phi = \pi$ are plotted as solid gray and dashed gray lines, respectively. The total wave amplitude at the focus is plotted as solid black line if a pinhole is centered on a transmissive (white) FZ, and as dashed black line if it is centered on an opaque (black) FZ (from [108]).

w of $\frac{d}{w} \approx 2.4, 4.4, 6.4, ...$ leads to a minimum in the PS diffraction efficiency. At $\frac{d}{w} \approx 1.5, 5.5, ...$, and $\frac{d}{w} \approx 3.5, 7.5, ...$ the efficiency is maximized, but with a change in the focal wave phase of $\Delta\Phi = \pi$ in the second case [108, 111, 128]. This behavior can be explained by a larger increase of constructive interfering wave paths (gray/transmissive underlying zones) in comparison to the destructive paths (black/opaque underlying zones) if the pinhole diameter is increased from $\frac{d}{w} = 1$ [Fig. 6.6(A)] to $\frac{d}{w} \approx 1.5$ [Fig. 6.6(B)]. A further increase leads to higher destructive contributions and finally to a total annihilation of the focal wave amplitude at $\frac{d}{w} \approx 2.4$. With larger pinhole diameters the absolute value of the amplitude increases again, but with a higher contribution of destructive wave paths so that the sign of the amplitude becomes negative. At $\frac{d}{w} \approx 3.5$ a minimum amplitude is reached. In changing the centers of such holes from transmissive to opaque underlaying Fresnel zones (Figs. 6.6(C) and 6.6(D) with $\frac{d}{w} \approx 4$), the change in phase can be compensated. Therefore, holes of different sizes (e.g., $\frac{d}{w} \approx 1.5$ and $\frac{d}{w} \approx 3.5$) can contribute constructively to the focal wave amplitude. The next point of zero amplitude is at $\frac{d}{w} \approx 4.4$. By increasing the pinhole diameter further, the focal wave amplitude increases again and the pinhole can be considered as belonging to a PS with an image distance three times larger, working in the third diffraction order. However, since the efficiency for higher order diffraction decreases due to a higher proportion of destructive interfering wave paths, a combination of different orders is favorable. The highest focal intensity employing such mixed–order photon sieves can be achieved by minimizing the value of $\frac{d}{w}$ in consideration of the minimum producible structure size, so that in general only the outer parts of the diffraction optics work in higher order diffraction. Using this scheme (which can also be applied for FZPs by combining adjacent FZs [129]) it is possible to create photon sieves with much higher resolution than can be achieved using a FZP with comparable minimum structure size [108, 130].

In order to achieve the design resolution of a FZP, the zones have to be positioned with an accuracy r_{acc} of about one third of the minimum structure size [114]. This relation can also be used to determine the resolution limit of higher order photon sieves:

$$\Delta X'_{FWHM} \approx 3 \cdot r_{acc} \ , \tag{6.16}$$

with $r_{acc} \approx 2$ nm today [131]. Since this limit is smaller than the minimum producible structure size, higher order photon sieves allow to increase the size of a diffraction optics leading to higher diffraction efficiency and increased spatial resolution.

It should be noted that the simple formula regarding the higher order diffraction efficiency of FZPs [see equation (6.11)] is not valid anymore for photon sieves, since their aperture function is more complex. Therefore, in general there are both even and odd higher orders. However, varying the new design parameters pinhole size and distribution it is even possible to diminish them [108, 132].

In order to determine the spatial resolution of an optical device, criteria like the Rayleigh–resolution [see equation (6.9)] or the FWHM–resolution [see equation (6.10)] are sometimes misleading. If, for example, the PSF of the optics is a periodic function with secondary maxima around the main peak, these so called side lobes can reduce the spatial resolution. In the case of a FZP the PSF can be approximated by an Airy pattern [see equation (6.8)] with a relative intensity of the first secondary maximum of about 2% in comparison to the main peak. As the intensity of the higher secondary maxima decreases [see Fig. 6.7(c)], especially the first side lobe diminishes the signal–to–background ratio and blurs the image. If for example a high–contrast object is scanned by the focal spot of a FZP, its weak features cannot be resolved if the main peak of the zone plate focus scans a weak

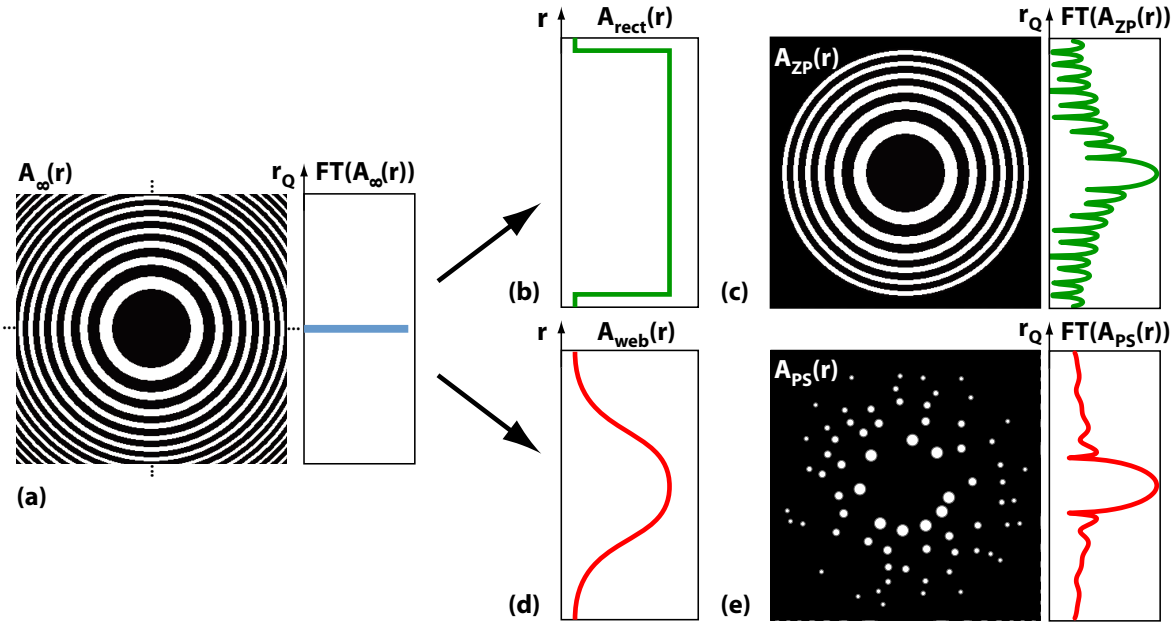

Figure 6.7: Illustration of (a) an ideal, infinitely expanded Fresnel zone plate with the aperture function $A_\infty(r)$ and its diffraction pattern $FT(A_\infty(r))$ in the image plane (r_Q, radial–symmetric geometry). A multiplication of $A_\infty(r)$ with (b) a circular shaped rectangle aperture function $A_{rect}(r)$ or (d) a smooth Weber–type aperture function $A_{web}(r)$ leads to (c) a real, finite FZP $A_{ZP}(r)$ or (e) a photon sieve $A_{PS}(r)$, each plotted with a cross section of the diffraction pattern in logarithmic scale. See also Fig. 6.3.

feature while the side lobes simultaneously scan an adjacent strong feature (for an example see [111]). Since the shape of the focal PSF is determined by the window function $A_{rect}(|\vec{r}|)$ (see section 6.1.1), the side lobes can be suppressed by implementing smoother window functions, which are similarly known for digital filters [133]. A filter function that enables an efficient side lobe suppression of more than three orders of magnitude in comparison to the main peak [108, 111] is the Weber–type transmission window after Cappellini [134]:

$$w_C(\vec{r}) = a\left(\frac{|\vec{r}| - r_{min}}{r_{max} - r_{min}}\right)^3 + b\left(\frac{|\vec{r}| - r_{min}}{r_{max} - r_{min}}\right)^2 + c\left(\frac{|\vec{r}| - r_{min}}{r_{max} - r_{min}}\right) + d\ , \qquad (6.17)$$

with the coefficients a, b, c, d from Tab. 6.1. In contrast to a FZP which is fundamentally connected to the rectangular window, for photon sieves the implementation of various

$\lvert\vec{r}\rvert < r_{min}$	$0 \leq \frac{\lvert\vec{r}\rvert - r_{min}}{r_{max} - r_{min}} < 0.75$	$0.75 \leq \frac{\lvert\vec{r}\rvert - r_{min}}{r_{max} - r_{min}} \leq 1.5$	$\frac{\lvert\vec{r}\rvert - r_{min}}{r_{max} - r_{min}} > 1.5$
a = 0	a = 0.828217	a = 0.065062	a = 0
b = 0	b = -1.637363	b = 0.372793	b = 0
c = 0	c = 0.041186	c = -1.701521	c = 0
d = 1	d = 0.99938	d = 1.496611	d = 0

Table 6.1: Coefficients of the two–dimensional Weber–type transmission window after Cappellini [134] smoothing the edges of a rectangular window between r_{min} and r_{max}.

window functions is possible by just varying the pinhole density following an aperture function $A_{PS}(|\vec{r}|)$. This can totally change the shape of the focal spot profile or compensate experimental parameters such as inhomogeneous illumination. To suppress the side lobes, the pinhole density has to distributed following the two–dimensional Weber–type transmission window $A_{PS}(|\vec{r}|) = w_C(|\vec{r}|)$ as illustrated in Fig. 6.7(d), (e), and experimentally demonstrated by [108, 135, 136]. But since in Weber–type photon sieves the outer parts of the diffraction optics contribute less to the focal intensity than the inner parts, both the diffraction efficiency and the resolution decrease in comparison to a photon sieve with rectangular window.

For example a photon sieve with the parameters $p = 3$ m, $q = 6$ mm, $\lambda = 254$ nm, $N = 192,220044$ pinholes, and rectangular window has a resolution of $\Delta X'_{FWHM} \approx 1.02\ \mu$m and a side lobe intensity of about 2% (equal to a zone plate with the same parameters). In contrast, a similar Weber–type PS has a resolution of $\Delta X'_{FWHM} \approx 1.48\ \mu$m and a seven times lower peak intensity. Using an increased hole–width to zone–width ratio of $\frac{d}{w} = 1.5$ as described above, the original resolution of $\Delta X'_{FWHM} \approx 1.02\ \mu$m can be reachieved without decreasing the minimum structure size of $d_{min} \approx 1\ \mu$m. As a diffraction efficiency of about 70% of the rectangular window PS is reached, the side lobes are strongly suppressed to about 0.03%. This corresponds to a contrast ratio of 3000 : 1 [111].

Therefore, a combination of both mixed–order diffraction and the implementation of window functions allow to overcome the restrictions in spatial resolution and contrast of Fresnel zone plates.

6.2 Fresnel Kirchhoff diffraction formula

In the case of photon sieves the diffraction properties like focal spot width, depth of focus, or side lobe suppression depend on parameters that cannot be considered simply by the general formulas of section 6.1.1. Therefore, a numerical simulation code [137] was used in this thesis that is based on the numerical integration of the Fresnel–Kirchhoff diffraction formula (FKDF):

$$\Psi(Q) = -\frac{i\ A}{2\lambda} \int\int_{aperture} \frac{e^{ik(r+s)}}{r \cdot s} \left(\cos(\theta_r) + \cos(\theta_s)\right) dS\ , \tag{6.18}$$

applying the notation of Fig. 6.5. As described in [110], equation (6.18) allows to calculate the diffraction of a spherical, monochromatic wave $\Psi(Q)$ in a variable point Q that is emitted in P and diffracted by an aperture (in consideration of a small wavelength λ in comparison to the aperture size d and the object– and image–distance p and q). As there are no restrictions regarding the shape of the aperture, the FKDF can be used to calculate the intensity distributions of FZPs (ring apertures), PSs (pinhole apertures), and tilted optics (distorted apertures). Employing Babinet's principle, i.e., the diffraction pattern of an object is the same as the diffraction pattern of the inverted object except a phase shift of $\Delta\Phi = 180°$, the FKDF can also be used to calculate the diffraction pattern formed by the reflected light (negative diffraction orders). This is of special interest in a tilted setup of so called reflective FZP and PS. An analytical approximation, the so called individual (quasi–)far–field model [128, 138], which was invented to calculate the imaging properties of pinhole apertures in transmissive photon sieves, was not used here but agrees with the FKDF calculations results [139]. Even though the calculation times for an analytical model are much shorter than for numerical integrations, in contrast to the analytical model the

FKDF is not restricted to pinhole structures. Therefore, it can also be used to calculate the imaging properties of reflective FZPs and PSs, that can consist of polygons instead of pinholes, built to focus synchrotron radiation as described in the next section.

6.3 Reflective Photon Sieves

A further development of the normal incidence diffraction optics to increase the focal signal–to–background ratio are the reflective Fresnel zone plates (RFZP) and reflective photon sieves (RPS). In a normal incidence setup stray light, originating mainly from the zero and higher diffraction orders, decreases the signal–to–background ratio in the image plane. In order to improve the contrast, a central stop and an OSA are generally used [see Fig. 6.8(a)]. The central stop, however, reduces the diffraction efficiency of the optical device and acts as additional rectangular window. This leads to further increased side lobes of about $10-15\%$ of the main peak intensity (see Fig. 6.9). Therefore, the size of the central stop should be minimized. As a further complication, the OSA has to be positioned very close to the focal plane for a nearly complete blocking of the stray light. If the diffraction at the OSA and the laterally extension of the light source (pinhole aperture) are neglected, the maximum distance between OSA and focal plane d_{max} for nearly complete blocking of the zero order light can be estimated by simple geometrical considerations:

$$d_{max} = \frac{p+q}{1+\frac{p}{q}\cdot\frac{r_N}{r_{CS}}} \approx q\cdot\frac{r_{CS}}{r_N} \quad \text{for} \quad p \gg q \quad , \tag{6.19}$$

where p and q are the object and image distances, r_{CS} is the radius of the central stop, and r_N the radius of the FZP or PS. Using $NA \approx r_N/q$, equation (6.19) can be written as $d_{max} \approx r_{CS}/NA$. Therefore, especially for high numerical aperture FZPs with large diffraction efficiencies (small r_{CS}) the OSA has to be positioned very close to the focal plane. For example a FZP with the lateral resolution of $\Delta X' \approx 300$ nm and a side lobe intensity of about 2% ($\lambda = 12.398$ nm, $p = 1$ m, $q = 20$ mm, $r_{CS} \approx 29.23$ μm, $r_N \approx 422.01$ μm) has a maximum OSA distance of $d_{max} \approx 1.41$ mm. This distance can be increased, e.g., to

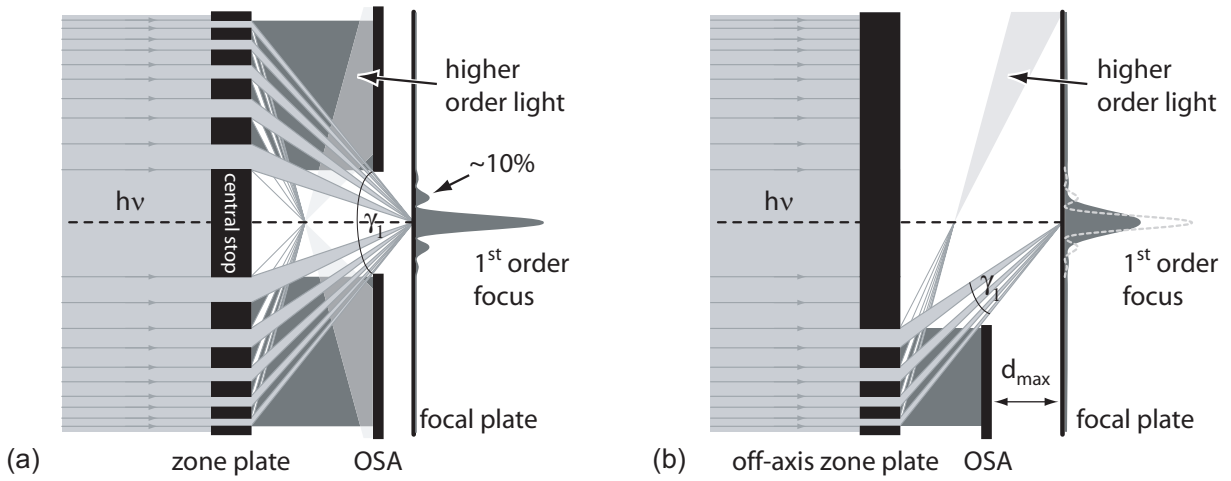

Figure 6.8: (a) On–axis illumination of a FZP with central stop and OSA, and (b) off–axis illumination with OSA only at one side in the maximum possible distance to the image plane d_{max} which is needed to block all zero order light.

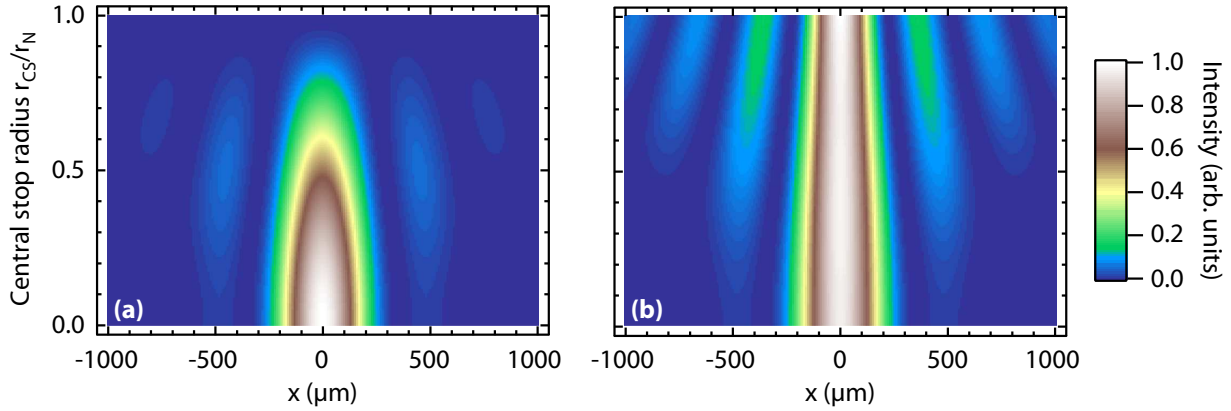

Figure 6.9: Calculated focal spot profile in the image plane (point–to–point imaging) of an on–axis FZP ($p = 1$ m, $q = 20$ mm, $\lambda = 12.398$ nm, $N = 267$, $r_N \approx 422.01$ μm) in dependence of the relative central stop radius r_{CS}/r_N. The intensity is normalized (a) with respect to the curve without central stop at $r_{CS}/r_N \approx 0.07$ (central ring opaque), and (b) for each curve to its maximum value.

6 mm with a central stop size of $r_{CS} \approx 127$ μm, leading to a side lobe intensity of nearly 5% and a reduced diffraction efficiency to about 83% (the focal spot size is slightly reduced to $\Delta X' \approx 290$ nm). A comparable PS with implemented Weber–type transmission window and the same lateral resolution ($\Delta X' \approx 300$ nm) needs an outer radius of $r_N \approx 611.83$ μm so that the OSA distance even decreases to $d_{max} \approx 0.97$ mm. Therefore, transmissive FZPs and PSs are particularly suited experiments in which there is no need to access the half space between OSA and focal plane. This is the case in X–ray microscopy experiments since a sample is inserted into the focal plane and only the transmitted radiation through the sample is observed (see e.g. [140]). However, in photoemission experiments the photoelectrons are emitted in the direction of the incoming light. Therefore, the small distances between OSA and sample (focal plane) make the detection of undisturbed electrons nearly impossible.

Fig. 6.8(b) shows that the off–axis illumination of a FZP [141,142] leads to a separation of the zero order light and the various diffraction orders, similar to a focusing grating. However, since the aperture angle γ_1 is significantly decreased, the numerical aperture is reduced in this setup. Using such an off–axis FZPs, a one sided OSA (knife edge) can be applied for blocking the zero order light. Therefore, the half space above the sample can partly be accessed, e.g., for reflection measurements or photoelectron detection. But depending on the parameters of the optics and the experimental geometry it might also be necessary to block the higher order light (diffraction angle β_m), although it is less intense and in general farther apart from the focal spot than the zero order light [Fig. 6.8(b)]. This can be done using a slit aperture, positioned farther away from the image plane than in an on–axis setup.

Applying off–axis illumination with a slanted diffraction geometry in which the optical device is tilted with respect to the angle of light incidence $\alpha_0 < 90°$, similar to the positive diffraction orders ($m > 0$) also the negative ones ($m < 0$) get farther separated from the incoming light. Therefore, it is possible to use the focal spots of the back diffracted light [143–145] as illustrated in Fig. 6.10(a). Additionally to a separation of the various diffraction orders also the above mentioned volume diffraction and the non–uniform phase shifting of the diffracted waves that pass the substrate under various angles of incidence –

each with different path lengths in the substrate – can be avoided in this reflective geometry.

Using the RFZP called "zp_3000" which was designed for visible light ($\lambda = 632.8$ nm, $\Delta X' \approx 3$ μm, $p = 4$ m, $q_1 = 40$ mm, $\alpha_0 = 34.4°$, $\beta_1 = 45°$, and $d_{min} = 1.5$ μm) and characterized in more detail in [135, 136, 139] the separation of the higher diffraction orders could clearly be observed experimentally. A two–dimensional numerical FKDF–simulation [see equation (6.18)] for the intensity distribution in the x–y–optics–plane which only uses the diffraction structures of "zp_3000" at $y = 0$ shows the higher diffraction orders clearly separated at $\beta_1 = 45°, q_1 = 40$ mm, $\beta_2 \approx 53.5°, q_2 \approx 25.8$ mm, and $\beta_3 \approx 61.6°, q_3 \approx 20.2$ mm. As illustrated in Fig. 6.11 the results – which were confirmed by 3D ray–tracing [136] and analytical calculations [139] – illustrate the increased image contrast in a wide area around the focal spot, even if no central stop or OSA are used.

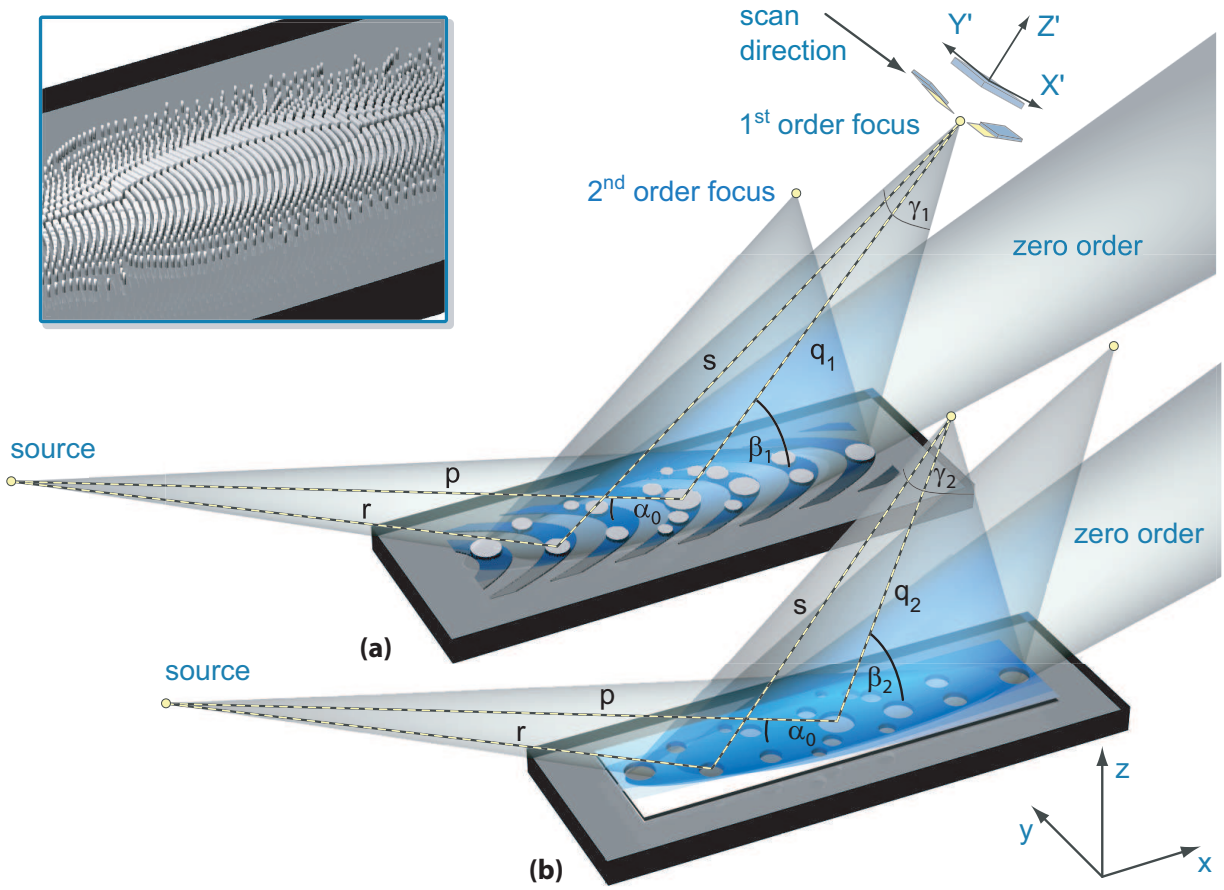

Figure 6.10: Schematic of the focusing process of a reflective diffraction optics. The incoming light (from source) is reflected into the zero diffraction order under the angle of incidence α_0 and focused into the different diffraction orders ($m = 1, 2, ...$) which are separated by different angles of diffraction β_m. (a) The dark, ring shaped structure illustrates the diffraction areas of a RFZP, whereas the circular structures centered on the rings are the diffraction structures (nano–mirrors) of the corresponding RPS with Weber–type transmission window. (b) The inverted RPS shows the same diffraction properties achieved by nano–absorbers instead of nano–mirrors. The central part of a hybrid RPS (inset) consists of ringlike zones in the center and fewer diffraction structures towards the border (Weber–type transmission window).

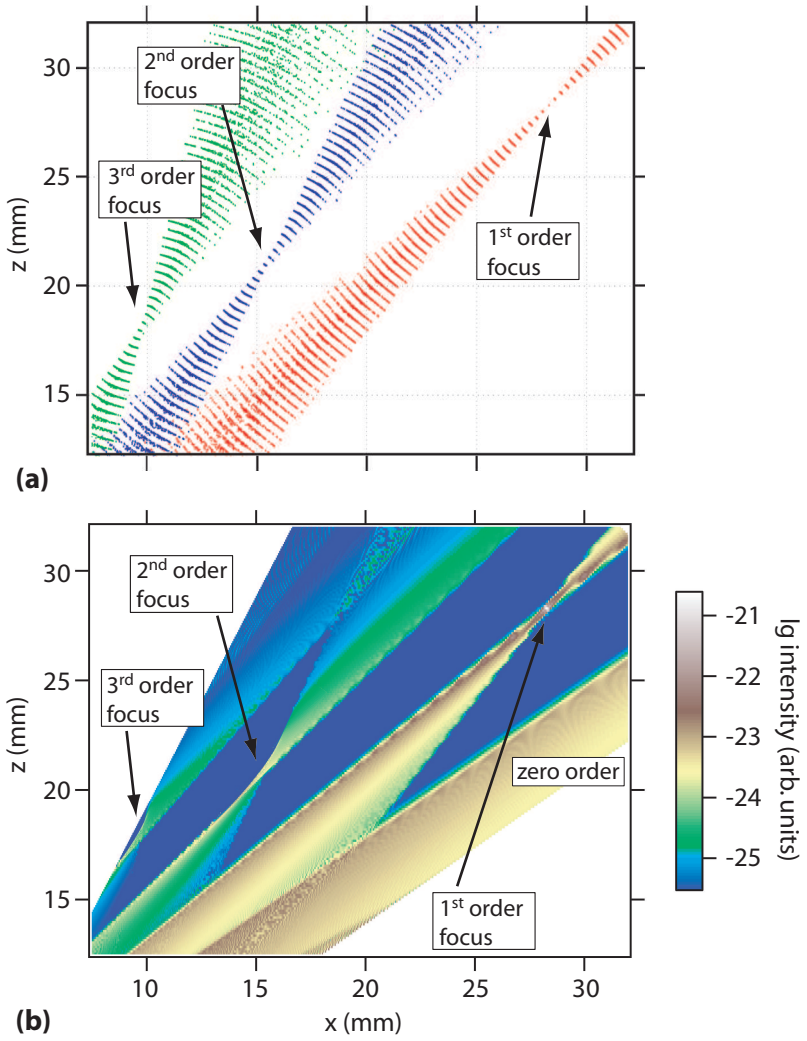

Figure 6.11: Simulated intensity distribution of the higher diffraction orders of a RPS ($\lambda = 632.8$ nm, $p = 4$ m, $q_1 = 40$ mm, $\alpha_0 = 34.4°$, $\beta_1 = 45°$, and $\Delta X' \approx 3$ μm with $d_{min} = 1.5\mu$m) using (a) a ray–tracing algorithm (from [136]) and (b) the Fresnel–Kirchhoff diffraction formula.

A direct comparison between the transmissive and reflective diffraction optics is illustrated in Fig. 6.12. The intensity profiles are calculated in the X'–direction towards the zero order (see Fig. 6.10), employing the FKDF for different soft X–ray optics with a resolution of $\Delta X'_{FWHM} \approx 302$ nm and the parameters $p = 1$ m, $q = 20$ mm, and $\lambda = 12.398$ nm. For the reflective optics $\alpha_0 = 21°$ and $\beta_1 = 24°$ are used. As all optical devices have the same focal width, the intensity profiles are very similar near the focal maximum in region (a). In the transition region (b) both the normal incidence as well as the reflective FZP show nearly the same intensity characteristics with strong side lobes, similar to the diffraction intensity of an Airy pattern [see yellow, dashed–dotted line and equation (6.8)]. Due to the implemented Weber–type transmission window, the side lobe intensity of the photon sieves is strongly suppressed. However, at a distance of some micrometer, the parasitic intensities of the normal incidence PS – originating from the zero and higher orders that point into the same direction as the first order focus – limit the signal–to–background ratio to about 10^4, while the intensity of the RPS decreases further. In region (c) at a distance of

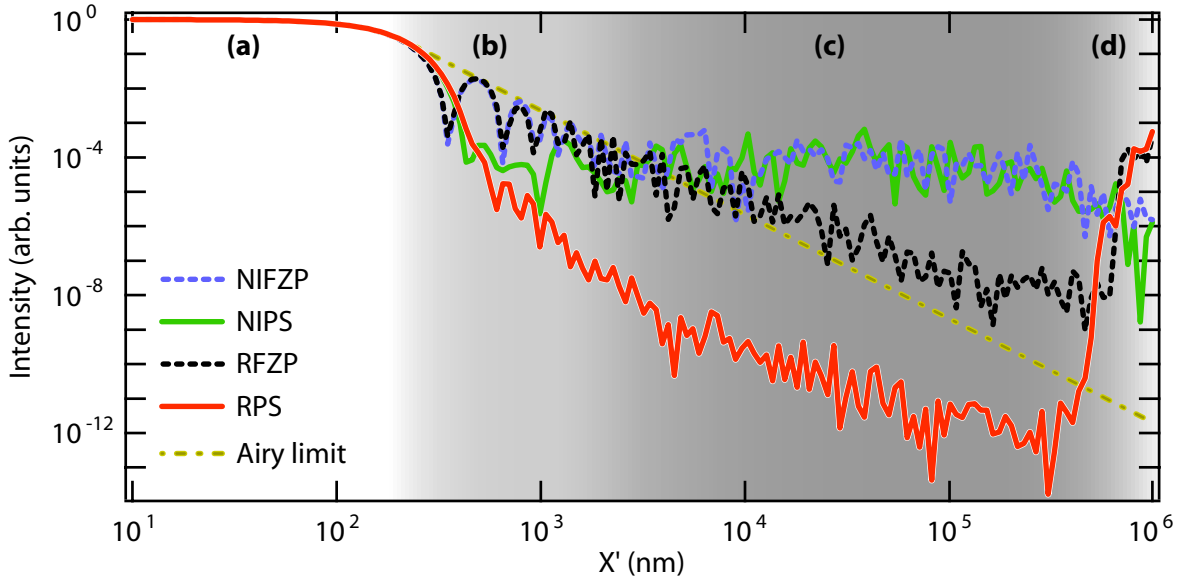

Figure 6.12: Calculated focal plane intensities of a normal incidence FZP (blue, continuous line: NIFZP), a normal incidence PS (green, dashed line: NIPS), a RFZP (gray, continuous line), and a RPS (red, dashed line), each with a focal width of $\Delta X'_{FWHM} \approx 302$ nm and the parameters $p = 1$ m, $q = 20$ mm, and $\lambda = 12.398$ nm. For description of the different regions (a)–(d) which are symbolized by different shades of gray see text.

some micrometers – in which the central stop does not block the zero order light anymore ($r_{CS} \approx 29.23$ μm) – the intensity profile of the normal incidence FZP is also dominated by the parasitic intensities, so that both normal incidence optics show approximately the same intensity values. Only in region (d) at X' values which are larger than the optics radius r_N ($r_N(FZP) \approx 422$ μm, $r_N(PS) \approx 612$ μm) the background intensity of the normal incidence optics decreases slightly. In contrast, the intensity profiles of the reflective optics have a strongly reduced background in region (c), since only the divergent order $m = 1$ points into the same direction as the first order light $m = -1$. While the RFZP nearly follows the theoretical intensity distribution of an Airy pattern in which parasitic intensities are neglected (yellow, dashed–dotted line), the RPS shows an about 10^4 times reduced background. Only at a distance of $X' \approx 500$ μm [region (d)] the directly reflected light blurs the intensity profile of the reflective optics. In comparison to an OSA with a diameter of less than 60 μm for a transmissive optics in a distance of about 1 μm in front of the image plane, at the reflective optics an OSA with a diameter of about 500 μm can be used. This allows a distance to the image plane of nearly $d_{max} \approx 6$ mm. Therefore, employing reflective diffraction optics a significantly increased signal–to–background ratio can be achieved, in particular if using reflective photon sieves.

Even though it is theoretically possible to use any angle of light incidence α_0 and various diffraction angles β_1, using small values of α_0 can be beneficial in order to separate the first order focus from the undiffracted zero order light. As illustrated in Fig. 6.13, for a RZP with $p = 1$ m, $q = 20$ mm, $h\nu = 100$ eV, and a constant final resolution of $\Delta X' = 200$ nm, at high values of α_0 the minimum structure size decreases very fast if a large separation of first– and zero–order is aimed for. But while for example a separation of $\beta_1 - \alpha_0 = 3°$

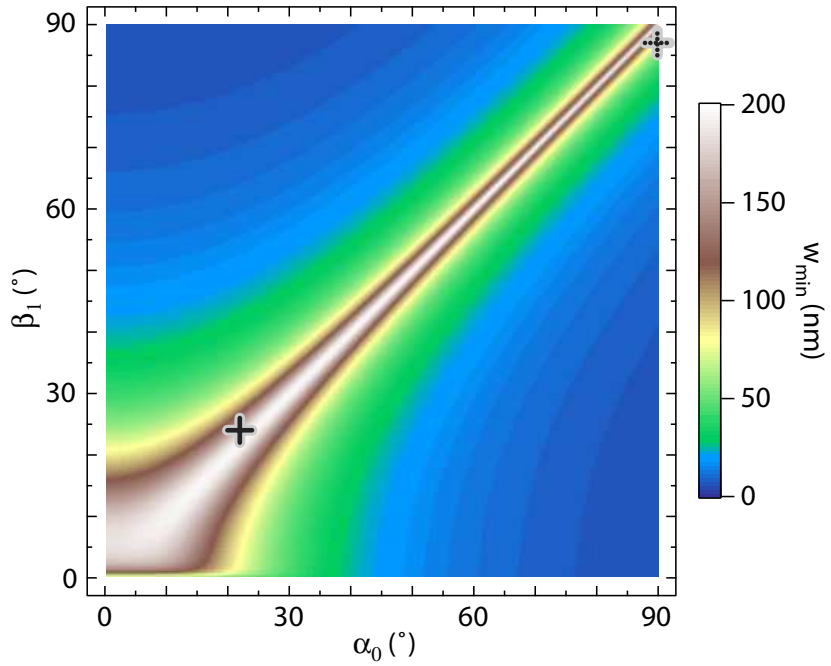

Figure 6.13: Smallest structure size w_{min} of a diffraction pattern with a focal resolution of $\Delta X' = 200\ nm$ in dependence of the angle of light incidence α_0 and the angle of the first diffraction order β_1 ($p = 1$ m, $q = 20$ mm, and $h\nu = 100$ eV). The markers indicate two positions with an angle separation of $|\beta_1 - \alpha_0| = 3°$. The solid cross marks the position $\alpha_0 = 21°$, $\beta_1 = 24°$ with a smallest structure size of $w_{min} \approx 158$ nm, while the dotted cross marks the position $\alpha_0 = 90°$, $\beta_1 = 87°$ of a normal incidence diffraction optics with a smallest structure size of $w_{min} \approx 74$ nm.

at $\alpha_0 = 90°$ (normal incidence diffraction optics) requires a minimum structure size of $w_{min} \approx 74$ nm, the same separation can be achieved at $\alpha_0 = 21°$ with a more than two times larger minimum structure size of $w_{min} \approx 158$ nm.

Constructed by using equation (6.1) the diffraction structures in this slanted setup are no more concentric rings, but show a distorted ring shape with decreasing structure sizes towards lower angles of incidence α (higher x–values). This is illustrated in Fig. 6.14 for a RFZP with the parameters $p = 1$ m, $q_1 = 20$ mm, $\alpha_0 = 21°$, $\beta_1 = 24°$, $\lambda = 12.398$ nm. Since the interdependency between the spatial resolution and the minimum structure size in this tilted geometry is more complicated than in the normal incidence setup, only the use of the more general physical value NA instead of the minimum structure size in equation (6.9), (6.10), and (6.15) is still valid. In order to achieve a symmetric focal spot profile in the lateral X'–Y'–direction, the boundary of the diffraction optics has an elliptical shape [see Fig. 6.14(a)] in which $NA = NA_x = NA_y$ determines the diameter of the optics in x– and y–direction. Therefore, by calculating the aperture angle $\gamma \approx 3.551°$ and the corresponding numerical aperture $NA \approx 0.03098$ for the optics of Fig. 6.14(a), the lateral spatial resolution and the depth of focus can be determined. The calculated values are $\Delta X' \approx 204$ nm and DOF $\approx \pm 6.5\mu$m, which is in accordance with numerical calculations using the Fresnel Kirchhoff diffraction formula.

A RFZP that was built for focusing synchrotron radiation is called "*zp_200*". It is characterized by the above described parameters but with $d/w = 3$, in order to increase the minimum structure size. The third order optics was constructed by combining three

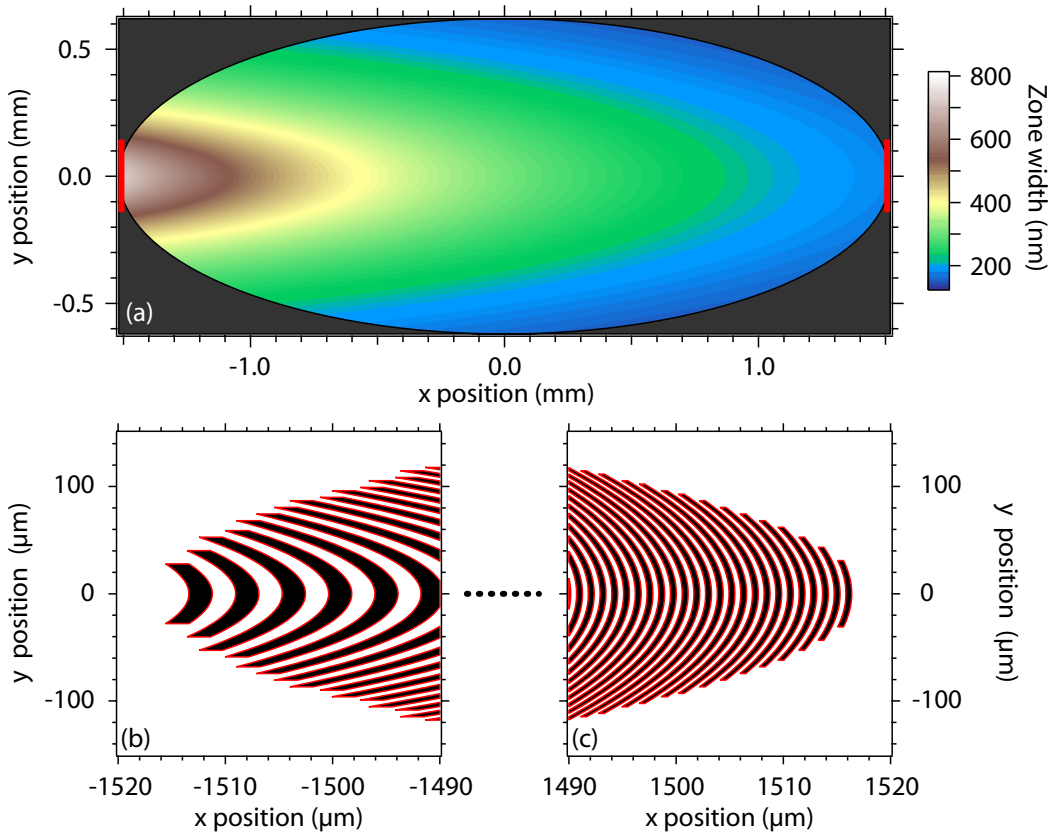

Figure 6.14: (a) Schematic of the zone width of a RFZP with the parameters p = 1 m, $q_1 = 20$ mm, $\alpha_0 = 21°$, $\beta_1 = 24°$, $\lambda = 12.398$ nm and a smallest zone width of 158 nm.The theoretical focal spot diameter is $\Delta x \approx 205$ nm. In the case of the the third order zone plate "*zp*_200" three adjacent zones are combined as illustrated for (b) the left and (c) the right border [regions of red lines in (a)] with a smallest zone width of $d_{min} \approx 474$ nm. Cr structures are illustrated in black while the SiO_2 substrate is white.

adjacent ring structures in which only one contributes to the focal intensity while the diffracted radiation from the remaining two rings interferes destructively. The optical device is designed with a theoretical resolution of $\Delta X' \approx 204$ nm and a minimum structure size of $d_{min} \approx 3 \cdot 158$ nm $= 474$ nm. It was produced by a commercial lithographic mask manufacturer (PHOTRONICS, Dresden) with a production limit of at least 400 nm for the structure sizes and a positioning accuracy of about $r_{acc} \approx 10$ nm. The distorted ring–shaped diffraction structures of "*zp*_200" [see Fig. 6.14(b), (c)] were manufactured by electron beam lithography and etched into an 80 nm thick, high reflecting chromium layer, situated on a quartz glass substrate which absorbs the incoming radiation.

The reflectivities of the diffraction structures ρ_{Cr} and the substrate ρ_{SiO_2} are important parameters which have to be taken into account during the design of reflective diffraction optics, since they strongly influence the diffraction efficiency. As calculated by the Fresnel–Kirchhoff diffraction formula for a 1^{st} and a 3^{rd} order RFZP with the parameters of "zp_200" (see Fig. 6.15), the diffraction efficiency η decreases if the diffraction contrast, i.e., the reflectivity ratio of both materials ρ_{Cr}/ρ_{SiO_2}, is reduced. Therefore, the diffraction contrast should be maximized in order to increase η, even though the focal spot shape is not affected.

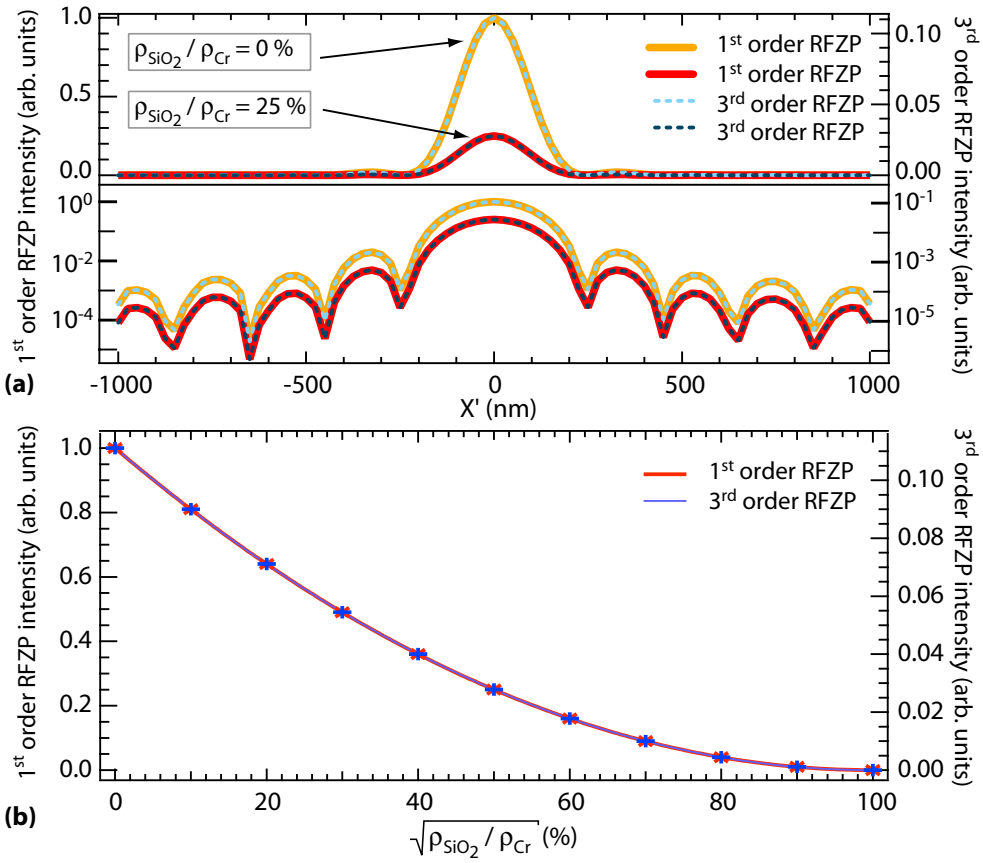

Figure 6.15: (a) Focal intensity profile (numerical FKDF simulation) of a reflective 1^{st} and 3^{rd} order zone plate with the same diameters (p = 1 m, q = 20 mm, $\alpha_0 = 21°$, $\beta_1 = 24°$, $\lambda = 12.398$ nm) and different values of SiO_2 reflectivity. All intensity profiles are calculated along the X' direction (see Fig. 6.11) and do not show any differences except for a constant intensity factor. (b) The simulated focal peak intensity in dependence of the inverse diffraction contrast ρ_{SiO_2}/ρ_{Cr} (markers) confirms equation (6.20)(continuous line).

The diffraction efficiency [see Fig. 6.15(b)] can be described by:

$$\eta \approx \epsilon \cdot \rho_{Cr} \left(\frac{1 - \sqrt{\rho_{SiO_2}/\rho_{Cr}}}{\pi \cdot (d/w)} \right)^2 , \tag{6.20}$$

noting that the order of the optical device d/w has to be an odd number and the factor of π is chosen similar to equation (6.11). The factor ϵ takes into account the lower diffraction efficiency of an optical device with window function in comparison to a zone plate (rectangular window function). In the case of a Weber–type transmission window the transmission is reduced to about $15 - 20\%$ leading to $\epsilon \approx 0.10$.

The diffraction contrast for p–polarized light was calculated for different angles of incidence and photon energies [146]. Therefore, a root mean square (RMS) roughness of $\sigma_{SiO_2} \approx 0.3$ nm and $\sigma_{Cr} \approx 3.4$ nm was assumed as measured during this thesis (for 80 nm high reflecting Cr on a SiO_2 substrate the values are not known by the mask producer). Fig. 6.16 shows the result of this calculations. A high diffraction contrast in consideration of small angles of incidence can be found at $\alpha_0 = 21°$ and $\lambda = 12.398$ nm. The reason for this relatively high value of $\rho_{Cr}/\rho_{SiO_2} \approx 11.6$ is the reduced reflectivity of the SiO_2

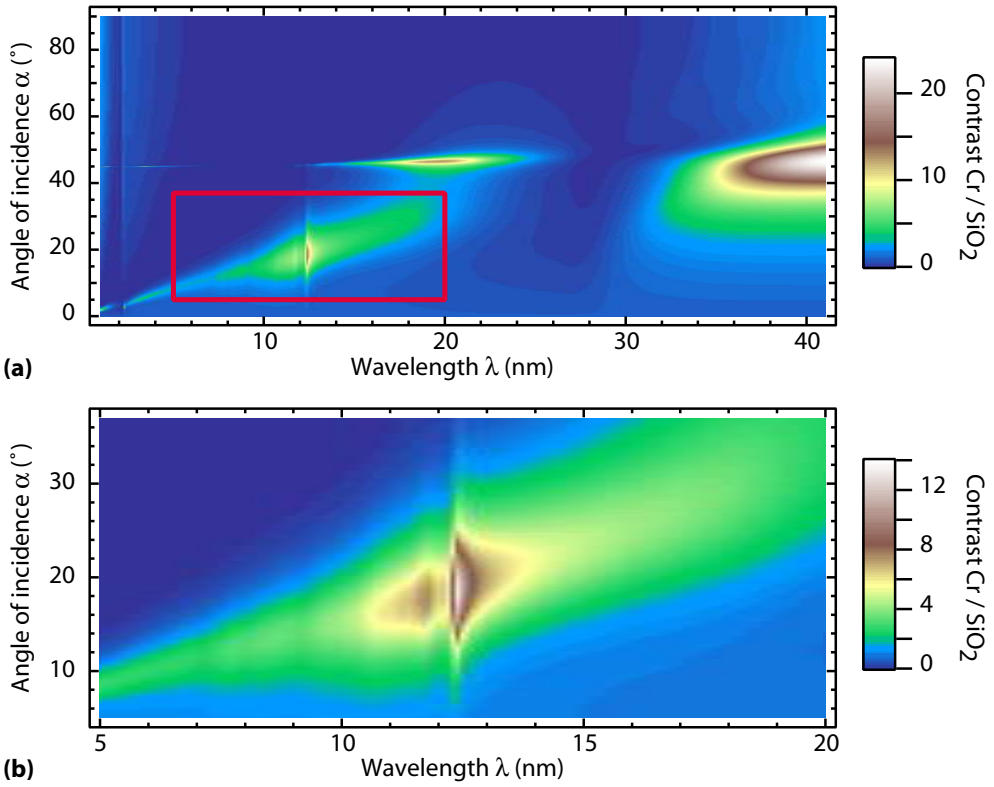

Figure 6.16: (a) Diffraction contrast of a 80 nm thick Cr film with surface root mean square (RMS) roughness of $\sigma_{Cr} = 3.4$ nm on a SiO_2 substrate with $\sigma_{SiO_2} = 0.3$ nm in dependence of the light wavelength λ and the angle of incidence α. (b) Magnification of the region with maximum diffraction contrast at small angle of incidence ($\alpha < 40°$) with ($\rho_{Cr}/\rho_{SiO_2} \approx 11.6$) at $\alpha = 21°$ and $\lambda \approx 12.398$ nm.

substrate due to the Si 2*p* absorption edge at a photon energy of about 100 eV. It should be mentioned that a higher diffraction contrast with up to $\rho_{Cr}/\rho_{SiO_2} \approx 25$ could be achieved if the Cr–roughness would be below $\sigma_{Cr} \approx 1$ nm.

Using the optics parameters that are already known from the RFZP "zp_200", an additional third order focusing device called "psi_w_200" was built (see Tab. 6.2). It is equipped with a Weber–type transmission window that leads to a suppression of side lobes in the focal diffraction pattern. The implementation of the window function does not differ from the normal incidence case, except for elliptical instead of circular symmetry of the window function due to the slanted geometry. In addition, polygons instead of circles were used as diffraction structures (nano mirrors/absorbers) such as illustrated in the inset of Fig. 6.10 for a so called hybrid photon sieve which is a combination of a RFZP in the inner parts (up to r_{min} of equation (6.17)) and a photon sieve in the outer parts (from r_{min} to the border at r_{max}). Since the use of this kind of optics at a high brilliance light source is planned for future applications, electrically and thermally connected diffraction structures are advantageous in order to dissipate the heat load and to avoid a charging of the optical device. In accordance with Babinet's principle the inversion of a diffraction optics does not change the focal spot pattern except for a phase shift of $\Phi = 180°$. Therefore, the original diffraction structure, consisting of separated nano–mirrors, can be swapped by interchanging Cr and SiO_2 regions. In this inverted structure nano–absorbers instead of

Parameter	zp_200	psi_w_200
λ	12.398 nm	12.398 nm
p	1 m	1 nm
q	20 mm	20 mm
Magnification V	1/50	1/50
α	21°	21°
β	24°	24°
d/w	3	3
Number of underlaying FZs	5009	5009
Number of diffraction zones	1669	1669
Optics semi–major axis: a_x	1.516773 mm	1.516773 mm
Optics semi–minor axis: b_y	0.619900 mm	0.619900 mm
w_{min}	474 nm	474 nm
Aperture angle γ	3.551°	3.551°
numerical aperture NA	0.03098	0.03098
Window type	rectangle	Weber–type
Theoretical PSF width	205 nm	302 nm
Inverted	no	yes

Table 6.2: Parameters of the reflective FZP "zp_200" and the reflective PS "psi_w_200" that were characterized at beamline BW3.

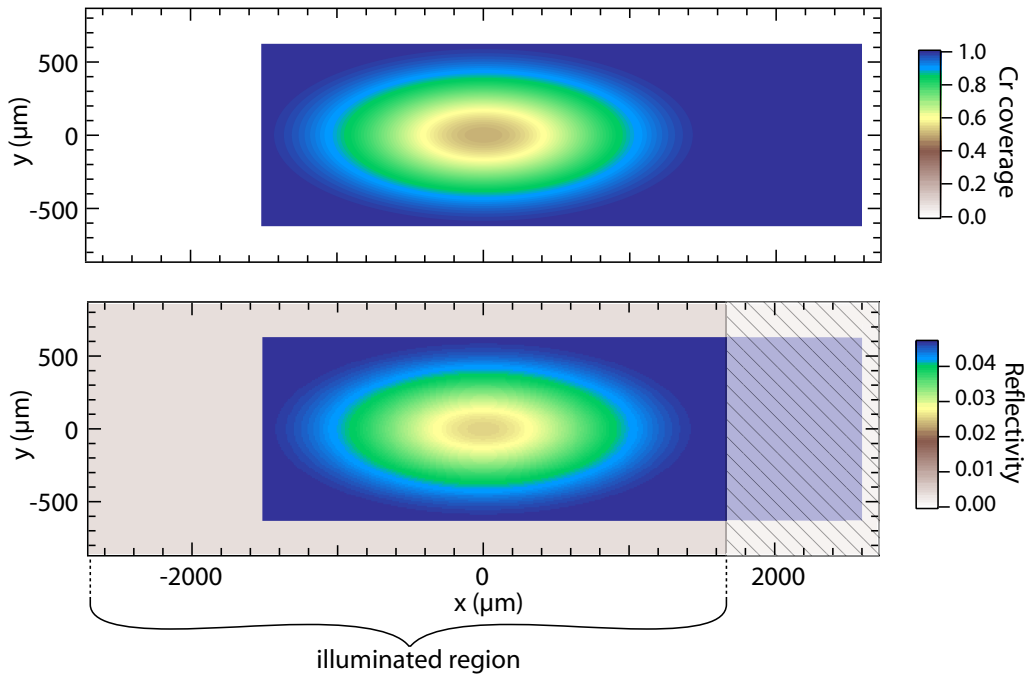

Figure 6.17: Cr coverage (top) and total reflectivity (bottom) of the inverted reflective photon sieve with Weber–type transmission window "psi_w_200" at hν = 100 eV and α_0 = 21°. The illuminated region of the photon sieve that is needed to get the best accordance with the measured reflected intensity (see Fig. 6.29) is marked.

nano–mirrors are responsible for the diffraction process [see Fig. 6.10(b)]. In Fig. 6.17 the Cr coverage and reflectivity of the inverted RPS with Weber–type transmission window "psi_w_200" is shown. Its absorber–density decreases from the center of the optics to the borders, leading to a decreased diffraction efficiency [see Fig. 6.17(bottom)] in the outer regions and a suppression of side lobes in the diffraction pattern, as already known from the normal incidence PSs. In order to ground the optics electrically and to connect it with a cooling device for the dissipation of possible heat load during the illumination, there is an additional Cr border around the RPS structure (see Fig. 6.17).

The optical device "psi_w_200" is mainly analyzed in the following, since it combines the above described advantages, i.e., the separation of the different diffraction orders, leading to higher image contrast and the possibility to use higher order optics with a decoupling of theoretical resolution and structure size, and the implementation of a Weber–type transmission window in order to suppress side lobes. Therefore, it was also used in the new spatially resolving photoemission setup which will be described in the next section.

6.4 Experimental setup

In order to apply combined angle and spatially resolved photoelectron spectroscopy using reflective photon sieves, a compact scanning system was developed and integrated into the ARPES setup of the Kiel group. The scanning system uses ten UHV–compatible piezo electric drives that allow the alignment of the optics as well as scanning a sample in the image plane of the demagnified synchrotron spot.

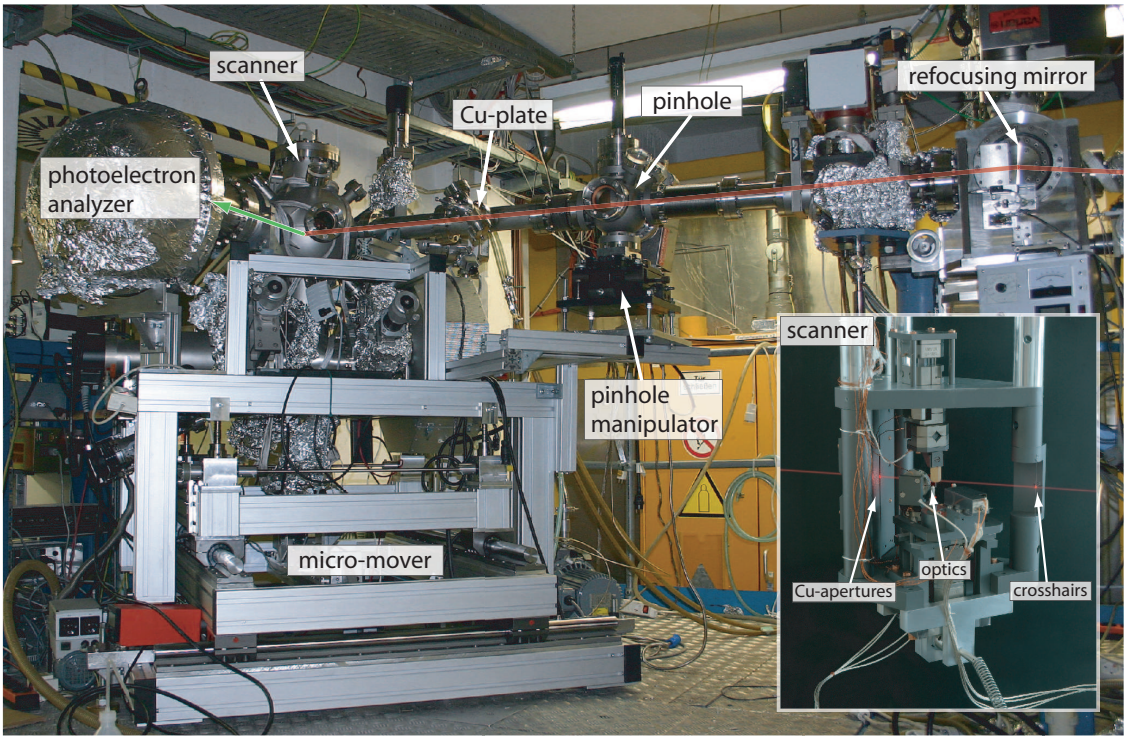

Figure 6.18: Setup of the spatially resolving photoemission experiment with scanner and SPECS Phoibos 150 photoelectron analyzer built up at the synchrotron beamline BW3 (HASYLAB). The red line illustrates the light path from the refocusing beamline mirror to the scanner while the green arrow represents the path of the emitted photoelectrons.

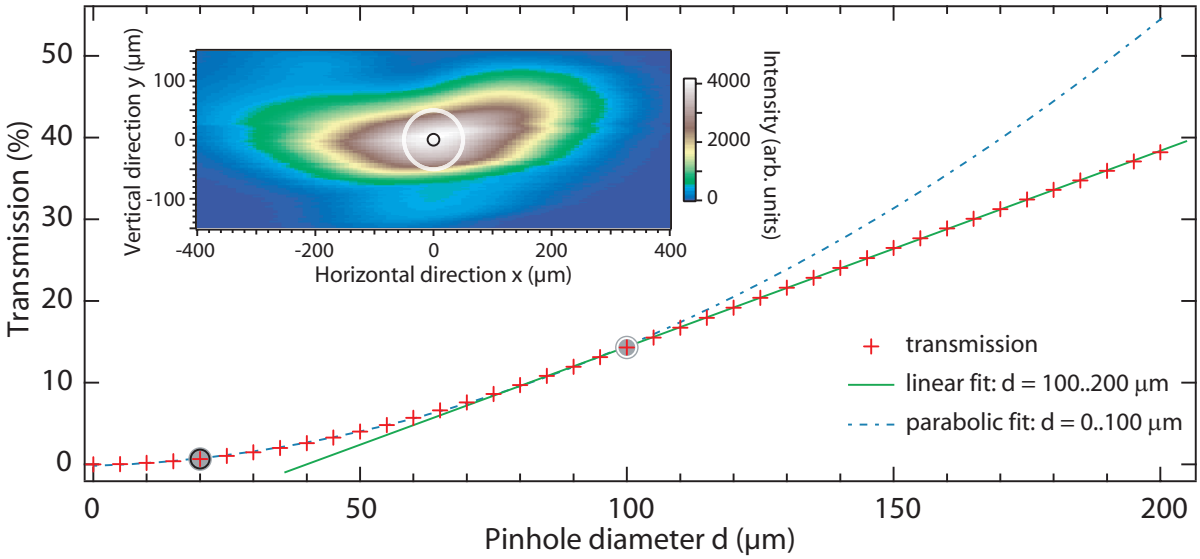

Figure 6.19: Measured refocused synchrotron spot profile (inset) at beamline BW3 ($h\nu = 100$ eV, spot size $hor._{FWHM} \times vert._{FWHM} \approx 318 \times 95$ μm^2) with sketched pinholes of 100 μm (white circle) and 20 μm (black circle) in diameter. (Main graph) Light transmission in dependence of pinhole diameter d with parabolic fit $y = -0.175 + 0.0211d + 0.00126d^2$ for $d = 0...100$ μm and linear fit $y = -9.58 + 0.240d$ for $d = 100..200$ μm.

In Fig. 6.18 the new experimental setup is shown, built up at the undulator beamline BW3 at HASYLAB (Hamburg). It uses the monochromatized synchrotron beam ($h\nu = 100$ eV) which is focused by the refocusing beamline mirror to one of four switchable pinholes with a diameter of 100 μm, 50 μm, 20 μm, and 10 μm. The pinholes act as light source and are demagnified by the RPS "psi_w_200" onto the sample plane that is tilted by an angle of 45°.

The pinhole position can be optimized by moving the pinhole chamber with an x–y–z–translational manipulator and by rotating it around its vertical axis, while the transmitted photon flux is measured with a copper plate. As illustrated in Fig. 6.19, the maximum light transmission in dependence of the pinhole diameter can be calculated out of the refocused synchrotron beam profile of BW3. It was scanned in the focal plane with a 20 μm pinhole aperture while measuring the transmitted light intensity on the copper plate. For small pinhole diameters $d \approx 0..100$ μm the transmission is nearly proportional to the pinhole area (quadratic dependence) with about 14.31% for the 100 μm pinhole, 4.02% for the 50 μm pinhole, 0.66% for the 20 μm pinhole, and 0.17% for the 10 μm pinhole (see Fig. 6.19). For larger diameters the transmission shows a more linear dependence due to the almost elliptical spot shape.

The transmitted light passes the entrance aperture of the scan system (see Fig. 6.18(inset) and Figs. 6.20 and 6.21). It consists of two perpendicular arranged Cu slit–apertures. The optical device (if tilted parallel to the beam: $\alpha_0 = 0°$), and crosshairs form a line that can be used to align the scanner orientation with respect to the synchrotron beam [see Fig. 6.18(inset)]. Afterwards, the Cu apertures with a slit size of $hor. \times vert. \approx 1.55 \times 1.70$ mm^2 allow an independent photocurrent measurement in all four space directions (up, down, left right) in order to optimize the scanner position by translating the full experimental setup with the micro–mover (see Fig. 6.18). In consideration

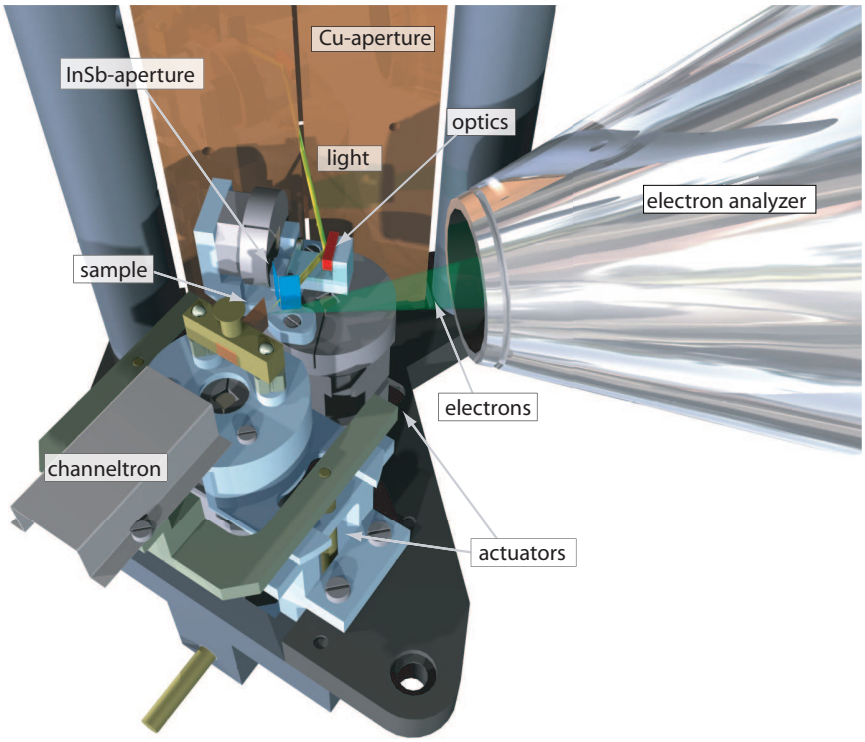

Figure 6.20: Render image of the photon sieve ARPES scan system with Cu–aperture, focusing device (reflective photon sieve), zero and higher order sorting aperture, sample, and channeltron. The light path (yellow line) as well as the path of the emitted photoelectrons towards the photoelectron analyzer are illustrated (from [83]).

of the beam divergence at BW3 ($\delta_{hor.} \approx 4$ mrad, $\delta_{vert.} \approx 0.64$ mrad, taken from [147, 148]), the transmission through these apertures can be calculated to be about 72%.

As illustrated in Figs. 6.20 and 6.21 the RPS images the light source (pinhole aperture) into the sample plane, while stray light can be blocked using a slit aperture. The alignment of the optical device is done by measuring the focal spot width while varying the alignment parameters. These parameters are the angles of light incidence and optics height which can be adjusted by applying two rotary and one translational (height) piezo electric drives.

Since the direct two–dimensional detection of the focal spot profile with a two–dimensional detector like a CCD camera is hardly applicable in the sub micrometer regime, the characterization is done by applying the knife edge scan method. According to Fig. 6.22(top), in this method the focal spot profile is successively shadowed by a crystalline sharp knife edge while the transmitted light is measured in dependence of the knife edge position (bottom: dotted, red line). As this intensity profile represents the integrated original spot profile, its differentiation leads to the one–dimensionally projected spot profile. It allows to reconstruct the spot width $\Delta X'_{FWHM}$, if the two–dimensional spot shape is known (see section 6.5). In the final scanner setup a slit aperture with a slit width of approximately 260 μm is used (see Fig. 6.10). It consists of two 125μm thick InSb wavers (n–doped with about 10^{15} Te atoms per cm^3, (100) oriented) which are covered with a thin gold film in order to avoid charging. These wavers have crystalline sharp cleaved edges, each tilted to the beam by 50° in order to avoid scattering at the side–faces (see Figs. 6.20 and 6.21). They absorb the synchrotron radiation very well with a transmission of less than 10^{-17} per micrometer at $h\nu = 100$ eV. The slit aperture can be transferred

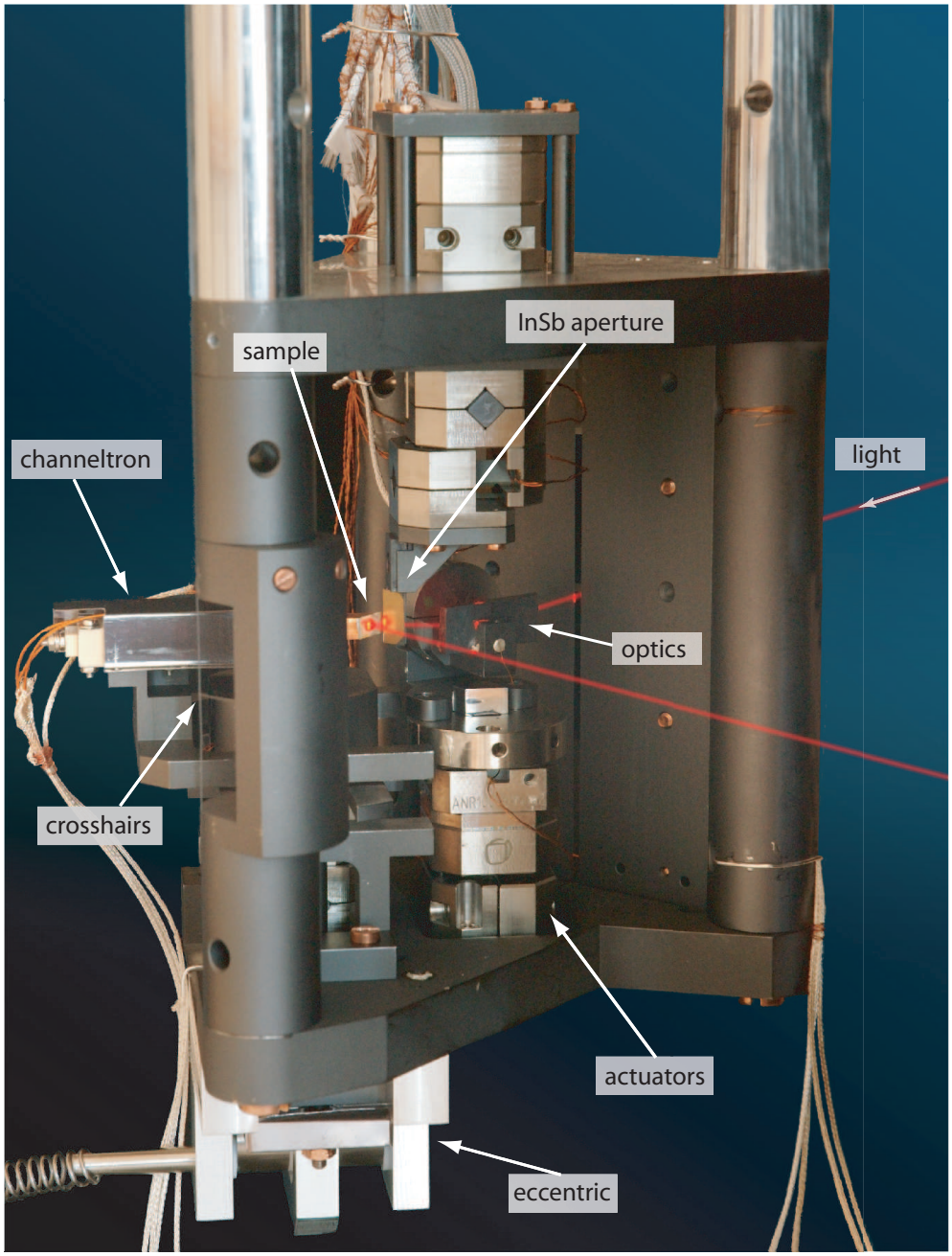

Figure 6.21: Photograph of the photon sieve ARPES scan system with Cu–aperture, focusing device (reflective photon sieve), zero and higher order sorting aperture, sample, and channeltron. The light and electron path is illustrated by a red laser beam.

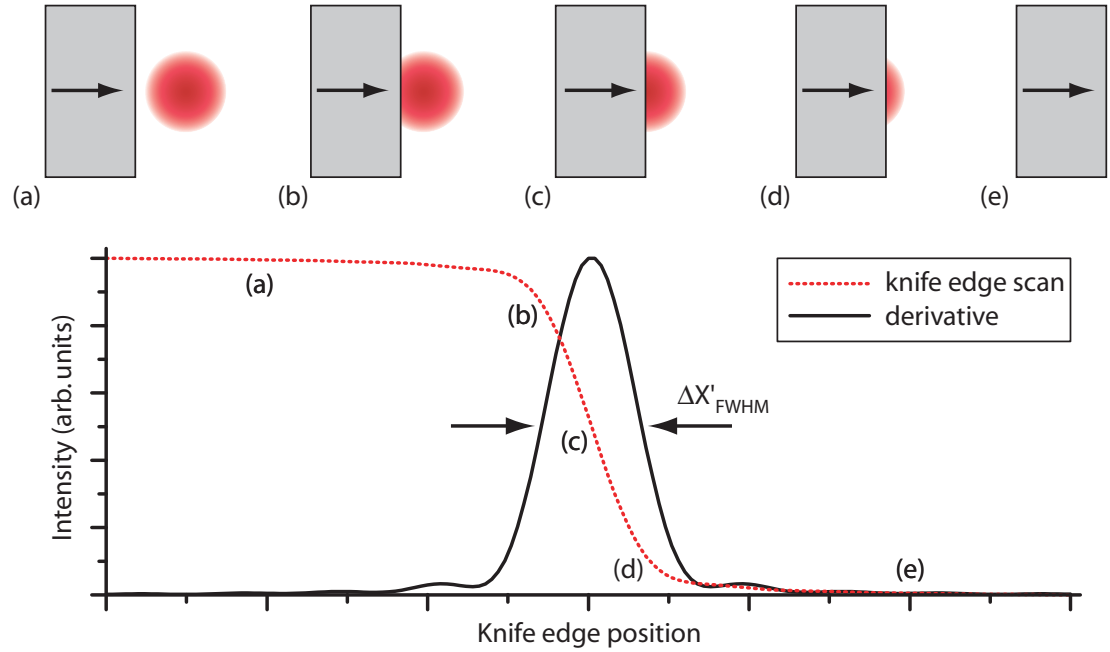

Figure 6.22: Illustration of the knife edge scan method: If a light spot is successively shadowed by a knife edge [top (a) to (e)] and the transmitted light intensity is measured in dependence of the knife edge position (bottom: dotted, red line), the differentiated signal allows the reconstruction of the spot profile width $\Delta X'_{FWHM}$.

into the sample position (image plane) by three translational piezo drives and shadows the beam while the transmitted intensity can be measured with a channeltron. The aligned optical device has a symmetric spot profile so that the spot width in the knife edge scan direction $\Delta X'$ should be identical with its perpendicular direction $\Delta Y'$. However, since in the current setup with tilted wavers no additional knife edge can be mounted in a maximum distance of $\pm DOF$ for a simultaneous scanning of the Y'–direction, a different spot width in the Y'–direction cannot totally be excluded (see [136]). A pinhole (at best with rectangular shape) instead of a slit aperture could avoid this uncertainty. But as the edges of a pinhole cannot be aligned tilted to the beam and the etched or laser printed side–faces are rougher than the sharp cleaved edges of crystalline wavers, the knife edge scan resolution would decrease. An alternative way to determine the two–dimensional focal spot profile would be using two perpendicular aligned wires for the knife edge scan. In addition, the direct scanning of a test pattern while measuring the photoelectron current with the ARPES analyzer also allows to determine the focal resolution if a clearly structured sample is used.

In the final photoemission process the slit aperture is drawn back and acts as order sorting aperture while the sample is transferred into the focal plane in front of the channeltron (see Figs. 6.20 and 6.21). There the sample surface can be scanned under the optimized focal spot profile via three linear piezo electric drives. The photoelectron spectrometer PHOIBOS 150 is able to detect photoelectrons in parallel with an detection angle of about $\pm 13°$ in the vertical direction. In addition, a rotary piezo electric drive was installed which allows to rotate the sample by $\pm 12°$ around the vertical axis, so that a full Brillouin zone at a photon energy of $h\nu = 100$ eV can be measured.

As mentioned above, the slit aperture as well as the optics and the sample are moved by piezo electric drives (manufactured by Attocube Systems). In order to allow a movement

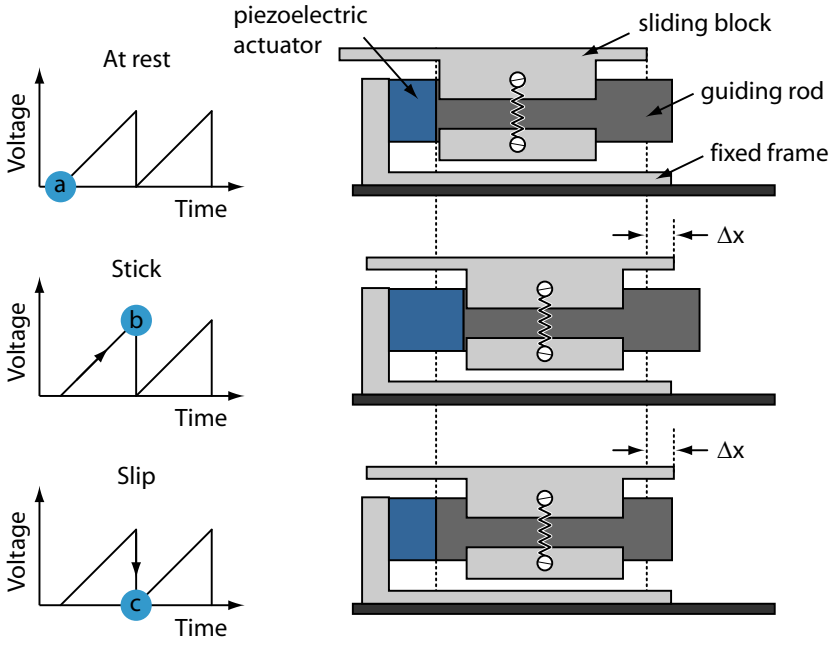

Figure 6.23: Illustration of slip–stick motion of the piezo electric drives that are used in the spatially resolving photoemission experiment (image after [149]).

over long distances (mm region) they utilize slip–stick motion. Therefore, according to Fig. 6.23, a sliding block with the ability to mount any construction up to a weight of 100 g is clamped to a guiding rod which is attached to a piezoelectric actuator. If the actuator is driven by a voltage of $U = 0...70$ V, it extends itself into one direction by several micrometers with a tuning accuracy of some nanometers. While at slow movements the sliding block sticks to the guiding rod and follows all movements of the piezo electric actuator [see Fig. 6.23(a)→(b)], at abrupt movements, the guiding rod moves to the new position, but the sliding block detaches its connection (slips) and stays at its position [see Fig. 6.23(b)→(c)]. Using a periodic voltage with sequential low and steep slope like a saw tooth voltage, the sliding block can be moved over long distances with high accuracy and a clearly defined step width which primary depends on the amplitude of the voltage and the mounted weight. However, since (unexpected by the manufacturer) the friction of the slip–stick motion in the UHV–classified piezo drives decreases strongly with the ambient pressure, crosstalking (especially the rotary piezo drive of the optics), the need of high piezo voltages and large step widths result. Therefore, after long term UHV studies in Kiel and at the HASYLAB, a redesign of guiding rod and coating material by the manufacturer was necessary to allow the reliable use of the piezo drives for further experiments. The main characterization of the new experiment and especially of the photon sieve shown in the next sections had to be done with the old piezo electric actuators. Therefore, the focal spot width optimization results are not as good as the best results of our prototype experiment which only allowed the optics alignment, but no photoemission experiments. However, the ability to do photoemission with the new setup could be demonstrated in a first experiment by investigating the misfit crystal $(PbS)_{1.13}TaS_2$ at beamline BW3.

6.5 Characterization of the VUV reflective photon sieve

The optical device which was integrated into the spatially resolving photoemission experiment is the inverted reflective photon sieve with Weber–type transmission window "psi_w_200" (parameters see Tab. 6.2). Applying the FKDF [see equation (6.18)], the optical properties like focal spot shape or depth of focus were numerically calculated for the RPS as well as for the RFZP "zp_200" in order to compare the different optical devices.

6.5.1 Aspects on the degree of coherence

The degree of coherence of the light source plays an important role for the focal spot characteristics and strongly influences the spot shape. In order to calculate the focal spot profile, it has to be taken into account that the symmetry axis in the reflecting geometry is not identical with the q–axis that points from the center of the optics to the center of the focal spot under the angle of diffraction of $\beta = 24°$ (see Fig. 6.10). If the intensity distribution in an image plane perpendicular to $\beta = 24°$ is calculated, it is slightly distorted with a spot width $\Delta X'_{FWHM} \neq \Delta Y'_{FWHM}$ [see Fig. 6.24(a),(b)]. If in contrast the image plane is aligned perpendicularly to the symmetry axis of the diffraction cone (aperture angle $\gamma/2$) with $\beta \approx 24.123°$, the intensity profile shows a symmetric shape with $\Delta X'_{FWHM} = \Delta Y'_{FWHM}$ [see Fig. 6.24(c), (d)]. Therefore, the further calculations were performed in this direction.

As shown in Fig. 6.24(c), (d), the width of the PSF derived by numerical simulations for the RFZP "zp_200" equals the simple calculation using equation (6.15) with $\Delta X'_{FWHM} \approx 204$ nm. Similar to the case of normal incidence zone plates, strong side lobes of about 2% of the main peak intensity are visible. If the zone plate images a pinhole, the PSF has to be convolved with the demagnified aperture function as described in section 6.1.1. For coherent illumination and a 20 μm pinhole the focal spot size increases slightly to about $\Delta X'_{FWHM} \approx 240$ nm, while the side lobe intensity decreases by nearly one order of magnitude to less than 0.3% [see Fig. 6.24(e), (f)]. Using incoherent illumination instead (for simulation details see section 6.1.1), the focal spot size increases much stronger to about $\Delta X'_{FWHM} \approx 374$ nm while the side lobes are smeared out to a wide halo with slowly decreasing intensity of, e.g., 1% in a distance of 500 nm and 0.1% in a distance of 1000 nm to the main peak [see Fig. 6.24(g), (h)].

The same behavior can be observed for the RPS "psi_w_200". However, since the side lobes have very low intensity due to the implementation of a Weber–type transmission window, a much lower noise level around the main peak is observed. As shown in Fig. 6.25(a)–(d), the PSF of the RPS shows a side lobe suppression of about two orders of magnitude (absolute value: $3{\cdot}10^{-5}$) in comparison to the RFZP. Using coherent illumination with a pinhole of 20 μm in diameter, the focal width increases from $\Delta X'_{FWHM} \approx 304$ nm (PSF) to about $\Delta X'_{FWHM} \approx 340$ nm with a side lobe intensity of about $1 \cdot 10^{-6}$ [see Fig. 6.25(e), (f)]. Assuming incoherent illumination instead, the peak width increases further to about $\Delta X'_{FWHM} \approx 402$ nm. While similar to the reflective FZP a halo with slowly decreasing intensity surrounds the main peak, the halo intensity of 0.4% at the distance of 500 nm is weaker and decreases much faster to about $4 \cdot 10^{-6}$ in a distance of 1000 nm to the main peak [see Fig. 6.25(g), (h)].

The calculations show that the use of filter functions such as the Weber–type transmission window increases the signal–to–background ratio for the reflective diffraction devices similar to the normal incidence case. Furthermore, if a pinhole acts as light source, the final spot profile depends on the degree of radiation coherence. Using totally coherent illumina-

tion, much smaller spot sizes and an additionally increased signal–to–background ratio can be achieved, even for the RFZP.

In contrast to highly coherent light sources like lasers, at synchrotron beamlines the provided radiation is in general only partially coherent. As our first diffraction and photoemission experiments were done at the undulator beamline BW3, its degree of coherence in view of both, the diffraction process at the optical device (leading to the PSF) and the image forming process in the case of an extended light source (pinhole aperture) had to be estimated. The diffraction process is mainly determined by the so called temporal (or longitudinal) coherence. It can be quantified by the coherence length l_{coh}, defined by the distance after that two waves, emitted from the same point source, but with a wavelength difference of $\Delta\lambda$, have a phase shift of $\Delta\Phi = 180°$ [12]. This leads to:

$$l_{coh} = \frac{\lambda^2}{2\Delta\lambda} \ , \tag{6.21}$$

where λ is the radiation wave length and $\Delta\lambda$ its spectral bandwidth. The maximum wave path difference of the reflective FZP and PS is proportional to the total number of underlaying Fresnel zones N. Therefore, longitudinal coherence can be achieved if $l_{coh} = N \cdot \lambda$, leading to:

$$\frac{\Delta\lambda}{\lambda} \leq \frac{1}{2N} \ , \tag{6.22}$$

which is equal to equation (6.13). For the experiments at beamline BW3 with $\lambda = 12.398$ nm the 5009 underlaying Fresnel zones of "psi_w_200" (see Tab. 6.2) require a coherence length of approximately 62.1 μm and a spectral bandwidth of $\Delta\lambda \approx 1.24$ pm. The corresponding energy resolution of $\Delta E \approx 6.3$ meV at $h\nu = 100$ eV can only be achieved if the monochromator exit slit at BW3 is nearly closed to $\mathrm{d}_{mono} \approx 30$ μm. This leads to an intensity loss of nearly two orders of magnitude in comparison to the largest monochromator exit slit width of $\mathrm{d}_{mono} = 500$ μm ($\Delta\lambda \approx 13.4$ pm, coherence length $l_{coh} \approx 5.7$ μm). Since the intensity of beamline BW3 is relatively low for this kind of experiments, a large monochromator exit slit width had to be used. Therefore, the contrast of the focal spot profile at BW3 is expected to be much lower than calculated above. The image forming process is mainly determined by the so called spacial (or transverse) coherence. Derived by the Heisenberg's uncertainty principle [12], the following equation desribes totally transverse coherence:

$$2\pi \cdot d \cdot \delta = \lambda \ , \tag{6.23}$$

where d is the diameter of the extended object acting as light source (pinhole aperture), and δ is the beam divergence, both in Gaussian root–mean–square quantities. If equation (6.23) is fulfilled, full spacial coherence is achieved. If this is the case, the wave phase in each point transverse to the propagation direction is totally correlated and interference in the image plane of waves that are emitted from different pinhole locations has to be taken into account. At beamline BW3 ($\delta_{hor.} \approx 4$ mrad, $\delta_{vert.} \approx 0.64$ mrad) equation (6.23) is not fulfilled for a pinhole diameter of 20 μm, neither for the horizontal direction (250 nm $\gg$ 12.398 nm) nor for the vertical direction (40 nm $>$ 12.398 nm). Therefore, no spacial coherence can be assumed. At the VUV–FEL the situation is totally different since its brilliance, i.e., the number of photons per time (s), divergence (mrad^2), spotsize (mm^2) and spectral bandwidth (0.01%), is about 10^6 to 10^7 times higher than at BW3. This allows higher energy resolution (smaller monochromator slits) and much smaller pinhole sizes so that both, full longitudinal and vertical coherence can be achieved.

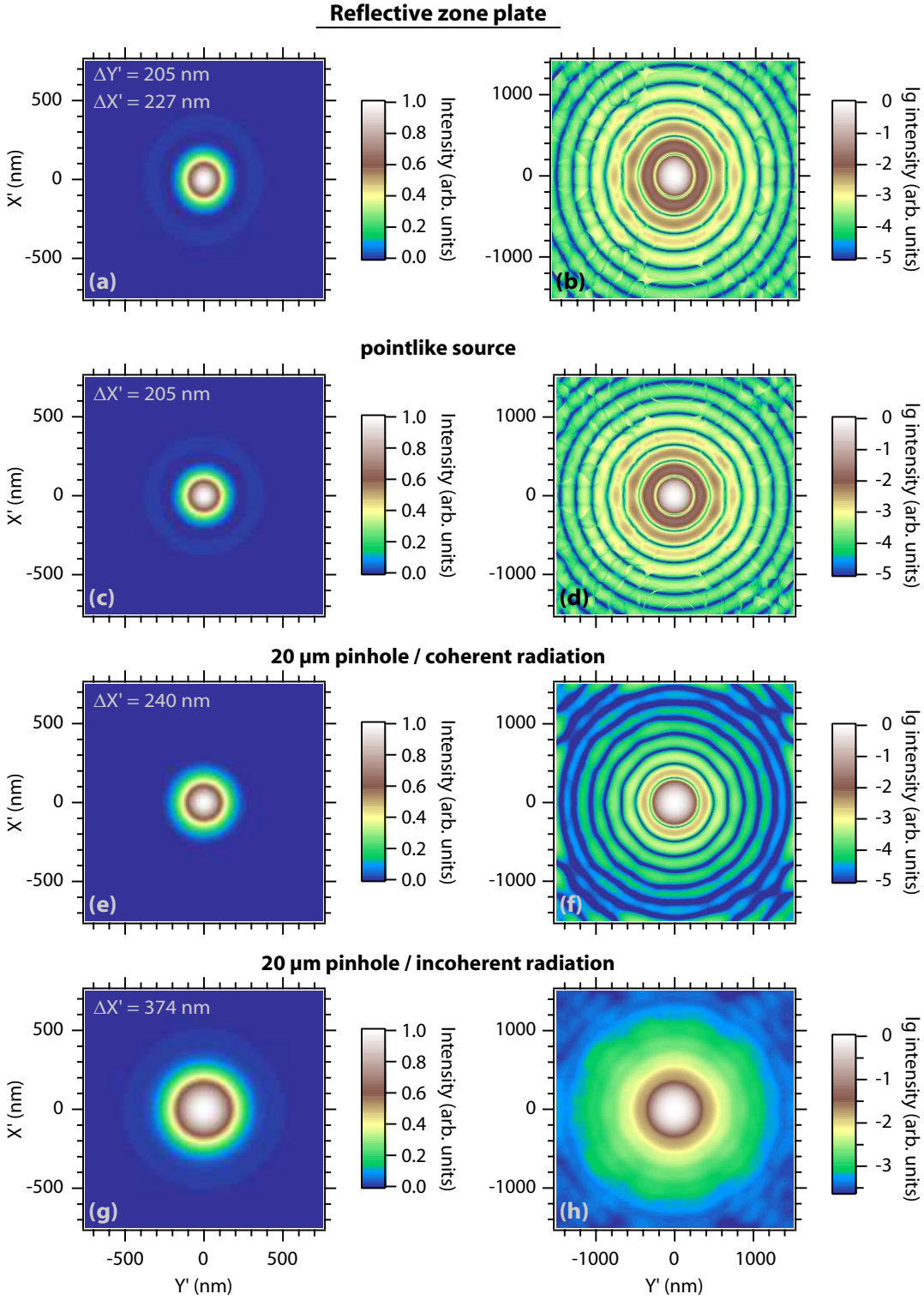

Figure 6.24: Simulation of the focal intensity profile in X'–Y' direction (see Fig. 6.10) of (a,b) the RFZP "zp_200" with image plane perpendicular to q ($\beta = 24°$), and (c,d) perpendicular to the symmetry axis of the diffraction cone ($\beta \approx 24.123°$), (e,f) convolved with a 20 μm pinhole aperture at totally coherent illumination, and (g,h) totally incoherent illumination with spot width $\Delta X'$ (FWHM). The plots on the left are in linear color scale, the plots on the right are in logarithmic color scale.

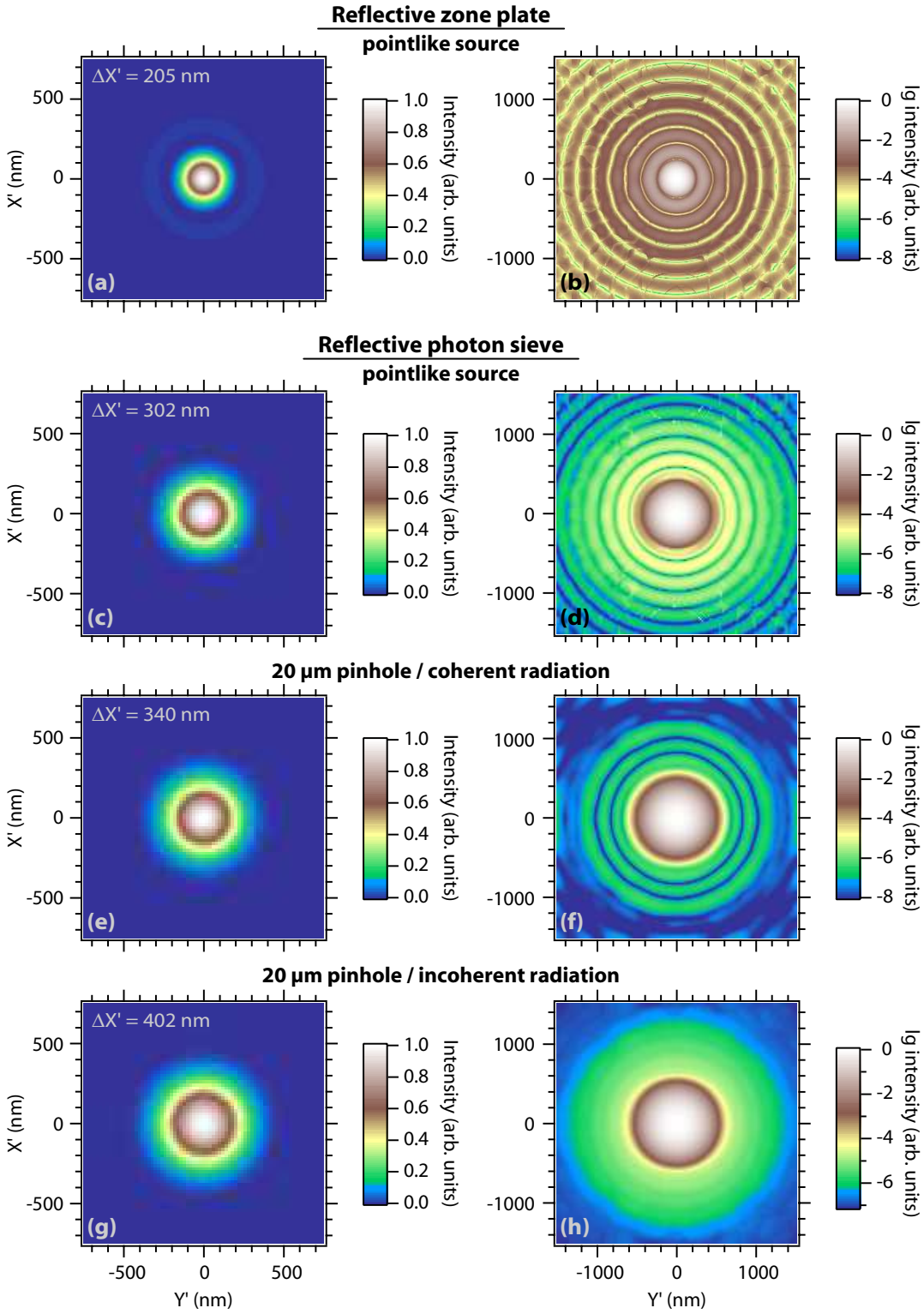

Figure 6.25: Simulation of the focal intensity profile in X'–Y' direction (see Fig. 6.10) of (a,b) the RFZP "zp_200" [same as Fig. 6.24(c), (d), but with the color scale range of Fig. 6.25(c), (d)] and of (c,d) the RPS with Weber–type transmission window "psi_w_200", (e,f) convolved with a 20 μm pinhole aperture at totally coherent illumination and (g,h) totally incoherent illumination with spot width $\Delta X'$ (FWHM). The plots on the left are in linear color scale, the plots on the right are in logarithmic color scale.

6.5.2 Measuring the focal spot size

To measure the focal spot size, the knife edge scan method was used. Simulations of knife edge scan profiles were performed, in order to compare the measurements with the theoretical focal widths. The simulations as well as the experimental datasets were fit by a sigmoid function:

$$f_{sigmoid}(x) = a + \frac{h}{1 + \exp(\frac{x - x_0}{w_s/4})} \ , \tag{6.24}$$

where a is an offset, h the height, x_0 the center, and w_s the width of the knife edge profile. To account for possible experimental linear or parabolic drifts, a term $s_1 x + s_2 x^2$ was added. The derivative of equation (6.24) leads to a peak profile with the peak width (FWHM):

$$\Delta X'_{FWHM,sigmoid} = w_s \cdot \ln(\sqrt{2} + 1) \approx 0.88 \cdot w_s \ . \tag{6.25}$$

According to Fig. 6.26 and Tab. 6.3, the widths of the simulated knife edge scans underestimate the width of the original simulated 2D intensity profiles by a nearly constant conversion factor of approximately 1.2 except for the PSF of "zp_200" (conversion factor 1.1). This underestimation results from the two–dimensional integration during the knife edge scan which overestimates the high intense, circular shaped central parts of the intensity profile. Even though the two–dimensional intensity profile can only be reconstructed out of the knife edge profile if its original shape is known, the similarities between the different conversion factors suggest a multiplication of the experimental fit results by a factor of 1.2 in order to get the width of the corresponding 2D profile.

The smallest knife edge scan profiles of "zp_200" and "psi_w_200" were measured with our prototype UHV–compatible knife edge scanner. It used a single knife edge instead of a slit aperture. Being built to characterize the optical devices without the ability to perform photoemission, it employed step motors from outside the vacuum in order to align

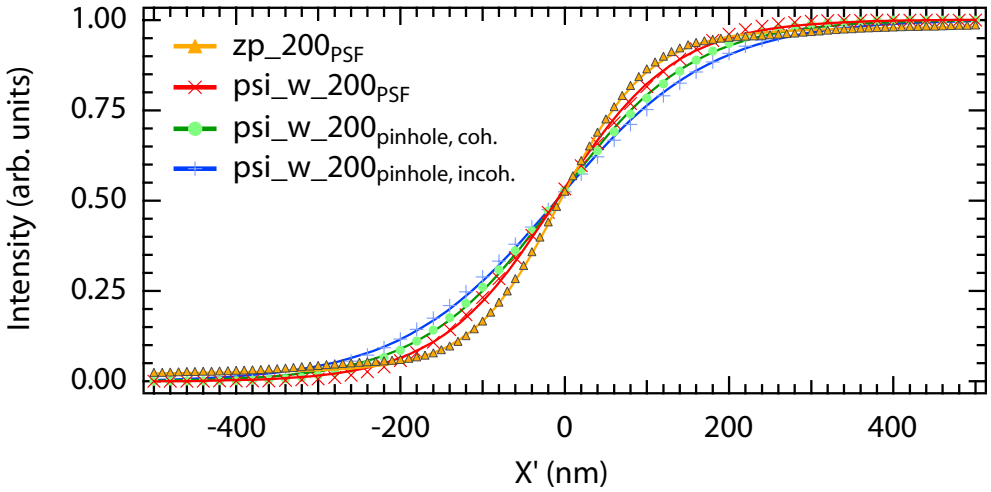

Figure 6.26: Simulation of a knife edge scan along the X' direction using two–dimensional intensity maps in the X'–Y' direction (see Fig. 6.24 and 6.25). The calculations were done for a point like light source and the RFZP with rectangular window (zp_200$_{PSF}$) and the RPS with Weber–type transmission window (psi_w_200$_{PSF}$), as well as for a circular, 20 μm wide coherent (psi_w_200$_{pinhole,coh.}$) and incoherent (psi_w_200$_{pinhole,incoh.}$) illumination. The calculated knife edge profile width values are shown in Tab. 6.3.

	Focal spot width (2D)	Knife edge scan width	Ratio
zp_200$_{PSF}$	205 nm	188 nm	1.09
zp_200$_{pinhole,coh.}$	240 nm	201 nm	1.19
zp_200$_{pinhole,incoh.}$	374 nm	308 nm	1.22
psi_w_200$_{PSF}$	302 nm	253 nm	1.19
psi_w_200$_{pinhole,coh.}$	340 nm	293 nm	1.16
psi_w_200$_{pinhole,incoh.}$	402 nm	332 nm	1.21

Table 6.3: Focal widths (FWHM) derived by FKDF calculations of the 2D intensity profile and simulated knife scan widths for the RFZP "zp_200" and the RPS "psi_w_200". The intensity pattern is called "PSF" in the case of a point like light source, while the use of a circular, 20 μm wide coherent or incoherent illuminated pinhole is called "pinhole, coh." and "pinhole, incoh.".

the optics and do the knife edge scans (for a detailed description of the setup see [135]). As illustrated in Fig. 6.27, the smallest measured spot size is $\Delta X'_{FWHM} \approx 720$ nm for the RFZP, and $\Delta X'_{FWHM} \approx 700$ nm for the RPS. The datasets were fit by a sigmoid function with an additional linear term and the results were converted to the FWHM spot size using equation (6.25) and the conversion factor between knife edge and 2D spot profile of 1.2. Even though very low contrast in both optical devices of about 1.2:1 for the RFZP, and only 1:2 for the RPS knife edge scan were observed, the measured spot widths are in the range of the simulation results. Since a low energy resolution of $\Delta E = 103$ meV had to be used due to the low intensity at beamline BW3, the low contrast can be explained by the small coherence length as mentioned above. For the deviations in spotwidth, experimental

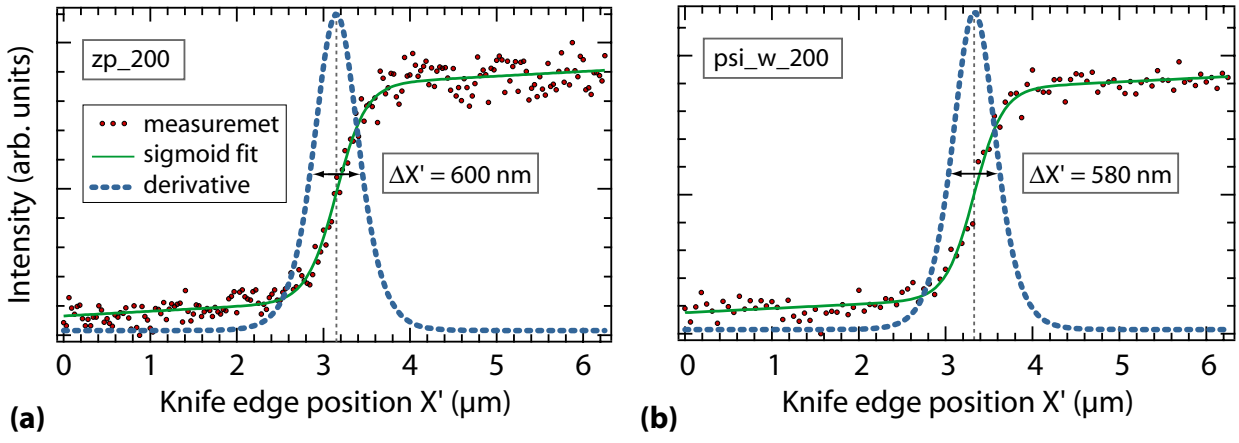

Figure 6.27: Measured (red dots) knife edge scan intensity profile in direction perpendicular to q (see Fig. 6.10) of (a) the RFZP "zp_200" and (b) the RPS with Weber–type transmission window "psi_w_200". The datasets are fit by a sigmoid function with additional linear term (green line) and plotted with its derivative (blue dashed line). The measurements were taken at the synchrotron beamline BW3 with the prototype knife edge scan system.

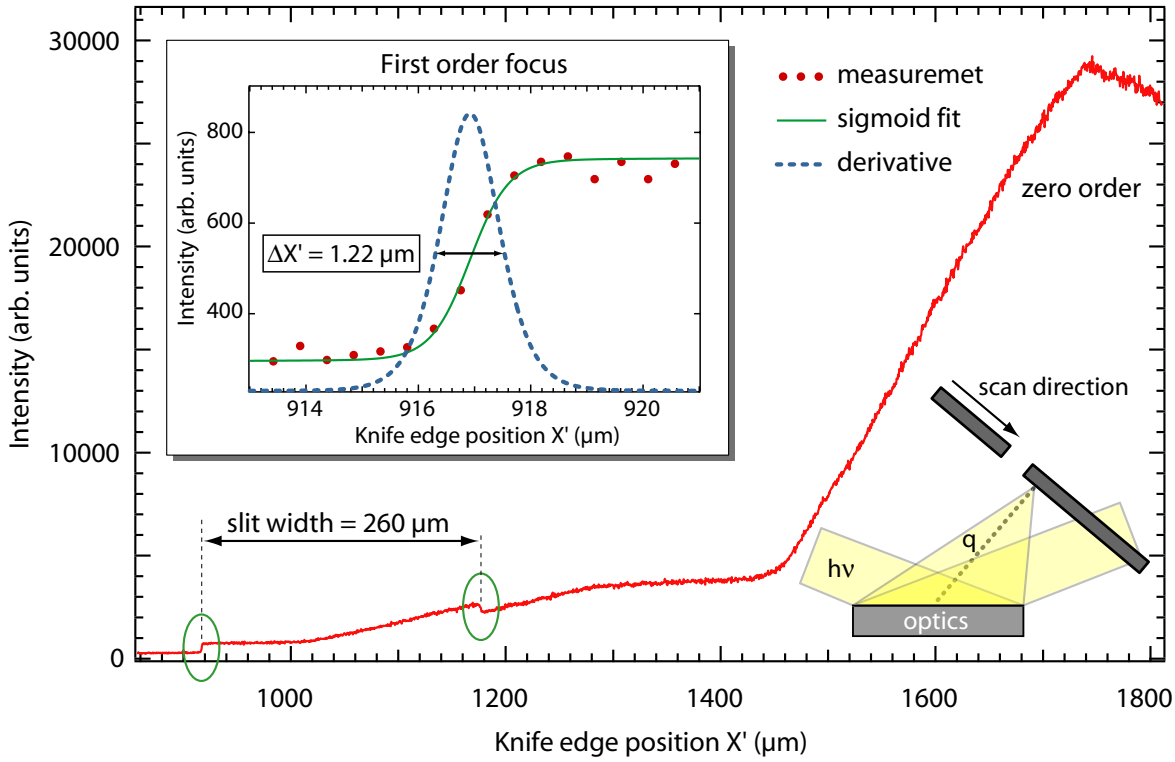

Figure 6.28: Measured wide range knife edge scan intensity profile (red line) in direction perpendicular to q of an RPS with Weber–type transmission window (hν = 100 eV, p = 1 m, q = 20 mm). The first diffraction order derived step in the intensity profile is shown magnified in the inset (red dots) with sigmoid fit (green line) and derivative (blue dashed line). The resulting width is $\Delta X'_{FWHM} \approx 1.22$ μm. The piezo motor step width can be calibrated to 476 $nm/step$ at $U_{piezo} = 20$ V.

conditions like vibrations and in particular drifts in the synchrotron beam position that were observed during the beam times have to be taken into account. This is of particular importance if the data acquisition times are very long so that also electron injections into the storage ring are performed during the measurements.

Using the new scanner module with the RPS, the low contrast of the focal spot profile could be increased by a factor of 5, since the slit aperture blocks the higher order light as well as the diffuse scattered light much better than a single knife edge. However, the synchrotron beam intensity had to be maximized in order to process photoemission. Therefore, a similar large bandwidth as in the above setting had to be used ($\Delta E = 108$ meV). Additionally to the low coherence and beam position fluctuations, in the new experiment principle problems concerning the piezo electric drives as mentioned in section 6.4 reduced the alignment accuracy.

The full knife edge profile including the first order focus as well as the reflected zero order light is shown in Fig. 6.28, measured with a piezo saw–tooth amplitude of $U_{piezo} = 20$ V. On the left side at $X' \approx 917$ μm, a steep onset, and after 576 piezo steps a similar steep drop–off is observable. This is caused by first order light, passing the 260 μm wide slit aperture. Therefore, it could be used to calibrate the step width, leading to about 476 $nm/step$. Using this calibration, the theoretical distance between first order focus and onset to the zero order light of 505 μm is very well reproduced by the experimental value of about

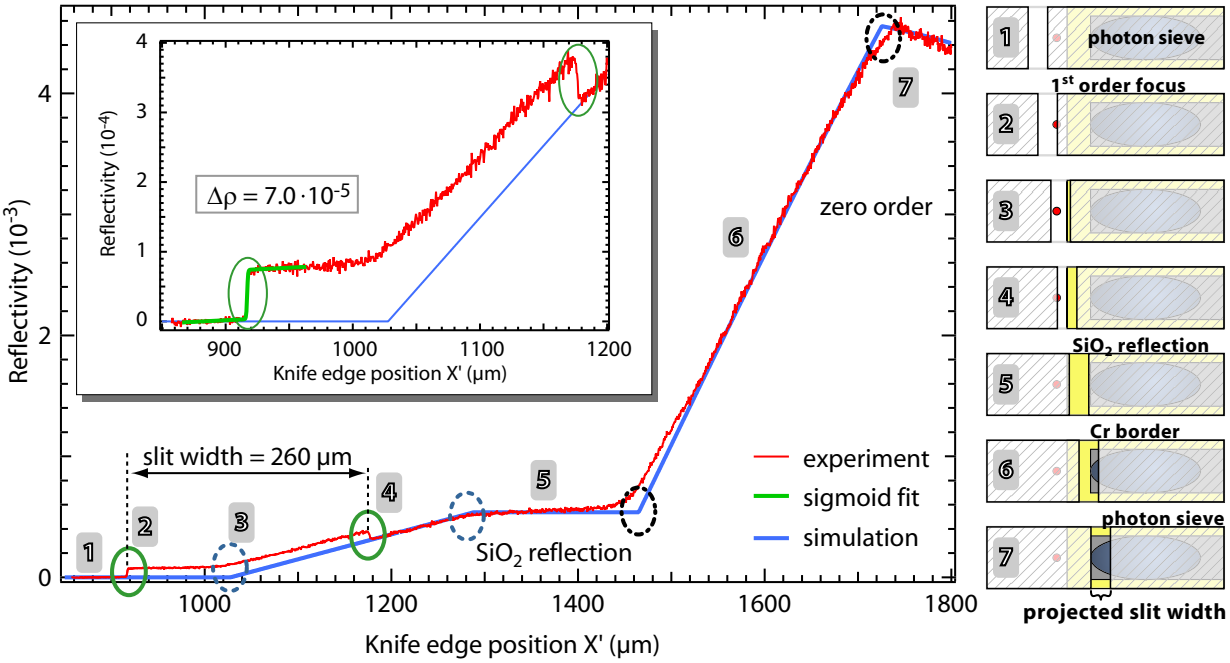

Figure 6.29: Measured wide range intensity distribution during a knife edge scan (red line) and simulation (blue line) for the inverted RPS with Cr–border. The distance between circles of the same kind equals the slit width of approximately 260 μm. In the right the different knife edge positions during the scanning are illustrated: (1) no intensity in the knife edge slit, (2) RPS focus enters the slit, (3) first reflected light from the SiO_2 substrate, (4) RPS focus leaves the slit, (5) pure SiO_2 reflections, (6) first reflected light from the Cr border, and (7) strong reflections from the Cr border. The inset shows a magnification of the knife edge scan region in which intensity from the first order focus illuminates the slit. The design angle of light incidence is $\alpha = 21°$ and the roughnesses are $\sigma_{Cr} = 3.4$ nm and $\sigma_{SiO_2} = 0.3$ nm, which fits best to the measured curve. The intensity scale of the y–axis is substituted by the reflectivity scale derived by the simulation.

510 μm. The intensity of the various diffraction orders which theoretically blurs the focal plane in a distance of at least 340 μm (slight intensity increase starts at about 150 μm) is not visible here, since its intensity contribution is much lower than the directly reflected light. The smallest measured spot width using the new setup is about 1.5μm [see Fig. 6.28(inset)].

Applying a simulation for the reflected light during the knife edge scan, the significant features of the scan profile can be reproduced (see Fig. 6.29). The reflectivity simulation is done in the geometry of the optics plane, where both, the Cu–aperture which restricts the illumination of the optics as well as the knife edge slit aperture are projected into. The simulation identifies the wide plateau in the center of the knife edge intensity plot as originating from reflections at the SiO_2 substrate and the intense peak at the right as originating mainly from the reflections at the Cr–border. It also allows to determine the illuminated area on the diffraction optics, since it influences the distance between the onset to the SiO_2 plateau and the Cr peak. The result is shown in Fig. 6.17(bottom). It indicates that the diffraction optics was totally illuminated during the measurements. By observing the illumination of the optical device at different angles of light incidence it is also possible to determine, whether the rotation axis in the experiment is identical with the symmetry axis of the optics.

In adjusting the intensity ratios of the SiO_2 and the Cr (zero order) plateaus, the unknown RMS–roughness of the Cr diffraction structures could be determined. As the reflectivity simulations only allow the determination of reflectivity ratios, the RMS–roughness of SiO_2 had to be assumed. A value of $\sigma_{SiO_2} \approx 0.3$ nm was chosen as a lower limit for the real roughness, corresponding to a reflectivity value of $\rho_{SiO_2} \approx 0.40\%$ which only deviates by about 1% from the value of a totally flat surface. The simulation result for the RMS–roughness of the Cr film is $\sigma_{Cr} \approx 3.4$ nm. Therefore, it is a lower limit and its corresponding reflectivity value of $\rho_{Cr} \approx 4.7\%$ is an upper limit for the real values.

Using the calculated reflectivity values during the knife edge scan, the measured intensity profile can be scaled in terms of reflection efficiency, i.e., the ratio of reflected light into the slit aperture and the total incident light. As illustrated in Fig. 6.29(inset) the first order focus intensity is as high as if the reflectivity was increased by a factor of $7 \cdot 10^{-5}$. Therefore, the diffraction efficiency of the reflective photon sieve "psi_w_200" can be estimated to be $\eta_{psi\_w\_200} \approx 7 \cdot 10^{-5}$. This value is confirmed by theoretical considerations: In contrast to the RFZP with a Cr coverage of 50%, the nano–absorber coverage in the elliptic diffraction area of the inverted RPS can be calculated to about 14%. This leads to a reduced diffraction efficiency and $\epsilon \approx 0.08$ [see equation (6.20)]. More detailed FKDF calculations result in an ϵ value of about 0.12 . Employing equation (6.20) with a SiO_2 reflectivity of 0.40% and a Cr reflectivity of about 4.7%, the diffraction efficiency of the third order RPS can be estimated to be $\eta_{psi\_w\_200,thoer.} \approx 3 \cdot 10^{-5}$.

6.5.3 Aspects on the brilliance

The total efficiency of the optical system for first order light J can be calculated using the diffraction efficiency of the optical device η and the transmissions through the pinhole T_{ph} and the Cu–aperture T_{Cu}. Taking into account that the illuminated area in the optics plane is larger than the optics (see $\tilde{D}$ and D in Fig. 6.30), the total efficiency is further decreased. Since this factor and T_{Cu} mainly depend on the beamline divergence, it can be combined to the illumination efficiency behind the pinhole $T_{diverge}$ so that the total efficiency of the optical system can be calculated by:

$$J = T_{ph} \cdot T_{diverge} \cdot \eta \ . \tag{6.26}$$

In order to get high total efficiency of the optical system in the final spatially resolving

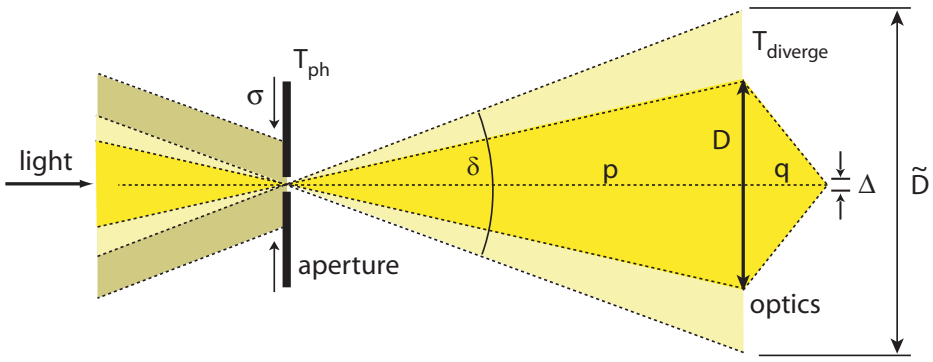

Figure 6.30: Influence of light source divergence δ and beam size σ on the total light transmission through a combination of pinhole aperture (diameter d) and optics (diameter D). The final spot width is Δ.

ARPES experiment the diffraction efficiency η as well as the transmission factors have to be maximized. The maximum diffraction efficiency that can be achieved for a RPS with Weber–type transmission window is $\eta_1 \approx 1.5\%$ for a first order RPS and $\eta_3 \approx 0.17\%$ for a third order device, assuming the highest possible diffraction contrast with the reflectivity values $\rho_{Cr} = 1$ and $\rho_{SiO_2} = 0$. However, this value cannot be realized for an 80 nm Cr monolayer on a SiO_2 substrate at $h\nu = 100$ eV and $\alpha = 21°$. The maximum diffraction efficiency for this parameters is about $\eta_1 \approx 2{\cdot}10^{-3}$ and $\eta_3 \approx 2{\cdot}10^{-4}$ [146]. Higher diffraction efficiencies can only be achieved in changing the angle of light incidence or in particular the material combination of the optical device. Inverting for example the material combination, so that a high reflecting substrate, such as a multilayer mirror, is covered by an absorbing or phase shifting material, highly efficient diffraction structures similar to Bragg–Fresnel lenses can be realized (see also [121]).

In contrast, an increase of the transmission factors primary regards the light source parameters and in particular its brilliance. Using the notation of Fig. 6.30, the transmission through the pinhole with diameter d can be described by:

$$T_{ph} = \frac{d^2}{\sigma_x \sigma_y} \ , \tag{6.27}$$

where σ_x and σ_y are the diameters of an elliptical synchrotron beam profile (assuming $d < \sigma_x, \sigma_y$). Similar to this, the fraction of light illuminating the optics (assuming circular shape) can be described by:

$$T_{diverge} = \frac{D^2 \cdot \pi/4}{(d + \tilde{D}_x) \cdot (d + \tilde{D}_y) \cdot \pi/4} = \frac{D^2/4}{\left(d/2 + p \tan \frac{\delta_x}{2}\right)\left(d/2 + p \tan \frac{\delta_y}{2}\right)} \ , \tag{6.28}$$

with the beam divergence δ_x, δ_y, the diameter of the radiation cone in the optics plane $\tilde{D}_x$ and $\tilde{D}_y$, and the optics diameter D. In consideration of a simple model with large object distances, the achievable spot width Δ of the whole optical system can be approximated by:

$$\Delta \approx \sqrt{\Delta x_{ph}^2 + \Delta x_{PSF}^2} \approx \sqrt{\left(\frac{q}{p} d\right)^2 + \left(\lambda \frac{q}{D}\right)^2} \ , \tag{6.29}$$

using equation (6.10) for the resolution of the optical device Δx_{PSF} and equation (6.14) for the size of the demagnified pinhole Δx_{ph}. Assuming further a small beam divergence and a large optical device in comparison to the pinhole, the total transmission through the optical system can be approximated by:

$$T_{total} = T_{ph} \cdot T_{diverge} \approx \frac{\lambda^2}{\sigma_x \sigma_y \delta_x \delta_y} \frac{\Delta^2 - \Delta x_{PSF}^2}{\Delta x_{PSF}^2} \ . \tag{6.30}$$

Equation (6.30) describes the achievable light transmission of the whole optical system. It depends on the the total resolution and the emittance, i.e., the product of beam size and divergence $\sigma_x \sigma_y \delta_x \delta_y$. In Fig. 6.31 the transmission through the optical system is illustrated for a photon energy of $h\nu = 100$ eV (left), and $h\nu = 5$ keV (right) with a resolution of the optical device of $\Delta x_{PSF} = 50$ nm (top), and $\Delta x_{PSF} = 200$ nm (bottom). It illustrates that in order to get high transmission not only the photon flux, but also the emittance plays an important role.

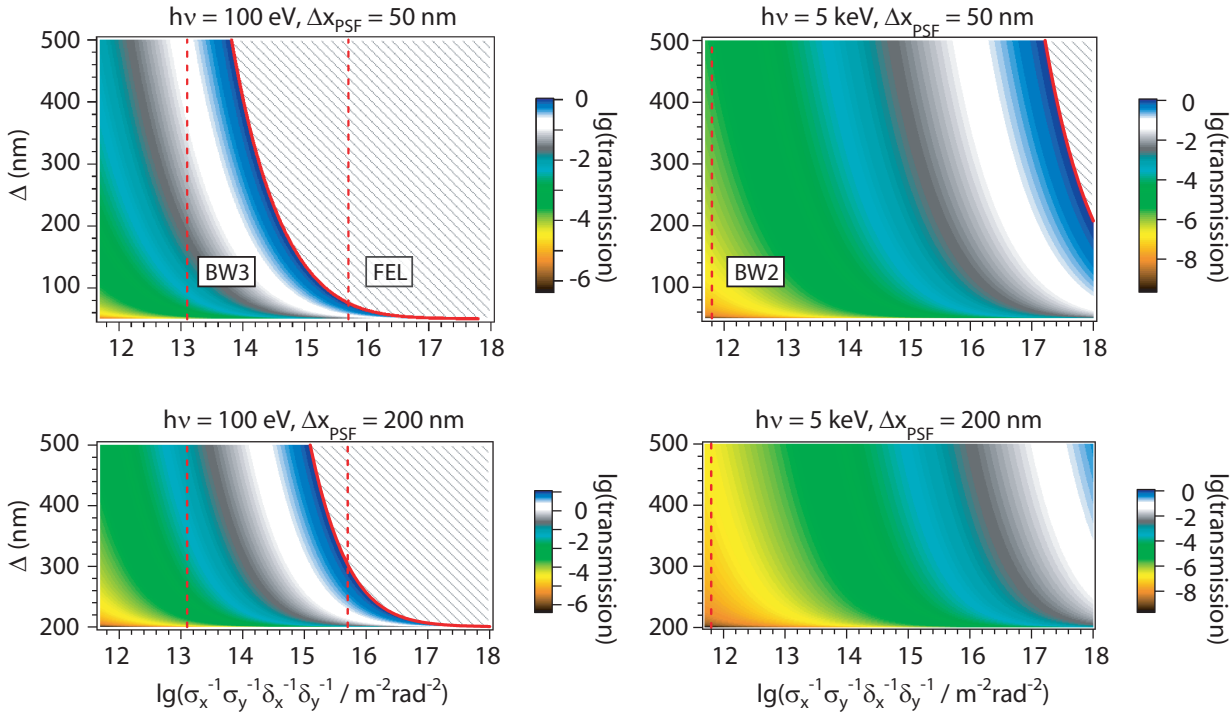

Figure 6.31: Transmission through an aperture and optical device, depending on the inverted emittance and the spot size of the optical system. The dashed lines indicate the emittance of the VUV–FEL and of the synchrotron radiation beamlines BW3 and BW2 at HASYLAB.

For example the total transmission at BW3 using the inverted reflected photon sieve "psi_w_200" and a 20 μm pinhole can be calculated to $T_{total,BW3} \approx 0.8\%$ [see Fig. 6.31], if the parameters of the underlaying reflective zone plate "zp_200" ($h\nu = 100$ eV, $\Delta x_{PSF} \approx 200$), the beamline emittance ($\delta_x \approx 4$ mrad, $\delta_y \approx 0.64$ mrad, $\sigma_x \approx 318\mu$m, $\sigma_y \approx 95\mu$m) and the demagnified pinhole diameter ($\Delta x_{ph} = 400$) are used. The total efficiency of the optical system can be calculated with equation (6.26), using the diffraction efficiency of the photonsieve $\eta_{psi\_w\_200,thoer.} \approx 3 \cdot 10^{-5}$ from section 6.5.2. The result of $J_{BW3,20\mu m} \approx 4 \cdot 10^{-7}$ is very similar to more precise calculations without the approximations of equation (6.30) ($J_{BW3,20\mu m} \approx 1 \cdot 10^{-7}$). With typically 10^{12} photons/s in 0.1% bandwidth at $h\nu = 100$ eV at BW3 [150] there will be about 10^5 photons/s in the first diffraction order to process photoemission. This is a very low number even if the photoelectron cross section is neglected. Since the photoelectrons leave the sample with different kinetic energies (up to nearly 100 eV) and are emitted into all directions, very low countrates in the order of 1 electron per second, 1° (solid angle) and 100 meV (energy) are expected (assuming equally distributed electrons in angle and energy and neglecting the photoelectron cross section). However, using the experimental station at the VUV–FEL with its about 400 times lower emittance than at BW3 [see Fig. 6.31(left)], an increased radiation intensity in the focal spot by this factor could be obtained without changing the resolution of the optical system. With about 10^4 times higher photon flux at the VUV–FEL a total increase of the first order focal intensity of about 10^6 to 10^7 (design parameters) can be expected. This indicates that high resolution experiments need high brilliant light sources.

6.5.4 Aspects on the depth of focus

In order to estimate the required accuracy of the distance between optics and image plane (sample), the depth of focus for both optical devices was simulated and measured. As illustrated in Fig. 6.32(left), a $DOF_{RFZP} \approx \pm 6.68$ μm can be determined for "zp_200" by numerically FKDF calculations. This value is very similar to the rough approximation of equation (6.12) leading to $DOF \approx \pm 6.5$ μm. The DOF of the RPS is $DOF_{RPS} \approx \pm 9.73$ μm, which is about 1.46 times larger than the zone plate value. As this is very similar to the focal width ratio $\Delta X'_{RPS}/\Delta X'_{RFZP} \approx 1.47$, the DOF and the focal width seem to scale in the same way. Since the calculation time does not allow to simulate a three–dimensional DOF profile of the full optical system – including the convolution with the pinhole and a knife edge scan – only very rough values for the experimental measured DOF can be determined. Assuming the same linear scaling of the DOF for an optical system with pinhole as for the focal width, the expected DOF at incoherent illumination increases to about $DOF_{RFZP,pinhole} \approx \pm 12.2\mu$m for the RFZP, and $DOF_{RPS,pinhole} \approx \pm 12.9\mu$m for the RPS. An extra scaling that represents the influence of the knife edge scan method should not be needed, since this scaling would concern all intensity profiles in the same way. The determination of the DOF using knife edge scans is a very indirect method and uses the differentiated knife edge (fit–)profile. The slope of the measured scan profile determines the peak intensity [see Fig. 6.33(c), (d)] which is very sensitive to differences in the measured and the fit profile shape. Since the knife edge profile shape also depends on the alignment parameters such as knife edge position or angle of light incidence, the measured DOF accuracy using the knife edge scan method is expected to be not very high.

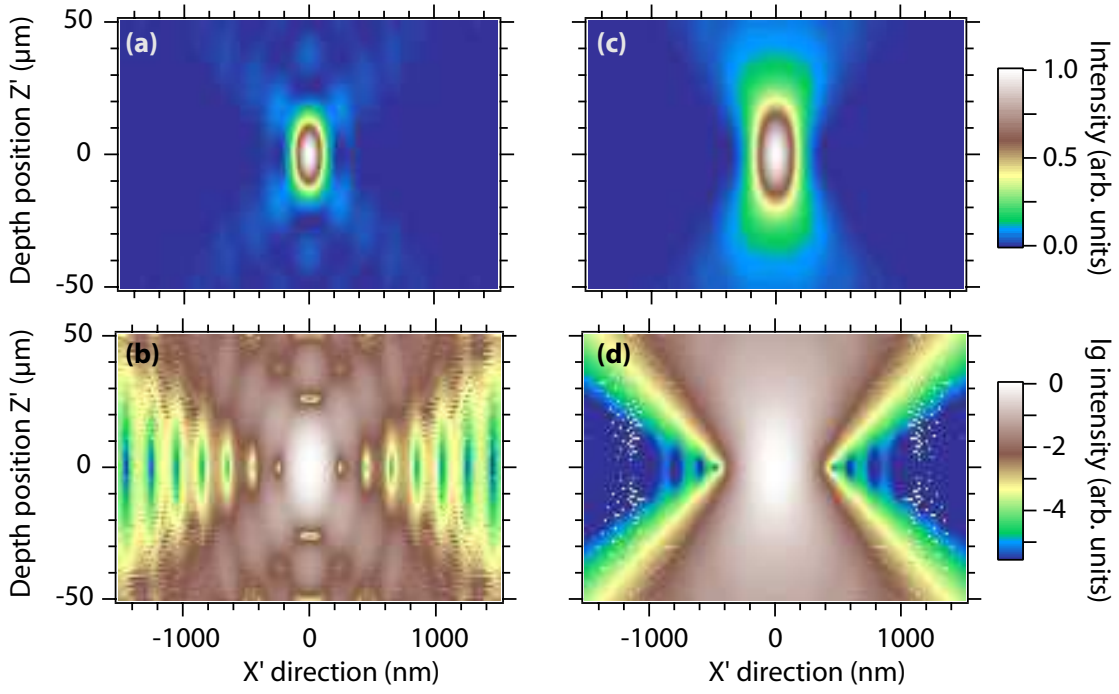

Figure 6.32: Simulated intensity distribution of (a,b) the RFZP with depth of focus $DOF_{RFZP} \approx \pm 6.68$ μm and (c,d) photon sieve with $DOF_{RPS} \approx \pm 9.73$ μm (hν = 100 eV, p = 1 m, q = 2 cm) depending on Z' – the distance between the optics and the focal spot.

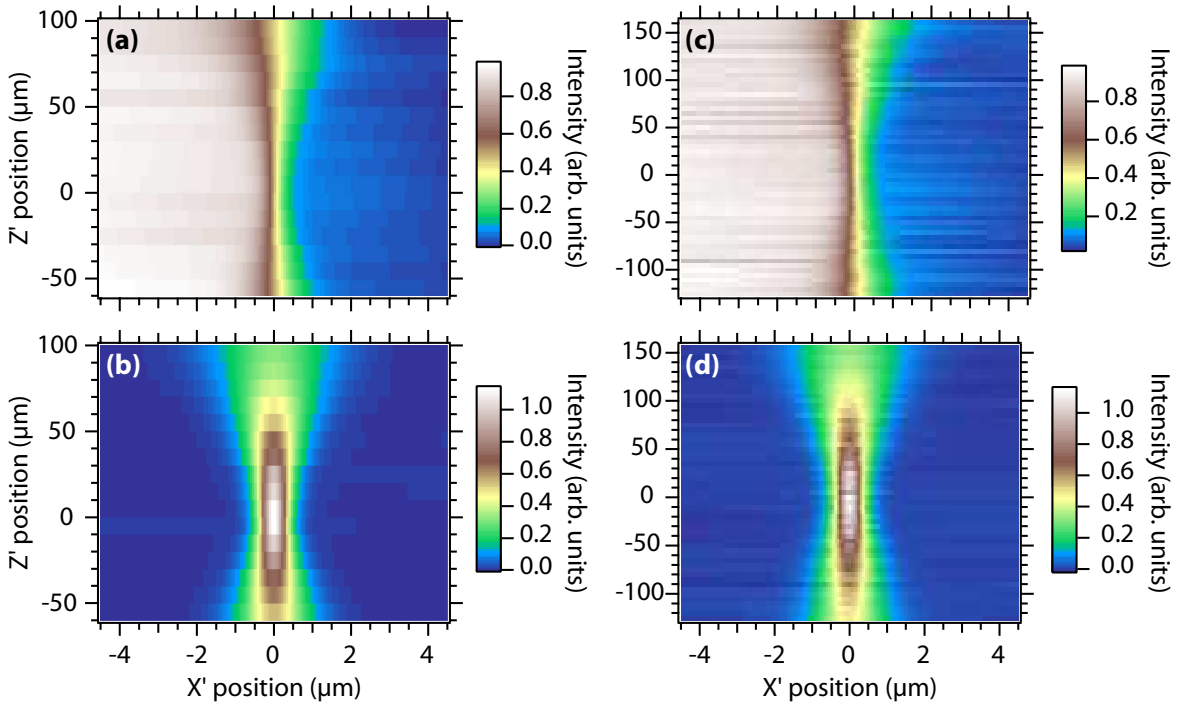

Figure 6.33: (Top) Fit results to the measured intensity distribution of (left) the RFZP "zp_200", and (right) the RPS "psi_w_200", depending on the distance between photon sieve and knife edge (Z'). (Bottom) The derivative of (top) allows to determine the DOF of the diffraction optics with $DOF_{RFZP,exp.} \approx \pm 27$ μm, and $DOF_{RPS,exp.} \approx \pm 47$ μm. The datasets are shifted to be symmetric to $X' = 0$ and were measured using the prototype knife edge scanner system.

The experimental values of $DOF_{RFZP,exp.} \approx \pm 27$ μm, and $DOF_{RPS,exp.} \approx \pm 47$ μm (see Fig. 6.33) deviate by a factor of two for the RZP and a factor of 4 for the RPS from the roughly estimated values above.

6.5.5 Calibration of the experimental setup

It is interesting to note that wide range knife edge scans as discussed before can be used to calibrate the angles of the rotary drive and that it is possible to distinguish between first and zero order features in the scan. The procedure developed here might also be used for automated optimization of the optical device in the future.

In Fig. 6.34 knife edge scans including light of the first diffraction order and the SiO_2 reflections at different angles of light incidence α are plotted. The angle of reflection is equal to α. Therefore, applying simple geometrical considerations (see inset in Fig. 6.34), the shift of the SiO_2 reflection onset $\Delta\beta_{reflect}$ (white dashed line) in dependence of $\Delta\alpha$ could be used to calibrate the rotary piezo drive. The resulting angle step width is $\Delta\alpha = 0.0228°$/step at $U_{rotator} = 50$ V. The step width is small enough to align the optical device. It should be noted that an angle inaccuracy of about 0.05° already broadens the focal spot width by a factor of two. However, since the piezo drives also work with lower voltages or can be operated with a linear voltage, they do not limit the alignment accuracy.

In comparison to the SiO_2 reflection the position change of the first order focus (yellow, dashed–dotted line) is smaller by a factor of $\Delta\beta/\Delta\alpha \approx 0.87$. A similar value of

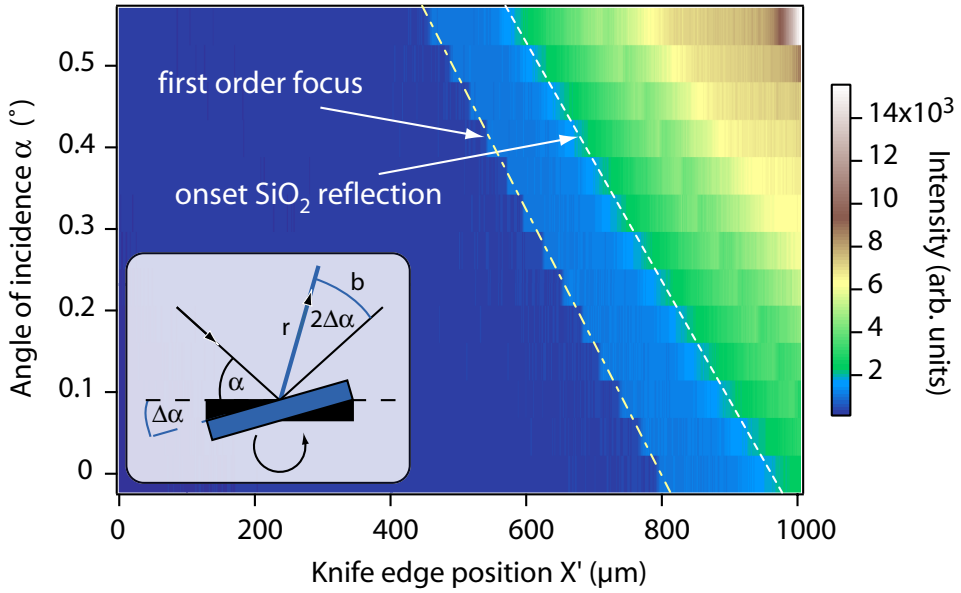

Figure 6.34: Intensity map of a knife edge scan series depending on the angle of incidence α (see Fig. 6.10). Maps in this $\Delta\alpha$–$2\Delta\alpha$–setup (see inset) allow a step size calibration for the rotary piezo drive of 0.0228°/step at $U_{rotator}$ = 50 V. Additionally the focal spot can clearly be identified since its angle dependent shift is 0.87 times smaller than the shift of the reflected light.

$\Delta\beta/\Delta\alpha \approx 0.86$ was derived for the above described optics "*zp_3000*" in [135], even though the parameters of the optics are totally different (λ = 632.8 nm, $\Delta X' \approx 3\mu$m, p = 4 m, q_1 = 40 mm, $\alpha_0 = 34.4°$, $\beta_1 = 45°$, and $d_{min} = 1.5\mu$m). The value of this angle ratio can be roughly estimated in calculating $\Delta\beta/\Delta\alpha$ for a RZP with parallel illumination and long object distances, leading to constant zone width w over the hole diffraction optics, similar to a linear grating. The condition for constructive interference simplifies to:

$$w\cos(\alpha) - w\cos(\beta) = n\lambda \ , \tag{6.31}$$

where n is the diffraction order. Solving this equation by β and differentiating it by α, the change in the diffraction angle β can be quantified by:

$$\frac{d\beta}{d\alpha} = \frac{\sin(\alpha)}{\sqrt{1-(\cos\alpha - n\lambda/w)}} \ . \tag{6.32}$$

Using equation (6.31), $\alpha = 21°$, $\beta = 24°$, λ = 12.398 nm, and $n = 1$, the simplified RFZP has a constant zone width of $w \approx 618.8$ nm, and the resulting angle ratio can be quantified to $d\beta/d\alpha \approx 0.881$, in good agreement with the measured angle ratio. Only for $n\lambda/w \ll \cos\alpha$, which is, e.g., the case for zero order light ($n = 0$) or large angles α (contrary to the design concept of RPS: see Fig. 6.13), equation (6.32) simplifies to $d\beta/d\alpha \approx 1$, so that no angle difference would be observable anymore. Therefore, the characteristic deviation in $\Delta\beta/\Delta\alpha$ is a good parameter in order to identify diffracted light from the background very clearly and possibly allows an automated optimization of the optical device in the future.

6.6 First spatially resolved photoemission measurements

First spatially resolved photoemission measurements were performed using the reflective photon sieve with Weber–type transmission window "psi_w_200". Data were taken employing the new scan system at beamline BW3.

6.6.1 Geometrical constraints

Employing angle resolved photoemission experiments it should be possible to detect photoelectrons originating from a full Brillouin zone and especially from the high symmetric Γ–point (normal emission). In order to achieve this aim, the sample has to be tilted with respect to the synchrotron beam. Therefore, the focal spot is projected in the sample plane by a tilt angle leading to an elliptical distortion of the spot profile. In Fig. 6.35 the smallest possible spot width $\Delta X'_{PSW}$ in the tilted direction is illustrated for a radiation wavelength of $\lambda = 12.398$ nm in dependence of the angle of light incidence χ and the maximum emission angle for photoelectrons ξ with $\xi = 90°$ for normal emission (see inset). For the calculations a parallel beam near the sample surface was assumed which seems to be adequate due to the large DOF of the optical devices (see Fig. 6.32). The yellow, dashed–dotted line indicates the maximum aperture angle $\gamma = 2 \cdot \chi$ of the optics at a given value of ξ. In our setup $\chi = 45°$ is used (green, dotted line) which is connected to a theoretical resolution limit of the optical device of $\Delta X'_{PSW} \approx 13$ nm. Our RPS has an aperture angle of $\gamma \approx 3.551°$, so that an electron acceptance angle of up to $\xi = 180° - \chi - \gamma/2 \approx 133°$ is the

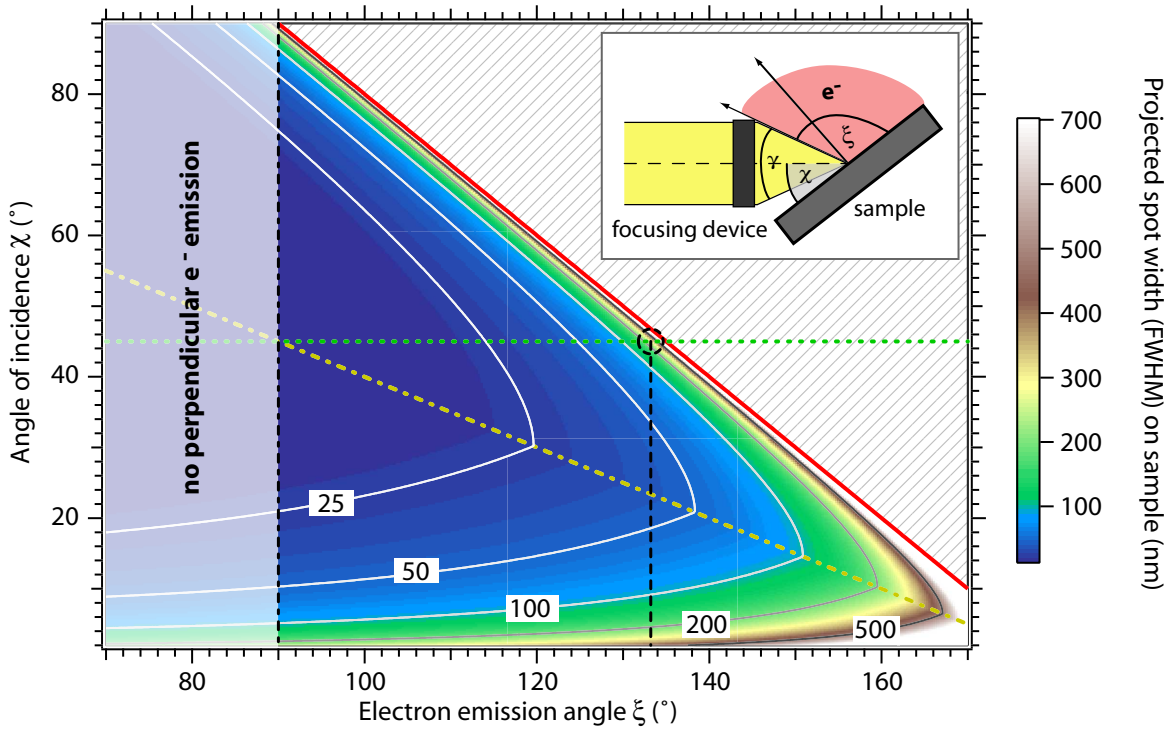

Figure 6.35: Smallest focal spot width (FWHM) on a tilted image plane with a radiation wavelength of $\lambda = 12.398$ nm. The spot width in the tilted direction is plotted in dependence of the angle of light incidence χ and the emission angle for photoelectrons ξ (see inset), assuming a nearly parallel beam to be projected on the sample surface. The yellow, dashed–dotted line indicates the highest possible resolution at given values of ξ.

theoretical limit in the tilted direction (black, dashed circle). Employing a 20 μm pinhole, a total spot width of approximately 400 nm in the vertical and 570 nm in the horizontal direction can be determined. It should be mentioned that this asymmetric spot profile in the sample plane can easily be corrected by increasing the numerical aperture of the optics in the x–direction. Since the optics minimum structure size is not located on the x–axis (see Fig. 6.14), the necessary extension of the optics semi-major axis to $a_x \approx 2.141179$ mm only slightly decreases the structure size from $w_{min} = 158$ nm to $w_{min} = 148$ nm (first order optics). Therefore, the third order reflective photon sieve with a symmetric focal spotsize of $\Delta X'_{PSF} \approx 300$ nm in the tilted image plane ($\chi = 45°$) needs a minimum structure size of $w_{min} \approx 443$ nm that is only 7% smaller than in the uncorrected device.

6.6.2 First experiments on $(PbS)_{1.13}TaS_2$

For the photoemission measurements a TMDC misfit crystal $(PbS)_{1.13}TaS_2$ was used. It has islands of both subsystems on the surface after cleavage in UHV which are typically 10 μm to 100 μm wide (see section 5.3). Using a photon energy of $h\nu = 100$ eV these crystals show intense Ta and Pb core level states that are accessible with photoemission measurements. Since in the final spatially resolved photoemission process the intensity was too low for employing smaller pinholes (see section 6.5), the 100 μm pinhole had to be used. Therefore, the theoretical spot size is approximately 2 μm in the vertical and 2.8 μm in the horizontal direction (assuming incoherent illumination).

In Fig. 6.36(top) a measured spectrum of $(PbS)_{1.13}TaS_2$ is shown. It was taken with the new scan system and the PHOIBOS 150 photoelectron analyzer with a total energy resolution of $\Delta E \approx 206$ meV at a photon energy of $h\nu = 100$ eV. In the spectrum which was

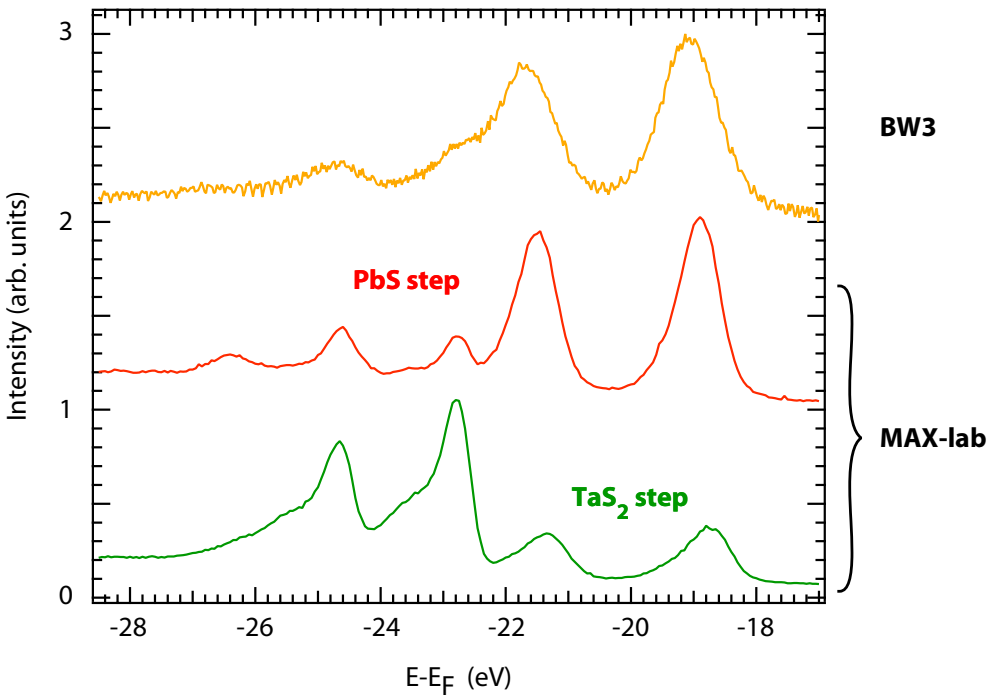

Figure 6.36: Spectra of the Ta $4f$ and Pb $5d$ core levels of $PbS_{1.13}TaS_2$, (top): measured with the new scan system at beamline BW3 (light spot diameter $\Delta X' > 2$ μm), (middle) taken at MAX–lab ($\Delta X' \approx 1.5\mu$m) on a site, terminated by PbS, and (bottom) by TaS_2.

measured with a spatial resolution of $\Delta X' > 2.8$ μm, the Ta $4f$ and Pb $5d$ core levels of the $PbS_{1.13}TaS_2$ sample can clearly be identified. For comparison, spatially resolved spectra of the same substance taken at BL31 (MAX–lab) with a photon energy of $E = 102.5$ eV and a spatial resolution of $\Delta X' \approx 1.5$ μm are also shown in Fig. 6.36. As already mentioned in chapter 5, spectra with high Pb $5d$ and low Ta $4f$ intensity are measured on PbS islands (middle), while spectra with low Pb $5d$ and high Ta $4f$ intensity are measured on TaS_2 islands (bottom). In the BW3 spectrum the Pb $5d$ core level peaks are much more intense than the Ta $4f$ core levels, and the Pb $5d$ core levels are shifted to higher binding energies, similar to measuring on PbS islands. Additionally, a second Ta $4f$ doublette, originating from Ta atoms in the PbS layer at $E - E_F \approx 26.8$ eV (see chapter 5), is slightly visible. Therefore, in comparison to spatially resolved spectra of MAX–lab the spatially resolved BW3 spectrum can be identified as originating from a PbS island.

Due to the low intensity at BW3, it took approximately 10 hours to record the spectrum. For this kind of experiment measurements at the FEL with approximately 10^6 to 10^7 times higher photon flux in the focal spot (assuming 72000 FEL-pulses per second) will lead to excellent statistics and will make it possible to measure with much higher contrast and better spatial resolution.

7 ARPES test experiments at the VUV–FEL

Free–electron lasers (FELs) are fourth generation synchrotron radiation sources, providing highly intense, short pulsed, coherent light. Exceeding the brilliance of third generation synchrotron radiation sources by multiple orders of magnitude, FELs are predestined for applications with high intensity requirements such as the spatially– and angle–resolved photoelectron spectroscopy experiments described in chapter 6.

In order to study the influence of highly intense, ultra short pulsed FEL radiation on the photoemission process we have performed ARPES measurements on $TiTe_2$ crystals at the monochromator beamline PG2 of the VUV–FEL at HASYLAB (now known as Free–Electron Laser in Hamburg: FLASH). Our intensity dependent measurements indicate that ARPES experiments are in principle possible at the FEL, but that at high photon intensities a significant peak broadening and an energy shift in the range of several eV occurs.

7.1 Introduction

Conventional third generation synchrotron radiation facilities provide polarized, partly coherent, and highly brilliant radiation with pulse lengths of several 10 ps and repetition rates in the sub GHz regime. Employing bending magnets, wigglers, and undulators, various radiation parameters such as polarization, coherence (partially), or radiation energy (microwave to hard X–ray radiation) can be tuned. On the other hand, modern laser sources exceed several parameters of synchrotron radiation sources regarding the degree of coherence, photon pulse intensities and pulse durations, but are in general limited in photon energy (infrared to soft UV regime).

Free–electron lasers like the VUV–FEL at HASYLAB close the gap between third generation synchrotron radiation sources and lasers. At the FEL a highly intense, ultra short

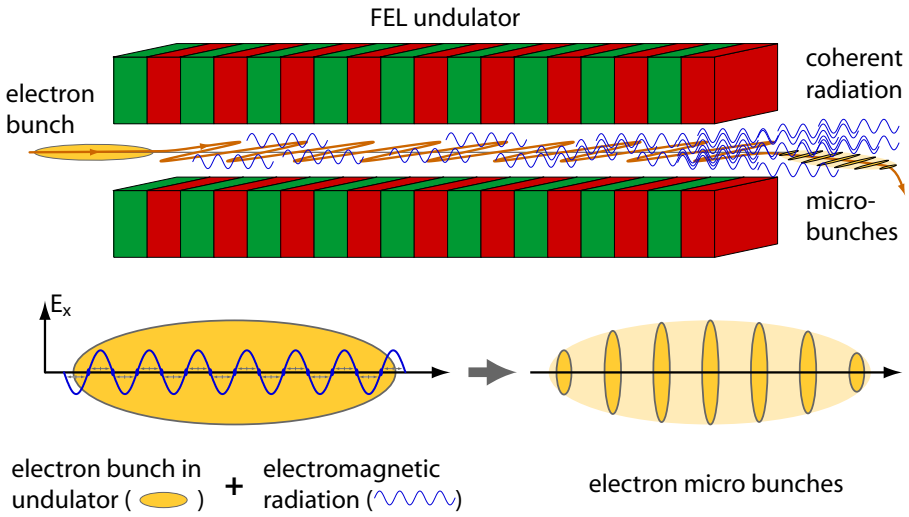

Figure 7.1: During a single pass of a highly compressed electron bunch (yellow ellipse) through the periodic magnetic field of the FEL undulator, photons (blue sine waves) are emitted spontaneously (top). The interaction (bottom) of the strong electromagnetic field (electric field E_x parallel to the transversal motion of the electron) with the electron bunch on its way through the undulator leads to a density modulation of the electron bunch with the periodicity of the radiation wavelength.

electron bunch is generated by a laser pulse, and accelerated to relativistic velocities by a linear accelerator. After being spatially compressed by bunch compressors, the highly dense electron bunch passes the FEL undulator and spontaneously emits electromagnetic radiation due to the acceleration in the periodic magnet structure [see Fig. 7.1(top)]. As the FEL undulator is extremely long (27 m at FLASH) and the electron density very high, the accelerated electron bunch interacts with its own radiation field, leading to a periodic density modulation with the periodicity of the radiation wavelength [see Fig. 7.1(bottom)]. In this microbunch formation self–amplified spontaneous emission (SASE) is achieved. Since the moment of the first spontaneously emitted photons changes from bunch to bunch, also the position in the undulator where SASE begins varies, leading to different photon pulse intensities from pulse to pulse. While the radiation intensity of bending magnets, wigglers, and conventional undulators is only proportional to the number of electrons, a square dependence of intensity and number of electrons exists at an FEL because all electrons radiate coherently. Therefore, FEL radiation exceeds the brilliance of third generation synchrotron radiation facilities by several orders of magnitude and provides nearly total transverse coherence.

The highly intense, short pulsed, coherent FEL radiation allows to perform a variety of novel experiments. These are, for example, fundamental experiments on the dissociation of molecules [151], electron correlations in noble–gas atoms [152], or Coulomb interactions in highly charged ions [153], all of which need the high brilliance of FEL radiation. Also short pulse lengths and high coherence are important, as needed, e.g., for X–ray diffraction experiments on biological substances that are sensitive to radiation damage and cannot be crystallized. In these experiments the whole diffraction pattern has to be obtained with one single radiation pulse before the specimen is destroyed [154].

Furthermore, in future experiments it is planned to investigate the possibility of controlling the electronic properties of solids by highly intense electromagnetic radiation. In particular for materials that are in the vicinity of a phase transition like Mott–insulators, charge–density wave systems, or high temperature superconductors, it seems to be possible to induce the phase transition by highly intense electromagnetic radiation. This would also allow to control the macroscopic properties of solids such as the electrical conductivity or optical properties. Since the coherence of FEL–radiation is very high, these experiments could be performed with an additional diffraction optics, as described in chapter 6, to focus the radiation to a sub μm spot. Utilizing the short pulse length, e.g., by performing pump–probe experiments, the angle–, space– and time–resolved electronic structure could be investigated.

As a first step in this direction the experimental conditions and parameters provided by FLASH were tested and the possibility to do photoelectron spectroscopy at all was investigated in performing intensity dependent ARPES measurements at the monochromator beamline PG2.

7.2 Experimental details

Performing an ARPES experiment at the VUV–FEL requires new considerations regarding the electron detection process. The FEL–radiation pulse lengths are very short (less than 100 fs, longer after passing the monochromator, depending on the energy resolution) and the intensity varies strongly from pulse to pulse. Therefore, it is essential to measure the ARPES spectra and corresponding photon intensities for every single pulse. The pho-

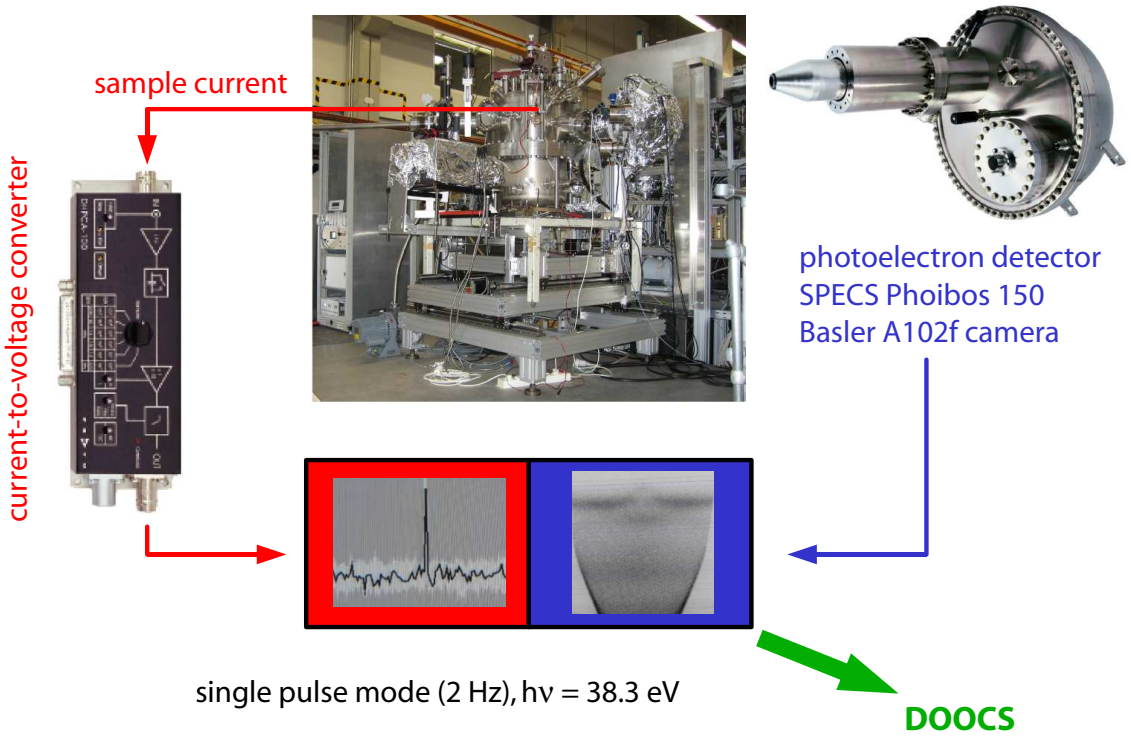

Figure 7.2: Experimental setup of the photoemission experiment at the VUV–FEL monochromator beamline PG2 with photoelectron analyzer (multichannel electron detection) and high speed current–to–voltage converter (sample current detection) (from [155]).

toemission spectra were taken with a SPECS PHOIBOS 150 analyzer that was equipped with a Basler A102f 2D–CCD camera [Fig. 7.2(right)], while the sample current was simultaneously measured with a Femto DHPCA–100 ultrafast current–to–voltage converter [Fig. 7.2(left)]. In order to correlate the datasets with other machine parameters such as the intensity in front of the monochromator or the photon energy, the HASYLAB data acquisition system DOOCS was used.

During our measurements, which were one of the first user experiments at the newly commissioned VUV–FEL in 2005, single photon pulses could be combined in bunch trains of 1 to 20 pulses (final setup: 7200 pulses per bunch train) with a pulse separation of about 1 μs and a bunch train repetition rate of 2 Hz (final setup: 10 Hz). These parameters allow two different intensity dependent measurement methods:

- multi–bunch mode with more than one photon pulse per bunch train and
- single–bunch mode.

Since the detection system consisting of multi–channel–plate (MCP), phosphorous screen and CCD camera, is not fast enough to resolve electrons from different pulses of the same bunch train (in particular the CCD camera does not provide the needed shutter times and repetition rates), in multi–bunch mode an ARPES spectrum is generated by a superposition of photoelectrons, originating from various photon pulses with different intensities. Therefore, it cannot directly be assigned to one pulse intensity. Even though only the maximum

intensity can be controlled, e.g., by adjustments of the beamline monochromator slit (or a gas absorber in the final setup), higher count rates by a factor of 20 (final setup: 7200) in comparison to the single–bunch mode can be achieved.

In the single–bunch mode each photoemission spectrum can be correlated with the intensity dependent, integrated sample current, so that a sorting of the experimental datasets according to the photon intensities is possible. Summing up datasets with comparable FEL–intensities, photoemission intensity maps with decent statistics can be created. The intensity monitors of the FEL such as gas monitor detectors that are situated in front of the monochromator cannot be used for the intensity determination at PG2 since not only the intensity but also the spectral distribution varies from pule to pulse. Even at very high pulse intensity the intensity of the photon pulses after passing the monochromator can be very low if the adjusted monochromator energy and the spectral center of gravity do not match. Therefore, using the integrated sample current and the single–bunch mode, more accurate intensity dependent measurements than in the multi–bunch mode are possible.

During our measurements there was no calibrated intensity monitor at PG2 indicating the absolute photon numbers (after passing the monochromator). Therefore, the intensities of the ARPES spectra presented in this chapter are given in relative units with respect to the integrated sample current. It should be mentioned that the measured integrated sample current may not be directly proportional to the photon intensity. As due to the high intensity in a very short time duration photoelectrons have the ability to reenter the sample directly after the photoemission process the measured sample current may be an underestimation of the real photon intensities. A voltage between sample and analyzer could reduce this effect, but also affects the photoemission spectrum if used during the ARPES measurements. Assuming a pulse energy of $1 - 10$ μJ ($h\nu \approx 38.5$ eV) and an effective intensity loss due to the monochromator of about two orders of magnitude [156], the pulse intensity can roughly be estimated to about 10^9 to 10^{10} photons/pulse.

Our ARPES measurements at FLASH were performed with photon energies of $h\nu \approx 38.32$ eV and $h\nu \approx 38.80$ eV for valence band measurements and a total energy resolution of $\Delta E \leq 1$ eV, and with the third FEL–harmonic of $h\nu \approx 116.35$ eV for core level measurements with $\Delta E \leq 0.5$ eV. The photoemission chamber and the sample were aligned with respect to the FEL–beam by using a phosphorous screen with cross hair to image the beam position of the VUV–FEL. The $TiTe_2$ crystals that were used for our experiments were attached to a sample holder with silver-filled epoxy resin. By cleaving them in the UHV system at a base pressure in the 10^{-10} mbar range a clean (0001) surface was obtained.

7.3 Results and discussion

The realization of ARPES at an FEL offers a variety of novel experiments such as described in the previous section 7.1. However, the peak brilliance of the FEL radiation is several orders of magnitude higher than at conventional synchrotron radiation sources such that radiation damages or small spectral shifts or broadening are likely to occur. Therefore, it has to be checked if performing ARPES at an FEL is possible at all. In particular, this leads to two questions that will be investigated in the following: Is there radiation damage on the samples after illumination with FEL radiation? Are there any high–intensity effects on the photoemission spectra caused by significant Coulomb interaction between the photoemitted electrons?

7.3.1 Radiation damage

In order to investigate possible radiation damage on our samples, the $TiTe_2$ crystals were illuminated by the zero order FEL radiation with an energy of about $1 - 10$ μJ per pulse for several hours at beamline PG2. As shown in Fig. 7.3, for some samples we observed a damaging of the crystal surface that shows a pattern of identically oriented triangle structures. Reflecting the hexagonal crystal symmetry of TMDCs, these structures were possibly created by melting and recrystallization of the crystal surface. Since the surface is only damaged locally and in particular visible along cracks or step edges (see Fig. 7.3), it may be concluded that radiation damage mainly occurs on sample areas with surface defects such as lattice defects or inhomogeneities. However, during the photoemission

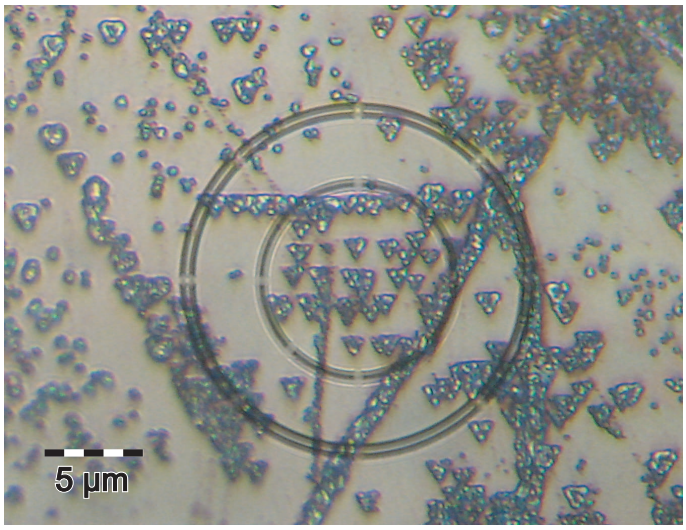

Figure 7.3: Crystal surface after illumination with zero–order FEL radiation for several hours with an energy of $1 - 10$ μJ per pulse (the black ring in the center of the image is part of the ocular of the microscope) [157].

measurements that are performed with monochromatized FEL radiation leading to lower intensity in comparison to zero order radiation, radiation damage of the crystal surfaces was not observed. Therefore, ARPES measurements with $TiTe_2$ crystals seem to be possible at the VUV–FEL using monochromatized radiation as it was used for the photoemission measurements presented in the following.

7.3.2 High–intensity effects

The possible influence of the highly intense FEL radiation on the photoemission spectra was investigated by intensity dependent ARPES measurements. In Fig. 7.4(top) we show ARPES spectra of $TiTe_2$ as gray scale images and angle–integrated spectra. The measurements were performed in multi–bunch mode of the VUV–FEL with about 20 photon pulses per bunch train. The maximum light intensity on the sample was controlled by setting the monochromator slit width between 32 μm and 72 μm. In the spectrum with the lowest intensity ($d = 32$ μm) three bands with different binding energies at the Γ(A)–point ($\Theta = 0°$) of about 0 eV (solid, red line), 2 eV (dashed, blue line), and 4 eV (dashed–dotted, green line) can be identified. In addition there is a weak signature of the Fermi edge (dashed, gray circle) at $E - E_F \approx 0$ eV. Comparing the spectra with the result of band structure

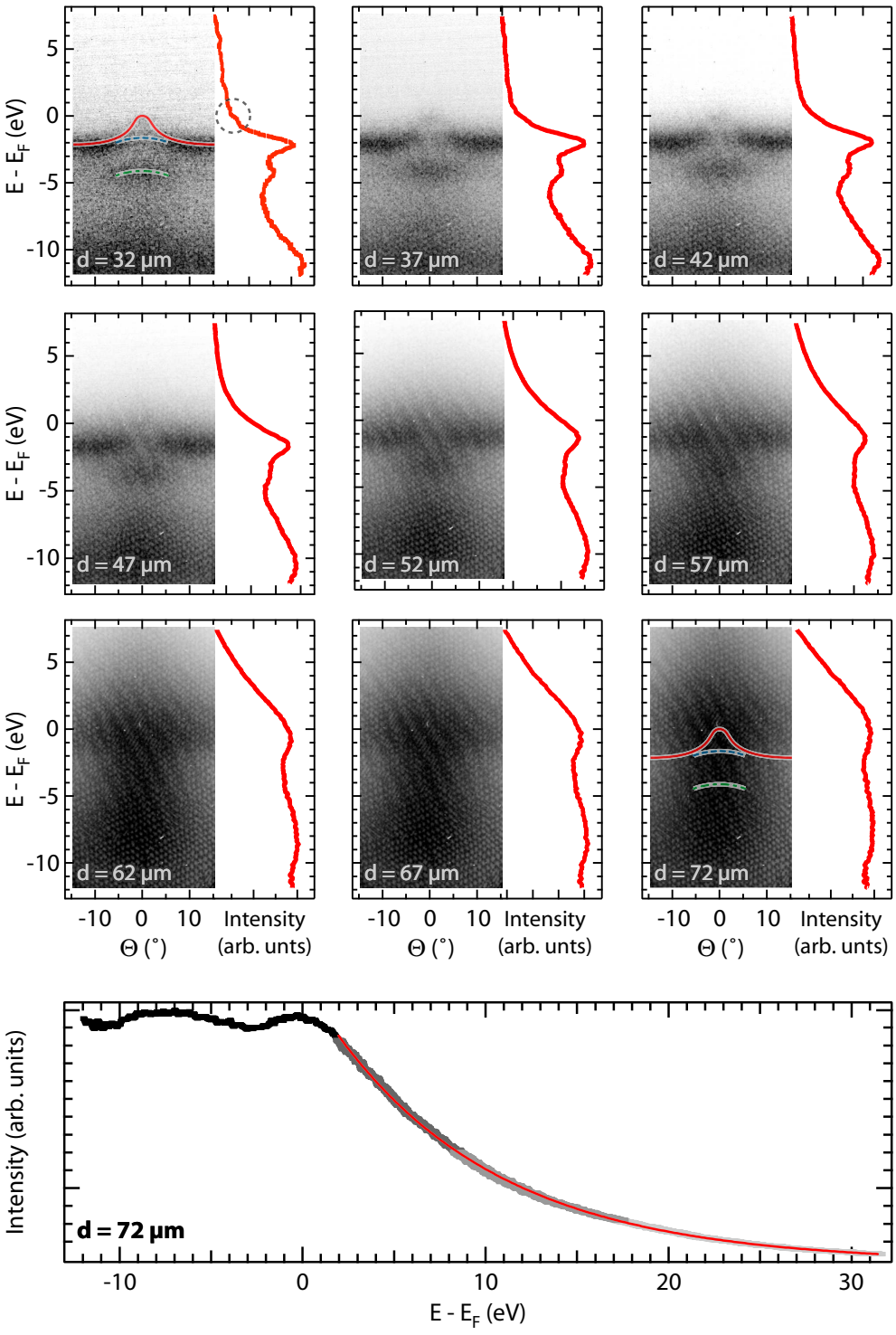

Figure 7.4: Top: Angle–resolved photoelectron valence band spectra (hν = 38.32 eV) of $TiTe_2$, taken in multi–bunch mode of the VUV–FEL with different monochromator exit slit widths d, illustrated as gray scale images (black indicates high intensity) and angle–integrated spectra (red lines). Bottom: For the widest slit width of d = 72 μm four angle–integrated spectra up to $E - E_F \approx 32$ eV are plotted (black to light gray) with exponential fit (red line) of the drop–off.

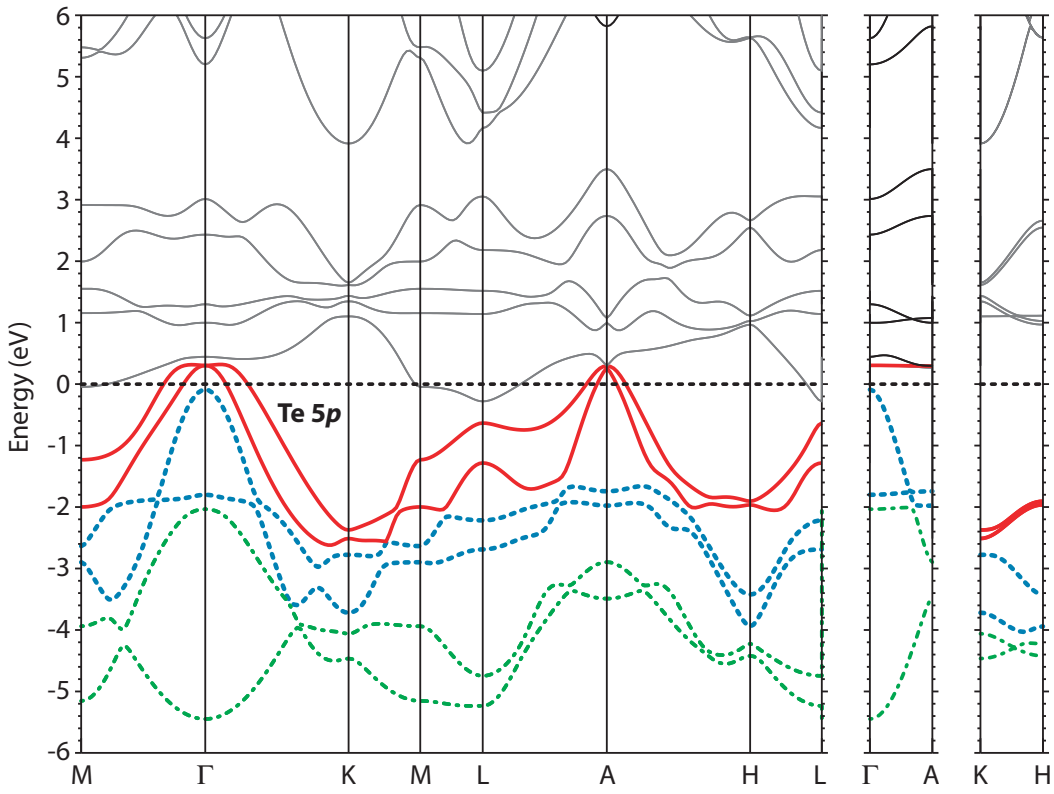

Figure 7.5: Calculated band structure of $TiTe_2$ along certain high–symmetry directions (from Ref. [158]). The mainly Te 5*p* derived bands are indicated as solid red, dashed blue, and dashed–dotted green lines.

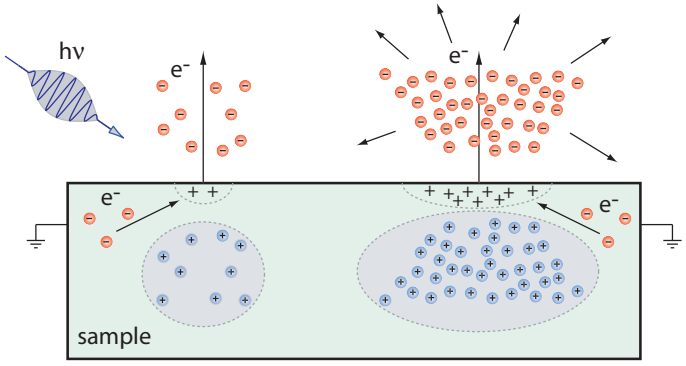

Figure 7.6: Illustration of space– and mirror–charge effects at low (left) and at high (right) electron densities. While the electrons are accelerated in different directions by repulsive Coulomb interactions between each other, the mirror charges attract the electrons towards the sample. Photoholes at the surface are compensated by grounding.

calculations (Fig. 7.5), there is a good agreement with the mainly Te $5p$ derived bands around the A–point.

With increasing light intensity, two changes can be observed in the spectra: a strong broadening of the spectral features and a shift towards lower binding energies. For example, at $d = 57$ μm the different bands can hardly be separated and almost no dispersion can be observed. In addition the spectrum is shifted to lower binding energies by more than 1 eV. In order to cover a wider energy range towards higher kinetic energies, in Fig. 7.4(bottom) four angle–integrated spectra for $d = 72$ μm are combined (gray curves). The resulting spectrum shows a drop–off with very slowly decreasing intensity to higher kinetic energies that can be fit well by an exponentially decaying fit function (red line: $I \propto e^{-E/\epsilon}$, $\epsilon \approx 9.1$ eV). Electrons with energies of more than $E - E_F = +30$ eV can be detected.

At the VUV–FEL the photoelectron density is much higher than at third generation synchrotron sources due to its high photon pulse intensities and the very short pulse durations. Therefore, Coulomb interactions between emitted photoelectrons cannot be neglected. In particular, the Coulomb interactions may affect the photoelectron spectra in two different ways: by space–charge effects resulting from photoelectrons interacting with each other and by mirror–charge effects resulting from the photoelectrons interacting with their mirror charges in the sample (Fig. 7.6). While the electrons are accelerated in different directions by repulsive Coulomb interactions between each other, the mirror charges attract the electrons towards the sample.

Performing photoelectron spectroscopy at a third generation synchrotron facility, Zhou et al. [159] found a linear dependence on the number of photoelectrons (for 60 ps synchrotron pulse duration) of both the energy shift and the energy broadening. They did not observe any interactions of successive photoelectron bunches that were emitted with a time separation of 2 ns (synchrotron operated at 500 MHz). A quantitative analysis including numerical simulations resulted in an energy broadening of the order of 10 μeV per electron and mm^2 (up to 2000 electrons per synchrotron radiation pulse) and a similar but slightly weaker energy shift for electron energies of about 30 eV (electrons emitted from the Fermi level), both decreasing for electrons with lower energies. The simulations are based on a Monte–Carlo model, analyzing the interaction of randomly generated test electrons with a number of 1 to 10000 interaction electrons. The test electrons are emitted perpendicular to the sample surface (to ensure the detection in the small acceptance angle of an electron energy analyzer) with random start positions (in the illuminated sample area) and times (during the photon pulse duration of 60 ps), but with predefined kinetic energy (up to the energy of electrons emitted from the Fermi level), and are influenced by the Coulomb forces of the interaction electrons. These are randomly generated in position, energy, and time, and move independently along straight lines, depending on their start parameters. The simulation results indicate that both space and mirror–charge effects have to be taken into account to reproduce their intensity dependent photoemission measurements ($h\nu = 34$ eV).

In contrast, Passlack et al. [160] performed photoemission using a low repetition, high intensity (nearly 10^5 electrons/pulse) femtosecond laser source with a very low photon energy of $h\nu = 2 \times 3.1$ eV (2PPE: two photon photoemission). They did not find any hint for mirror–charge effects in their experiments. Observing an energy broadening proportional to the square root of the electron number with about 275 meV at 10^5 photoelectrons/pulse, no indication of significant energy shifts were found (a shift in the order of 20 meV towards lower binding energies at about 10^5 photoelectrons/pulse is attributed to momentum blurring in their spectra). Simulations that are based on a mean–field model, originally

invented for short pulsed (pulse duration in the fs region), high energy ($E_{kin} \approx 30$ keV) electron packets [161], are in good agreement with their measurements. The model reduces the interaction electron cloud to a disk, moving with a constant mean kinetic energy perpendicular to the surface, neglecting electron–electron interaction in the disc. Therefore, no energy shift but only energy broadening occurs, described by [160]:

$$\Delta E_{mean}(eV) \approx 0.001477 \cdot \sqrt{\frac{N \cdot E_{kin}(eV)}{r_0(mm)}} \,, \tag{7.1}$$

where N is the number of photoelectrons, E_{kin} is the mean kinetic electron energy in eV, and r_0 is the radius of the emission area in mm.

While the models of Passlack et al. [160] and Zhou et al. [159] are roughly comparable for energy broadening in the range of about 10^5 photoelectrons per pulse and mm^2 spot area at kinetic electron energies of about 30 eV – such as used in our measurements at FLASH – they strongly differ for higher electron densities. In particular with respect to the energy shift, which is neglected by Passlack et al. [160], both models differ significantly, probably due to the much shorter pulse durations of the laser system in comparison to traditional synchrotron radiation. It should be mentioned that the assumption of a mean kinetic electron energy in the model of Passlack et al. [160] seems to be a useful approximation only for a narrow energy window (e.g., E_{kin} = 0..1 eV), such as found in photoemission experiments with small photon energies. Applying higher photon energies, a larger energy dispersion results, leading to an increased elongation of the emitted photoelectron cloud so that a mean field may not describe the Coulomb interactions of the photoelectrons well.

Measuring angle–resolved valence band spectra of $TiTe_2$ in single–bunch mode on a second sample at the VUV–FEL ($h\nu$ = 38.80 eV) with a monochromator exit slit width of $d = 52$ μm, and sorting them by the integrated sample current afterwards, we created six different ARPES maps with decent statistics [Fig. 7.7(top)] and compared the results to both theoretical models. The pulse intensity from the first to the last intensity sorted map covers at least one order of magnitude (see section 7.2). Similar to the measurements in multi–bunch mode the single–bunch ARPES measurements show a strong broadening of the spectral features accompanied by a loss in dispersion and an energy shift towards lower binding energies. As directly observable in the ARPES gray scale images and the adjacent angle integrated spectra (red lines), with increasing pulse intensities the Te 5p derived bands are shifted to lower binding energies in the range of several eV. Comparing, e.g., the spectrum with the lowest FEL–intensity ($I = I_0$) to the spectrum with a five times higher intensity ($I = 5 \cdot I_0$) the energy broadened Te 5p peak is shifted by about 3 eV almost completely above the Fermi level so that momentum blurring cannot explain the large shift.

Fitting the Te 5p peaks in the sum spectra by a gaussian and its low energy drop–off by a sigmoid function (which appears to be a better approximation for the higher intensity case), a rough approximation of the peak shift and broadening can be derived [Fig. 7.7(bottom)]. If the resulting curves are fit linearly, slopes of about 1 eV/I_0 for the energy shift and width, respectively, can be estimated. In comparison to the calculations of Passlack et al. [160] and Zhou et al. [159], an electron density of $I_0 \approx 10^5$ electrons per pulse and mm^2 during our measurements seems to be adequate, in rough agreement with both models, except for energy shifts that are not described by Passlack et al. [160].

However, an electron density of $I_0 \approx 10^5$ electrons per pulse and mm^2 seems to be relatively small with respect to the highly intense photon pulses at FLASH. Using the

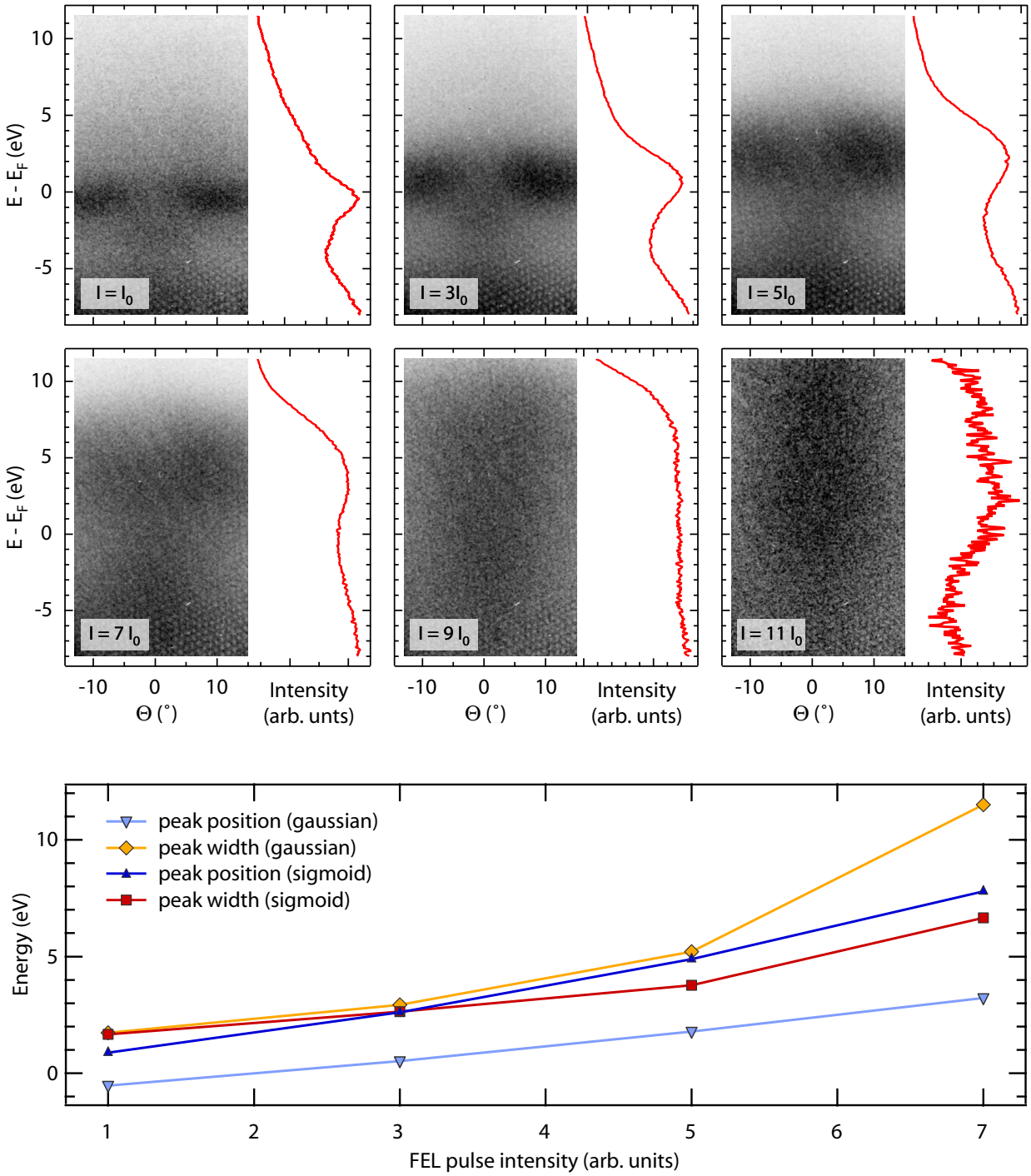

Figure 7.7: Top: Angle–resolved photoelectron valence band spectra of $TiTe_2$, taken in single–bunch mode of the VUV–FEL ($h\nu = 38.80$ eV) with a monochromator slit width of $d = 52$ μm. The spectra are sorted by intensity using the sample current signal. The ARPES measurements are illustrated as gray scale images (black indicates high intensity) and angle–integrated spectra (red lines). Bottom: Position and width of the Te $5p$ peak and drop–off, fit by a gaussian and a sigmoid function, respectively.

photon pulse energy in front of the monochromator of about $1 - 10$ μJ ($h\nu = 38.5$ eV), and assuming an effective transmission through the monochromator of about 1% [156], the intensity of the most intense photon pulses during our measurements with a monochromator exit slit width of $d = 52$ μm (open exit slit: $d = 500$ μm) can be estimated to about 10^8 – 10^9 photons per pulse – about 10^5 – 10^6 times higher than delivered by a third generation synchrotron radiation source. Taking a photoemission cross section of about 10% and the refocused FEL light spot size of about 300×300 μm^2 during our measurements into account, the electron density is roughly $I_0 \approx 10^8$ electrons per photon pulse and mm^2, which is three orders of magnitude larger than estimated above. However, only a minority of photon pulses preserve their high intensity while passing the monochromator. The reason might be the large spectral shift between different FEL–pulses (about 0.5 % of the nominal wavelength [162]) exceeding the spectral resolution of the monochromator. If the selected photon energy of the monochromator does not equal the energy of a photon pulse, the pulse intensity on the sample is much lower than in front of the monochromator, so that the number of photon pulses towards higher intensities should be drastically reduced. Therefore, assuming a continuously decreasing number of photon pulses with the pulse intensity, a photoemission spectrum measured in multi–bunch mode might be approximated by the superposition of differently shifted and broadened single spectra, each created by photon pulses with different intensity.

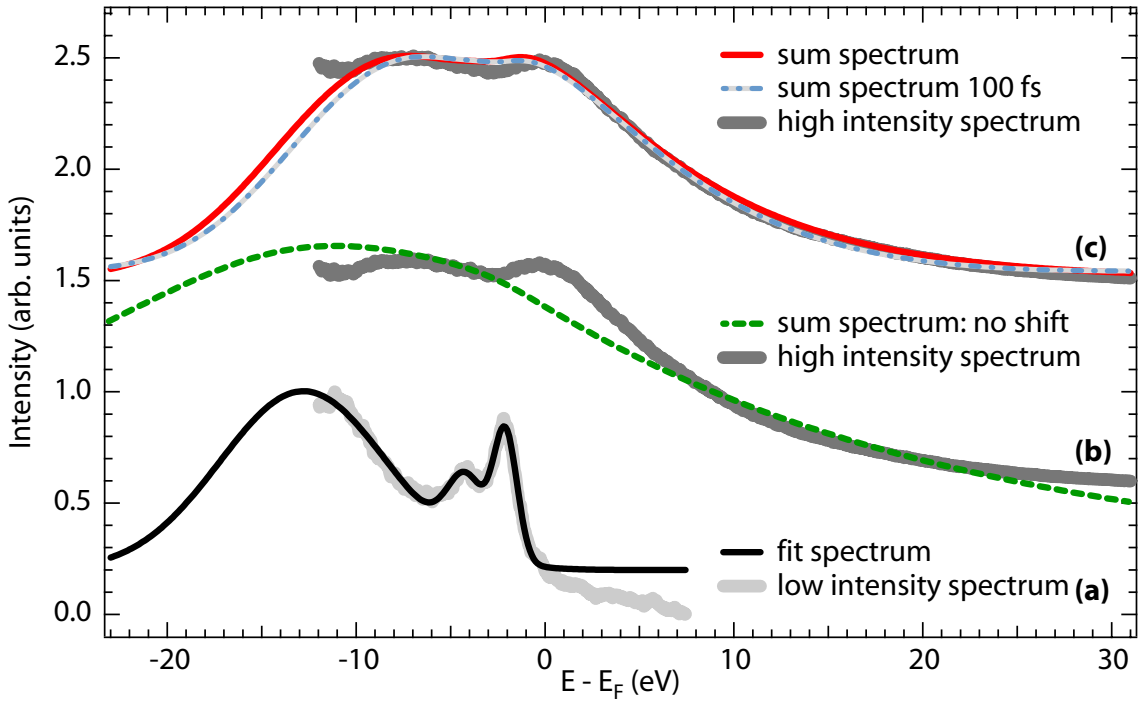

Figure 7.8: (a) Low intensity photoemission spectrum, measured in multi–bunch mode at small monochromator slit width d = 32 μm (light gray line) and fit spectrum (black line), consisting of three Gaussians. (c) The high intensity photoemission spectrum (dark gray line), measured at large monochromator slit width d = 72 μm, is fit by a superposition of the shifted and broadened low intensity fit spectrum, applying a linear relation between peak shift and broadening (red line) and the simulation results of equation (7.3) and (7.4). (b) Fit result, neglecting peak shifting (green, dashed line).

In order to test this assumption and the models of Zhou et al. [159] and Passlack et al. [160], we approximated the high intensity multi–bunch photoemission spectrum from Fig. 7.4(bottom) [also shown in Fig. 7.8(dark gray line)] by a superposition of differently shifted and broadened "base spectra". A "base spectrum" was created by fitting the low intensity photoemission spectrum from Fig. 7.4(d = 32 μm) [see also Fig. 7.8(light gray line)], measured at small monochromator slit width, by three Gaussians [Fig. 7.8(black line)], assuming only low Coulomb interactions due to the mainly low photon pulse intensity. Describing the number of photons per pulse after passing a narrow–band monochromator at FLASH by an exponential decay towards higher pulse intensities [162, 163] and a linear dependence between the number of photons per pulse after the monochromator N_{ph} and the number of emitted photoelectrons, a superposed multi–bunch photoemission spectrum $I_{phot}(E)$ can be described by:

$$I_{phot}(E) \propto \int_0^\infty N_{ph} \cdot e^{-\frac{N_{ph}}{\langle N_{ph}\rangle}} \cdot \sum_{i=1}^{3} \frac{1}{\sqrt{2\pi}\sigma_i(N_{ph})}\, e^{-\frac{(E-\mu_i(N_{ph}))^2}{2\sigma_i^2(N_{ph})}}\, dN_{ph} \ , \tag{7.2}$$

with the mean photon number after the monochromator $\langle N_{ph}\rangle$. The peak positions of the three Gaussian fit peaks $\mu_i(N_{ph}) = \mu_{0,i} + \Delta E_{shift}(N_{ph})$ consist of the unshifted peak positions $\mu_{0,i}$ and a photon density dependent peak shift $\Delta E_{shift}(N_{ph})$, while the peak widths $\sigma_i(N_{ph}) = \sigma_{0,i} + \Delta E_{broad}(N_{ph})$ consist of the intrinsic peak widths $\sigma_{0,i}$ and an additional photon density dependent peak broadening $\Delta E_{broad}(N_{ph})$. Assuming additionally a linear dependence between the photoelectron density and the peak shifting and broadening, such as derived by Zhou et al. [159], the slowly descending drop–off as well as the peak positions in the high intensity multi–bunch photoemission spectrum [Fig. 7.8(dark gray line)] can be fit well (Fig. 7.8(c), red line). The fit parameters are the exponential decay constant $\langle \Delta E_{shift}(N_{ph})\rangle \propto \langle N_{ph}\rangle$ that describes the mean energy shift, and the ratio between peak broadening and shift $\eta_{lin} = \Delta E_{broad}(N_{ph})/\Delta E_{shift}(N_{ph})$, quantitatively resulting in $\langle \Delta E_{shift}(N_{ph})\rangle \approx 4.7$ eV and $\eta_{lin} \approx 0.31$. In contrast to that, neglecting peak shifts a slowly descending drop–off, but no shifting in the superposed peak (see Fig. 7.8(b), green, dashed line) can be achieved, contradictory to our experimental results.

However, even though our measurements at high photon pulse intensities seem to be in fairly good agreement with the model of Zhou et al. [159] and the mean energy shift of about 5 eV leads to a reasonable mean photoelectron number in the range of 10^5 electrons/pulse, the ratios between peak broadening and shift only correspond very roughly. Since our fit results indicate larger energy shifts than energy broadening ($\eta_{lin} \approx 0.3$), after Zhou et al. [159] both are in the same order of magnitude, slightly dominated by peak broadening. Simulating the Coulomb interactions with the model of Zhou et al. [159] for shorter photon pulse lengths of 100 fs at FLASH (in comparison to 60 ps at the ALS), the relation between electron density N_{el} and peak shifting $\Delta E_{shift,100fs}(N_{el})$ seems to remain highly linear [164]:

$$\Delta E_{shift,100fs}(N_{el}) \approx 4.5 \cdot 10^{-5} \cdot N_{el} \ , \tag{7.3}$$

while the peak broadening deviates from linear dependence and can be approximated by [164]:

$$\Delta E_{broaden,100fs}(N_{el}) \approx 5.2 \cdot 10^{-5} \cdot N_{el}^{0.76} \ . \tag{7.4}$$

Inserting these results in equation (7.2), the fit results of the high intensity multi–bunch photoemission spectrum are similar to the fit results with a linear peak broadening

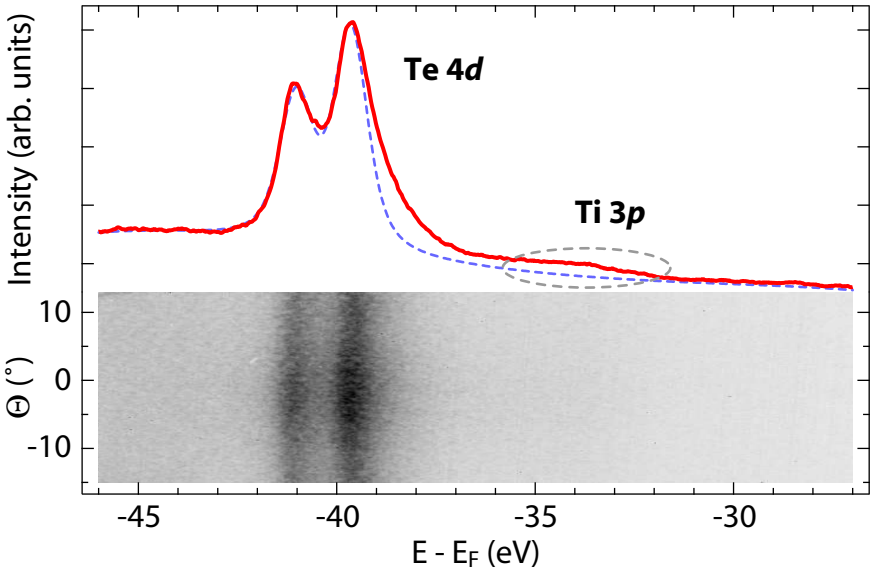

Figure 7.9: Photoemission spectrum (top: red line, and bottom: gray scale image) of the Te 4*d* core level of $TiTe_2$, measured with the third harmonic of the VUV–FEL ($h\nu$ = 116.35 eV, d = 77 μm, multi–bunch mode), and fit result (dashed, blue line) using two Voigt profiles. Additionally, the Ti 3*p* core level at $E - E_F \approx 33$ eV is observable (dashed ellipse).

[Fig. 7.8(blue, dashed–dotted line)], leading to a mean photoelectron number of about $1.0 \cdot 10^5$ electrons per photon pulse. Since only one fit parameter in equation (7.2) remains, the adjusted calculation results allow to estimate the mean photoelectron number much more precisely. Using the results for the photon distribution after the monochromator and simulating the Coulomb interactions of a full photoelectron spectrum at high electron densities, in the future it should become possible to uncover the spectral features of a high intensity photoelectron spectrum. This would allow to extract the unbroadened and unshifted spectrum so that the electronic structure under highly intense electromagnetic radiation becomes observable.

In addition to valence bands, the Te 4*d* core levels could be investigated, using the third harmonic of the FEL ($h\nu$ = 116.35 eV, d = 77 μm, multi–bunch mode). As illustrated in Fig. 7.9, the Te $4d_{3/2}$ and Te $4d_{5/2}$ spin orbit splitting is clearly resolved. But even though the intensity of the third harmonic is only about 0.1 to 1% of the first harmonic [165], the lower binding energy Te $4d_{5/2}$ peak decreases very slowly, observable by the large difference between a peak fit with two Voigt profiles and the measured sum spectrum in Fig. 7.9(top). Similar to the case of the valence band spectra this indicates Coulomb shifting and broadening due to the high electron numbers, but with an increased exponential decay (ϵ = 1 eV). It should be mentioned that the increased intensity at $E - E_F \approx 33.5$ eV (dashed ellipse) can be attributed to the Ti 3*p* core levels.

Monitoring the absolute intensity after the monochromator, in future experiments a more detailed study of the intensity dependence of core level line shapes and positions should lead to more quantitative results for the Coulomb interaction in high intensity photoemission experiments.

7.4 Conclusions

In summary, even at high photon densities [$\approx 10^6$ photons/(pulse mm^2)] with very short pulse lengths ($\Delta t \approx 100$ fs) ARPES can be performed. For measurements with monochromator radiation no radiation damage on $TiTe_2$ could be observed. Only after illumination with zero order light for several hours some samples showed radiation induced defects at local points of the interface. However, the crystallinity of the whole surface was not affected. Performing photoemission with higher photon densities in the range of $\approx 10^6$ to 10^7 photons/(pulse mm^2), strong energy shifts and broadenings in the range of several eV was observed.

8 Conclusions and perspectives

In this thesis the electronic structure of the layered, incommensurate transition metal dichalcogenide (TMDC) misfit compounds $(PbS)_{1.13}TaS_2$, $(PbS)_{1.14}NbS_2$, $(PbS)_{1.14}(NbS_2)_3$, $(SnS)_{1.17}NbS_2$, and $(BiS)_{1.11}NbS_2$ was investigated. These compounds show a remarkable stability although their incommensurability, the alternation of different layers, and the occurrence of monochalcogen bilayers all act against a low total energy. Performing angle–resolved photoelectron spectroscopy (ARPES) and photoelectron microscopy (PEM), the interlayer bonding was studied in detail. It turned out that the origin of the bonding – the occurrence of a metal–cross substitution induced charge transfer between the layers – could only be understood if the results of the angularly resolved and spatially resolved experiments were combined. In particular, the following topics regarding the stability of TMDC misfit compounds were clarified in this thesis:

- In order to study the interlayer bonding in the TMDC misfit compounds, the electronic band structure in the direction perpendicular to the layers was traced by ARPES measurements with varying photon energy. While strong matrix element effects obscured the band structure, a more detailed analysis at different binding energies and momentum values indicated that no band dispersion perpendicular to the layers occurs. Therefore, covalent bonding between adjacent layers appears to be weak.

- By investigating the electronic conduction band structure in more detail, a clear separation of the relevant bands near the Fermi energy, i.e., the transition metal derived *d*–type bands and the mainly sulfur derived *p*–type bands, was observed, in contrast to pristine TMDC compounds. In all compounds this p/d–gap amounts to about 0.5 eV, similar to intercalated TMDC compounds. Furthermore, the Fermi surfaces of the different compounds could be determined with high accuracy. This allowed the direct determination of the band filling and led to much higher accuracy than in other, indirect methods such as Hall effect measurements. The underlying charge transfer could be quantified to about 0.2..0.4 electrons per transition metal atom, increasing from Ta to the Nb compounds and from Sn over the Pb to the Bi compounds. Therefore, a significant ionic contribution to the interlayer bonding in the TMDC misfit compounds has to be taken into account.

- In the investigations of the full electronic valence band structure signatures of both subsystems were observed. Even though there is no translational symmetry in the incommensurate direction, in particular at the Γ point and at low momentum values, there was a highly symmetric band dispersion. However, at higher momentum values into the incommensurate direction where a large misfit between the Brillouin zone boundaries of both subsystems occurs, a deviation from a pure superposition of the band structure of both subsystems was found. In addition, in the TMDC dominated Fermi surfaces backfolding at the Brillouin zone boundaries of both subsystems appears. Since the misfit only weakly affects the electronic structure of the subsystems, the interlayer interaction seems to be weak.

- By photoemission microscopy measurements on the TMCD misfit compound $(PbS)_{1.13}TaS_2$ the origin of the additional conduction band electrons was investigated. Since PbS is a semiconductor and the band structure measurements of the

misfit compound indicate fully occupied PbS derived bands, the increased filling of the TaS_2 derived conduction band cannot originate from the semiconducting subsystem. The spatially resolved photoemission spectra directly showed the substitution of Ta atoms into the PbS layers as well as the substitution of Pb atoms into the TaS_2 layers, that was roughly quantified to about 5% - 20%. This metal cross–substitution can explain an effective charge transfer of about 0.1 electrons per Ta atom and does not need a depopulation of the PbS derived bands which is in good agreement with the electronic band structure measurements.

The results of the ARPES and PEM measurements clearly indicate the need for a combination of momentum and spatial resolution in photoelectron spectroscopy experiments. However, there is currently no experimental technique available which allows the measurement of the momentum resolved electronic structure with simultaneous high spatial resolution. Therefore, band structure investigations of nanostructured surfaces or heterostructures can only be performed reliably if the band structure of the different subsystems can clearly be separated such as on the TMDC misfit compounds.

During this thesis a novel spatially resolved ARPES experiment was developed (see Fig. 8.1). The instrument consists of a SPECS PHOIBOS 150 photoelectron analyzer with a two-dimensional CCD detector and a reflective photon sieve as optical device. This novel type of diffraction optics allows focusing synchrotron radiation with suppressed side lobes and reduced background. The different aspects regarding the design and test of the reflective photon sieve as well as the first spatially resolved photoelectron measurements that were treated in this thesis are:

- The photon sieve as a new type of diffraction optics was designed in a reflective geometry in order to separate the various diffraction orders. Thus, the implementation of a central stop – an additional aperture that blocks the undiffracted light in a transmissive geometry but also increases the side lobe intensity – as well as volume diffraction effects, blurring the focal spot area, could be avoided. The diffraction structures were distributed according to an inverted Weber-type transmission window function. This leads to a suppression of the side lobe intensity by about three orders of magnitude and guarantees the electrical and thermal connection of the diffraction structures in order to dissipate the heat load and avoid a charging of the optical device. The reflective photon sieve was produced by a commercial lithographic mask manufacturer with a minimum structure size of 474 nm for the use of the third diffraction order at a photon energy of $h\nu = 100$ eV.

- The reflective photon sieve was characterized in comparison to a reflective zone plate by employing the Fresnel–Kirchhoff diffraction formula. The intensity distribution in the focal plane shows an increase of the theoretical signal–to–background ratio of about three orders of magnitude in comparison to the zone plate. Additionally, the diameter of the point spread function was calculated to be about 300 nm, leading to a focal spot diameter of about 340 nm if used at a coherent light source with a source diameter of 20 μm.

- The photon sieve was tested at the synchrotron beamline BW3 at HASYLAB. As the coherence of this beamline is rather low, only a low signal–to–background ratio could be observed. However, a focal spot diameter of about 700 nm was measured in fairly good agreement with the simulations.

- The new spatially and angularly resolved photoelectron spectroscopy experiment was tested at the HASYLAB synchrotron beamline BW3 by analyzing the Pb $5d$ and Ta $4f$ core level peaks of the TMDC misfit compound $(PbS)_{1.13}TaS_2$. The core level peaks could be identified as originating from a PbS terminated surface region and the working principle of the instrument could be demonstrated. In order to achieve higher count rates, further spatially resolved experiments are planned to be performed at highly coherent and brilliant synchrotron radiation sources such as PETRA III or the VUV–FEL at HASYLAB.

- In order to study the influence of highly intense, ultra short pulsed FEL radiation on the photoemission process, ARPES measurements on $TiTe_2$ crystals at the monochromator beamline PG2 of the VUV–FEL at HASYLAB (now known as Free–Electron Laser in Hamburg: FLASH) were performed. Our intensity dependent measurements indicate that even at high photon densities [$\approx 10^6$ photons/(pulse mm^2)] and very short pulse lengths ($\Delta t \approx 100$ fs) ARPES experiments are in principle possible at the VUV–FEL. For measurements with monochromator radiation no radiation damage on $TiTe_2$ could be observed. Only after illumination with zero order light for several hours some samples showed radiation induced defects at local points of the interface. However, the crystallinity of the whole surface was not affected. By performing photoemission with higher photon densities in the range of $\approx 10^6$ to 10^7 photons/(pulse mm^2), strong energy shifts and broadenings in the range of several eV have been observed.

Even if photoemission at the VUV–FEL is a challenging task, the VUV–FEL offers the opportunity to perform a variety of novel types of experiments. Its high brilliance and the

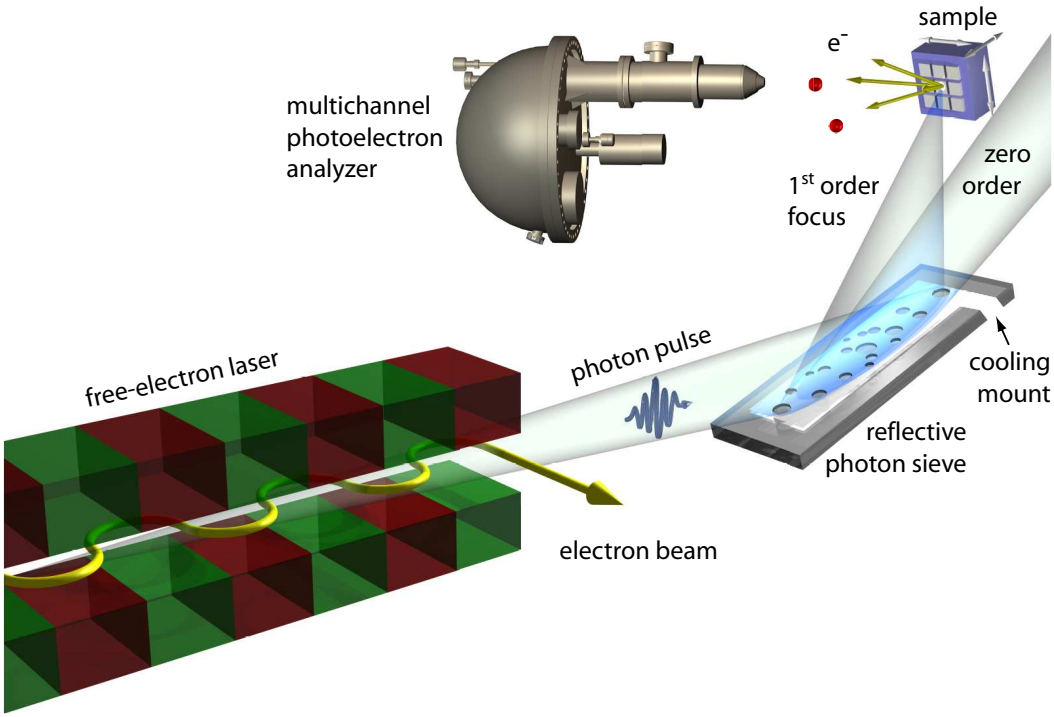

Figure 8.1: Illustration of a possible setup for a spatially resolved ARPES experiment at the VUV–FEL, employing an inverted reflective photon sieve as focusing device.

nearly total coherence are adequate for introducing an additional diffraction optics such as an inverted, reflective photon sieve into the FEL beam. Thus, photoelectron spectroscopy experiments with combined momentum and spatial resolution as illustrated in Fig. 8.1 can be carried out. These will allow local electronic structure investigations with spatial resolution in the 10 nm regime, momentum resolution of about 0.01Å^{-1}, energy resolution of about 1 meV, and time resolution of below 100 fs. Using the high resolution of such a nano–spectroscope, spatially inhomogeneous electronic states which, for example, occur in high temperature superconductors or colossal magneto resistance materials, but also dynamical processes such as surface reactions can be investigated. With the nano–spectroscope, it will be possible to gain much deeper insight into the properties of solids than feasible today.

9 Appendix

9.1 Integrated PC control of an experimental station at a synchrotron beamline

Angle resolved photoelectron spectroscopy experiments at synchrotron radiation facilities are performed to investigate the electronic structure of solids and allow measuring five–dimensional datasets $I(E, k_x, k_y, k_z)$ (see chapter 2). However, even with modern electron analyzers, equipped with 2D parallel detection units for simultaneous photoelectron energy and emission angle detection, data acquisition times can easily take several days. If, for example, the electronic structure in a full three–dimensional Brillouin zone is measured, equally spaced scanning of the parameter–space favors automatized, computer controlled experiments, in particular with respect to measurement accuracy and economy of time. On the other hand, for high resolution photoemission experiments or measurements including interactions with external apparatus such as additional light sources, cameras or shutters (e.g. knife edges for photon sieve photoemission) the standard photoemission measuring modes (see chapter 2.2) are not sufficient, so that flexible programming of measurement sequences with the controlling software is required.

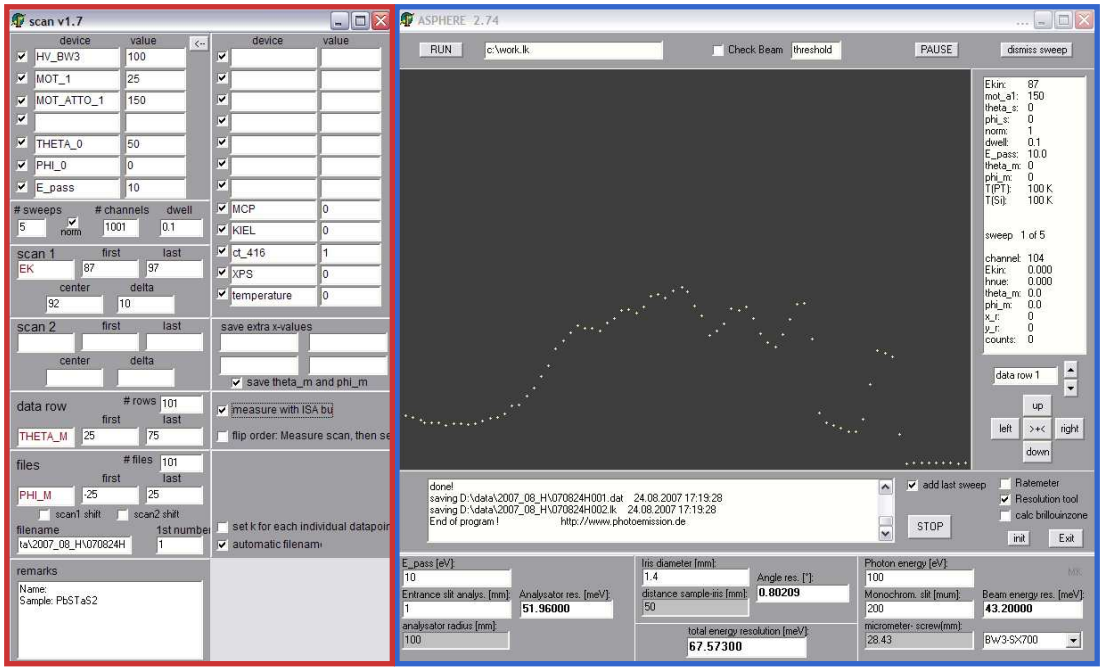

Figure 9.1: Measurement software ASPHERE (right, blue box) and user interface "scan" (left, red box) used for creating ASPHERE script files.

Therefore, we developed the measurement software ASPHERE [137] (see Fig. 9.1), capable of reading out and controlling all important instruments of our experimental stations at the synchrotron beamlines at HASYLAB. These are the photoelectron analyzer ASPHERE (Angular Spectrometer for Photoelectrons with High Energy Resolution, developed in Kiel), the monochromators at beamlines W3.2 (HONORMI) and BW3, up to eight stepper motors, three piezo driven actuators with position controlling fabricated by Klocke Nanomotors, and 12 UHV compatible piezo driven actuators fabricated by attocube systems. Furthermore, it is possible to read out the temperature of our sample cryostats

(PT–100 resistors and Si diodes) as well as to count TTL pulses if the computer is equipped with the ISA–bus based plugin counter boards with timer ct32 or ct416 [166]. Additionally, the execution of external programs is implemented, which is important for the data acquisition with a MCP/2D–delayline–detector unit, applied at the ASPHERE analyzer [167], or the framegrabbing with external CCD cameras.

A measurement campaign, consisting of a sequence of different measurement jobs, is controlled by a text based script file containing three types of commands, i.e., standard variables, action variables, and loops. While standard variables set internal software parameters such as network ports for the monochromator control, limits for the operating range of the stepper motors, or the pass energy of the photoelectron analyzer, action variables directly interact with the hardware. This can be, for example, the setting of a monochromator energy so that the monochromator and the undulator gap are moved, the direct movement of a stepper motor to a specific position, or the impression of voltages to the photoelectron analyzer and its lens system, necessary for measuring photoelectrons with a specific kinetic energy. For the different variables there are in general absolute and relative representations. Relative coordinates are particularly important if the commands are repeated in loops. In order to create the script files, the program "scan" (current version v1.7) can be used, in particular if standard measurement modes with up to three loop layers are needed. For more complex measurement campaigns, the script files created by "scan" (e.g., work.lk) can easily be modified and extended with a text editor or just be rewritten by using the ASPHERE syntax. All commands accepted by ASPHERE (current version v2.74) are listed in detail in the ASPHERE manual, saved as "manual.txt" in the ASPHERE program folder.

The script files can be executed by ASPHERE. In order to check if the script syntax is correct and the operating range of all devices is not exceeded during the planned measurement campaign, each script file is precompiled by ASPHERE before it is allowed to control the hardware. Only if this simulated measurement campaign does not show any errors, the measurement process will be started.

During the measurement process two file types are saved, i.e., the datafiles (*.dat) and the log–files (*.lk), each containing the current date, a capital letter (describing the current experiment: H: HONORMI, B: BW3, K: Kiel, P: photon sieve, or S: STM), and a unique number in the filename (e.g., "070824H001.dat" and "070824H001.lk"). A datafile contains columns with the different measurement values. These are all parameters, changed in the measurement campaign (e.g., stepper motor positions or the kinetic electron energy for each datapoint) as well as the measurement result (e.g., the photoelectron intensity). A log–file contains the syntax of the script file that controlled the measurement campaign and various additional information (e.g., time and duration of synchrotron beam losses), so that the correct work flow of a measurement campaign can be examined afterwards. Applying the remote control function of the Windows operating system, it is even possible to monitor or control the campaigns from outside a beamline via the internet so that access to the experimental parameters is possible anytime from anywhere.

Therefore, by using the script based measurement software ASPHERE it is possible to predefine complex measurement campaigns in which all important parameters of the (synchrotron) experiment can be controlled and logged by only one PC. This allows controlling interactions between all relevant experimental parameters, so that a variety of synchrotron and non–synchrotron experiments – such as diffraction experiments at photon sieves with visible laser light – can easily be performed.

References

[1] A. Einstein, Ann. d. Physik **17**, 132 (1905).

[2] W. E. Spicer, Phys. Rev. **112**, 114 (1958).

[3] P. J. Feibelman, D. E. Eastman, Phys. Rev. B **10**, 4932 (1974).

[4] L. Hedin, S. Lundqvist, Solid State Phys. **23**, 1 (1969).

[5] M. P. Seah, W. A. Dench, Phys. Rev. B **1**, 2 (1979).

[6] K. Siegbahn, Nobel Lecture (1981).

[7] H. P. Hughes, J. A. Scarfe, J. Phys.: Condens. Matter **8**, 1421 (1996).

[8] P. Aebi, J. Osterwalder, P. Schwaller, L. Schlapbach, M. Shimoda, T. Mochiku, K.Kadowaki, Phys. Rev. Lett. **72**, 2757 (1994).

[9] H. Hertz, Ann. Physik (Leipzig) **31**, 983 (1887).

[10] J. W. Zahlmann–Nowitzki, Diploma thesis, Institut für Experimentelle und Angewandte Physik (Universität Kiel), 1996.

[11] http://hasylab.desy.de/facilities/doris_iii/beamlines/bw3/index_eng.html.

[12] D. Attwood, *Soft X–rays and extreme ultraviolet radiation* (Cambridge University Press, Cambridge, 1999).

[13] http://www-als.lbl.gov/als/techspecs/bl7.0.1.html.

[14] U. Johansson, Ph.D. thesis, Department of Physics (Lund University, Sweden), 1997.

[15] R. L. Withers, J. A. Wilson, J. Phys. C **19**, 4809 (1986).

[16] K. Motizuki, in *Structural Phase Transitions in Layered Transition Metal Compounds*, edited by K. Motizuki (Reidel, Dordrecht, 1986).

[17] G. Allan, Phys. Rev. B **43**, 9594 (1991).

[18] W. Hoffmann, Z. Kristallogr. **92**, 161 (1935).

[19] H. Wiedemeier, F. J. Csillag, Z. Kristallogr. **149**, 17 (1979).

[20] H. Wiedemeier, H. G. Schnering, Z. Kristallogr. **156**, 143 (1981).

[21] Nimitz, in *Lanoldt-Börnstein* (Springer, Berlin, 1983), p. 17f.

[22] W. Albers, C. Haas, H. J. Vink, J. D. Wasscher, J. Appl. Phys. **10**, 2220 (1961).

[23] J. A. Leiro, K. Laajalehto, I. Kartio, M. H. Heinonen, Surf. Sci. **412/413**, (1998).

[24] J. A. Leiro, K. Laajalehto, M. S. Peltoniemi, M. Torhola, A. Szczerbakow, Surf. Interface Anal. **33**, 964 (2002).

[25] U. Becker, M. F. Hochella Jr., Geochim. Cosmochim. Acta **60**, 2413 (1996).

[26] J. Muscat, J. D. Gale, Geochim. Cosmochim. Acta **67**, 799 (2002).

[27] I.G. Batyrev, L. Kleinman, Phys. Rev. B **70**, 073310 (2004).

[28] A. A. Lazarides, C. B. Duke, A. Paton, Phys. Rev. B **52**, 14895 (1995).

[29] J.D. Levine, P. Mark, Phys. Rev. **144**, 751 (1965).

[30] T. Grandke, M. Cardona, Surf. Sci. **92**, 385 (1980).

[31] B. M. Trafas, I. M. Vitomirov, C. M. Aldao, Y. Gao, F. Xu, J. H. Weaver, Phys. Rev. B **39**, 3265 (1989).

[32] F. Cerrina, R. R. Daniels, V.Fano, Appl. Phys. Lett. **43**, 182 (1983).

[33] J. Wilson, A. Yoffe, Adv. Phys. **18**, 193 (1969).

[34] K. Rossnagel, Ph.D. thesis, Institut für Experimentelle und Angewandte Physik (Universität Kiel), 2001.

[35] J. Rouxel, in *Intercalated Layered Materials*, edited by F.A. Lévy (Reidel, Dordrecht, 1979), p. 201.

[36] R. B. Somoano, J. A. Woollam, in *Intercalated Layered Materials*, edited by F.A. Lévy (Reidel, Dordrecht, 1979), p. 307.

[37] W. Y. Liang, in *Intercalation in Layered Materials*, edited by M.S. Dresselhaus (Plenum, New York, 1986), p. 31.

[38] R. H. Friend, A. D. Yoffe, Adv. Phys. **36**, 1 (1987).

[39] A. R. Ubbelohde, in *Intercalated Layered Materials*, edited by F.A. Lévy (Reidel, Dordrecht, 1979), p. 1.

[40] H. I. Starnberg, H. E. Brauer, H. P. Hughes, Surf. Sci **377-379**, 828 (1997).

[41] A. R. Beal, in *Intercalated Layered Materials*, edited by F.A. Lévy (Reidel, Dordrecht, 1979), p. 251.

[42] P. Ganal, W. Olberding, T. Butz, G. Ouvrard, Solid State Ionics **59**, 313 (1993).

[43] M. S. Whittingham, Prog. Sol. St. Chem. **12**, 41 (1978).

[44] J. Wulff, A. Meetsma, R. J. Haange, J. L. de Boer, G. A. Wiegers, Synth. Metals **39**, 1 (1990).

[45] A. Lafond, C. Deudon, A. Meerschaut, A. Sulpice, Eur. J. Solid State Inorg. Chem. **31**, 967 (1994).

[46] J. Wulff, A. Meetsma, S. van Smaalen, R. J. Haange, J. L. de Boer, G. A. Wiegers, J. Solid State Chem. **84**, 118 (1990).

[47] G. A. Wiegers, A. Meetsma, R. J. Haange, S. van Smaalen, J. L. de Boer, A. Meerschaut, P. Rabu, J. Rouxel, Acta Crystallograph. **B46**, 324 (1990).

[48] A. Meerschaut, L. Guemas, C. Auriel, J. Rouxel, Eur. J. Solid State Inorg. Chem. **27**, 557 (1990).

[49] A. Meetsma, G.A. Wiegers, R. J. Haange, J. L. de Boer, Acta Crystallograph. **A45**, 285 (1989).

[50] G.A. Wiegers, A. Meetsma, R. J. Haange, J. L. de Boer, Mat. Res. Bull. **23**, 1551 (1988).

[51] S. van Smaalen, J. Phys. Condens. Matter **1**, 2791 (1989).

[52] S. Kuypers, G. van Tendeloo, J. van Landuyt, S. Amelinckx, Acta Crystallograph. **A45**, 291 (1989).

[53] Y. Gotoh, J. Akimoto, M. Goto, Y. Oosawa, M. Onoda , J. Solid State Chem. **116**, 61 (1995).

[54] A. Meetsma, G. A. Wiegers, R.J. Haange, J. L. de Boer, Acta Cryst. **C46**, 1598 (1990).

[55] C. H. Rüscher, C. Haas, S. van Smaalen, G. A. Wiegers, J. Phys.: Condens. Matter **6**, 2117 (1994).

[56] Y. Ren, J. Baas, A. Meetsma, L. de Boer, G. A. Wiegers, Acta Cryst. **B52**, 398 (1996).

[57] L. Cario, D. Johrendt, A. Lafond, C. Felser, A. Meerschaut, J. Rouxel, Phys. Rev. B **55**, 9409 (1995).

[58] Y. Ohno, Phys. Rev. B **44**, 1281 (1991).

[59] A. Santoni, G. Paolucci, G. Santoro, K. C. Princel, N. E. Christensen, Solid State Commun. **79**, 1081 (1991).

[60] A. R. H. F. Ettema, G. A. Wiegers, C. Haas, T. S. Turner, Surf. Sci. **269-270**, 1161 (1991).

[61] A. R. H. F. Ettema, C. Haas, J. Phys.: Condens. Matter **5**, 3817 (1993).

[62] A. R. H. F. Ettema, C. Haas, T. S. Turner, Phys. Rev. B **47**, 12794 (1993).

[63] C. M. Fang, A. R. H. F. Ettema, C. Haas, G. A. Wiegers, Phys. Rev. B **52**, 2336 (1995).

[64] J. Brandt, L. Kipp, M. Skibowski, E.E. Krasovskii, W. Schattke, E. Spiecker, C. Dieker, W. Jäger, Surf. Sci. **532-535**, 705 (2003).

[65] C. Auriel, A. Meerschaut, C. Deuden, G. A. Wiegers, J. Baas, J. Chen, P. Monceau, Eur. J. Solid State Inorg. Chem. **38**, 565 (1995).

[66] J. Muscat, C. Klauber, Surf. Sci **491**, 226 (2001).

[67] A. Santoni, G. Paolucci, G. Santoro, K. C. Princel, N. E. Christensen, J. Phys.: Condens. Matter **4**, 6759 (1992).

[68] J. Brandt, J. Kanzow, K. Rossnagel, L. Kipp, M. Skibowski, E.E. Krasovskii, W. Schattke, M. Traving, J. Stettner, W. Press, C. Dieker, W. Jäger, J. Electron Spectrosc. Relat. Phenom. **114-116**, 555 (2001).

[69] J. Brandt, Ph.D. thesis, Institut für Experimentelle und Angewandte Physik (Universität Kiel), 2003.

[70] Xian–Rong Huang, lauept 2.1 from http://www.ccp14.ac.uk/ccp/web-mirrors/xianrong-huang/.

[71] J. Voit, L. Perfetti, F. Zwick, H. Berger, G. Margaritondo, G. Grüner, H. Höchst, M. Grioni, Science **290**, 501 (2000).

[72] L. Perfetti, H. Berger, A. Reginelli, L. Degiorgi, H. Höchst, J. Voit, G. Margaritondo, M. Grioni, Phys. Rev. Lett. **87**, 216404 (2001).

[73] J. Schäfer, E. Rotenberg, S. D. Kevan, P. Blaha, R. Claessen, R E. Thorne, Phys. Rev. Lett. **87**, 196403 (2001).

[74] C. M. Fang, R. A. de Groot, G. A. Wiegers, C. Haas, J. Phys.: Condens. Matter **8**, 1663 (1996).

[75] C. M. Fang, S. van Smaalen, G. A. Wiegers, C. Haas, R. A. de Groot, J. Phys.: Condens. Matter **8**, 5367 (1996).

[76] L. Cario, J. Rouxel, A. Meerschaut, Y. Moëlo, B. Corraze and O. Chauvet, J. Phys.: Condens. Matter **11**, 2887 (1999).

[77] Y. Moëlo, A. Meerschaut, J. Rouxel, C. Auriel, Chem. Mater. **7**, 1759 (1995).

[78] A. Meerschaut, Y. Moëlo, L. Cario, A. Lafond,C. Deudon, Mol. Cryst. Liq. Cryst. **341**, l (2000).

[79] G.A. Wiegers, A. Meetsma, R. J. Haange, J. L. de Boer, Solid State Ionics **32/33**, 183 (1988).

[80] K. Matsuura, T. Wada, N. Suzuki, T. Nakamizo, S. Ikegawa, H. Yamauchi, S. Tanaka, Jpn. J. Appl. Phys. **29**, (1990).

[81] G. A. Wiegers, Prog. Solid State Chem. **24**, l (1996).

[82] http://www-als.lbl.gov/als/als_users_bl/7.0.1-Overview.pdf.

[83] T. Riedel, private communication.

[84] C. Kreis, Ph.D. thesis, Institut für Experimentelle und Angewandte Physik (Universität Kiel), 2002.

[85] E. Krasovskii, W. Schattke, Phys. Rev. B **63**, 235112 (2001).

[86] R. L. Barnett, A. Polkovnikov, E. Demler,W.-G. Yin, W. Ku, Phys. Rev. Lett. **96**, 026406 (2006).

[87] N. V. Smith, S. D. Kevan, F. J. DiSalvo, J. Phys. C: Solid State Phys. **18**, 3175 (1985).

[88] K. Rossnagel, O. Seifarth, L. Kipp, M. Skibowski, D. Voss, P. Krüger, A. Mazur, J. Pollmann, Phys. Rev. B **64**, 235119 (2001).

[89] J. Rouxel, A. Meerschaut, G. A. Wiegers, J. Alloys Compd. **229**, l44 (1995).

[90] H. J. M. Bouwmeester, A. van der Lee, S. van Smaalen, G. A. Wiegers, Phys. Rev. B **43**, 9431 (1991).

[91] H. Rydberg, M. Dion, N. Jacobson, E. Schröder, P. Hyldgaard, S. I. Simak, D. C. Langreth, B. I. Lundqvist, Phys. Rev. Lett. **91**, 126402 (2003).

[92] J. A. Wilson, F. J. DiSalvo, and S. Mahajan, Adv. Phys. **24**, 117 (1975).

[93] H. Rose, D. Preikszas, Nucl. Instr. & Meth. A **363**, 201 (1995).

[94] R. Fink, M. R. Weiss, E. Umbach, D. Preikszas, H. Rose, R. Spehr, P. Hartel, W. Engel, R. Degenhardt, R. Wichtendahl, H. Kuhlenbeck, W. Erlebach, K. Ihmann, R. Schlogl, H. -J. Freund, A. M. Bradshaw, G. Lilienkamp, Th. Schmidt, E. Bauer, G. Benner, J. Electron Spectrosc. Relat. Phenom. **84**, 231 (1997).

[95] Th. Schmidt, U. Groh, R. Fink, E. Umbach, O. Schaff, W. Engel, B. Richter, H. Kuhlenbeck, R. Schögl, H.–J. Freund, A. M. Bradshaw, D. Preikszas, P. Hartel, R. Spehr, H. Rose, G. Lilienkamp, E. Bauer, G. Benner, Surf. Rev. Lett. **9**, 223 (2002).

[96] T. Schmidt, private communication 2005 (SMART project).

[97] J. A. Scarfe, H. P. Hughes, J. Phys.: Condens. Matter **1**, 6865 (1989).

[98] M. Kalläne, K. Rossnagel, L. Kipp, to be published.

[99] J. J. Yeh, I. Lindau, At. Data Nucl. Data Tables **32**, 1 (1985).

[100] M. S. Silverman, Inorg. Chem. **5**, 2067 (1966).

[101] A. Snigiref, V. Kohn, I. Snigireva, B. Lengeler, Nature **384**, 49 (1996).

[102] B. Cederström, R. Cahn, M. Danielsson, M. Lundquist, and D. Nygren, Nature **404**, 951 (2000).

[103] S. Matsuyama, H. Mimura, H. Yumoto, Y. Sano, K. Yamamura, M. Yabashi, Y. Nishino, K. Tamasaku, T. Ishikawa, K. Yamauchi, Rev. Sci. Instrum. **77**, 103102 (2006).

[104] K. Schwarzschild, Astronomische Mitteilungen der Königlischen Sternwarte zu Göttingen **10**, 9 (1905).

[105] N. Yamaguchi, Z. Takahashi, Y. Nishimura, K. Watanabe, Y. Okamoto, A. Sakata, H. Azuma, T. Hara, J. Electron Spectrosc. Relat. Phenom. **144-147**, 1183 (2005).

[106] G. Schmahl, D. Rudolph, P. Guttman, O. Christ, in *Zone Plates for X–ray Microscopy, Springer Series of Optical Science*, edited by G. Schmahl, D. Rudolph (Academic, London, 1984), Vol. 43, pp. 63–74.

[107] J. Thieme, G. Schmahl, D. Rudolph, E. Umbach, *X–Ray Microscopy and Spectroscopy* (Springer, Berlin, 1996).

[108] L. Kipp, M. Skibowski, R. L. Johnson, R. Bernd, R. Adelung, S. Harm, R. Seemann, Nature **414**, 184 (2001).

[109] W. Chao, B. H. Harteneck, J. A. Liddle, E. H. Anderson, D. T. Attwood, Nature **435**, 1210 (2005).

[110] M. Born, E. Wolf, *Principles of optics*, 7. ed. (Camebridge University Press, Camebridge, 1999).

[111] M. Kalläne, Diploma thesis, Institut für Experimentelle und Angewandte Physik (Universität Kiel), 2003.

[112] D. J. Stigliani, R. Mittra, R. G. Semonin, J. Opt. Soc. Am. **57**, 610 (1967).

[113] J.–Ao Sun, A. Cai, J. Opt. Soc. Am. A **8**, 33 (1991).

[114] M. J. Simpson, A. G. Michette, J. Mod. Optic. **30**, 1455 (1983).

[115] C. Bergemann, H. Keymeulen, J. E. van der Veen, Phys. Rev. Lett. **91**, 204801 (2003).

[116] A. N. Kurokhtin, A. V. Popov, J. Opt. Soc. Am. A **19**, 315 (2002).

[117] F. Pfeiffer, C. David, J. F. van der Veen, C. Bergemann, Phys. Rev. B **73**, 245331 (2006).

[118] J. Kirz, J. Opt. Soc. Am. **64**, 301 (1974).

[119] B. Lai, W. B. Yun, D. Legnini, Y. Xiao, J. Chrzas, P. J. Viccaro, V. White, S. Bajikar, D. Denton, F. Cerrina, E. Di. Fabrizio, M. Gentili, L. Grella, M. Baciocchi, Appl. Phys. Lett. **61**, 1877 (1992).

[120] G. Schneider, Appl. Phys. Lett. **71**, 2242 (1997).

[121] A. G. Michette, S. J. Pfauntsch, A. Erko, A. Firsov, A. Svintsov, Opt. Commun. **245**, 249 (2005).

[122] V. V. Aristov, A. I. Erko, A. Yu. Nikulin, A. A. Snigirev, Opt. Commun. **58**, 300 (1986).

[123] V. V. Aristov, Yu. A. Basov, S. V. Redkin, A. A. Snigirev, V. A. Yunkin, Nucl. Instrum. Methods Phys. Res., Sect. A **261**, 72 (1987).

[124] A. I. Erko, X–ray Sci. Technol. **2**, 297 (1990).

[125] A. Erko, Yu. Agafonov, L.A. Panchenko, A. Yakshin, P. Chevallier, P. Dhez, F. Legrand, Opt. Commun. **106**, 146 (1994).

[126] L. Haroutunyan and G. Hovhannisyan, J. Synchrotron Radiat. **13**, 343 (2006).

[127] S. Lipson, H. Lipson, D. Tannhauser, *Optik* (Springer, Berlin, YEAR).

[128] Q. Cao, and J. Jahns, J. Opt. Soc. Am. A **19(12)**, 2387 (2002).

[129] A. G. Michette, in *Optical Systems for Soft X–Rays* (Plenum, New York, 1986), pp. 193–194.

[130] R. Menon, D. Gil, G. Barbastathis, H. I. Smith , J. Opt. Soc. Am. A **22(2)**, 342 (2005).

[131] S. J. Spector, C. J. Jacobsen, D. M. Tennant, J. Vac. Sci. Technol. B **15**, 2872 (1997).

[132] Q. Cao, and J. Jahns, J. Opt. Soc. Am. A **21(4)**, 561 (2004).

[133] S. A. Azizi, *Entwurf und Realisierung digitaler Filter* (Oldenbourg, München, 1983).

[134] V. Capellini, A. G. Constantinides, P. Emiliani, *Digital Filters and their Applications* (Academic Press, London, 1981).

[135] J. Buck, Diploma thesis, Institut für Experimentelle und Angewandte Physik (Universität Kiel), 2004.

[136] J. Bartussek, Diploma thesis, Institut für Experimentelle und Angewandte Physik (Universität Kiel), 2006.

[137] Joint development with L. Kipp.

[138] Q. Cao, and J. Jahns, J. Opt. Soc. Am. A **20(6)**, 1005 (2003).

[139] D. Rahn, Diploma thesis, Institut für Experimentelle und Angewandte Physik (Universität Kiel), 2004.

[140] C. Jacobsen, S. Williams, E. Anderson, M. T. Browne, C. J. Buckley, D. Kern, J. Kirz, M. Rivers, X. Zhang, Opt. Commun. **86**, 351 (1991).

[141] B. Niemann, P. Guttmann, D. Hambach, G. Schneider, D. Weiss, G. Schmaal, Nucl. Instrum. Methods Phys. Res., Sect. A **467–468**, 857 (2001).

[142] D. Hambach, M. Peuker, G. Schneider, Nucl. Instrum. Methods Phys. Res., Sect. A **467–468**, 877 (2001).

[143] B. Niemann, T. Wilhein, T. Schliebe, R. Plontke, O. Fortagne, I. Stolberg, M. Zierbock, Microelectron. Eng. **30**, 49 (1998).

[144] T. Wilhein, D. Hambach, and B. Niemann, M. Berglund, L. Rymell, H. M. Hertz, Appl. Phys. Lett. **71**, 190 (1997).

[145] T. Wilhein, D. Altenbernd, U. Teubner, E. Förster, R. Hässner, W. Theobald, R. Sauerbrey, J. Opt. Soc. Am. B **15**, 1235 (1998).

[146] Center for X–Ray Optics, X-Ray Interactions with Matter Calculator.

[147] R. Reininger, V. Saile, Nucl. Instrum. Methods Phys. Res., Sect. A **288**, 343 (1990).

[148] T. M. Grehk, W. Drube, L. Kipp and G. Materlik, J. Synchrotron Rad. **8**, 1015 (2001).

[149] http://www.attocube.com/nanoPOSITIONING/working_principal.htm.

[150] http://hasylab.desy.de/facilities/doris_iii/beamlines/bw3/index_eng.html.

[151] H. B. Pedersen, S. Altevogt, B. Jordon-Thaden, O. Heber, M. L. Rappaport, D. Schwalm, J. Ullrich, D. Zajfman, R. Treusch, N. Guerassimova, M. Martins, J.–T. Hoeft, M. Wellhöfer, A. Wolf, Phys. Rev. Lett. **98**, 223202 (2007).

[152] R. Moshammer, Y. H. Jiang, L. Foucar, A. Rudenko, Th. Ergler, C. D. Schröter, S. Lüdemann, K. Zrost, D. Fischer, J. Titze, T. Jahnke, M. Schöffler, T. Weber, R. Dörner, T. J. M. Zouros, A. Dorn, T. Ferger, K. U. Kühnel, S. Düsterer, R. Treusch, P. Radcliffe, E. Plönjes, J. Ullrich, Phys. Rev. Lett. **98**, 203001 (2007).

[153] S. W. Epp, J. R. Crespo Lopez–Urrutia, G. Brenner, V. Mäckel, P. H. Mokler, R. Treusch, M. Kuhlmann, M. V. Yurkov, J. Feldhaus, J. R. Schneider, M. Wellhöfer, M. Martins, W. Wurth, J. Ullrich, Phys. Rev. Lett. **98**, 183001 (2007).

[154] H. N. Chapman, A. Barty, M. J. Bogan, S. Boutet, M. Frank, S. P. Hau-Riege, S. Marchesini, B. W. Woods, S. Bajt, W. H. Benner, R. A. London, E. Plönjes, M. Kuhlmann, R. Treusch, S. Düsterer, T. Tschentscher, J. R. Schneider, E. Spiller, T. Möller, C. Bostedt, M. Hoener, D. A. Shapiro, K. O. Hodgson, D. V. D. Spoel, F. Burmeister, M. Bergh, C. Chaleman, G. Huldt, M. M. Seibert, F. R. N. C. Maia, R. W. Lee, A. Szöke, N. Timneanu, J. Hajdu, Nat. Phys. **2**, 839 (2006).

[155] L. Kipp, private communication.

[156] M. Martins, M. Wellhöfer, J. T. Hoeft, W. Wurth, J. Feldhaus, R. Follath, Rev. Sci. Instrum. **77**, 115108 (2006).

[157] M. Marczynski–Bühlow, private communication.

[158] K. Rossnagel, L. Kipp, M. Skibowski, C. Solterbeck, T. Strasser, W. Schattke, D. Voss, P. Krüger, A. Mazur, J. Pollmann, Phys. Rev. B **63**, 125104 (2001).

[159] X.J. Zhou, B. Wannberg, W.L. Yang, V. Brouet, Z. Sun, J.F. Douglas, D. Dessau, Z. Hussain, Z.–X. Shen, J. Electron Spectrosc. Relat. Phenom. **142**, 27 (2005).

[160] S. Passlack, S. Mathias, O. Andreyev, D. Mittnacht, M. Aeschlimann, M. Bauer, J. Appl. Phys. **100**, 024912 (2005).

[161] B. J. Siwick, J. R. Dwyer, R. E. Jordan, R. J. Dwayne Miller, J. Appl. Phys. **92**, 1643 (2002).

[162] E.L. Saldin, E.A. Schneidmiller, M.V. Yurkov, Nucl. Instrum. Methods Phys. Res., Sect. A **562**, 472 (2006).

[163] E.L. Saldin, E.A. Schneidmiller, M.V. Yurkov, Opt. Commun. **148**, 383 (1998).

[164] K. Rossnagel, private communication.

[165] S. Düsterer, P. Radcliffe, G. Geloni, U. Jastrow, M. Kuhlmann, E. Plönjes, K. Tiedtke, R. Treusch, J. Feldhaus, P. Nicolosi, L. Poletto, P. Yeates, H. Luna, J. T. Costello, P. Orr, D. Cubaynes, M. Meyer , Opt. Lett. **31**, 1750 (2006).

[166] S. Harm, Ph.D. thesis, Institut für Experimentelle und Angewandte Physik (Universität Kiel), 1994.

[167] M. Marczynski, Diploma thesis, Institut für Experimentelle und Angewandte Physik (Universität Kiel), 2004.

List of abbreviations

ALS	**A**dvanced **l**ight **s**ource
APSF	**a**mplitude **p**oint **s**pread **f**unction
ARPES	**a**ngle–**r**esolved **p**hotoelectron **s**pectroscopy
BW3	**b**ypass–**w**iggler beamline **3** at HASYLAB
BL7	undulator **b**eam**l**ine **7** at the ALS
BL31	undulator **b**eam**l**ine **31** at the MAX–lab
BZ	**B**rillouin **z**one
DESY	**D**eutsches **E**lektronen–**S**ynchrotron
DORIS	**Do**ppel**ri**ng**s**peicher
DOF	**d**epth **o**f **f**ocus
DOS	**d**ensity **o**f **s**tates
EDC	**e**nergy **d**istribution **c**urve
EDX	**e**nergy **d**ispersive **X**–ray analysis
FEL	**f**ree–**e**lectron **l**aser
FLASH	**f**ree–electron **las**er in **H**amburg
FKDF	**F**resnel–**K**irchhoff **d**iffraction **f**ormula
FT	**F**ourier **t**ransform
FWHM	**f**ull **w**idth at **h**alf **m**aximum
FZ	**F**resnel **z**one
FZP	**F**resnel **z**one **p**late
FS	**F**ermi **s**urface
HASYLAB	**Ha**mburger **Sy**nchrotronstrahlungs**la**bor
LEED	**l**ow **e**nergy **e**lectron **d**iffraction
NA	**n**umerical **a**perture
OSA	**o**rder **s**orting **a**perture
PAD	**p**hotoelectron **a**ngular **d**istribution
PEM	**p**hoto**e**lectron **m**icroscope
PS	**p**hoton **s**ieve
PSF	**p**oint **s**pread **f**unction
RFZP	**r**eflective **F**resnel **z**one **p**late
RMS	**r**oot **m**ean **s**quare
RPS	**r**eflective **p**hoton **s**ieve
SASE	**s**elf **a**mplified **s**pontaneous **e**mission
STM	**s**canning **t**unneling **m**icroscopy
TEM	**t**ransmission **e**lectron **m**icroscopy
TMDC	**t**ransition **m**etal **d**ichal**c**ogenide
UHV	**u**ltra**h**igh **v**acuum
vdW	**v**an **d**er **W**aals
VUV	**v**acuum **u**ltra**v**iolet
UV	**u**ltra**v**iolet
XPS	**X**–ray **p**hotoelectron **s**pectroscopy

List of publications

International journals

1. M. Kalläne, K. Rossnagel, M. MarczynskiBühlow, L. Kipp, H. I. Starnberg, and S. E. Stoltz
   Metal cross–substitution in the misfit layer compound $(PbS)_{1.13}TaS_2$,
   submitted.

2. M. Kalläne, D. Rahn, J. Buck, K. Rossnagel, S. Harm, and L. Kipp,
   Focusing X-rays with arrays of nanomirrors or nanoabsorbers,
   in preparation.

3. M. Kalläne, K. Rossnagel, and L. Kipp,
   Charge transfer and incommensurability in TMDC misfit compounds,
   in preparation.

Research reports

1. M. Kalläne, S. Harm, R.L. Johnson, L. Kipp,
   Focussing XUV photons with high contrast,
   HASYLAB Annual Report 2003.

2. M. Kalläne, J. Buck, S. Harm, K. Rossnagel, R.L. Johnson, L. Kipp,
   Advances in nanofocusing with reflective photon sieves,
   HASYLAB Annual Report 2004.

3. J. Iwicki, B. Murphy, M. Kalläne, K. Rossnagel, L. Kipp,
   Electronic structure of pentacene on layered materials,
   HASYLAB Annual Report 2004.

4. M. Marczynski, M. Kalläne, S. Harm, K. Rossnagel, L. Kipp,
   A multichannel detection photoemission experiment,
   HASYLAB Annual Report 2004.

5. M. Kalläne, S. Stoltz, H. Starnberg,
   Photoelectron spectromicroscopy study of the misfit layer compound $(PbS)_{1.13}TaS_2$ *and its interaction with deposited Cs*,
   MAX-lab Activity Report 2004.

6. M. Marczynski, M. Kalläne, T. Riedel, S. Harm, K. Rossnagel, L. Kipp,
   Angle resolved photoemission at the VUV–FEL,
   HASYLAB Annual Report 2005.

7. B. Murphy, M. Quitzau, J. Buck, M. Kalläne, K. Rossnagel, R.L. Johnson, L. Kipp,
   Structural changes to $NbSe_2$ *upon iron intercalation*,
   HASYLAB Annual Report 2005.

8. M. Kalläne, D. Rahn, S. Harm, J. Buck, M. Marczynski–Bühlow, T. Riedel, K. Rossnagel, L. Kipp,
First spatially resolved photoemission measurements at BW3 using reflective photon sieves,
HASYLAB Annual Report 2006.

List of presentations

National conferences

1. L. Kipp, M. Kalläne, M. Skibowski, R.L. Johnson, R. Berndt, R. Adelung, S. Harm, R. Seemann,
Sharper images by focusing soft X-rays with photon sieves,
DPG spring meeting, Regensburg 2002, poster presentation.

2. M. Kalläne, S. Harm, M. Skibowski, R.L. Johnson, R. Seemann, L. Kipp,
Focusing and imaging with photon sieves,
DPG spring meeting, Dresden 2003, poster presentation.

3. J. Buck, M. Kalläne, S. Harm, M. Skibowski, R.L. Johnson, L. Kipp,
Focussing XUV photons with high contrast,
DPG spring meeting, Regensburg 2004, poster presentation.

4. J. Iwicki, A. Kamenz, O. Seifarth, S. Habouti, M. Kalläne, L. Kipp,
Geometric and electronic structure of epitaxial PbS on HfS_2,
DPG spring meeting, Regensburg 2004, poster presentation.

5. M. Marczynski, K. Rossnagel, M. Kalläne, E.E. Krasovskii, M. Skibowski, W. Schattke, L. Kipp,
High energy conduction band states in layered materials,
DPG spring meeting, Regensburg 2004, poster presentation.

6. M. Helle, M. Marczynski, M. Kalläne, S. Harm, K. Rossnagel, L. Kipp,
A multichannel detection photoemission experiment,
DPG spring meeting, Berlin 2005, poster presentation.

7. J. Bartussek, J. Buck, M. Kalläne, S. Harm, K. Rossnagel, L. Kipp,
Advances in nanofocusing with reflective photon sieves,
DPG spring meeting, Berlin 2005, poster presentation.

8. D. Rahn, B. Murphy, J. Iwicki, M. Kalläne, K. Rossnagel, F. Tuczek, L. Kipp,
An investigation of Nitrogen interaction at the Iron Pyrite (100) surface,
DPG spring meeting, Berlin 2005, poster presentation.

9. F. Baehr, J. Iwicki, B. Murphy, M. Kalläne, K. Rossnagel, L. Kipp,
Geometric and electronic structure of pentacene on layered materials,
DPG spring meeting, Berlin 2005, poster presentation.

10. M. Kalläne, H. Starnberg, K. Rossnagel, S. Stoltz, L. Kipp,
Electronic structure of misfit layer chalcogenides,
DPG spring meeting, Berlin 2005, oral presentation.

11. M. Marczynski, M. Kalläene, T. Riedel, S. Harm, K. Rossnagel, L. Kipp,
Angle Resolved Photoemission Spectroscopy at VUV-FEL,
DPG spring meeting, Dresden 2006, poster presentation.

12. D. Rahn, J. Bartussek, C. Hamann, J. Buck, M. Kalläne, S. Harm, K. Rossnagel, L. Kipp,
Theoretical and experimental approaches to the characterization of reflective nano-focusing photon sieves,
DPG spring meeting, Dresden 2006, poster presentation.

13. M. Marczynski, M. Kalläne, T. Riedel, S. Harm, K. Rossnagel, L. Kipp,
Angle Resolved Photoemission Spectroscopy at VUV–FEL,
Deutsche Tagung für Forschung mit Synchrotronstrahlung, Neutronen und Ionenstrahlen an Großgeräten, Hamburg 2006, poster presentation.

14. M. Kalläne, T. Riedel, D. Rahn, S. Harm, K. Roßnagel, J. Buck, M. Marczynski–Bühlow, C. Thede, L. Kipp
Spatially resolved photoemission measurements using reflective photon sieves,
DPG spring meeting, Regensburg 2007, poster presentation.

Eidesstattliche Erklärung

Hiermit erkläre ich an Eides Statt, daß ich diese Arbeit selbständig unter der Beratung meiner wissenschaftlichen Lehrer und nur mit den angegebenen Hilfsmitteln erstellt habe. Diese Arbeit wurde weder ganz noch in Teilen an anderer Stelle im Rahmen eines Prüfungsverfahrens vorgelegt.
Frühere Promotionsversuche wurden von mir nicht vorgenommen.

Kiel, den